UAB
Universitat Autònoma de Barcelona

A Network Synthesis Approach to Microwave Acoustic Filters and Multiplexers
Bridging the fields of filter synthesis and acoustic waves

Eloi Guerrero Menéndez

Universitat Autònoma de Barcelona

Department of Telecommunications and Systems Engineering

A Network Synthesis Approach to Microwave Acoustic Filters and Multiplexers

Bridging the fields of filter synthesis and acoustic waves

Ph. D. dissertation in Electronic and Telecommunication Engineering by

Eloi Guerrero Menéndez
eloi.guerrero@uab.cat

Doctoral Supervisor
Professor Pedro de Paco Sánchez
pedro.depaco@uab.cat

September, 2023

"It requires a much higher degree of imagination to understand the electromagnetic field than to understand invisible angels. [...] I speak of the E and B fields and wave my arms and you may imagine that I can see them [...] but I cannot really make a picture that is even nearly like the true waves."

Richard P. Feynman,
The Feynman Lectures on Physics

Abstract

Microwave acoustic technology is a fundamental enabler of the now ubiquitous wireless communication devices (let them be smartphones, routers, sensing nodes or even small base stations, to name a few): an unmatched miniaturization capability paired with excellent performance make it the mainstay for the filtering stages of modern radio frequency front-end modules for mobile devices. Even further, with the current deployment of 5G and the already ongoing development of 6G, a bright future for the technology is foreseeable together with a plethora of challenges still to be solved. In this context, this thesis aims at tackling the complexity of microwave acoustic filter and multiplexer design building on concepts from a not very well known but very interesting research field named network synthesis.

In this work, the discussion of network synthesis techniques in the context of microwave acoustic technology is constructed in two separated paths. Starting from the consideration of two-port networks, this thesis covers the exploitation of the input and output reflection phase of a filter describing its impact in final device parameters and develops both the intrinsic considerations of ladder filters starting in shunt resonator and the possibility to compose devices with two passbands by considering reflection phases of two separate ladder structures. Building on the findings from such discussion, an approach to compose ladder filters with transmission zeros at unexpected positions is discussed and demonstrated with a fabricated prototype.

The second network synthesis discussion path in this work is devoted to extending the already developed synthesis techniques to consider multiplexers. A core component in modern front-ends implementing carrier aggregation, and a true design challenge. The multiplexer synthesis technique proposed for the first time in this thesis is based on computing how must a set of filter responses be such that when connected together at a common port, the desired multiplexer response fulfilling specifications is obtained.

From a technological perspective, in parallel to the developed network synthesis techniques, this work also presents the results obtained from the initial manufacturing and characterization stages of microwave acoustic resonators based on exploiting the zeroth-order shear horizontal mode on a thin film of lithium niobate with the objective of developing a demonstration platform for some of the synthesis techniques in this thesis. The discussion of such results is focused on the effects of electrode thickness and transducer apodization patterns on the suppression of spurious modes both in the longitudinal and transversal directions, respectively.

Resum

La tecnologia acústica de microones és el fonament que possibilita la gran quantitat de dispositius de comunicació sense fils que ens envolta (siguin aquests des de telèfons mòbils, encaminadors, sensors o fins i tot petites estacions base): una capacitat de miniaturització sense precedents emparellada amb un rendiment excel·lent fan d'aquesta tecnologia la base de les etapes de filtrat de les capçaleres de radiofreqüència per a dispositius mòbils. Aquests fets, afegits al desplegament de la tecnologia 5G i els treballs en el desenvolupament de 6G, permeten preveure tant un futur brillant per la tecnologia com una llarga llista de reptes per resoldre. En aquest context, aquesta tesi aspira a enfrontar la gran complexitat de dissenyar filtres i multiplexors microacústics construint sobre conceptes d'un camp poc conegut però molt interessant anomenat síntesis de xarxes.

En aquesta tesi, la discussió sobre síntesi de xarxes en el context de la tecnologia microacústica es desenvolupa en dos camins. Començant per considerar xarxes de dos ports, la tesi se centra en com explotar la fase de reflexió tant a l'entrada com a la sortida d'un filtre per descriure l'impacte que aquesta té sobre els paràmetres finals del filtre i desenvolupa les consideracions necessàries per a sintetitzar un filtre en escala començant en ressonador paral·lel així com la possibilitat d'obtenir dispositius implementant dues bandes de pas considerant les fases de reflexió de dos filtres en escala diferents. A partir de les conclusions extretes en aquesta discussió, també es presenta la possibilitat de sintetitzar filtres microacústics en escala amb zeros de transmissió en posicions no esperades i es demostra un prototip fabricat.

El segon camí de discussió de la síntesi de xarxes en aquest treball se centra en estendre les tècniques de síntesi ja conegudes i presentades a la tesi per a considerar també, per primera vegada, multiplexors. Un tipus de dispositiu fonamental en les capçaleres modernes que permeten agregat de portadores i que suposa un veritable repte de disseny. La tècnica de síntesi per a multiplexors presentada en aquesta tesi es basa en calcular com han de ser les respostes d'un conjunt de filtres per tal que quan es connecten junts en un port comú, la resposta de multiplexor obtinguda sigui la desitjada i compleixi les especificacions.

En paral·lel a les tècniques de síntesi de xarxes desenvolupades, aquest treball també presenta els resultats obtinguts en les fases inicials de fabricació i caracterització de ressonadors microacústics explotant el mode transversal horitzontal d'ordre zero en una làmina fina de niobat de liti amb l'objectiu de desenvolupar una plataforma de demostració de les tècniques de síntesi presentades en aquesta tesi. La discussió d'aquests resultats tecnològics se centra en els efectes del gruix de l'elèctrode i dels patrons d'apoditzat del transductor interdigital en la supressió de modes espuris tant en la direcció longitudinal com la transversal, respectivament.

Acknowledgements

At first, I would like to express my deepest appreciation to my supervisor, Professor Pedro de Paco, for giving me the opportunity to pursue this research, for patiently answering all my questions and for letting me spend much time (and resources) in many side projects in the lab. Besides all the discussions related to the content in this thesis, I am indebted to him for the many very fruitful discussions on a very long list of microwave topics.

Moreover, I would like to thank Jordi Verdú, for his support, the fruitful discussions and his involvement in this work, and the rest of professors of the Waves Lab team at UAB, Josep Parrón and Gary Junkin, for answering many of my questions on antenna design. Additionally, I am grateful to Angel, Patricia and Carlos, the past and present office mates who have endured my presence around them, along Daniel and Ivan, Ph.D. program colleagues, for all the fun and good times. Not listing them all not to leave anyone out, I appreciate the collaboration and good times with all the recent incorporations to the Waves Lab graduate students team.

Besides the UAB environment, I would like to express my deep gratitude to Alfred Giménez, manager of the Advanced Design group, BAW R&D at Qorvo Inc., as well as Yazid Yusuf, Paul Stokes, Mudar Al-Joumaily and Gernot Fattinger, all from Qorvo's BAW R&D, for accepting me for an internship in the US, for the many things I have learned from them and for giving me the opportunity to be a part of the BAW R&D team at the moment of writing these lines.

In parallel, I would like to extend my thanks to all of those who have contributed to the results obtained in these three years of research: Professor Songbin Gong and Yansong Yang for sharing some of their measurements with us, to Jaume Esteve, Xavier Borrisé and Albert Guerrero from IMB-CNM-CSIC for their discussions and effort in the manufacturing of the LNOI devices, to Ernesto Díaz for all the help with hardware manufacturing in the lab and to Luca Colombo for the interesting collaboration on acoustic wave matching networks and the discussions on lithium niobate resonator manufacturing.

To close, on a more personal dimension, words cannot fully express my gratitude to my family and friends, for all their support, and to Lluís, my friend, office mate and Ph.D. colleague, for always being there not only during the Ph. D. but since high school. His contribution and our many discussions in the most unexpected situations have been key to many outcomes in this thesis.

Eloi

Contents

List of Figures

List of Tables

CHAPTER 1

Introduction

At the moment of reading this introduction, the reader is completely surrounded by a rare, critical and finite resource that is much more expensive than any other material on earth: the electromagnetic (EM) spectrum. It cannot be observed or felt but plays a major role in most of our daily activities. From the simple act of listening to FM radio or opening a car with a key fob to a video call using a smartphone, spectrum is involved as the fundamental enabler resource. Given its criticality, managing it correctly and ensuring the coexistence of multiple communication systems in closely spaced frequencies has historically been a topic of concern for microwave engineers. Radio frequency (RF) filters, frequency-selective components that allow to reject portions of the spectrum while accepting others, constitute a very intensive field of research that spans a wide range of microwave technologies and passbands located all along the frequency spectrum. RF filters are a cornerstone of almost every system utilizing the electromagnetic spectrum and are found inside the great majority of RF front end modules (RF-FEM).

The scope of this thesis is centered around a specific type of filters: those that are integrated inside the now ubiquitous smartphones and many mobile devices. Without diving yet into the technological details of such filters and the fascinating world they compose, let us first justify the important role they play in many parts of our day to day life. While key fobs and FM radio might seem simple systems and not specially spectrum-hungry, mobile communications have become a basic part of daily life and are one of the most spectrum-demanding services. To exemplify it, considering statistics from the Nov. 2022 Ericsson Mobility Report [1], mobile communications are responsible for 90 exabytes (EB) of monthly data traffic at the end of 2022 and are expected to generate 324 EB per month at the end of 2028. Not only this is an enormous amount of data but also must be transmitted as fast as possible and with minimum latency to allow real time applications. In this scope, consider that channel capacity is directly related to usable bandwidth and signal to noise ratio (SNR) [2, 3]

and such relation has a strong impact on the importance of spectrum management devices. It drives the appetite for more bandwidth, thus requiring more bands dedicated to mobile communications, and also, considering a denser network of base stations to increase SNR without increasing transmit power due to mobile devices being battery-powered, the need to handle higher interference levels, hence requiring enhanced rejection.

The increasing need for more bandwidth can be exemplified with the evolution of mobile communication standards over the last decades: from the analog Advanced Mobile Phone System (AMPS) operating a single band at 850 MHz to the currently under deployment fifth generation of communications (5G) featuring 62 different frequency bands within frequency range 1 (FR1) from 410 to 7125 MHz [4] and up to 6 bands distributed along the frequency range 2 (FR2) from 24.25 to 71 GHz [5], meanwhile academia is already discussing technological approaches and applications of 6G. Higher bandwidths are not only achieved by the allocation of new bands to mobile communications and moving up to higher frequencies but also through additional techniques such as multiple input/multiple output (MIMO) strategies allowing frequency re-use within the same mobile device thanks to antenna diversity or carrier aggregation (CA) [6] (Ch. 4), the concurrent operation of multiple carriers both within and among frequency bands to achieve higher instantaneous bandwidth[1]. Such strategies play an important role in defining the filtering requirements of a mobile device and pose complex hardware design challenges. To name an example, CA is of specific interest for this thesis because aggregation of carriers among different bands involves the joint connection of multiple filters to a single antenna forming a multiplexer. A very complex design problem to which a chapter is devoted.

The brief description of the basic spectrum aspects of 5G in the above paragraph is intended as a justification of why RF filters are an essential part of communication systems. Even further, note that the number of bands inside FR1 mentioned above are only those specifically licensed for mobile communications. Many other services using the spectrum in that frequency range such as for example global navigation satellite systems (GNSS) (e.g., Galileo or GPS), unlicensed bands also used for wireless communications such as those part of IEEE 802.11 (i.e., WiFi) or terrestrial trunked radio, to name a few, must coexist with cellular bands. The reader is encouraged to consult the FCC Radio Spectrum Allocation chart [7] for a better understanding on how crowded the spectrum is and the demanding performance requirements it poses on RF filters in terms of rejection to adjacent bands and response selectivity.

[1] Up to 5 sub-channels of 20 MHz in LTE initial releases, achieving up to 100 MHz instantaneous bandwidth, and extended to 32 aggregated carriers in Release 13 enabling up to 640 MHz bandwidth. Total bandwidth of 1 GHz can now be achieved through the so-called Dual Connectivity in 5G [6] (Ch. 5).

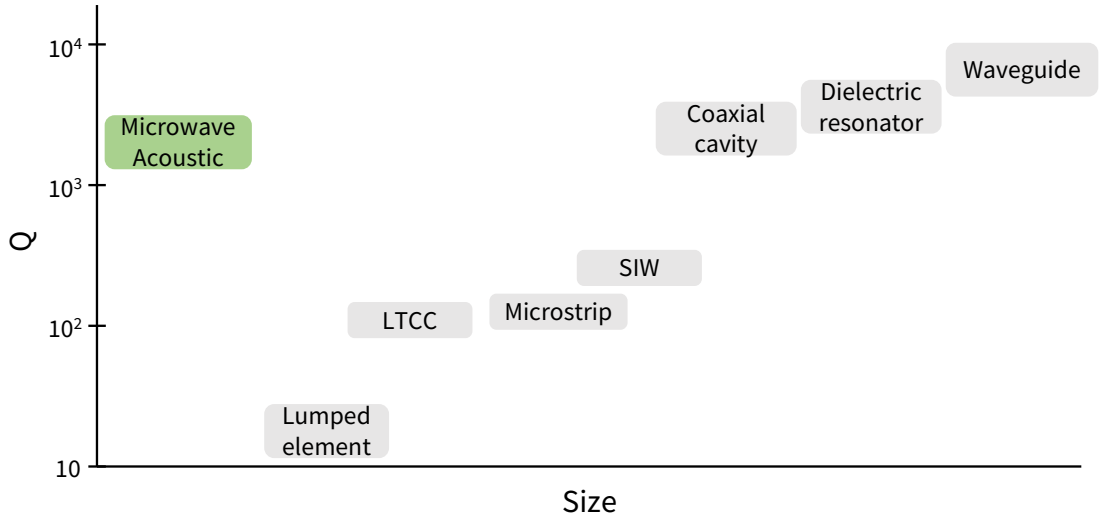

Figure 1.1: Qualitative map of common microwave resonator technologies as a function of achievable Q and resonator size for a reference frequency of 3 GHz.

1.1 A Filter Technology for Mobile Devices

Having introduced the need for RF filters to manage the spectrum, the attention must now be directed to two very critical assets from a mobile phone perspective: space and energy. The scarcity of space might be described with a very simple example if one assumes a premium smartphone equipped to work both in Europe, North America and China, featuring GNSS, Bluetooth and WiFi connectivity both in the 2.4 and 5 GHz bands. From the brief introduction to 5G spectrum needs, the total filter count inside such smartphone, without considering any advanced feature such as duplicated bands for receiver diversity or MIMO, is well above 70. Clearly, for the device to comfortably fit in the users hands and pockets, extreme miniaturization requirements must be imposed on the filter side. However, miniaturization when dealing with RF usually involves a cost.

Let us briefly introduce here that the basic building blocks of RF filters are resonators. Elements whose frequency-dependent electrical performance is characterized by frequencies at which they behave as either an open or a short circuit depending on how the energy distributes inside the structure. From an EM point of view, at resonance, a resonator dynamically exchanges energy between the electric and magnetic fields. In addition, an important figure of merit of resonators is the quality factor Q that describes the inherent losses in the resonator per oscillation cycle at the resonance frequency. While this is an extremely simplified conceptual description of a resonator, it allows to introduce that the losses experienced by the frequencies within the passband of an RF filter (i.e., insertion losses) are ultimately related to the quality factor of the resonators that compose it. From this fact, energy, the second scarce asset pointed out at the beginning of this section, gains importance. Since mobile devices are powered by batteries and lifetime is a priority, it is of the utmost importance to minimize losses of transmitter power at the filters of RF-FEMs to avoid increasing battery con-

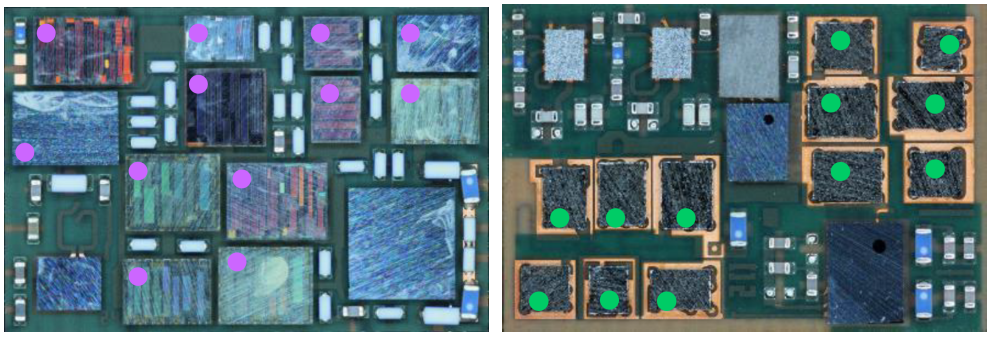

(a) (b)

Figure 1.2: Pictures of two RF front-end modules for mobile devices by Qorvo Inc. ©2017 (extracted from [8]) both having a footprint of 45 mm^2. (a) Low-band RF-FEM featuring 12 SAW filters (purple dots). (b) Mid-band RF-FEM featuring 12 BAW filters (green dots).

sumption. Even further, resonator Q factor not only defines insertion losses but also has an impact on the achievable selectivity of a given filter. A key figure in a crowded spectrum situation.

The challenge for mobile phone filters is then double: achieving miniaturization while keeping a superior Q performance. To exemplify the trade-off between miniaturization and intrinsic losses, Fig. 1.1 shows a qualitative map positioning the main microwave resonator technologies and their achievable Q values at a given frequency as covered in [9] (Ch. 11). This map highlights two very important facts. At first, the clear cost of miniaturization in terms of losses is observed with the disposition of grey boxes and the trend they depict. These technologies share the common characteristic of all being EM resonators and show how volume is an important aspect in maximizing Q when dealing with electromagnetic fields. On the other hand, the map shows a clear outlier to the trend pointing out that microwave acoustic technology can achieve extreme miniaturization while providing Q factors in the order of thousands. For this reason, microwave acoustic or acoustic wave (AW) resonators are the basic building block of RF filters for mobile devices due to enabling unmatched degrees of miniaturization, for example, allowing the fabrication of several thousands of filters on a 6-inch wafer, while providing very high Q values. No other microwave technology is capable of achieving such performance and that is why AW filters have dominated the market of RF filters for mobile devices since its introduction at GHz frequencies [10–13]. Fig. 1.2a and 1.2b exemplify the degree of miniaturization provided by AW technology with two photographs of RF-FEMs by Qorvo Inc. each featuring 12 acoustic wave filters in 45 mm^2.

The superior performance of AW resonators is achieved by a complete change of the domain in which waves propagate and resonance takes place: as the name indicates, they are based in acoustic or mechanical waves propagating in solids to achieve the desired electrical performance. Resonant structures of microscopic dimensions can be constructed via the proper confinement of mechanical waves given that the velocity of such waves in solids is 10^5 times slower than electromagnetic

waves in vacuum and thus, mechanical wavelengths lie in the order of magnitude of microns at GHz frequencies. For such dimensions, manufacturing of AW devices involves processes common to microelectronic and integrated circuit (IC) fabrication.

Nevertheless, since wireless communications are based on EM waves, the key enabler to attain the mentioned change of domain is piezoelectricity, the capacity of a crystalline material of transducing mechanical energy into electromagnetic energy, and vice versa. Not all crystalline materials are piezoelectric and not all piezoelectric materials are equally efficient in such transduction. The specific properties of materials along with the fact that many acoustic propagation modes exist giving rise to different resonator structures make microwave acoustics a complete and complex field of research. To dive into the different types of AW resonators currently in use in RF-FEMs and to present the structures fabricated in this work, a complete chapter is devoted to microwave acoustic resonators in this dissertation.

As is covered in forthcoming chapters, many types of acoustic wave resonators exist depending on the mechanical wave they exploit. From an RF filter perspective, the two main resonator structures that fill the majority of the RF filter market for mobile devices are the bulk acoustic wave (BAW) and surface acoustic wave (SAW) resonators, each based on a different piezoelectric material. Additionally, in recent years a third type, namely plate wave resonators, have gained attention due to their interesting capabilities in terms of achievable filter bandwidth, as is discussed in this thesis. For the purpose of this introduction, let us remain in the electrical performance side and highlight that irrespective of the type of resonator structure, the electrical response of an AW resonator can be circuitally represented, in its fundamental mode of resonance, with the Butterworth-Van Dyke (BVD) model [14, 15] shown in Fig. 1.3a along with the traditional schematic symbol of an AW resonator that is used throughout this thesis.

The BVD model is of paramount importance since it allows to abstract from the mechanical domain and represent, in a completely electrical manner, the essential behavior of an AW resonator. In its fundamental mode of operation, the BVD model features the so-called motional arm composed of a series LC resonator (circuital elements L_a and C_a) that represents the resonance happening in the mechanical domain. The motional arm is in parallel to the so-called static arm composed of a capacitor C_0 representing the natural capacitive nature of the piezoelectric transducer. The BVD model, through its level of abstraction, is a fundamental tool in the early stages of filter design and allows fast and simple evaluation of filter responses. Moreover, although the example shown here is ideal and lossless, the complexity of the model can be scaled to reflect many physical parameters of an AW resonator. The simplest upgrade of it is including losses, both in the electrical and mechanical domains as in [16], but can also reflect spurious resonance modes in the mechanical domain through additional motional branches in parallel, for example.

By simple inspection of the circuit, it is clear that an AW resonator features two distinct reso-

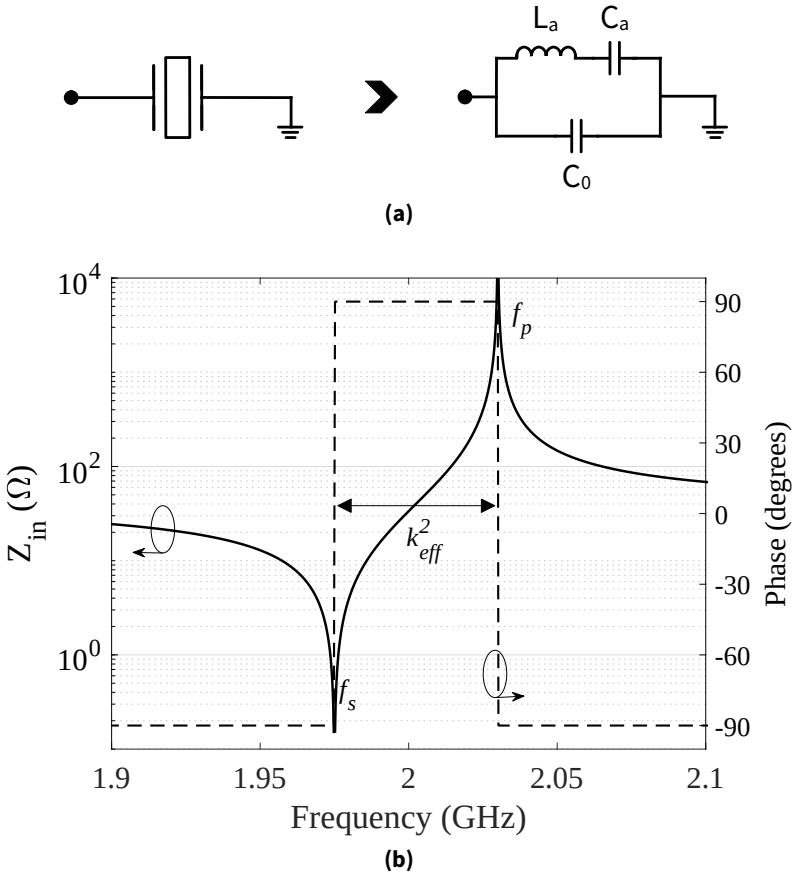

Figure 1.3: Fundamental electrical representation of an acoustic wave resonator. (a) Schematic representation of an AW resonator and the Butterworth-Van Dyke circuital model. (b) Input impedance and phase of the input impedance of an ideal and lossless AW resonator connected to ground.

nances with opposite behavior: a series resonance (f_s) at the frequency where the motional arm resonates and behaves as a short circuit and a parallel resonance (f_p) at which the inductive behavior of the motional arm at frequencies above f_s resonates with capacitance C_0, imposing an open circuit. Their expressions are easily derived as in (1.1) and the input impedance of an ideal AW resonator connected to ground is shown in Fig. 1.3b having $f_s = 1.975$ GHz, $f_p = 2.030$ GHz and $C_0 = 1.94$ pF. Notice the fact that the AW resonator depicts a capacitive behavior away from resonances (due to the nature of the capacitive transducer) and thus, it always holds that $f_s < f_p$ and only between f_s and f_p the resonator shows an inductive behavior.

$$f_s = \frac{1}{2\pi\sqrt{L_a C_a}} \qquad \text{and} \qquad f_p = \frac{1}{2\pi}\sqrt{\frac{C_a + C_0}{L_a C_a C_0}} = f_s\sqrt{1 + \frac{C_a}{C_0}} \tag{1.1}$$

More importantly, Fig. 1.3b introduces another fundamental parameter of AW resonators that has enormous implications in filter performance and is closely related to device physics, that is the effective electromechanical coupling coefficient (k^2_{eff}) that throughout this thesis is defined (follow-

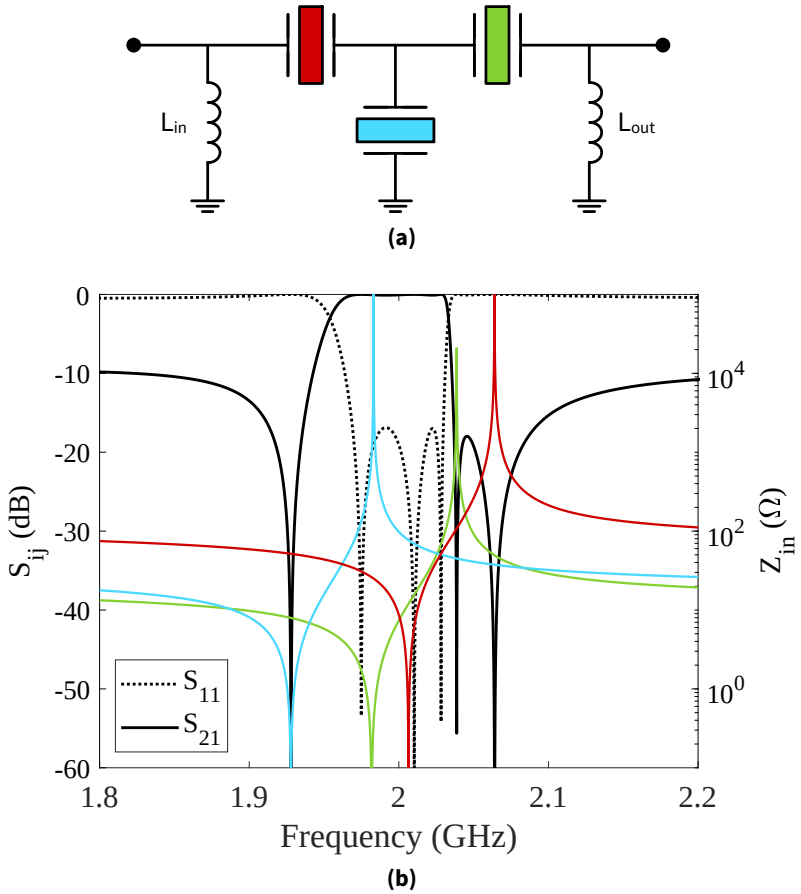

Figure 1.4: The AW ladder filter. (a) Schematic representation of an $N = 3$ ladder filter starting in series resonator. (b) Ideal lossless response of an $N = 3$ ladder filter with the input impedance of each of its resonators superimposed.

ing the definition by J. Kaitila in [17] (Ch. 3) for BAW resonators and as discussed in [18]) as:

$$k^2_{\text{eff}} = \frac{\pi}{2}\frac{f_s}{f_p}\cot\left(\frac{\pi}{2}\frac{f_s}{f_p}\right) \tag{1.2}$$

This coefficient, that relates the frequency separation between resonances, can be experimentally obtained by measuring f_s and f_p for a given AW resonator and is physically related to the transduction efficiency between the electrical and mechanical domains of a given piezoelectric material and strongly dependent on the direction of wave propagation and type of wave excited. At this point, to provide a clear description of the impact of k^2_{eff} in the context of AW filters and the achievable filter performance, let us briefly introduce the workhorse topology used for RF filters with AW resonators: the ladder topology. A schematic representation of the topology, in this case starting in series resonator, is shown in Fig. 1.4a for a filter of order $N = 3$.

The AW ladder filter is composed of AW resonators disposed in alternating series and shunt positions and implements filter responses of order N, where N is the number of AW resonators. Notice

that the AW ladder is an electrically connected filter, meaning that resonators form the filter via connections made in the electrical domain while resonances physically happen in the mechanical domain. Additionally, consider the presence of input and output shunt inductors L_{in} and L_{out}. These elements, as is discussed in this thesis, have a specific role directly related to the phase of the filter and can only be avoided if a set of specific conditions are applied. Moreover, the ladder structure can also start in shunt resonator and in that case, input and output inductors are connected in series. An specific study on the design of ladder filters starting in shunt resonator is provided in this dissertation.

To conceptually describe the working principle of the ladder filter, Fig. 1.4b depicts an ideal lossless response of an $N = 3$ AW ladder filter alongside the input impedance of each of the resonators composing it. This filter has been designed to implement a passband between 1.970 and 2.030 GHz and features three transmission zeros (TZs). That is, frequencies at which S_{21} is null. Considering the disposition of resonators in the topology and the fact that $f_s > f_p$, the origin of TZs in the ladder filter is directly related to the resonances of the AW resonators: shunt resonators place TZs below the passband at their f_s (because they impose a short circuit to ground) and series resonators place TZs above the passband at their f_p (because they impose an open circuit on the main path of the filter). This is highlighted in Fig. 1.4b where the blue line corresponds to the shunt resonator and red and green traces correspond to the two series resonators. From this conceptual description, two interesting observations can be easily highlighted: the type of filter response implemented by an AW ladder features as many TZs as resonators, an important aspect with implications in a forthcoming chapter, and an AW ladder filter has as many TZs above/below the passband as series/shunt resonators, respectively. This latter fact has been considered an unbreakable rule for many years and has been widely exploited in the design of RF filters for mobile devices. Although it holds true for the vast majority of cases, this thesis demonstrates that under certain circumstances and taking careful consideration of the phase of the filter such restriction can be overcome and ladder filters in which some resonators place TZs in the opposite side of the passband can be designed.

To close this section, an important remark can be intuitively derived from the example shown in Fig. 1.4b. While filter TZs are directly related to either f_s or f_p of shunt or series resonators, notice that the remaining resonance of each of these resonators (i.e., f_p of shunt and f_s of series resonators) is actually in charge of forming the passband. At f_p of a shunt resonator there is an open circuit between the filter mainline and ground and therefore no signal can leak through the resonator to ground and, similarly, series resonators at their f_s act as short circuits allowing all signal to flow through the filter. Therefore, observe the clear relation between the achievable bandwidth of the ladder filter and k^2_{eff}, the relative distance between the two resonances of the acoustic wave resonators. This relation is historically stated, as a rule of thumb, as requiring a k^2_{eff} around twice the fractional bandwidth (FBW) of the filter in question [17] (Ch. 4). Such a relation has implications in selecting the piezoelectric material and type of resonator that best suits each application, as is covered in the following

chapter, and is the driver of research in new materials and resonator structures to cover the wider bands introduced with 5G.

1.2 The Challenge of Acoustic Wave Filter Design

Up to this point, this introduction has provided an overview of the need for RF filters to manage a crowded spectrum from a mobile device point of view along a brief description of acoustic wave technology and some of its key characteristics required for a better comprehension of the purpose of this dissertation. Although the working principle of the AW ladder filter has been conceptually described, such description does not depict the true complexity of designing RF filters with acoustic wave devices.

AW devices can be located at the intersection of material science and mechanics, microfabrication and microwave engineering. Although the ultimate performance of an AW resonator is evaluated from a microwave point of view, its behaviour has its roots in mechanical phenomena (i.e., acoustic waves) which in turn are strongly dependent on the physical properties of the material used as a medium for propagation. Moreover, given the microscopic dimensions of acoustic waves in the GHz frequency range, AW resonators are also tied to the fabrication capabilities in a clean room environment such as photolithography, metal deposition or the epitaxial growth of thin films of piezoelectric materials, to name a few. Clearly, the design and fabrication of an AW resonator with outstanding performance is a complex task and thus, the complete design of an AW filter, a device composed of many AW resonators at different frequencies, is directly a challenge if one also takes into account that the filter is not only evaluated from a response perspective but also must consider area requirements, power handling capabilities and non-linearities, among others.

On its own, microwave filter design constitutes an active field of research for the microwave community to which great efforts have been devoted during the last century [9, 19, 20] and that is very active given the ever-increasing performance requirements of RF filters today as spectrum is more populated. A key topic within filter design, in which this dissertation is focused and that is intensively used in the design of cavity and waveguide filters, is network synthesis. As opposed to network analysis, the mathematical procedures to compute the response of a circuit from which the elements and their disposition are known, network synthesis deals with the opposite problem. Computing the circuital elements and the disposition they must have to implement a desired response that is defined, a priori, at the mathematical level. Network synthesis techniques have been of interest since the beginning of the past century, as is covered with more detail in Chapter 3, and are extremely useful in the design of RF filters because they analytically provide a circuital model that implements a desired response and push the largest part of the effort into the physical realization of such circuit using EM resonators (either with waveguide cavities or coaxial resonators, to name a few). However, due to the relative novelty of the technology and the complexity outlined in the

previous paragraph, AW filters have not been treated from a network synthesis point of view until recent years with the works by the group hosting this thesis [21–26].

Building on network synthesis knowledge originally developed for traditional microwave filters, it is possible to develop techniques applicable to ladder filters made of acoustic wave resonators and exploit them to accelerate and improve AW filter design. At this point, let us highlight again the abstraction provided by the BVD model that accurately represents the electrical performance of the AW resonator at the circuital level. Being able to represent each AW resonator with its equivalent circuit model allows to approach the AW ladder filter from a network synthesis point of view and analytically compute how should those resonators be to compose a desired filter function. This analytical approach to AW filter design is in complete contrast with approaches (e.g., as described in [11]) that strongly rely on hard optimization stages at the circuital level to obtain the initial circuit seed from which a design cycle starts.

To better justify the importance of an analytical approach to AW filter design, let us briefly recall here a very important requirement for an AW ladder filter to be feasible, that is later expanded in Chapter 2. Since k^2_{eff} is tied to physical properties of the piezoelectric material and the type of resonator, due to process complexity and also piezoelectric material limitations (the reader has to consider that AW filters are fabricated on wafers already made of the piezoelectric material or on which such material is deposited) all resonators composing an AW ladder feature approximately the same electromechanical coupling coefficient [11]. To provide an example, for a BAW filter using aluminum nitride (AlN) as piezoelectric material, all resonators feature $k^2_{\text{eff}} \approx 6.7\%$, at most. Such coupling factor is inherently defined by the piezoelectric characteristics of AlN for vertically-propagating longitudinal waves. Back to the example in Fig. 1.4b, the $N = 3$ filter example is composed of three resonators having $k^2_{\text{eff}} = 6.7\%$.

For a brute-force optimization approach in which all BVD elements of a ladder filter are optimized to fulfill a set of rejection specifications and area requirements, imposing that all resonators must have evenly-distributed k^2_{eff} (i.e., the same relative frequency distance between resonances) is an added degree of complexity that turns the process into a very time consuming task. Moreover, it is easily seen that in such an optimization approach, many of the optimizer iterations might not even be close to a filtering response and might lead the process to fall into local minima. At this point, the filter designer has lost part of control on the network and is tied to the output of the optimizer.

On the contrary, exploiting a network synthesis approach avoids hard optimization stages and faces the problem in an alternative way. Given the synthesis provides the exact representation of a filter response with the circuit implementing it, the initial design of an AW ladder filter can be approached as surfing among all filter responses that already fulfill rejection specifications to find those that fulfill a given set of technological constraints such as k^2_{eff} for all resonators or filter area, among others. This philosophy becomes even more important by considering that an AW filter de-

sign might involve going back to the initial circuital stage if the design needs to be reworked at a later stage of the design cycle (let it be when evaluating non-linear effects or modifications of port impedance, to name a few). All in all, synthesis techniques for AW ladder devices have demonstrated their power both in industry and academia and many players in the AW industry are currently using network synthesis approaches.

More importantly, network synthesis not only serves as an analytical lever for filter design but also can be exploited as a *forensic* tool to understand the behaviour of already manufactured filters. One key example was demonstrated in [27, 28] by presenting the relation between electromagnetic parasitic paths and response distortion in AW ladder filters, highlighting the ultimate control that network synthesis provides on the role of all elements within a network. In Chapter 4 of this dissertation, another example of post-fabrication analysis using synthesis is provided for an AW ladder filter starting in shunt resonator.

Nevertheless, notice that synthesis has been presented to deal with an AW ladder filter. That is, a single filter. This is the context in which network synthesis has been traditionally developed. Now, as introduced in the initial paragraphs of this chapter, carrier aggregation schemes require multiple filters connected together, at the same time, to a common antenna port. The design challenge then involves the design of many AW ladder filters and must consider not only the response of each filter and the related technological constraints but also the reactive loading effects between the filters. Thus, the complexity of multiplexer design is well beyond that of a single filter. To face such a challenge from a network synthesis perspective, Chapter 5 this thesis presents an analytical technique to synthesize the entire multiplexer composed of AW ladder filters. A problem that had not been analytically approached previously in the literature.

To finish this introduction, an important objective of this thesis is to provide a link between the world of AW devices, diving into the fabrication of resonators and filters as a vehicle for demonstration, and the world of network synthesis to demonstrate its power and the important features it offers both for standalone filters and multiplexer modules.

1.3 Structure of this Thesis

After this introductory chapter that has provided an initial description of acoustic wave technologies, highlighting the central role they play in mobile communication RF-FEMs along a brief explanation of how network synthesis techniques provide an analytical way of facing the complexity of AW filter design to accelerate design cycle time, this thesis is structured into four more chapters.

At first, Chapter 2 dives deeper into the physical side of this thesis and aims to provide a description of acoustic wave technology from a microwave engineering point of view starting from the well-known SAW and BAW resonators and covering the more recent plate wave modes. Regard-

ing the latter, this chapter presents manufactured results of resonators exploiting the zeroth-order shear horizontal mode on thin films of lithium niobate ($LiNbO_3$) that are used in other sections of the thesis as a demonstration platform for the synthesis of AW filters.

Chapter 3 is devoted to a detailed description of the mathematical side of this thesis and presents the synthesis of AW filters providing a complete view to the synthesis cycle: from the definition of the filter function to implement to the method that allows to compute the circuital elements that compose the filter. At this point, the synthesis of AW filters is focused on single filters (i.e., two-port networks).

After describing how network synthesis is applied to AW ladder filters, Chapter 4 is focused around a very interesting feature of synthesis methods: the important role of controlling reflection phase. Firstly, this chapter reviews the synthesis of the AW ladder topology when starting in shunt resonator, highlighting interesting properties and outlining rules for the design of such filters, and then expands the phase modification to describe how reflection phase can be exploited to design dual-band filters by connecting two ladder filters in parallel. Finally, the chapter presents an interesting exploit of reflection phase to achieve filter responses with transmission zeros in unexpected positions. A manufactured example using the $LiNbO_3$ on insulator (LNOI) technology presented in Ch. 2 is provided in this chapter as a demonstration.

Finally, Chapter 5 is devoted to the problem of multiplexer synthesis. Going beyond the consideration of two-port networks, this chapter faces the synthesis of an entire multiplexer composed of AW ladder filters from an analytical point of view. The mathematical formulation to compute multiport functions is presented along the specific techniques that are needed to deal with high order polynomials and provides examples of synthesized multiplexers.

This thesis is closed with a conclusions chapter that summarizes the most important aspects developed throughout the text and also provides a set of recommendations regarding ongoing work and future lines of research.

1.4 Research Results

This dissertation gathers the outcome of the work developed during the Ph.D. studies and as a result, articles have been published in academic journals and have been presented at international conferences. The following is a list of the published contributions:

Journal articles

- E. Guerrero, L. Acosta, J. Verdú and P. de Paco, "Direct Synthesis of Acoustic Wave Multiplexers Built on Fully Canonical Multiport Functions," in *IEEE Transactions on Microwave Theory and Techniques*, vol. 71, no. 4, pp. 1391-1401, April 2023, doi: 10.1109/TMTT.2022.3222426.

- E. Guerrero, P. Silveira, J. Verdú, Y. Yang, S. Gong and P. de Paco, ”A Synthesis Approach to Acoustic Wave Ladder Filters and Duplexers Starting With Shunt Resonator,” in *IEEE Transactions on Microwave Theory and Techniques*, vol. 69, no. 1, pp. 629-638, Jan. 2021, doi: 10.1109/TMTT.2020.3033554.
- E. Guerrero, J. Verdú and P. de Paco, ”Synthesis of Extracted Pole Filters With Transmission Zeros in Both Stopbands and Nonresonant Nodes of the Same Nature,” in *IEEE Microwave and Wireless Components Letters*, vol. 31, no. 1, pp. 17-20, Jan. 2021, doi: 10.1109/LMWC.2020.3035848.

Co-authored journal articles

- C. Caballero, L. Acosta, E. Guerrero, J. Verdú and P. de Paco, ”Nonstandard Transmission Responses Enabling Feasible Microwave-Acoustic Ladder Filters,” in *IEEE Transactions on Microwave Theory and Techniques*, vol. 71, no. 9, pp. 3712-3721, Sept. 2023, doi: 10.1109/TMTT.2023.3251101.
- L. Acosta, E. Guerrero, J. Verdú and P. de Paco, ”Topology Assessment for Dual-Band Filters Based on Acoustic Wave Resonators,” in *IEEE Transactions on Microwave Theory and Techniques*, vol. 71, no. 4, pp. 1402-1411, April 2023, doi: 10.1109/TMTT.2022.3222327.
- J. Verdú, E. Guerrero, L. Acosta and P. de Paco, ”Exact Synthesis of Inline Fully Canonical Dual-Band Filters Using Dual Extracted-Pole Sections,” in *IEEE Microwave and Wireless Components Letters*, vol. 31, no. 12, pp. 1255-1258, Dec. 2021, doi: 10.1109/LMWC.2021.3114436.
- Á. Triano, P. Silveira, J. Verdú, E. Guerrero, P. de Paco, ”Phase Role in the Non-Uniformity of Main-Line Couplings in Asymmetric Extracted-Pole Inline Filters,” in *Electronics* 2021, 10, 3058. doi: 10.3390/electronics10243058
- J. Verdú, I. Baro, E. Guerrero, P. Silveira, A. Triano, G. Junkin and P. de Paco, ”Sensitivity Considerations for Inline Fully Canonical Filters at Ku-Band,” *Progress In Electromagnetics Research M*, Vol. 95, 125-133, 2020.

Other Journal Contributions

- E. Guerrero, J. Brugués, J. Verdú and P. de. Paco, ”Microwave Microphone Using a General Purpose 24-GHz FMCW Radar,” in *IEEE Sensors Letters*, vol. 4, no. 6, pp. 1-4, June 2020, Art no. 3501004, doi: 10.1109/LSENS.2020.2997978.
- J. Verdú, E. Guerrero, J. Parrón, A. Lázaro and P. de Paco, ”Star-Shaped Wheel for Mechanical Micro-Doppler Modulation,” in *IEEE Antennas and Wireless Propagation Letters*, vol. 20, no. 12, pp. 2452-2456, Dec. 2021, doi: 10.1109/LAWP.2021.3114440.

International conferences

- E. Guerrero, L. Acosta, J. Verdú and P. De Paco, "Acoustic Wave Multiplexer Modules: A Completely Analytical Synthesis Method," *2022 IEEE International Ultrasonics Symposium (IUS)*, 2022, pp. 1-3, doi: 10.1109/IUS54386.2022.9957168.
- E. Guerrero, L. Acosta, C. Caballero, J. Verdú, A. Guerrero, X, Borrisé, J. Esteve and P. De Paco, "On the Influence of Electrode Thickness in the Spurious Mode Reduction of Lithium Niobate-On-Insulator SH_0 Acoustic Wave Resonators," *2022 IEEE/MTT-S International Microwave Symposium (IMS)*, 2022, pp. 1037-1040, doi: 10.1109/IMS37962.2022.9865464.
- E. Guerrero, L. Acosta, J. Verdú and P. de Paco, "Analytical Synthesis of Acoustic Wave Duplexers and Multiplexers," *2022 IEEE MTT-S International Conference on Microwave Acoustics and Mechanics (IC-MAM)*, 2022, pp. 5-8, doi: 10.1109/IC-MAM55200.2022.9855339.
- E. Guerrero, J. Verdú and P. de Paco, "On the Influence of Input Phase on the Allocation of Transmission Zeros in Acoustic Ladder Filters," *2021 IEEE MTT-S International Microwave Filter Workshop (IMFW)*, 2021, pp. 102-105, doi: 10.1109/IMFW49589.2021.9642282.
- E. Guerrero, L. Acosta, J. Verdú and P. de Paco, "Exploiting Input Phase in Extracted Pole Filters With a Single Nature for All Non-Resonant Nodes," *2021 IEEE MTT-S International Microwave Filter Workshop (IMFW)*, 2021, pp. 211-213, doi: 10.1109/IMFW49589.2021.9642316.
- E. Guerrero, J. Verdú and P. de Paco, "Considerations for Dual-Band Responses with Parallel-Connected Acoustic Wave Ladder Filters," *2021 IEEE International Ultrasonics Symposium (IUS)*, 2021, pp. 1-4, doi: 10.1109/IUS52206.2021.9593602.
- E. Guerrero, J. Verdú and P. de Paco, "Breaking the Ladder: Synthesis of Acoustic Wave Ladder Filters with Series Resonators Placing Transmission Zeros Below the Passband," *2021 IEEE International Ultrasonics Symposium (IUS)*, 2021, pp. 1-4, doi: 10.1109/IUS52206.2021.9593457.
- E. Guerrero, J. Verdú and P. de Paco, "A Synthesis View to Dual-Band Responses With Parallel-Connected Acoustic Wave Filters," *2021 IEEE 21st Annual Wireless and Microwave Technology Conference (WAMICON)*, 2021, pp. 1-4, doi: 10.1109/WAMICON47156.2021.9443627.
- E. Guerrero, P. Silveira, J. Verdú and P. de Paco, "Design Guidelines for Acoustic Wave Ladder Filters Starting in Shunt Resonator," *2020 IEEE International Ultrasonics Symposium (IUS)*, 2020, pp. 1-4, doi: 10.1109/IUS46767.2020.9251832.
- E. Guerrero, P. Silveira, A. Triano, J. Verdú and P. de Paco, "Synthesis Considerations for Shunt-Starting Acoustic Wave Ladder Filters and Duplexers," *2020 IEEE/MTT-S International Microwave Symposium (IMS)*, 2020, pp. 920-923, doi: 10.1109/IMS30576.2020.9224085.

- E. Guerrero, J. Brugués, J. Verdú and P. de Paco, "Sound Retrieval Using 24 GHz FMCW Radar," *2020 IEEE Radio and Wireless Symposium (RWS)*, 2020, pp. 191-193, doi: 10.1109/RWS45077.2020.9050012.

International conferences as a co-author

- L. Acosta, E. Guerrero, C. Caballero, J. Verdú, A. Guerrero, X, Borrisé, J. Esteve and P. De Paco, "Suppression of Transverse Spurious Modes on 30°YX-Cut Lithium Niobate-On-Insulator SH_0 Resonators Through Electrode Rhomboidal Apodization," *2023 53rd European Microwave Conference (EuMC)*, 2023 - pending publication.

- L. Acosta, E. Guerrero, C. Caballero, J. Verdú, A. Guerrero, X, Borrisé, J. Esteve and P. De Paco, "L-Band Lithium Niobate-on-Insulator SH_0 Resonators Avoiding Transverse Spurious Modes through Electrode Apodization," *2023 IEEE International Ultrasonics Symposium (IUS)*, 2023 - pending publication.

- D. Eslava, E. Guerrero, L. Acosta, P. Jamet, Y. Chen, J. Pérez, C. Hensel, A. Solana, D. Szombati, R. Sagastizabal, P. de Paco, P. Forn-Díaz, "Surface Acoustic Wave Filters for Superconducting Qubits," *APS March Meeting 2023*, 2023.

- D. Eslava, E. Guerrero, L. Acosta, R. Sagastizabal, P. Jamet, P. Forn-Díaz, P. de Paco, "Surface Acoustic Wave Filters for Superconducting Qubits," *2023 IEEE MTT-S International Microwave Symposium (IMS)*, 2023, pp.676-679, doi:10.1109/IMS37964.2023.10188070.

- L. Acosta, E. Guerrero, C. Caballero, J. Verdú and P. de Paco, "Dual-Band Acoustic Wave Filter Synthesis Based on the Conventional Standalone Ladder Topology," *2022 IEEE International Ultrasonics Symposium (IUS)*, 2022, pp. 1-4, doi: 10.1109/IUS54386.2022.9958046.

- L. Acosta, E. Guerrero, C. Caballero, J. Verdú and P. De Paco, "Synthesis Approach to Ladder-DMS Mixed Structures," *2022 IEEE International Ultrasonics Symposium (IUS)*, 2022, pp. 1-4, doi: 10.1109/IUS54386.2022.9957195.

- L. Colombo, E. Guerrero, N. Casilli, G. Giribaldi, B. Herrera-Soukup, P. de Paco, M. Rinaldi, "A Lithium Niobate MEMS-coupled Matching Network for BFSK Modulated Signal Amplification in Spectrum Monitoring Applications," *2022 IEEE International Ultrasonics Symposium (IUS)*, 2022, pp. 1-3, doi: 10.1109/IUS54386.2022.9958508.

- C. Caballero, L. Acosta, E. Guerrero, J. Verdú and P. de Paco, "Non-Standard Functions Enabling Feasible Microwave- Acoustic Ladder Filters," *2022 IEEE International Ultrasonics Symposium (IUS)*, 2022, pp. 1-4, doi: 10.1109/IUS54386.2022.9958077.

- L. Acosta, E. Guerrero, C. Caballero, J. Verdú and P. de Paco, "Coupling Matrix Approaches for the Synthesis of Acoustic Wave," *2022 52nd European Microwave Conference (EuMC)*, Milan, Italy, 2022, pp. 428-431, doi: 10.23919/EuMC54642.2022.9924462.
- L. Acosta, E. Guerrero, C. Caballero, J. Verdú and P. de Paco, "Synthesis Perspective to Technology Accommodation Approaches in Shunt Resonators for Wide-Band Acoustic Wave Filters," *2022 IEEE MTT-S International Conference on Microwave Acoustics and Mechanics (IC-MAM)*, Munich, Germany, 2022, pp. 94-97, doi: 10.1109/IC-MAM55200.2022.9855304.
- L. Acosta, E. Guerrero, C. Caballero, J. Verdú and P. de Paco, "Synthesis of Acoustic Wave Multiport Functions by using Coupling Matrix Methodologies," *2022 IEEE MTT-S International Conference on Microwave Acoustics and Mechanics (IC-MAM)*, Munich, Germany, 2022, pp. 56-59, doi: 10.1109/IC-MAM55200.2022.9855304.
- C. Caballero, L. Acosta, E. Guerrero, J. Verdú and P. de Paco, "Enabling Microwave-Acoustic Ladder Filters Feasibility by Bounded Filter Reflection Responses," *2022 IEEE MTT-S International Conference on Microwave Acoustics and Mechanics (IC-MAM)*, Munich, Germany, 2022, pp. 41-44, doi: 10.1109/IC-MAM55200.2022.9855211.
- L. Acosta, E. Guerrero, J. Verdú and P. De Paco, "Synthesis Guidelines for Acoustic Wave Standalone Ladder Filters with Dual-Band Responses," *2022 IEEE/MTT-S International Microwave Symposium - IMS 2022*, Denver, CO, USA, 2022, pp. 5-7, doi: 10.1109/IMS37962.2022.9865323.
- J. Verdú, M. Faura, L. Acosta, E. Guerrero, C. Caballero and P. de Paco, "Synthesis of the Double-Ladder Topology with Arbitrary Bandwidths and Dual-Band Response," *2022 IEEE/MTT-S International Microwave Symposium - IMS 2022*, Denver, CO, USA, 2022, pp. 8-11, doi: 10.1109/IMS37962.2022.9865451.
- J. Verdú, P. Silveira, E. Guerrero, L. Acosta and P. de Paco, "Effects of SiO2 layer on the performance of a LNOI Acoustic Wave Resonator," *2021 IEEE International Ultrasonics Symposium (IUS)*, 2021, pp. 1-3, doi: 10.1109/IUS52206.2021.9593789.
- L. Acosta, E. Guerrero, P. Silveira, J. Verdú and P. de Paco, "Synthesis Methodology of AW filters for RF applications based on Matrix Rotations to overcome round-off errors," *2021 IEEE International Ultrasonics Symposium (IUS)*, 2021, pp. 1-4, doi: 10.1109/IUS52206.2021.9593498.
- J. Verdú, P. Silveira, E. Guerrero, L. Acosta and P. de Paco, "Capabilities of LiNbO3 Based Acoustic Wave Resonators for Wideband Applications," *2020 IEEE MTT-S Latin America Microwave Conference (LAMC 2020)*, 2021, pp. 1-4, doi: 10.1109/LAMC50424.2021.9601614.

CHAPTER 2

Microwave Acoustic Resonators: BAW, SAW and Plate Waves

The introduction to this dissertation has outlined the importance of microwave acoustics in current wireless communications RF-FEMs and the intrinsic role that piezoelectricity plays as the key enabler. Thanks to the capacity of transducing electromagnetic energy into mechanical energy, extreme miniaturization of devices at RF and microwave frequencies is enabled while maintaining outstanding performance. However, such a change of domain also entails an increased level of complexity in terms of device physics, performance and manufacturing. With that in mind, this chapter aims at providing a microwave engineering view to the field of microwave acoustic resonators considering their main characteristics, types of mechanical wave exploited, suitable applications and circuital models to represent their behaviour in the electromagnetic domain. The concepts provided in this chapter are of great interest for the network synthesis contents covered in forthcoming chapters since many particularities of the proposed synthesis techniques are directly related to characteristics of microwave acoustic resonators and filters.

At first, this chapter provides a brief historical introduction to microwave acoustics to describe the foundation references and other important contributions that allowed the field to attain its current state of development. After the initial introduction, the chapter focuses on the main types of microwave acoustic resonator technologies, starting with bulk acoustic wave (BAW) and surface acoustic wave (SAW) resonators, those that currently fill modern RF-FEMs, down to to the more recently proposed plate wave resonators that show very interesting performance for future applications. In any case, the fundamental mechanism of operation and the main advantages and disadvantages of each resonator technology are provided along their core application spaces.

It is important to consider that the scope of the first part in this chapter is to provide a conceptual

description and a qualitative comparison of the main acoustic technologies in the RF-FEM industry. A deep dive into the physical foundations and particularities of each resonator technology, a topic that constitutes a complete field of research on its own, falls out of scope of this thesis but, in an effort to provide a complete picture of the presented technologies, references for further reading are provided along the chapter.

Finally, with the aim to connect the described technologies and concepts with a real world implementation, this chapter is closed with the exploration and experimental validation of one of the mentioned resonator technologies demonstrating manufactured resonators at the L band exploiting the shear horizontal (SH_0) mode on a thin film of lithium niobate ($LiNbO_3$) bonded to a silicon (Si) carrier substrate through a thin layer of silicon oxide (SiO_2).

2.1 Historical Perspective of Microwave Acoustics

As already mentioned in the introduction to this chapter, the fundamental enabler of microwave acoustic devices is piezoelectricity. A characteristic of solids that is only manifested if the crystal structure of the material does not have a center of symmetry and, thus, enables the appearance of electric dipole moments when the material is subject to a deformation. In this way a net electric charge within the material is the result of an external force applied to it, attaining a transduction between the mechanical and electrical domains through the piezoelectric effect. In the opposite direction, material deformations are obtained by applying an electric potential across the material through the inverse piezoelectric effect [29].

The phenomenon of piezoelectricity was first demonstrated by Pierre and Jacques Curie in 1880 and found its initial application in the context of electrical engineering in the proposal by Paul Langevin of a submarine detection mechanism in 1917 using a quartz-based device. In parallel, Walter G. Cady, who is now considered one of the fathers of modern piezoelectricity, developed a similar concept in 1918 using Rochelle salt and started his prolific work in the field that led to proposing and patenting the first piezoelectric resonator [30] in 1922. This contribution sparked the efforts by many others but specially by Warren P. Mason at the Bell Telephone Laboratories that developed an extensive work in quartz crystal resonators, their modeling and their application and proposed, for the first time, the use of crystal resonators to design filter circuits [31][1]. Another fundamental contribution by Mason was the proposal of a transmission line analogy between electromagnetic and mechanical waves to provide a one-dimensional model (i.e., Mason's model) of waves propagating through solids while incorporating the piezoelectric transduction [33]. A brief presentation of this model, that is still a widely used tool in the context of BAW resonators, are briefly discussed in a fol-

[1] Although the first reference to the ladder structure is due to Espenschied [32], Mason's patents are parallel in time. Moreover, Mason was the first to provide a mathematical explanation of how to construct filters using crystals in the referenced contribution.

lowing section as a demonstration of the fundamental behaviour of a microwave acoustic resonator. At this point, to provide a more accurate description of the mechanical waves exploited for quartz resonators, it is interesting to mention that such resonators were initially developed by laying a top and a bottom metal electrode at the two sides of a thinned down quartz plate thus exploiting a wave propagating vertically through the bulk of the material (thus, similarly to what is later described as a BAW resonator) but many other modes and resonator shapes were exploited such as the longitudinal and thickness shear modes or the tuning fork resonators. In any case, such devices were developed for very low frequencies.

In parallel to the work in quartz resonators and their application in oscillators and filters for fixed telephony networks, the proposal of pulse-compression techniques for radar after World War II lead to many efforts in developing delay devices that could provide delays in the order of tenths of microseconds without incurring in prohibitively large physical sizes. For such reason, attention was directed to acoustic devices that provided extremely reduced dimensions due to wave velocities being 10^5 times slower than in the electromagnetic domain while also allowing to design devices with a strong dispersive behaviour as desired to achieve pulse compression [34]. A breakthrough contribution was the invention of the interdigital transducer (IDT) by White and Voltmer [35] in 1965 that allowed to efficiently excite a surface acoustic wave (SAW) or Rayleigh wave (since they were initially demonstrated in an isotropic medium by Lord Rayleigh in 1885 in the context of seismology) while concurrently enabling to control the dispersion of the device by introducing variations of the pitch along the transducer. This can be considered the beginning of the SAW filter field since in parallel to pulse compression, bandpass filtering responses could be attained by modifying the overlap lengths of a constant-pitch IDT (a term that was ultimately known as apodization) through a control of the time response of the transducer. The attained filter responses, that initially were in the order of 6 MHz bandwidth at a central frequency of 30 MHz, were specially interesting for the intermediate frequency (IF) filtering stages of TV receivers [36]. Note that at this point filters using SAW were based on the response of the IDT rather than the electrical connection of resonators as in the ladder. However, with the introduction of the grating reflector by Ash [37] in 1970 to confine the surface wave within the IDT region and achieve a resonant element, SAW resonators were developed to be used also as building units of ladder filters.

A key aspect to consider is that the resonance frequency of SAW resonators is directly related to the pitch of the IDT while the frequency in resonators that exploit bulk waves is tightly related to the thickness of the piezoelectric material. Therefore, spurred by the need to scale up in frequency into the UHF regime for wireless communications systems of the time, while SAW involved lithography complexity to scale in frequency, material thinning techniques to compose bulk wave resonators were at the limit [38]. In this scope, Ken Lakin proposed the monolithic integration of mechanical resonators made of zinc oxide (ZnO) on a silicon substrate using integrated circuit (IC) fabrication techniques for thin film processing [39] opening the path for the integration of acoustic wave de-

vices. The frequency scaling of BAW filters using microfabrication techniques opened two different families of BAW resonators: the film bulk acoustic resonator (FBAR) industrially demonstrated by Ruby and Merchant [40] in which the resonator is acoustically isolated at top and bottom through air interfaces and the solidly-mounted resonator (SMR) initially mentioned by Newell in 1964 [41] but later developed by Lakin [42] in which the resonator is isolated from the carrier substrate through a Bragg reflector.

The development of the mentioned technologies was additionally driven by the development of mobile telephony systems and the need to implement RF filtering stages inside portable phones. While the Motorola DynaTAC x8000 featured a large ceramic-resonator duplexer as the only RF filter stage when it was released in 1973, the need to reduce filter size and support more frequency bands led to SAW and BAW filters becoming the mainstay for mobile phone RF-FEMs. Interestingly, it must be mentioned that SAW initially had a core position in GSM phones to implement IF filters in heterodyne architectures, but the transition to homodyne architectures in the 2000s eliminated the need for such devices. All in all, both BAW and SAW have, for now, found their own space within the mobile communications RF-FEM market and keep competing and complementing each other.

As a closing note it is important to stress that the aim of this brief historical introduction is providing an image of the evolution of microwave acoustic resonator technology rather than the most accurate historical review, a topic to which other contributions have already been devoted. Therefore, it is possible that some topics are omitted or briefly mentioned. As a source for further reading, references to specific works on the history of microwave acoustic resonators and applications are, among others, [10, 17, 36, 43–46].

2.2 Resonator Characteristics

After the brief historical introduction to the field of microwave acoustic resonators, this section is devoted to a brief review of the performance and behavior of acoustic wave resonators and to present some important figures and parameters used for acoustic resonator characterization that are mentioned throughout this chapter to compare the available microwave acoustic technologies.

The fundamental behavior of an acoustic wave resonator in its fundamental mode, independent of the type of resonator, is represented by the Butterworth-Van Dyke model as already introduced in Ch. 1 to describe the basics of the ladder topology. This model, initially outlined by Butterworth [14] when describing the mechanical oscillation of galvanometers and later demonstrated by Van Dyke from the first resonator proposed by W. G. Cady [15], is a purely electrical representation of the resonator and its resonances and is composed of lumped elements.

While such a purely electrical representation is very useful in the context of this thesis, for a better justification of the origin of the two resonances shown in Fig. 1.3b and the relation between the

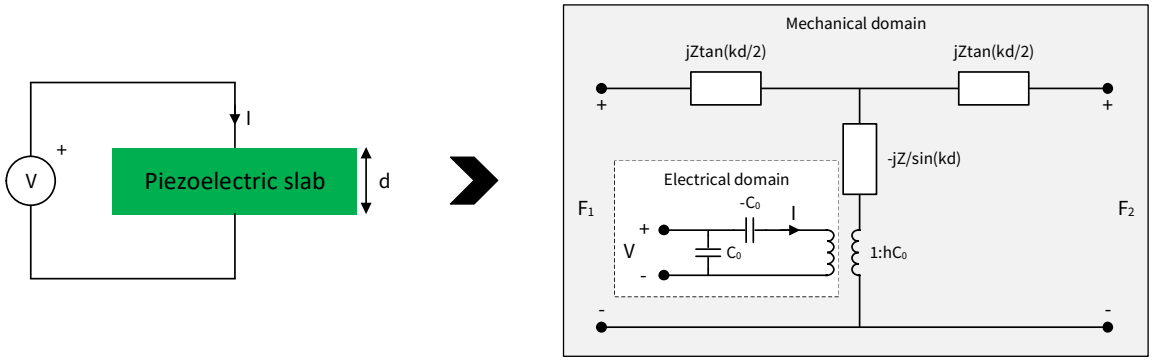

Figure 2.1: Equivalence between a simple piezoelectric slab subject to an electric field across it and the Mason model that joins both the electrical and mechanical domains of wave propagation.

effective electromechanical coupling coefficient and the strength of piezoelectric transduction, it is interesting to briefly discuss the following situation: let us consider a slab of piezoelectric material of thickness d, assuming an infinite extent in the lateral dimension, while considering the application of an electric field across the slab.

It is not in the scope of this thesis to dive into the mathematical derivation of the proposed situation, since detailed descriptions of it can be found in many other references such as [29, 33, 47, 48], but let us state a key analogy, proposed by Mason, to attain a circuital model joining the electrical excitation of the piezoelectric slab with the propagation of mechanical waves across it. To this end, let us consider that while a distributed transmission line in the electromagnetic domain can be represented, by considering the voltage and current boundary conditions, with a T circuital equivalent with impedance elements related to the characteristic impedance of the medium and the length of the line, a mechanical wave propagating through a solid slab of a given length can be equivalently modeled by treating force F (or tension) and particle velocity v in the mechanical equation of motion as the voltage and current, respectively . This analogy, that in the case of a simple non-piezoelectric slab would lead to a T equivalent circuit having two ports in the mechanical domain, can also incorporate the effect of piezoelectricity of the slab by considering a third port, now in the electrical domain to consider the electric potential that builds across the slab, giving rise to the so-called Mason model depicted in Fig. 2.1. Such model shows the two ports in the mechanical domain, one per slab interface to allow the propagation of acoustic waves into other adjacent materials, and the third port in the electrical domain.

In this case, let us assume that the piezoelectric slab is not in contact with any other material at any of the interfaces and thus, assuming contact with air, note that there are no exerted forces on any of the two mechanical ports. Thus, let us fix $\mathrm{F}_1 = \mathrm{F}_2 = 0$. With these conditions, following the derivation in [47], the input impedance seen from the electrical port results in

$$Z_{\text{in}} = \frac{1}{j\omega C_0}\left(1 - k_t^2 \frac{\tan\left(kd/2\right)}{kd/2}\right) \tag{2.1}$$

where k is the wave number, d is the plate thickness, C_0 is the intrinsic capacitance through the slab, due to it being dielectric and having an electric field across it, and term k_t^2 is the electromechanical coupling constant directly related to the piezoelectric constants of the material. Undoubtedly, note that such an input impedance expression has a zero and a pole, as depicted in the BVD model, whose separation is completely defined by the electromechanical coupling constant. Thus, the expressions and relations briefly introduced in Ch. 1 are demonstrated. Note here, that the effective electromechanical coupling presented in (1.2) is related to measured resonances, thus the outcome of a given resonator structure and design, while k_t^2 in (2.1) is the electromechanical coupling constant defined by the piezoelectric constants of the given piezoelectric material.

Although the brief presentation of the Mason model is just intended to relate the basic BVD model with the underlying mechanical and piezoelectric phenomena, note the importance of linking the interpretation of acoustic waves in a resonator with a circuital form made of transmission lines. A very common tool used by electrical engineers. Moreover, it is interesting to mention that although the Mason model is in close relation to bulk acoustic wave resonators due to it directly representing the excitation of waves in the thickness direction, such a one-dimensional interpretation was also proposed by Smith [49] to model IDT excitation both introducing the in-line and the cross-field models [29, 34, 47], yielding very good results for low frequency devices. For higher frequencies, as mass loading effects become more important and scattering between electrodes of the IDT increase, a more complex model is required and commonly, coupling-of-modes (COM) analysis is used for a better representation of the entire IDT [50] (Ch. 7).

Another very important aspect of acoustic wave resonators is their Q factor, the loss mechanisms that contribute to it and the methods used to characterize it from measured responses. While in an EM resonator environment losses are related to the Joule effect due to electrical currents flowing through finite resistivity metals or lossy dielectrics, for resonators combining both the electrical and the mechanical domains, two main factors are considered to characterize losses [51] (Ch. 5): electrical losses and mechanical or elastic losses.

On the one hand, electrical losses are those associated with the finite resistance of electrodes and leads in a resonator and to the dielectric losses of the piezoelectric material, both contributing to the generation of heat from electrical current. To consider them, resistive terms are commonly added to the BVD model in the form of a resistance in series to model electrode conductivity and as a parallel resistance to C_0 to model the complex permittivity of the piezoelectric material [16]. On the mechanical side, elastic losses include those related to the exchange of mechanical energy into heat due to viscosity and also the leakage of mechanical energy from the resonator due to imperfect confinement or due to unwanted wave excitation [17] (Ch. 8). Commonly, loss terms coming from the mechanical domain are added to the parallel resistive term collecting dielectric losses in the BVD.

In any case, the Q value of an acoustic wave resonator gathers the contribution of all loss factors to

provide an overall figure that has a key role in filter design and performance. To characterize it, note that considering fabricated resonators their characterization is possible from measured electrical data such as their S parameters and thus, perfectly separating the loss-contributing terms becomes exceedingly complex. Nevertheless, computing the Q factor from measured S parameters is a historical topic with fundamental contributions in the field of EM resonators but with relatively recent discussions on the field of acoustic wave resonators. In the context of this thesis, the Q factor of the manufactured resonators is computed from the measured S_{11} parameter as proposed in [52, 53] and recently extended in [54], through the following expression based on the group delay:

$$Q(\omega) = \omega \frac{\partial \phi}{\partial \omega} \frac{|S_{11}|}{(1 - |S_{11}|)^2} \tag{2.2}$$

To close this section, it is interesting to consider the figure of TCF (temperature coefficient of frequency) measured in ppm/°C that considers the effect of temperature on the resonator. TCF can be mathematically described in terms of the linear and volumetric thermal expansion coefficients and a term describing how the stiffness of the material changes with temperature [17] (Ch. 3). Commonly, the most contributing factor is the latter and due to most materials becoming softer with temperature the TCF of acoustic wave resonators is a negative value. From a filter perspective, TCF is a very important factor since rejection specifications of a given filter must be fulfilled within a range of operation temperatures (commonly from -25°C to 85°C) and thus, very low TCF values are desired.

2.3 Bulk Acoustic Wave Resonators

In its simplest form, a bulk acoustic wave resonator can be described as a slab of piezoelectric material placed between two thin metal electrodes, similar to the case discussed to present the Mason model. By applying an electric potential between the electrodes, an electric field is excited through the piezoelectric slab thus allowing transduction of electromagnetic energy into the mechanical or acoustic domain. With this configuration, a vertically propagating longitudinal wave can be efficiently excited and, by imposing the proper boundary conditions both at the top and bottom interfaces of the structure, a resonant device can be achieved.

Let us initially consider the simplified structure of the BAW resonator, a slab sandwiched between two electrodes, from a purely mechanical perspective and let us theoretically assume a perfect reflection of the acoustic wave at both the top and bottom interfaces. In this situation, without considering how the acoustic wave has been excited, a resonance is achieved whenever the slab thickness is a multiple of $\lambda/2$, where λ is here the wavelength of the acoustic wave. Therefore,

$$f_r = \frac{vN}{2d} \tag{2.3}$$

where v is the wave phase velocity, d is the thickness of the slab and N is an integer to represent

the multiple resonances due to wave periodicity. However, if one considers that the excitation of the acoustic wave is due to the piezoelectricity of the slab, only for odd values of N a mechanical resonance can be excited by applying an electromagnetic excitation as demonstrated by [17, 55]. Nevertheless, in the majority of cases, a BAW resonator aims at exploiting the fundamental longitudinal mode ($N = 1$), that is, implementing a piezoelectric layer of $\lambda/2$ thickness. As an example, assuming a longitudinal wave velocity in the order of 10^4 m/s, note that a resonator at 2 GHz involves a piezoelectric layer of thickness $d = 3$ μm, what clearly highlights the importance of thin film deposition techniques to manufacture filters at GHz frequencies[2].

Having presented the basic description of a BAW resonator, consider that achieving the desired wave confinement within the resonator is a key factor to attain resonator performance. From an acoustic perspective, the ideal way to achieve a perfect reflection at the interfaces is having the electrodes directly in contact with air, imposing a stress free surface condition and thus acting as an acoustic short [56] (Ch. 3). While such a condition might be attainable above the resonator (i.e., for the top electrode), considering that the piezoelectric thin films involved need be deposited on a carrier substrate, achieving acoustical isolation from the substrate involves a higher degree of complexity. The two main approaches, that actually are the two main families of BAW devices in the RF-FEM market, are the solidly mounted resonator, that achieves acoustical isolation by mounting the resonator on an acoustic Bragg reflector, and the FBAR, in which a cavity is etched on the substrate underneath the resonator to achieve an air interface also below the resonator.

In the context of BAW filters for communications, although the initial developments exploited ZnO as the piezoelectric medium, aluminum nitride (AlN) is the most common choice for the piezoelectric layer. Among its characteristics it is important to highlight that it is a CMOS compatible material, thus interesting for development within an IC fab environment, and also a good thermal conductor, what allows acceptable power handling capabilities of the resonator [56] (Ch. 4). From the point of view of piezoelectricity, AlN is not a strong piezoelectric material but offers an achievable coupling of $k^2_{\text{eff}} \approx 6.7\%$ when exploiting the fundamental longitudinal mode [57, 58], what, if one considers the filter bandwidth to electromechanical coupling relation stated in the introduction of this thesis, is enough for the initial 3G and LTE frequency bands below 2.8 GHz such as n1, n3 or n7 that have fractional bandwidths in the $3 \sim 4\%$ range.

Nevertheless, with the introduction of wider bands such as the n79 or some of the UNII bands, to name a few, with fractional bandwidths in the order of 10% and above, the fundamental contribution by Akiyama *et al.* [59], that demonstrated the enhanced piezoelectricity of scandium aluminum nitride (ScAlN) films and the ability to control it with the concentration of scandium in the material, has resulted in ScAlN becoming another mainstay material for BAW resonators. However, it must be mentioned that while enabling a higher electromechanical coupling, ScAlN also involves a

[2] As a source for further reading, works [17, 47] provide a deeper view of the physical foundations of BAW resonators and their performance.

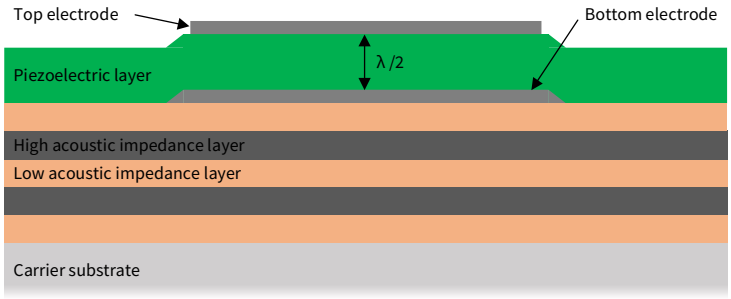

Figure 2.2: Cross-sectional drawing of an SMR resonator. The piezoelectric layer is commonly AlN or ScAlN in the context of BAW resonators for wireless communications filters.

reduction of the achievable Q of the resonator [58].

In general terms, the application space for BAW technology in the context of filters for communications lies in the range of frequencies above 1.5 GHz, approximately. This is the traditional frequency transition between SAW and BAW technologies, as is discussed in the SAW section, and is mainly due to material layers increasing in thickness for low frequencies, thus increasing process complexity, and due to SAW requiring less manufacturing steps, what ultimately reduces the cost-effectiveness of BAW for the lower frequency bands.

2.3.1 SMR

As introduced, the solidly mounted resonator is characterized by implementing an acoustic Bragg reflector below the resonator to isolate it from the carrier substrate, commonly, a silicon wafer. To provide a physical representation of an SMR, a simplified cross-section is depicted in Fig. 2.2 showing a piezoelectric layer of $\lambda/2$ thickness, let it be AlN, a pair of metal electrodes, commonly made of tungsten (W) due to its high acoustic impedance, and a set of alternating high and low acoustic impedance layers below the bottom electrode. These layers compose the acoustic reflector and, commonly, are made of tungsten and silicon oxide as the high and low acoustic impedance materials, respectively [60, 61].

At first, a direct way of achieving high reflection for the longitudinal wave propagating vertically through the resonator using such superposition of layers with different impedances is to directly set the length of each layer to $\lambda/4$, where λ is computed using v_l, the phase velocity of the longitudinal mode. Considering the impedance inverter nature of $\lambda/4$ layers, an almost perfect reflection can be achieved by considering 5 to 7 layers.

Initially, the quarter-wavelength approach for the mirror was used for SMRs and Q values in the order of $400 \sim 600$ were obtained. However, if one considers the phase velocity of the thickness longitudinal wave $v_l = 11250$ m/s and the phase velocity of the thickness shear wave $v_s = 6329$ m/s, both on c-axis AlN [55], note that v_s is roughly half of v_l. Therefore, a reflector structure made of

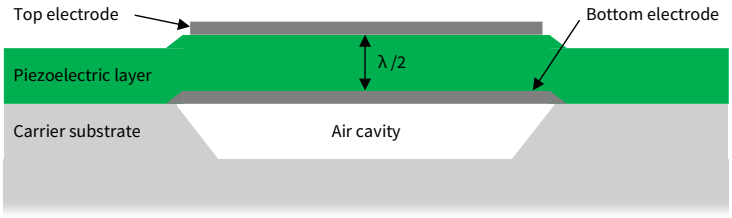

Figure 2.3: Cross-sectional drawing of an FBAR resonator. The piezoelectric layer is commonly AlN or ScAlN in the context of BAW resonators for wireless communications filters.

$\lambda/4$ layers is perfectly reflective for the main longitudinal wave but acts as an almost perfect through for any shear wave propagating in the vertical direction. This issue was investigated and solved by Marksteiner *et al.* in [62] at Infineon by proposing to optimize the thickness of all layers in the reflector not only for reflection to the longitudinal mode but also for the shear waves and boosted the Q value of SMR resonators up to 2000.

The main advantages of an SMR are, among others, related to the fact that it is solidly mounted on the carrier substrate: apart from an increased robustness of the structure, it depicts very good thermal dissipation and thus, higher power handling capability, due to the reflector effectively providing a thermal path towards the substrate. Moreover, considering that the topmost layer of the reflector can be made of SiO_2, that in its amorphous state has an inverted temperature behaviour with respect to AlN, the TCF of SMR resonators is low, in the order of -20 ppm/°C [63, 64].

On the other hand, some disadvantages inherent to SMR resonators are an increased process complexity regarding the multiple layers involved in the reflector and resonator and the need to accurately control all their thicknesses due to their impact in resonator performance.

2.3.2 FBAR

In contrast to SMR, FBAR resonators achieve wave confinement within the resonator by effectively releasing the resonator from its carrier Si substrate. By creating an air cavity below the resonator, as depicted in Fig. 2.3, the same acoustic short condition achieved over the resonator can be replicated below it achieving excellent wave confinement and thus, higher Q values than SMR resonators [65]. From a historical perspective, an interesting description of the industrial development of the FBAR resonator is provided in [17] (Ch. 5).

To consider the advantages of FBAR, aside the higher Q values attainable, note that the material deposition steps required are less than those of the SMR. However, in this case the complexity lies in the process to isotropically etch the Si below the resonator creating an air cavity while maintaining yield. Moreover, the fact that the resonator is a released membrane has an effect on the robustness of the structure when considering wafer dicing and packaging. In terms of power handling, consider that heat can only be dissipated laterally and the fact that due to the anchor points between the

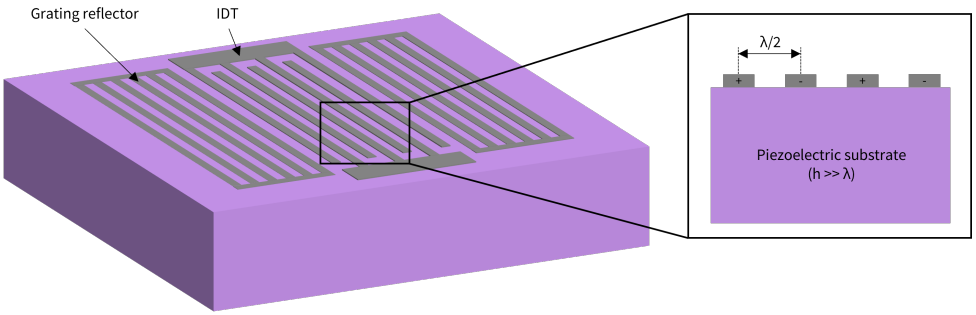

Figure 2.4: Cross-sectional drawing of a SAW resonator. The piezoelectric substrate is commonly $LiTaO_3$ or $LiNbO_3$ in the context of filters for wireless communications.

resonator and the substrate being smaller than the total resonator circumference (because of the opening of windows for the Si etching process), the thermal dissipation of FBAR resonators is worse than that of SMRs and thus can handle slightly lower power levels.

As a closing remark, regarding the effects of temperature on performance, due to the lack of an SiO_2 layer below the resonator as in the acoustic reflector of SMRs, FBAR TCF is larger than that of SMR resonators, in the order of -35 ppm/°C. Although approaches to integrate an oxide layer above the bottom electrode have been demonstrated [66], they involve a loss in resonator Q due to the losses in the oxide, and most applications appear oriented to the oscillator and timing market and not to RF filters.

2.4 Surface Acoustic Wave Resonators

As the name indicates, SAW resonators exploit a type of wave that propagates along the surface of a solid, that in this case is the piezoelectric material. In brief, surface acoustic waves are characterized by depicting particle displacement in the plane containing the direction of propagation and the surface normal and are composed by two wave components, a shear and a longitudinal term that jointly generate an elliptical motion of the particles [34, 50]. As in the BAW case, wave properties such as the phase velocity or the achievable electromechanical coupling are related to the material in which the wave is excited and its crystalline orientation.

As in BAW, using the proper transducer and wave confinement mechanism, surface waves can be exploited to obtain resonating elements to compose filtering devices. To this end, the key enablers are the IDT, that allows to excite surface waves on piezoelectric materials, and the grating reflectors that allow to confine the wave within the IDT to attain a resonator. To provide a physical description of a typical SAW resonator, Fig 2.4 depicts a simplified drawing of a SAW resonator showing the piezoelectric material, the IDT and a pair of grating reflectors, one at each side of the resonator. In this case, the surface wave would propagate across the IDT between the two gratings and the resonance frequency would be fixed by the pitch of the IDT, that is, the distance between the centers

of two opposite-polarity fingers in the IDT, by setting it to half an acoustic wavelength.

In the scope of resonators for communications applications, the main materials used for SAW devices are lithium tantalate ($LiTaO_3$) and lithium niobate ($LiNbO_3$) in a specific set of crystal cuts that have been historically exploited because of their interesting properties. Among others, some traditional cuts for SAW on $LiNbO_3$ are the YZ cut (that means the surface normal is the crystal Y axis and the wave propagates in the Z direction), the 128°YX cut (surface normal is rotated 128° from the crystal Y axis and the wave propagates along the X axis), and the most common cut for SAW on $LiTaO_3$ is the 36°YX cut [34,45,67]. Differences between them correspond to the attainable electromechanical coupling, the ease with which surface waves couple to unwanted bulk waves and also temperature behaviour. For example, both the mentioned materials show strong piezoelectricity, $LiNbO_3$ being slightly higher, but 36°YX $LiTaO_3$ has a reduced temperature coefficient of frequency of approximately -32 ppm/°C [34] (Ch. 4), what makes it a very common material for SAW filters. In any case, temperature compensation by depositing a thin layer of silicon oxide over the IDT and gratings are available and widespread in the industry [68].

At this point, let us consider that a surface wave is mathematically defined for a half space [34,50]. That is, the material through which it propagates is very thick with respect to the acoustic wavelength. For this reason, SAW devices, until very recent times, have been manufactured directly on the surface of thick wafers of the piezoelectric material that have been cut to attain the desired crystal orientation from a single-crystal ingot. On the one hand, this simplifies the SAW device manufacturing process down to deposition of IDTs and gratings on the surface of such a wafer but on the other hand, has important implications. Although the wave propagates along the surface, part of its shear component can also direct into the bulk of the material leading to some energy leakage in the form of bulk waves. A leakage that is very dependent on the crystal orientation on which the wave is excited.

In this direction, a ground breaking advancement by Murata [69, 70] is the so-called IHP (incredible high performance) SAW structure in which, thanks to Smart-Cut techniques that allow the transfer of thin crystalline layers into carrier substrate [71], by thinning $LiTaO_3$ thickness down to the order 20λ and transferring the piezoelectric layer into a carrier wafer with already deposited layers of alternating high and low acoustic impedance to better confine energy leaking vertically, resonator quality factors of 4000 along an increase of electromechanical coupling and a very low TCF (-9 ppm°C/) thanks to using SiO_2 as a low impedance layer below $LiTaO_3$, are obtained.

Nevertheless, for both traditional SAW and the more recent IHP approaches, in part due to the need of an interdigitated electrode structure, the dominating application space in the context of wireless communications is traditionally defined in the so-called low band range, from 700 to 1500 MHz, approximately. If one considers that phase velocity of surface waves for the mentioned cuts in $LiNbO_3$ and $LiTaO_3$ range from $3000 \sim 4000$ m/s, scaling in frequency above 2 GHz (e.g., an

electrode with of 875 nm for $v_p = 3500$ m/s at 2 GHz) results in an increased lithography complexity that questions the cost-effectiveness of SAW. Moreover, the IDT and its dimensions also lead to one of the main weak points of SAW resonators that is their power handling capabilities. Due to the thin electrodes required for high frequency resonators and the strong electric fields that build up between electrodes of opposite polarity, increasing power leads to electromigration of electrode metal and finally, to catastrophic resonator failure. This fact, becomes more concerning as frequency increases and IDT pitch reduces.

2.5 Lamb and Shear Waves on Thin Plates

After describing the two types of acoustic resonators currently dominating the RF-FEM industry, this section directs the attention to a third type of waves, namely plate waves, that have received a growing attention in recent years because of their interesting properties and also because of the technical advances in process technology that have enabled their feasibility in the scope of resonators for filtering devices.

To discuss plate waves, let us consider a situation similar to the initial slab used to exemplify the BAW resonator, having a thickness in the order of λ, but not considering the vertical propagation through the slab as a pure thickness longitudinal mode, but in parallel to the two surfaces of the plate. In 1917, mathematician Horace Lamb proposed the wave solutions propagating in a thin solid plate if particle motion is confined to the saggital plane (that containing the direction of propagation and the normal to the surface of the plate) and derived two forms, the so-called Lamb waves: the symmetric (S) or extensional mode, as depicted in Fig. 2.5a, and the asymmetric (A) or flexural mode, depicted in Fig. 2.5b. In brief, two important facts about Lamb waves are that infinite modes of both types can exist in a thin plate and that phase velocity of Lamb waves is strongly related to the thickness of the plate [34, 72]. At the same time than Lamb waves, the plate allows for a third plate mode called the shear horizontal (SH) wave, whose displacement is shown in Fig. 2.5c, that also propagates in parallel to the surfaces of the plate but now with particle motion on a plane parallel to the plate surface and in perpendicular to the direction of propagation. Such a mode is tightly related to the excitation of Lamb waves when considering thin plates and has an important role in the present chapter.

Although the properties and usage of plate waves was studied in parallel to the advancements of SAW and BAW, and sometimes even as a by-product of them because of the need to avoid spurious modes in SAW and BAW, manufacturing complexities related to thin plates and their handling was the main barrier for their competition with the other two dominating technologies. At first, some of their initial applications were in the field of sensors, delay lines and non-destructive testing. Nevertheless, contributions such as the work by Adler [73] and Jin and Joshi [74] regarding the coupling to Lamb and shear horizontal modes in piezoelectric materials through IDT structures and the theoret-

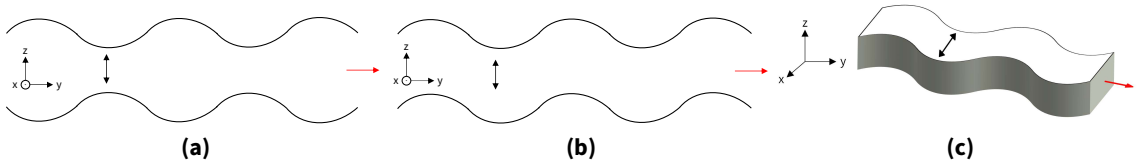

Figure 2.5: Simplified depiction of the instantaneous displacement of a plate for Lamb and shear horizontal waves, red arrow indicates direction of propagation and double black arrow indicates direction of plate displacement. (a) Zeroth-order symmetric or extensional Lamb wave. (b) Zeroth-order asymmetric or flexural Lamb wave. (c) Zeroth-order shear horizontal wave.

ical demonstration by Kuznetsova et al. [75] of the very high electromechanical coupling achievable on different cuts of thin $LiNbO_3$ and $LiTaO_3$ highlighted the interesting properties of such waves in the context of microwave acoustic resonators. Theoretically, k^2_{eff} values higher than 30% could be achieved for certain propagation directions on X- and Y-cut $LiNbO_3$, for example. However, the main drawback to the advancement of these devices was the complexity of attaining the desired thin plates with very specific crystalline orientations due to the lack of epitaxy methods for $LiNbO_3$ and $LiTaO_3$.

Initial approaches exploited to possibility to deposit AlN thin films to develop Lamb wave resonators on AlN [76, 77], among others, showing high Q but very low k^2_{eff} values due to the weak piezoelectricity of AlN for this type of waves. More recently, progress in manufacturing techniques and layer transfer technologies has enabled other demonstrations of the very high k^2_{eff} attainable with $LiNbO_3$ such as the SH_0 resonators by Kadota *et al.* [78–80] achieving $k^2_{\text{eff}} = 30\%$, the works in S_0-mode resonators by Gong *et al.* [81–83] or the extension into higher frequencies using higher-order Lamb modes [84], among many others. An interesting mention is the proposal of the so-called XBAR [85], a $LiNbO_3$ plate wave resonator exploiting the A_1 mode attaining $k^2_{\text{eff}} \approx 25\%$ proposed by Resonant Inc., a company recently acquired by Murata. In all the above cases, the possibility transfer very thin layers of the desired cuts of $LiNbO_3$ through Smart Cut techniques has been a fundamental enabler from the process perspective, allowing to compose resonators with plate thicknesses in the order of hundreds of nanometers.

Clearly, plate waves show very interesting properties in the scope of resonators for communication filters because of the very high attainable coupling, thus fitting the need for wider filters, but, in comparison with the main two technologies, still entail some drawbacks. From a plate perspective, releasing the piezoelectric membrane composing the resonator from its carrier substrate is a very important step to attain the maximum achievable k^2_{eff} when considering Lamb waves. Releasing the membrane involves etching through $LiNbO_3$, a process known to be complex and prone to generate by-products [51] (Ch. 4), to allow the isotropic etch of the Si and SiO_2 underneath the plate. Moreover, since the wave propagates parallel to the surface, wave confinement within the resonator is imposed either in the form of grating reflectors or as an interface with air via openings

through the piezoelectric layer, what also increases etching complexity since accurate control on the interface steepness is required. As expected, since such waves are IDT-excited, suffer from the same power handling limitations as SAW, even increased if the piezoelectric membrane is released due to a smaller lateral thermal dissipation path, and lead, as well, to lithography challenges for higher frequencies.

Interestingly, an alternative to overcome part of such process-related challenges while harnessing the properties of plate modes, approaches oriented towards solidly mounted structures such as the IHP SAW example but in this case exploiting a pure shear horizontal wave have received growing interest in recent times and, in the context of this thesis, are chosen as a case of study and demonstration.

2.6 L-Band Lithium Niobate on Insulator Resonators

Based on the brief description on the different microwave acoustic technologies provided in the above sections, the forthcoming content focuses on the theoretical and practical description of resonators exploiting the SH_0 mode on a thin film of $LiNbO_3$ at 1.5 GHz, at the center of the L band. The objective of this resonator development is double: on one side demonstrating the performance of plate wave resonators and, on the other, attaining an experimental platform on which some of the filter synthesis methodologies developed in this thesis can be physically demonstrated, as is done in Ch. 4.

In this case the selected approach is to exploit a type of plate resonator structure that is receiving attention due to a simplified manufacturing process that avoids having to release the plate from its carrier substrate, that is commonly referred to as $LiNbO_3$ on insulator (LNOI, note from here onwards the reference to $LiNbO_3$ as LN) [86–89]. It involves exciting the SH_0 mode on a thin plate that is solidly mounted on a thin layer of SiO_2 with a pre-defined thickness that plays an acoustic isolation role from the Si substrate, as is described in the forthcoming paragraphs. In this context, the procedure to select the material orientation and decide on several parameters of the resonator follows the seminal contribution by Zou *et al.* [90] that provides the theoretical analysis of resonators exploiting the SH_0 mode on $LiNbO_3$ plates.

2.6.1 Physical Description and Analysis

As already introduced, Kuznetsova *et al.* [75] provide the theoretical demonstration that $k^2_{\text{eff}} \approx 35\%$ with a phase velocity of 4500 m/s are obtained on a Y-cut $LiNbO_3$ plate with a thickness of $h/\lambda = 0.1$ through the SH_0 mode propagating in the X direction. In the mentioned work, the study only considers the different directions of propagation possible in each of the three axis cuts of the material. However, Kadota *et al.* demonstrate in [78] that even higher electromechanical coupling can be

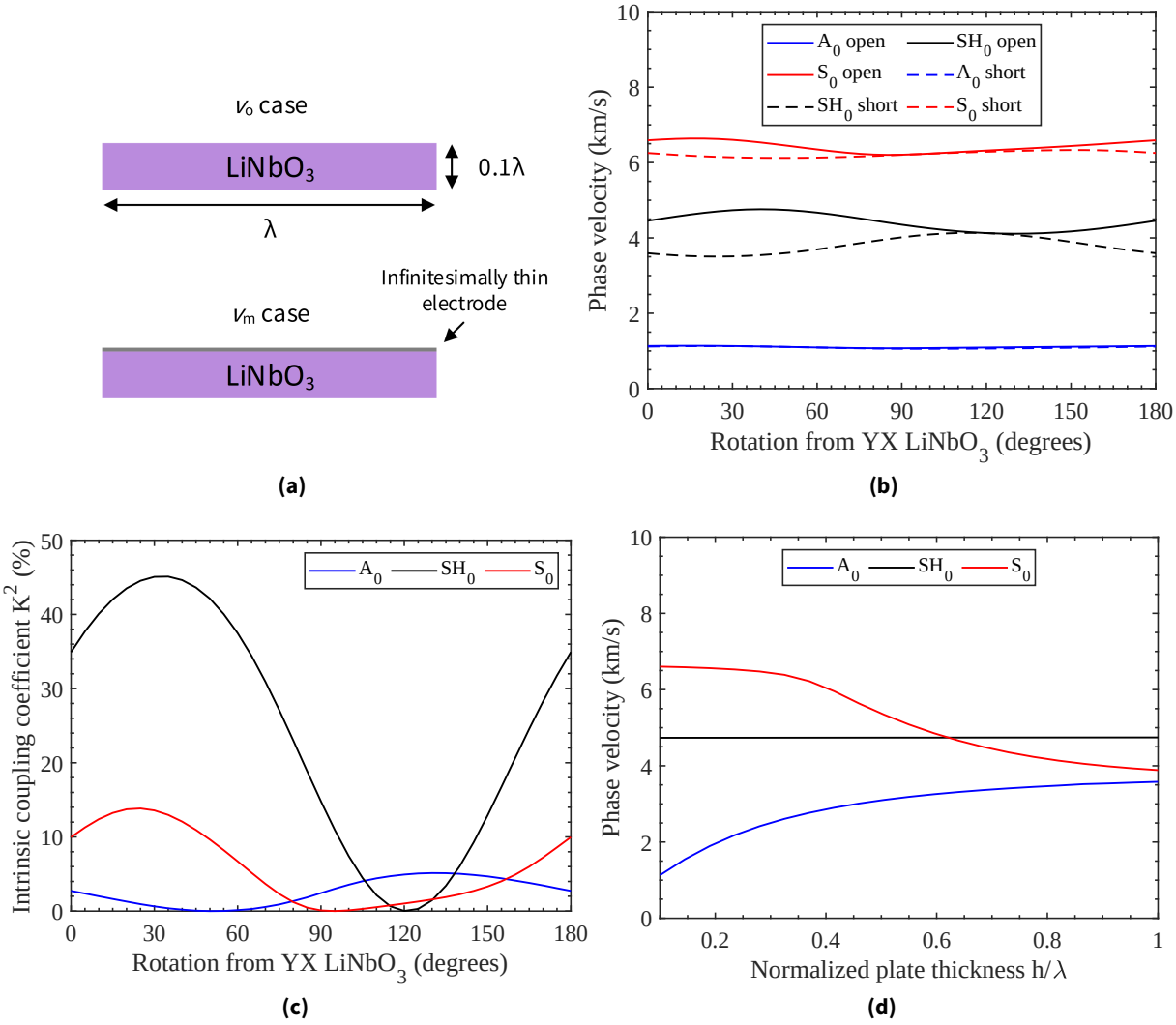

Figure 2.6: FEM simulation set-up and data on a thin plate of $LiNbO_3$. (a) Electrical boundary conditions used to simulate v_o and v_m. (b) Open (free) and short (metallized) phase velocities with respect to rotation angle from the Y axis on a plate of thickness h/λ = 0.1. (c) Estimated intrinsic coupling coefficient K^2 from the simulated phase velocities, as a function of rotation angle from the Y axis. (d) Simulated phase velocity with respect to plate thickness on a 30°YX LN plate with a DF = 0.5 IDT.

attained with the SH_0 mode propagating in the X direction if the cut is rotated approximately 30° with respect to the Y axis obtaining theoretical coupling values higher than 50%.

In this case, considering the $LiNbO_3$ parameters in [67], an eigenmodes analysis via COMSOL of a simple LN plate with thickness $h_{LN}/\lambda = 0.1$ both for a free surface condition (open circuit) on top and bottom faces of the plate and for an infinitesimally thin electrode condition (short circuit) on the top face, has been conducted for all rotation angles of LN with respect to the Y axis in the range $\theta = [0, 180]°$ considering the zeroth-order SH and Lamb modes [91]. The computed open and short phase velocities are depicted in Fig. 2.6b and, from them, the intrinsic electromechanical coupling

can be estimated through the following expression [75, 90, 92]:

$$K^2 = \frac{v_o^2 - v_m^2}{v_o^2} \tag{2.4}$$

where v_o is the open circuit condition phase velocity and v_m is the short circuit condition phase velocity (where m stands for metallized). The computed electromechanical coupling values with respect to the rotation angle are depicted in Fig. 2.6c showing that for a rotation of $30 \sim 35°$ with respect to the Y axis, a maximum coupling is attained for the SH_0 mode, in line with the results in [78].

Let us then select the 30°YX cut of LN as the one for the proposed experiment. In order to evaluate the impact of the plate thickness, let us consider the selected cut and compute, the phase velocity of the zeroth order SH and Lamb waves through FEM. In this case, the simulation is conducted assuming an IDT on the top face of the plate with 0.5 duty factor (DF) of the IDT (the ratio of metallized surface in a plate cell of length λ) with infinitesimally thin electrodes of $\lambda/4$ width. The simulated phase velocities are shown in Fig. 2.6d demonstrating that the SH_0 shows no dispersion with respect to plate thickness, a very important feature when considering thickness variations along the wafer, and an ideal phase velocity $v_p = 4800$ m/s. More importantly, for thickness plates of $h/\lambda = 0.3$ and below, the two lowest order Lamb wave modes (A_0 and S_0) show phase velocities away from that of the SH_0 mode thus allowing to excite the latter with a given IDT pitch without exciting spurious Lamb waves in the same frequency range. Moreover, as shown in [90], first-order Lamb and SH modes show very high dispersion for the mentioned h/λ range along very high phase velocities. Given the simulation results, with the objective of resonator operation at 1.5 GHz, let us select an LN thickness of $h_{LN} = 540$ nm, thus $h/\lambda = 0.17$.

Given the LN plate thickness, let us now consider the wave displacement of the SH_0 mode. Due to its shear nature, note that a wave excited on the plate, if not isolated from the carrier substrate, leaks part of its energy in the form of shear waves propagating vertically towards the silicon, thus reducing the Q of the resonator. While released membrane approaches avoid this leakage by effectively creating an air cavity below the plate, in this case let us consider an SiO_2 layer below the LN. This oxide layer is already present in wafers with thin LN plates because it is used as a bonding oxide when transferring the layer from the LN ingot into the Si carrier substrate. However, such a layer can in this case be exploited with an acoustic role if one considers the phase velocity of shear waves in SiO_2 [93] $v_{p-SiO_2} = 3966$ m/s and the low acoustic impedance of the material. For the oxide layer to have an isolation role, let us use it to implement an impedance inverter, that is, a $\lambda/4$ layer, to the shear waves propagating vertically. Considering operation at 1.5 GHz, the desired thickness of the SiO_2 layer is $h_{SiO_2} = 660$ nm.

Having computed the desired LN plate and oxide thicknesses, an LNOI wafer from the vendor NanoLN is used as the technological platform in this thesis, with the only drawback that due to availability reasons an oxide layer thickness of 620 nm is the closest possible value. For a clearer

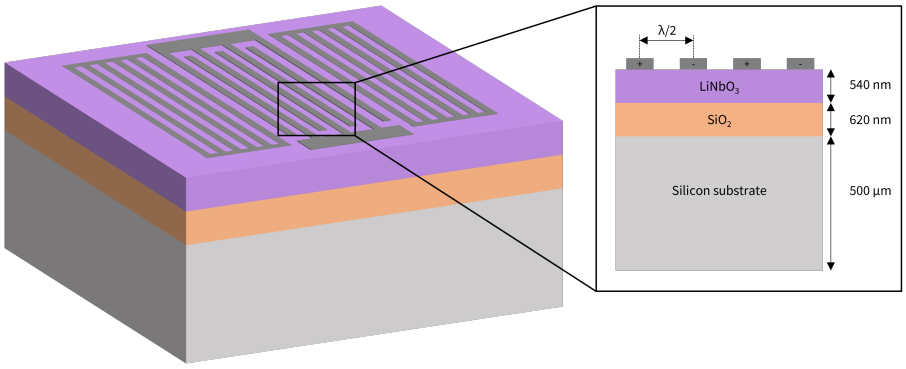

Figure 2.7: Drawing of the LNOI structure with layer thicknesses shown in the cross-section inset.

view of the complete LNOI structure, a drawing of the multilayer structure is depicted in Fig. 2.7 with a cross-sectional inset highlighting the thickness of each layer. Notice here an important aspect of the proposed structure: while the oxide layer provides isolation from the substrate, confinement of the wave within the resonator is achieved through grating reflectors, as in SAW resonators. In this case, gratings are composed of $\lambda/4$-wide metal strips shorted through a bus bar at each side and keeping a distance of $\lambda/2$ between the centers of consecutive strips. As discussed in [90], a number of gratings per reflector of $N_g = 40$ is sufficient to achieve very high reflection.

From a process perspective, the only steps involved in the fabrication of these resonators is a lift-off process to define the IDT, involving lithography and deposition of metal. Considering that the electrode width to excite the SH_0 mode at 1.5 GHz assuming $v_p = 4800$ m/s is 800 nm, electron beam lithography (EBL) through the RAITH-150 TWO tool at IMB-CNM[3] is employed to define the IDTs and gratings of resonators. On the other hand, probing pads are defined through laser lithography due to their larger dimensions. Aluminum is selected as the metal for electrodes due to its good conductivity, its reduced density to reduce mass loading on the resonator and the fact that it is widely available in the clean room. Evaporation is chosen as the method to deposit metal on the resonators with a Leybold UNIVEX 400 tool.

2.6.2 Effect of Electrode Thickness

At this point, the only remaining dimension to define is electrode thickness. A feature that, although simple, has important implications in resonator performance since, as introduced in [90], it is a key parameter to control the excitation of longitudinal modes. To demonstrate it, let us present the following experimental demonstration that consists in the comparison of two equal sets of resonators for nine different frequencies around 1.5 GHz, from the set $\lambda_k = [2.7, 3.5]$ μm, in steps of 100 nm. All resonators are designed implementing 81 fingers per IDT and an aperture (the length of overlap of each finger in the IDT with its adjacent finger of opposite polarity) of 60 μm. With these dimen-

[3]Institut de Microelettrònica de Barcelona - Centre Nacional de Microelettrònica.

sions, resonators yield static capacitance values around 0.6 pF. Scanning electron microscope (SEM) images of both an entire resonator with probing pads and a close-up of the IDT structure are shown in Fig. 2.8a and 2.8b, respectively.

Having defined the resonator dimensions and frequencies, the same set of resonators is manufactured twice using two different electrode thicknesses and in both cases considering aluminum as electrode material, as already introduced. In this case, the two selected thicknesses are 120 nm and 180 nm what in turn correspond to $h_{Al}/\lambda = [3.5, 6.5]$ %, respectively. As a demonstration of the layer thicknesses and the deposited electrode thickness, Fig. 2.8c shows an SEM image of a focused ion beam (FIB) cut performed in the IDT of one of the manufactured resonators and Fig. 2.8d shows the SEM cross-section of the cut, in this case for $h_{Al} = 180$ nm.

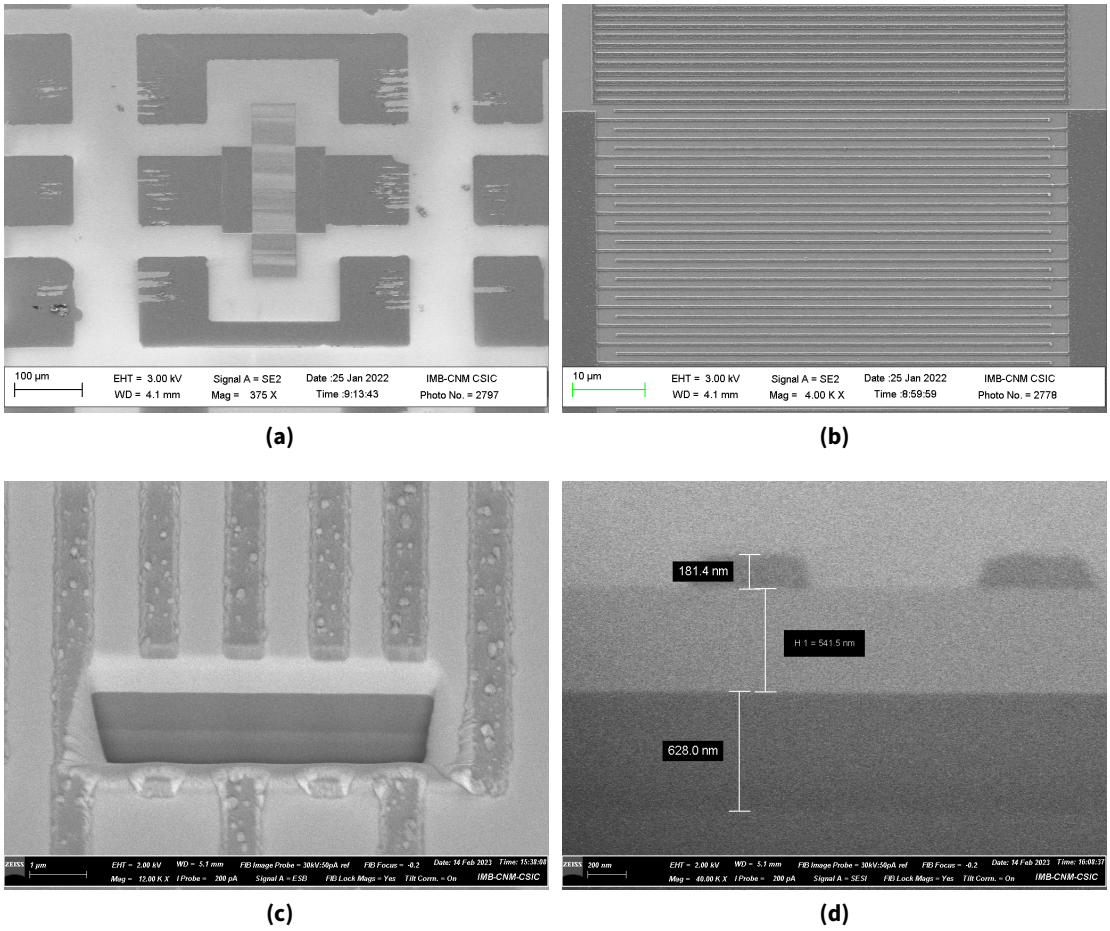

Figure 2.8: SEM images of the LNOI resonators for the electrode thickness experiment. (a) Overview of a resonator showing IDT, gratings and probing pads. (b) Close-up of the IDT body showing electrodes and part of the top grating. (c) Overview of a resonator region where a focused ion beam (FIB) cut is conducted. (d) Cross-section of the cut through the LNOI structure with measured layer thicknesses.

The manufactured sets of resonators are measured with 150 μm-pitch probes with beryllium copper (BeCu) tips on an Agilent PNA-X network analyzer and the measured input impedance of

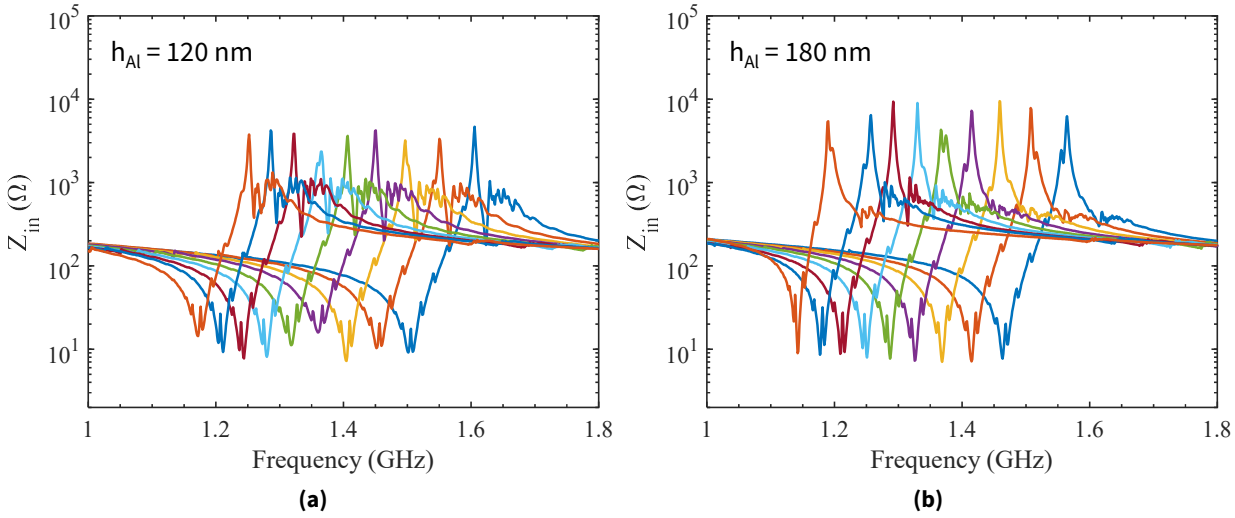

Figure 2.9: Measured input impedance for the set of nine resonators with λ_k = [2.7, 3.5] μm in steps of 100 nm. (a) Electrode thickness h_{Al} = 120 nm. (b) Electrode thickness h_{Al} = 180 nm.

each resonator is shown in Fig. 2.9a and 2.9b for the two electrode thickness cases. Focusing initially on Fig. 2.9a, note the presence of both spurious modes between f_s and f_p, modes that are discussed in a forthcoming section, and a strong presence of spurious spikes above the anti-resonance frequency f_p. In contrast, Fig. 2.9b shows resonators that feature the same spurious modes between the two resonances but with a greatly reduced spurious excitation above f_p and so, a much higher impedance value at such resonance frequency. The presence of spurious mode above f_p is due to the excitation of longitudinal modes across the resonator that propagate between the two gratings of the structure. This undesired modes, that are also discussed in [94] and [90], are already present in regular SAW resonators due to the dispersive behaviour of gratings as introduced in [50] (Ch. 5) but, in the case of plate wave resonators, their presence is more pronounced due to the wave being guided by the lower interface of the plate. Due to the periodicity of the IDT structure, only odd-order longitudinal modes are correctly confined.

To avoid the presence of such undesired modes, increasing electrode thickness is a way to reduce the wave phase velocity, thus shifting the resonator downwards in frequency and moving the undesired longitudinal modes (that remain at the same frequency because the physical dimensions of the IDT and gratings are not modified) into the stopband bandwidth of the grating, thus hindering their propagation. The measured phase velocity of the SH_0 mode for the 120 nm electrode is 4090 m/s while a velocity of 3975 m/s is obtained for 180 nm electrodes. As clearly observed in Fig. 2.9b, by increasing electrode thickness, resonance frequencies f_s have shifted downwards (37 MHz) with respect to the 120 nm case and longitudinal modes are partly suppressed.

With the purpose of resonator characterization, three resonators of the manufactured set are selected for further analysis. They correspond to wavelengths 2.8, 2.9 and 3 μm, those operating

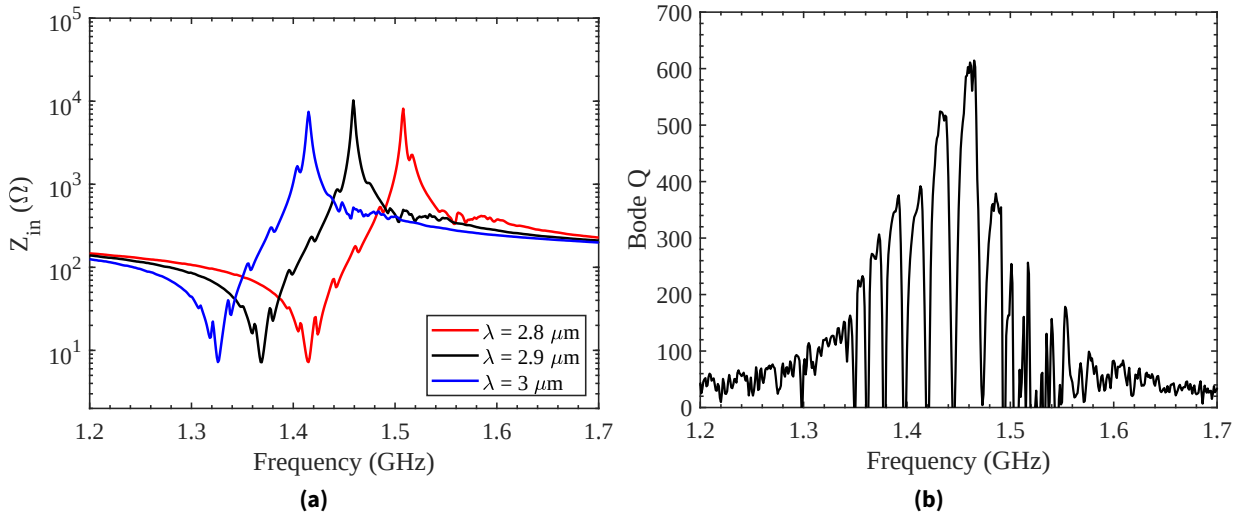

Figure 2.10: Three best resonators of the h_{Al} = 180 nm set. (a) Close-up of the measured input impedance curve. (b) Computed Bode Q of the λ = 2.9 μm resonator.

Table 2.1: Measured parameters of the three best resonators with h_{Al} = 180 nm.

λ (μm)	f_s (MHz)	C_0 (pF)	k^2_{eff} (%)	Q_{max}	Z_r (dB)
2.8	1415	0.58	14.3	698	61
2.9	1369	0.57	14.3	614	63
3	1326	0.57	14.5	627	60

at the frequency where the SiO_2 layer provides best isolation from the substrate and a close-up of their input impedance curves is shown in Fig. 2.10a. Let us highlight that although longitudinal modes have been greatly reduced, ripples between f_s and f_p can be observed stressing the need for further design optimization. Such modes are related to transverse waves propagating through the resonator and are discussed in the following subsection. Given the reduction in longitudinal mode excitation thanks to increasing h_{Al}, the quality factor of the resonator is enhanced. Fig. 2.10b depicts the measured Bode Q of the $\lambda = 2.9$ μm resonator, computed from its S_{11} parameter as introduced previously in this chapter [52], yielding a maximum quality factor $Q_{max} = 614$.

As a summary, the measured parameters of the three selected resonators are shown in Table 2.1 stating frequency, static capacitance, attained k^2_{eff} , Q and impedance ratio. The latter parameter is defined as $20\log_{10}(Z_{f_p}/Z_{f_s})$ and is commonly used as a resonator performance figure. It is important to highlight that the measured effective electromechanical coupling $k^2_{eff} = 14.3$ % is less than the theoretically achievable results for this LN cut. While the simulation study on an ideal LN plate has allowed to select the most favorable cut from an SH_0 perspective, note that it has not considered the oxide layer and the silicon carrier, a fact known to reduce electromechanical coupling due to the stress conditions imposed at the interfaces, nor the mechanical loading imposed by the elec-

trode material. These two reasons lead to a reduction of the attainable coupling with respect to that ideally achievable. Additionally, the demonstrated resonators still show undesired spurious modes in-between the two resonances and thus, k^2_{eff} can be further improved if such modes are suppressed to get to the already demonstrated values of around 20% [86]. Nevertheless, the achieved results yield k^2_{eff} values higher than those of regular SAW and BAW and thus, the proposed LNOI approach provides a very promising platform to develop AW filters.

2.6.3 Effect of Transducer Apodization

As demonstrated through the discussion of the effect electrode thickness has on the performance of the proposed resonator structure, although unwanted modes above f_p can be partially suppressed through controlling electrode thickness, spurious modes between f_s and f_p are still present. While the unwanted modes above f_p are specially harmful for the shunt resonators in a ladder filter, because f_p falls inside the passband and such modes add an unwanted ripple to it, modes between the two resonances are even more harmful because all resonators in the ladder contribute to ripples in the filter passband. In this direction, the effort in this subsection is focused on exploring a mechanism to avoid the presence of such unwanted modes.

The presence of spurious modes between f_s and f_p in resonators with IDT excitation is a topic of discussion to which many contributions have been devoted. In general terms, the unwanted modes are due to waves propagating in the transverse direction of the resonator, that is, between the two bus bars of the IDT. These unwanted modes, as explained in [50] (Ch. 5) in the context of SAW resonators and as discussed in many other contributions such as [56,95–98], are caused by a wave guiding effect due to the difference in phase velocity of the electrode in the transducer (lower velocity region) and the gap between the end of the electrode and the busbar (higher velocity region). Interestingly, the frequency and number of transverse modes are related to the transducer aperture [50] (Ch. 5). To this end, several techniques have been proposed for SAW resonators in both $LiNbO_3$ and $LiTaO_3$ such as apodization of the IDT (i.e., the addition of a shape to the IDT by using the end position of each electrode so to describe a desired shape, such as a rhomboid, along the transducer), addition of dummy electrodes in each gap between electrode and bus bar or novel transducer layouts such as the one in [96] to achieve the so-called *piston mode* or the one by Stettler and Villanueva in [98] for released membrane SH_0 resonators.

In the context of the proposed SH_0 resonators, the proposed transverse mode suppresion technique is applying an apodization pattern to the IDT while considering dummy electrodes. For a better depiction of the proposed layout, Fig. 2.11a shows an SEM image of one of the manufactured resonators depicting a rhomboidal apodization pattern. In the proposed case, the distance between the end of each electrode and the beginning of each dummy electrode is 1 μm, as shown in the close-up in Fig. 2.11b. The rhomboidal shape of apodization has already been proposed in [99] suggesting an

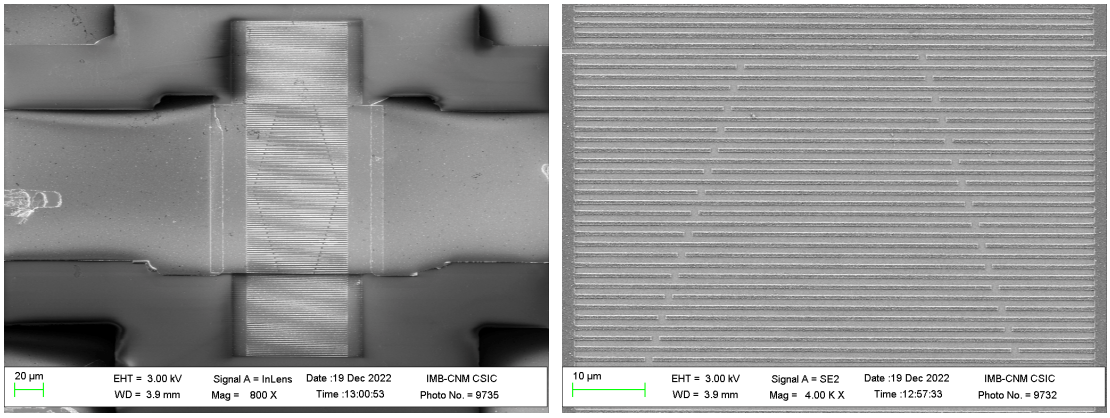

(a) t **(b)** t

Figure 2.11: SEM images of an apodized resonator with AR = 40%. (a) General image of a resonator including probing pads. (b) Close-up view of the resonator showing electrodes with their respective dummy electrodes.

optimal apodization ratio of 60%, with apodization ratio being defined as in [94]

$$AR = \left(1 - \frac{A_{\text{min}}}{A_{\text{max}}}\right) \cdot 100 \tag{2.5}$$

where A_{min} and A_{max} are the minimum and maximum apertures of the IDT, respectively. In other words, the electrode overlap length at the end of the resonator (last electrode before the grating) and the electrode overlap length at the center of the resonator, respectively.

Considering the proposed apodization optimum by Kadota *et al.*, let us take two of the resonators analyzed in the previous section, let them be $\lambda = 2.8$ and 2.8 μm, and let us manufacture them once again, considering $h_{\text{Al}} = 180$ nm but now applying a rhomboidal apodization pattern with a 60% ratio. The manufactured resonators are measured with the same set-up used in the previous section and the input impedance curve of the apodized resonators is shown in Fig. 2.12b while Fig. 2.12a depicts the input impedance of the two same resonators but without apodization, for comparison purposes. The inset in each figure highlights the IDT layout of each case.

At a first glance note clearly how the apodized reasonator is clean of unwanted spurious modes between f_s and f_p and how, by simple inspection, such resonators show a higher impedance ratio and a higher quality factor value. Such an increase in quality factor can be observed in Fig. 2.12c that compares, for the $\lambda = 2.9$ μm resonator, the measured Bode Q with and without apodization. For completeness, Fig. 2.12d shows the wideband input impedance, up to 6 GHz, of the two apodized resonators. In this case, the spurious peak located at 1.15 GHz corresponds to the A_0 Lamb wave and the peak at 1.9 GHz corresponds to the S_0 Lamb wave. Such unwanted excitation of Lamb modes is a common issue of plate wave resonators and avoiding it is an open topic of research.

From the measured impedance of the apodized resonators, the parameters summarized in Table 2.2 can be computed. By direct comparison with Table 2.1, note that Q_{max} has increased up

Table 2.2: Measured parameters of the two resonators with AR = 60% and h_{Al} = 180 nm.

λ (μm)	C_0 (pF)	k_t^2 (%)	Q_{max}	Z_r (dB)
2.8	0.57	17.0	726	67
2.9	0.53	17.2	818	69

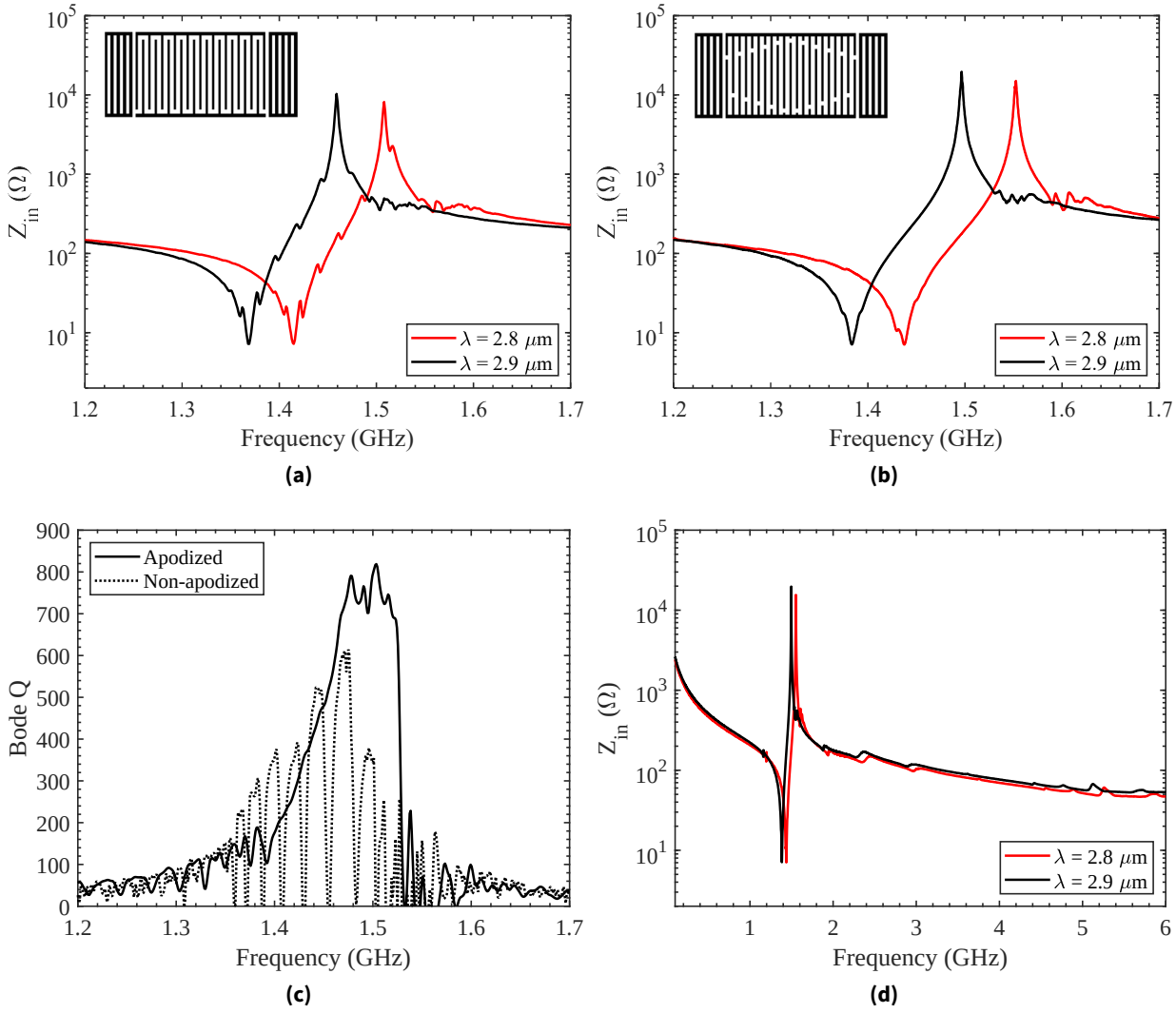

Figure 2.12: Measured impedance of the manufactured LNOI resonators with and without apodization for λ = [2.8, 2.9] μm. (a) Input impedance of non-apodized resonators. (b) Input impedance of apodized resonators with AR = 60%. (c) Comparison of Bode Q for the λ = 2.9 μm resonator with and without apodization. (d) Wideband input impedance of the apodized resonators.

to 800, the impedance ratio has increased 6 dB and, even further, electromechanical coupling k_{eff}^2 has increased to 17%. On the negative side, an important feature to improve is the excessively high electrode resistance that can be observed in all the presented input impedance measurements consistently showing a series electrode resistance of 7 Ω. Such a high resistance is associated with poor

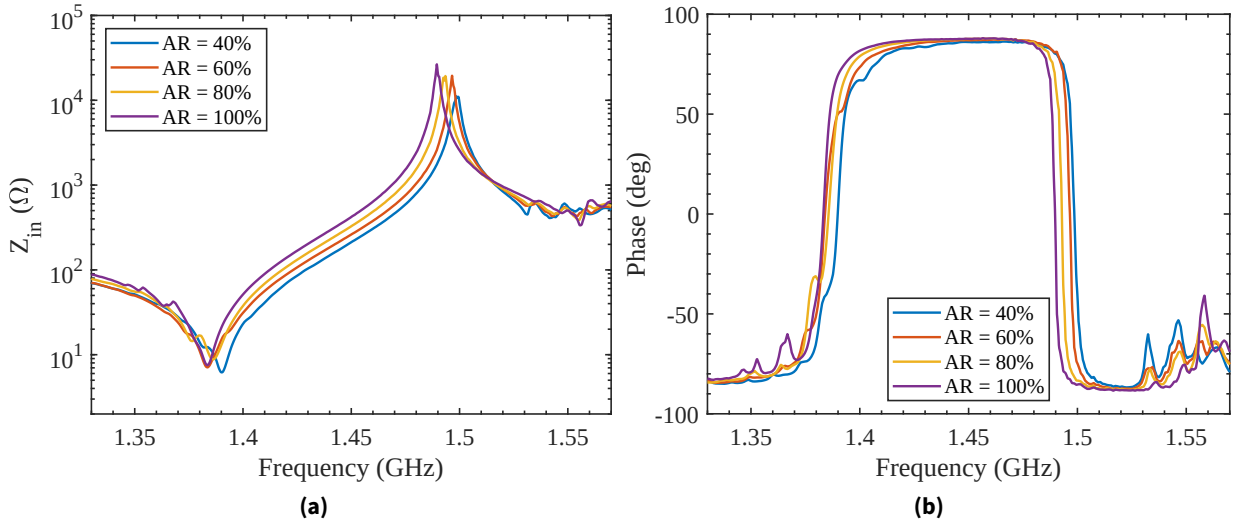

Figure 2.13: Measured impedance of $\lambda = 2.9\ \mu$m resonators for the apodization ratio sweep AR = [40%, 60%, 80%, 100%]. (a) Input impedance magnitude. (b) Input impedance phase.

film quality of the evaporated aluminum and efforts to improve sheet resistance are required.

Finally, once the usefulness of IDT apodization for SH_0 resonators has been demonstrated, also a discussion on the optimum apodization ratio can be provided. While the proposal of a 60% AR as an optimum proposed by Kadota *et al.* has proven useful, a sample resonator of $\lambda = 2.9\ \mu$m has been fabricated for the set of apodization ratios AR = [40%, 60%, 80%, 100%] to observe the differences in resonator performance and assess the choice of 60% as an optimum point. The measured input impedance of the fabricated set of resonators is depicted in Fig. 2.13a and the phase of the measured input impedance is shown in Fig. 2.13b. The input impedance phase trace is very helpful to observe the presence of unwanted spurious modes when their amplitude is not observable in the impedance magnitude plot.

At first, let us clarify that the resonator corresponding to AR = 40% is slightly higher in frequency (8 MHz) due to a lithographic deviation but shows $k^2_{\text{eff}} = 17\%$, that of the resonator with 60% apodization. However, notice in its corresponding phase trace that although transverse modes are partially suppressed, ripples still appear within the two frequencies of the resonator. For this resonator, Q_{max} = 625. On the other hand, for apodization ratios higher than 60% notice how the k^2_{eff} reduces in exchange of a higher Q. For example for an apodization ratio of 100%, $k^2_{\text{eff}} = 16.5\%$ and $Q_{max} = 950$. Moreover, note also that for AR = 100%, spurious modes both above f_p and f_s are more pronounced. All in all, this results confirm that the AR = 60% is the optimal choice in terms of k^2_{eff} and Q because spurious modes are properly suppressed without incurring in any loss of k^2_{eff} .

As a last remark, notice an interesting observation from Fig. 2.13b that allows to highlight the fact that spurious modes above f_p are due to longitudinal modes that depend on the size of the acoustic cavity created by the gratings and IDT. For the four $\lambda = 2.9\ \mu$m resonator, independent of

the apodization ratio applied, such modes remain at the same exact positions.

2.6.4 Comparison with Other Literature

To close this chapter, as a means to compare the achieved resonator performance with other recent contributions exploiting also the SH_0 mode on LN, a brief state of the art survey is provided analyzing a traditional figure of merit in microwave acoustic resonators that is the $k^2_{\text{eff}} \cdot Q$ product. Due to wide variety of $LiNbO_3$ cuts being used to excite the SH_0 mode and the different approaches to obtain wave confinement within the plate, this brief survey does not separate in terms of LN cut but distributes results among four main implementation strategies, namely, LNOI (within which the results in this thesis must be counted), released membrane approaches, LNOI on silicon carbide (SiC) and LNOI with an additional polycrystalline silicon layer between the oxide and the silicon carrier. Survey results are summarized in Table 2.3 and shown in terms of FoM with respect to frequency in Fig. 2.14.

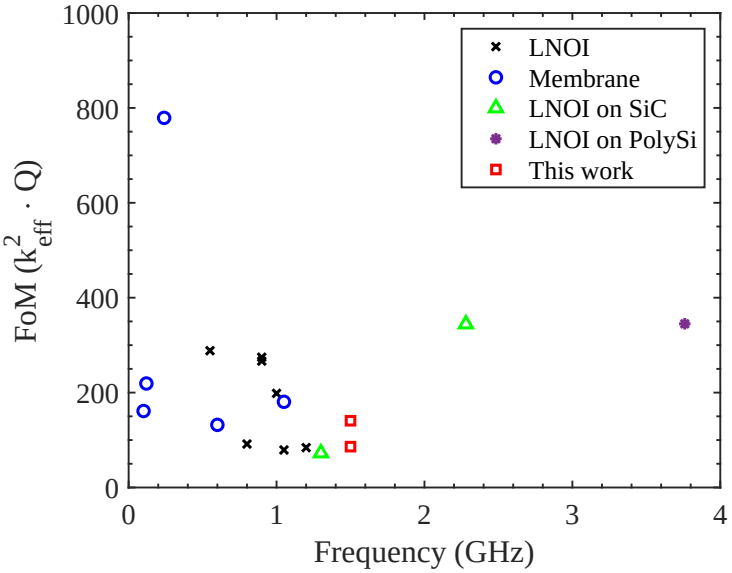

Figure 2.14: Figure of merit FoM = k^2_{eff}·Q as a function of resonance frequency for the examples of SH_0 resonators on thin $LiNbO_3$ found in the literature as of Dec. 2022.

2.7 Chapter Summary

This chapter provides a qualitative description of the main microwave acoustic resonator technologies and introduces some fundamental aspects on their performance and manufacturing that are important to understand the filter synthesis methods provided in this thesis. Starting from a brief historical introduction of how microwave acoustics have achieved their leading role in RF-FEM filtering stages, the two main acoustic technologies that have reached industrial production, SAW and

Table 2.3: Survey of SH_0 resonators on $LiNbO_3$

Reference	Cut	Type	Frequency (GHz)	k^2_{eff} (%)	Q	FoM
[100]	X	LNOI	550	21.2	1360	288.3
[87]	10°YX	LNOI	800	36.5	251	91.6
[101]	30°YX	LNOI	900	24.4	1092	266.4
[102]	30°YX	LNOI	900	24.8	1107	274.5
[86]	X	LNOI	1000	21.8	910	198.3
[103]	15°YX	LNOI	1050	23.9	331	79.1
[89]	15°YX	LNOI	1200	24	350	84
This work	30°YX	LNOI	1500	14	615	86.1
This work	30°YX	LNOI	1500	17.2	818	140.7
[104]	170°YX	Membrane	101	12.4	1300	161.2
[105]	10°YX	Membrane	120	20.6	1064	219.2
[106]	X	Membrane	240	41	1900	779
[99]	30°YX	Membrane	600	22	600	132
[107]	36°YX	Membrane	1050	28	645	180.6
[108]	15°YX	LNOI-SiC	1300	22	330	72.6
[88]	X	LNOI-SiC	2280	26.9	1280	344.3
[109]	32°YX	LNOI-PolySi	3760	23	1500	345

BAW, are presented with their main advantages and disadvantages and their application spaces. Additionally, the more recently explored plate modes in strong piezoeletric material to achieve very high electromechanical coupling values are also introduced.

After the conceptual presentation of the different technologies, the chapter focuses on the experimental validation of shear horizontal mode resonators on the so-called LNOI structure with the main objective of attaining a platform on which the filter synthesis techniques developed in this thesis can be demonstrated. The chapter provides a discussion on the role of electrode thickness in the excitation of spurious modes above the anti-resonance frequency as well as on the importance of transducer apodization to avoid in-band spurious modes. Finally, the achieved results show a promising performance with higher k^2_{eff} values than those of regular SAW and BAW and acceptable Q values. As is demonstrated in Ch. 4 in this thesis, the developed LNOI platform is used to implement a ladder filter exploiting some of the proposed synthesis techniques.

CHAPTER 3

Network Synthesis as Applied to Microwave Acoustic Filters

Network synthesis can be described as the complete opposite of network analysis. While given a circuit and its component values one can apply a set of mathematical tools to analyze it and derive its response, network synthesis faces the problem in the opposite direction: finding the element values and their connection such that they implement a desired response that is expressed as a mathematical function, for example, of frequency. Such a definition, although simple, opens the gate to a complete field of research with many applications.

The objective of this chapter is to provide the theoretical foundations of the application of network synthesis techniques to acoustic wave filters and to present the synthesis procedure that is used throughout this thesis. Starting with a brief historical introduction to the field, this chapter initially focuses on the first requirement in any network synthesis problem: the transfer function to implement. Working in the so-called normalized domain of the complex variable $s = \Sigma + j\Omega$, the properties of functions that can be implemented by acoustic wave ladder filters are described along the specific method to compute the general class of Chebyshev filter functions, the optimal filter function in terms of flexibility and achievable rejection and steepness.

After presenting the transfer functions to use, the focus is set on the prototype networks capable of implementing certain types of transfer functions. In this thesis, attention is paid to inline networks composed of extracted pole sections and such structures are presented along with their nodal representation to allow the introduction of the normalized prototype equivalent of the Butterworth - Van Dyke model. This equivalent was originally derived in works [22, 23] and is the workhorse of microwave acoustic filter synthesis and design. Having discussed functions and the circuits that can implement them, this chapter describes the mathematical procedure to compute the circuital ele-

ments that implement a desired transfer function. To join all the concepts in the chapter, examples of synthesized AW ladder filters are presented in the last section.

The contents of this chapter only constitute a summarized version of the vast knowledge that can be found in basic references such as [9, 110–112], among others, but represent the basis on which forthcoming chapters are built.

3.1 Brief Historical Note

Key names in network synthesis such as Darlington and Belevitch [113, 114] trace the foundation of the field back to the 1920s with the contribution by Cauer [115] regarding the realization of one-port networks whose response is defined as a function of frequency and the publication of Foster's reactance theorem [116]. From such contributions, a growing interest in circuit theory along the wide deployment of telephony networks led to many advances by important names such as H. W. Bode, O. Brune, S. Butterworth, to name a few, highlighting the one by Darlington from the Bell Telephone Laboratories [117] proposing a general method to obtain a two-port reactance network with a prescribed insertion loss. This work, along with the demonstration by Cauer of the use of elliptic functions as the optimal base for transfer functions, led to establishing network synthesis as an important topic in electrical engineering[1].

At first, state-of-the-art frequency-selective circuits aimed to operate at very low frequencies, initially in the order of hundreds of kHz extending to the MHz range during World War II and circuital implementations using lumped inductors, capacitors and resistors were common. As the capability to operate at higher frequencies evolved, the scaling of networks only using lumped components became very difficult when not impossible and distributed structures became the standard thanks to Richard's transformation [118]. At that point, the need of immitance inverters to avoid the implementation of complex distributed structures was highlighted in the fundamental contribution by Cohn [119] establishing their interpretation as electromagnetic coupling between resonators. From that point onwards, network synthesis for microwave filters became a topic in close relation with applied electromagnetics and part of the microwave filter design field.

With the availability of computing power and advances in electromagnetic simulation, many contributions provided methods to easily compute transfer functions without relying on tabulated data and increased the complexity of state-of-the-art microwave filters. Such advances, among others, are summarized in the reference book by Cameron, Kudsia and Mansour [9] and nowadays, synthesis techniques are an important research topic with impact across many technologies ranging from dielectric, coaxial cavity and waveguide filters for base stations and satellite communications

[1] While this note and this thesis focus on the aspects of network synthesis related to filters, other contributions have also directed the field of network synthesis towards techniques for networks including active devices such as operational amplifiers.

to acoustic wave technologies for integrated RF-FEMs. In all these cases, synthesis techniques act as the initial step in any design flow linking the desired response with a circuital implementation of it.

3.2 Transfer Function Characteristics

As already introduced in the first paragraphs, the first requirement in any network synthesis procedure is to define the transfer function that the network must implement as a function of the complex variable $s = \Sigma + j\Omega$, where $j\Omega$ is the frequency axis. Let us highlight here that instead of defining transfer functions directly in the frequency range where the filter passband is implemented, filter synthesis techniques usually work in the so-called normalized frequency domain such that the filter passband is defined from $s = -j$ to $s = j$. Such normalization also assumes that the load impedances at each port of the filter are normalized to 1 Ohm and is useful since the circuital output after synthesizing such normalized function is the so-called lowpass or normalized prototype circuit. From it, via a frequency transformation expression that is presented in a forthcoming section, the filter response is brought into the so-called bandpass domain where the lower and upper passband edges are located at f_1 and f_2, respectively, allowing to define different filter networks all along the electromagnetic spectrum from the same synthesized prototype. Alternatives to this, proposing direct synthesis of filters in the bandpass domain have already been discussed for microwave acoustic filters in [23,24,120] but resulting in a more complex scenario regarding the computation of the transfer function and numerical stability issues due to high order polynomials.

Before diving into the mathematical formulation of filter functions it is important to consider some general aspects of the transfer functions implemented by acoustic wave ladder filters. Considering the electrical response of AW resonators, already presented with the Butterworth - Van Dyke model in Ch. 1, and the example response of a ladder filter depicted in Fig. 1.4b, interesting conclusions can be drawn. At first, notice that an AW ladder filter has as many finite transmission zeros as resonators, giving rise to the concept of fully canonical functions, that is described in this chapter. An inherent characteristic of such functions is their finite out-of-band rejection level. Moreover, considering that transmission zeros are directly related to the resonance frequencies of AW resonators composing the ladder (TZs above the passband are defined by the anti-resonance of series resonators and TZs below the passband are the resonance frequency of shunt resonators), filter functions for AW ladder filters are asymmetric by nature. In other words, there is no response symmetry with respect to the central frequency (f_0) of the filter. These two facts have important implications in the mathematical formulation that follows and are discussed in detail along this chapter.

To begin, let us define the transfer function of a given two-port[2] lossless network in terms of how

[2]Microwave filters are generally two-port networks and thus, the mathematical framework for filter synthesis is devoted to them. In the context of the present chapter, two-port networks are the object under study while extending this synthesis framework for multiport networks is the purpose of Ch. 5 in this thesis.

power injected in the network is transmitted or reflected with respect to the frequency. Consider from transmission line theory that parameters defining transfer and reflection of energy are the reflection $\rho(s)$ and transmission $t(s)$ coefficients, both a function of the normalized input impedance of the network, let it be $z_{\text{in}}(s)$.

$$z_{\text{in}}(s) = \frac{n(s)}{d(s)} \tag{3.1}$$

From the fact that a filter is a passive network composed of reactive elements, the derivation in [9] (Ch. 2) and [110] (Ch. 3), states that the input impedance $z_{\text{in}}(s)$ of a network whose response is symmetric about the zero frequency is a positive real function. That is, its numerator and denominator polynomials have real and positive coefficients. However, from the fact that response asymmetry is required for AW ladder filters, it is necessary that both numerator and denominator of $z_{\text{in}}(s)$ have complex coefficients imposing $z_{\text{in}}(s)$ to be a positive function [9] (Ch. 3).

From (3.1), let us revisit the basic definition of the reflection coefficient,

$$\rho(s) = \frac{z_{in}(s) - 1}{z_{in}(s) + 1} = \frac{n(s) - d(s)}{n(s) + d(s)} = \frac{F(s)}{E(s)} \tag{3.2}$$

where two characteristic polynomials $F(s)$ and $E(s)$ can be defined.

From the lossless assumption of the network, let us impose, along the frequency axis,

$$|\rho(j\Omega)|^2 + |t(j\Omega)|^2 = 1 \tag{3.3}$$

and stating that $t(j\Omega) = 1 - \rho(j\Omega)$, polynomial $P(s)$ related to the transmission of the network can be introduced,

$$|t(j\Omega)|^2 = 1 - |\rho(j\Omega)|^2 = \frac{E(s)E(s)^* - F(s)F(s)^*}{E(s)E(s)^*} = \frac{P(s)P(s)^*}{E(s)E(s)^*} \tag{3.4}$$

yielding the polynomial definition of transmission coefficient:

$$t(s) = \frac{P(s)}{E(s)} \tag{3.5}$$

At this point, it is important to mention that operator * located after the variable dependency of the polynomial refers to the para-conjugation operation in complex-variable polynomials. A further detail of this operation, as stated in [9] (Ch. 6) is provided in appendix A.1 for completeness.

From the above derivation, it is demonstrated that a given network response can be represented by a set of so-called characteristic polynomials $P(s)$, $F(s)$ and $E(s)$. These polynomials, in order to represent an implementable filter function, must fulfill the following properties:

- $E(s)$ must be an N-th order Hurwitz polynomial to ensure system stability, being N the order of the filter. Polynomial $E(s)$ has all its roots in the left half of the s-plane as a consequence of the Routh-Hurwitz criterion that states that the real part of all roots of $E(s)$ must be negative so that when excited with a driving function, all exponential terms $e^{\alpha t}$ are decreasing (being α the real part of a root of $E(s)$).

- $F(s)$ is an N-th degree polynomial with, in the context of this chapter, purely imaginary roots. Reflection zeros (i.e. frequencies at which reflected power is null) are the roots of $F(s)$.
- $P(s)$ is an n_{tz}-th order polynomial, being n_{tz} the number of finite transmission zeros of the filter. The roots of $P(s)$ lie on the imaginary axis, in the context of this thesis, but might as well lie as conjugate pairs in the real axis or as complex quads in the s-plane [9]. For all-pole networks (those where all TZs are located at infinity) $P(s)$ is a constant.

In general terms, when working on filter networks, it is desired that all roots of $F(s)$ lie within the passband, i.e., inside the $s = [-j, j]$ interval of the normalized domain, as reflection zeros, and all roots of $P(s)$ lie outside the passband as transmission zeros to provide rejection.

Having presented the three characteristic polynomials composing the response of a network, let us now switch to a more convenient notation for microwave engineers in terms of scattering parameters. Given the network is connected to normalized reference impedance loads, it can be stated that $\rho(s) = S_{11}(s)$ and $t(s) = S_{21}(s)$. Then, considering that a filter is a passive, lossless and reciprocal two-port network, the S-parameters of the filter function can be defined as follows, where terms ε and ε_r are normalization constants used to express $P(s)$ and $F(s)$ in monic form (i.e., to set their highest-degree coefficient to unity).

$$S_{11}(s) = \frac{F(s)/\varepsilon_r}{E(s)} \tag{3.6}$$

$$S_{22}(s) = \frac{F_{22}(s)/\varepsilon_r}{E(s)} \tag{3.7}$$

$$S_{21}(s) = S_{12}(s) = \frac{P(s)/\varepsilon}{E(s)} \tag{3.8}$$

Revisiting the lossless condition imposed in (3.3), let us impose conservation of energy through the unitarity of S-parameters,

$$S_{11}(s)S_{11}(s)^* + S_{21}(s)S_{21}(s)^* = 1 \tag{3.9}$$

$$S_{22}(s)S_{22}(s)^* + S_{12}(s)S_{12}(s)^* = 1 \tag{3.10}$$

and impose orthogonality

$$S_{11}(s)S_{12}(s)^* + S_{21}(s)S_{22}(s)^* = 0. \tag{3.11}$$

By imposing conservation of energy with (3.9) and (3.10) a very important expression known as Feldtkeller's equation is obtained,

$$E(s)E(s)^* = \frac{F(s)F(s)^*}{\varepsilon_r^2} + \frac{P(s)P(s)^*}{\varepsilon^2} \tag{3.12}$$

having an important role in the computation procedure of many filter functions since it allows to obtain polynomial $E(s)$ if the other two polynomials, $P(s)$ and $F(s)$, and their normalization constants are known.

Let us now focus in (3.11) to provide a deeper description of phases, both reflection and transmission, of the filter function, a fundamental topic for the next chapter in this thesis. Transforming the expression to its polar form, dropping the s dependence here for formulation simplicity and applying the reciprocity of the network (i.e., $S_{21}(s) = S_{12}(s)$), the following expression can be obtained:

$$|S_{11}|e^{j\theta_{11}} \cdot |S_{21}|e^{-j\theta_{21}} + |S_{21}|e^{j\theta_{21}} \cdot |S_{22}|e^{-j\theta_{22}} = 0 \tag{3.13}$$

Also through reciprocity, this time on (3.9) and (3.10), notice that $|S_{11}| = |S_{22}|$, yielding

$$|S_{11}||S_{21}|\left(e^{j(\theta_{11}-\theta_{21})} + e^{j(\theta_{21}-\theta_{22})}\right) = 0 \tag{3.14}$$

what consequently implies that the expression only holds if

$$e^{j(\theta_{11}-\theta_{21})} = -e^{j(\theta_{21}-\theta_{22})}. \tag{3.15}$$

Note that the negative sign in the right-hand side of the expression can be replaced by $e^{j(2k\pm1)\pi}$. By taking only the exponents, a fundamental relation on the phase of the filter function can be stated:

$$\theta_{21} - \frac{\theta_{11} + \theta_{22}}{2} = -\frac{\pi}{2}(2k \pm 1) \tag{3.16}$$

Since scattering parameters $S_{11}(s)$, $S_{22}(s)$ and $S_{21}(s)$ share the common denominator $E(s)$, their phases can be interpreted as the subtraction of two phases, one from the numerator and one from the denominator (e.g. $\theta_{21}(s) = \theta_{n21}(s) - \theta_d(s)$). This fact, allows an interesting rewriting of (3.16), considering that denominator phase terms $\theta_d(s)$ cancel out, as

$$-\theta_{n21}(s) + \frac{\theta_{n11}(s) + \theta_{n22}(s)}{2} = \frac{\pi}{2}(2k \pm 1) \tag{3.17}$$

where s dependency has been re-introduced to clarify that as the right-hand side is an odd multiple of $\pi/2$ and has no dependence in frequency, the difference between the average of phases of S_{11} and S_{22} numerator polynomials and the phase of S_{21} numerator, must be orthogonal at all frequencies. From (3.17) and following a fine mathematical development of the roots of $F(s)$ detailed in [9], one can reach an interesting equation,

$$(N - n_{\text{tz}})\frac{\pi}{2} - k'\pi = -\frac{\pi}{2}(2k \pm 1) \tag{3.18}$$

where N is the order of the filter, n_{tz} is the number of transmission zeros and k' and k integers. Here, for the right-hand side to be satisfied, it is mandatory that $N - n_{\text{tz}}$ is odd. Therefore, notice that for networks where this quantity is even, for example fully canonical ones (where $n_{\text{tz}} = N$, those implemented by acoustic wave ladder filters) an extra $\pi/2$ radians must be added to the right-hand side of the above equation to fulfill the orthogonality condition in (3.11). This is attained by adding a shift of $\pi/2$ to $\theta_{n21}(s)$ or, equivalently, multiplying polynomial $P(s)$ by j.

Additionally, the same development allows to define that $F_{22}(s) = (-1)^N F(s)^*$. Given these two results, the S-parameters in (3.8) can be rewritten in their matrix form for the two cases:

$$\mathbf{S} = \begin{bmatrix} S_{11}(s) & S_{12}(s) \\ S_{21}(s) & S_{22}(s) \end{bmatrix} = \frac{1}{E(s)} \begin{bmatrix} F(s)/\varepsilon_r & jP(s)/\varepsilon \\ jP(s)/\varepsilon & (-1)^N F(s)^*/\varepsilon_r \end{bmatrix} \qquad \text{for } N - n_{\text{tz}} \text{ even} \tag{3.19a}$$

$$\mathbf{S} = \begin{bmatrix} S_{11}(s) & S_{12}(s) \\ S_{21}(s) & S_{22}(s) \end{bmatrix} = \frac{1}{E(s)} \begin{bmatrix} F(s)/\varepsilon_r & P(s)/\varepsilon \\ P(s)/\varepsilon & (-1)^N F(s)^*/\varepsilon_r \end{bmatrix} \qquad \text{for } N - n_{\text{tz}} \text{ odd} \tag{3.19b}$$

Following the derivations up to this point, the fundamental relations of how a set of characteristic polynomials represent the S-parameters of a desired network response are presented. Moreover, note that through Feldtkeller's equation (3.12), it is possible to obtain the common denominator polynomial $E(s)$ if polynomials $P(s)$ and $F(s)$ have been defined. To clarify the importance of this relation, let us go back to the reflection and transmission coefficients to relate the reflected and transmitted power through the so-called characteristic function $K(s)$:

$$|K(s)|^2_{s=j\Omega} = \frac{|\rho(j\Omega)|^2}{|t(j\Omega)|^2} \tag{3.20}$$

Considering again that $\rho(j\Omega) = 1 - t(j\Omega)$, one can get to the following expression

$$|t(j\Omega)|^2 = \frac{1}{1 + |K(s)|^2_{s=j\Omega}} \tag{3.21}$$

and realize, from (3.20), that

$$K(s) = \frac{F(s)}{P(s)}. \tag{3.22}$$

A given transmission response is ultimately described by a characteristic function, that already includes both the information of reflection zeros and transmission zeros, if any. Once this characteristic function is split into its numerator and denominator polynomials, it is Feldtkeller's equation that yields the common denominator polynomial that ensures the three polynomials describe a unitary and orthogonal response. In other words, the problem of computing a desired filter function lies into finding an adequate characteristic function and then obtain its characteristic polynomials. Even further, the different types of filter functions are classified with respect their characteristic function: starting from the maximally flat, also called Butterworth filter, that makes use of the polynomials of the same name and shows a maximally flat passband, through elliptic function filters, also called Cauer filters due to Wilhelm Cauer, that describe an equiripple (equalized ripple) response both in the stopband and the passband, to Chebyshev filters, whose characteristic function is a Chebyshev polynomial and depict equiripple passbands (type I) or equirriple stopbands (type II). Interestingly, Chebyshev filter are a limit case of Cauer filters since elliptic functions lead to Chebyshev polynomials when the stopband ripple of a Cauer filter is reduced to zero [112].

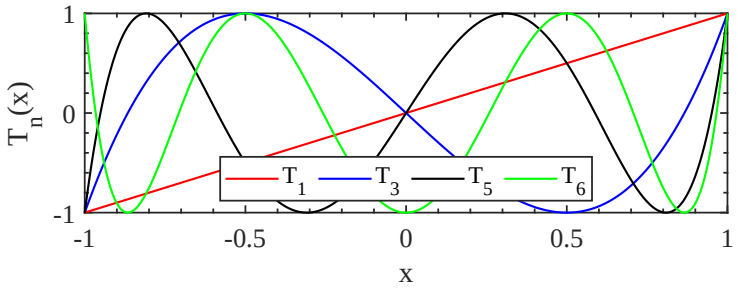

Figure 3.1: Chebyshev polynomials of the first kind $T_N(x)$ for $N = 1, 3, 5, 6$.

Although Cauer filters are proven to provide the highest rejection with the least amount of circuital elements, they do not allow transmission zeros to be set freely. To this end, the fundamental contribution by Cameron [121] that generalized the computation of Chebyshev filter functions to place transmission zeros as desired, overcoming the previous approaches by Orchard and Temes [122] and Rhodes and Alseyab [123], has elevated such functions to be the standard in microwave filter design. From an AW ladder filter perspective, the ability to freely set the position of finite transmission zeros is key due to the direct relation between zeros and resonances of resonators in the ladder. In that direction, previous contributions [22, 23, 124] by the group hosting this thesis demonstrated that a generalized Chebyshev function can be perfectly implemented by a ladder of AW resonators.

3.2.1 A General Class of the Chebyshev Filter Function

This subsection focuses on the procedure to compute the generalized Chebyshev filter function following the method by Cameron. Presenting the characteristic function to synthesize and the iterative procedure to find polynomial $F(s)$ once a set of transmission zeros are defined in $P(s)$, the discussion is focused on fully canonical functions, those implemented by AW ladder filters.

Prior to diving in the generalized case, let us revise the basic rationale behind the use of Chebyshev functions in the scope of all-pole microwave filters (without finite transmission zeros, $n_{\text{tz}} = 0$) those commonly presented in microwave engineering references such as [125]. The main reason to exploit Chebyshev functions for a filter is to achieve a steeper rejection than that provided by Butterworth filters: exchanging the flat passband of the latter for a certain level of ripple within the passband allows to achieve a higher steepness of the filter skirt. To do so, the historical approach is to fix $K(j\Omega) = \varepsilon T_N(\Omega)$ where N is the order of the filter and T_N is the N-th degree Chebyshev polynomial of the first kind, as shown in Fig. 3.1 for $N = 1, 3, 5, 6$. Since for all pole filters, polynomial $P(s)$ is a constant, ε, parameters $S_{21}(s)$ and $S_{11}(s)$ are directly defined through (3.21) and the roots of $F(s)$ are directly found as the zeros of T_N.

However, aiming to implement a filter function with equiripple return loss while having up to N arbitrary transmission zeros, the problem requires a new procedure such that the characteristic

function $K(s)$ of the network is a generalized version of the Chebyshev polynomial of the first kind (C_N instead of T_N) but now subject to $P(s)$ having N finite roots outside the $s = [-j, j]$ interval[3].

Polynomial synthesis of generalized Chebyshev functions

Let us start by expressing parameter $S_{21}(\Omega)$ in terms of the generalized Chebyshev characteristic function $C_N(\Omega)$,

$$|S_{21}(\Omega)|^2 = \frac{1}{1 + |kC_N(\Omega)|^2} = \frac{1}{1 + \left|\frac{\varepsilon}{\varepsilon_r}\frac{F(\Omega)}{P(\Omega)}\right|^2} \tag{3.23}$$

where, as expected, poles and zeros of $C_N(\Omega)$ are transmission and reflection zeros respectively, that is, the roots of $P(\Omega)$ and $F(\Omega)$. Function $C_N(\Omega)$ is the expression of the Chebyshev polynomials of the first kind, namely $T_N(x)$, but stating x as a function of frequency, $x_n(\Omega)$, instead of a simple variable[4].

$$C_N(\Omega) = \cosh\left[\sum_{n=1}^{N} \cosh^{-1}(x_n(\Omega))\right] \tag{3.25}$$

As proposed by Cameron, function $x_n(\Omega)$ must fulfill some properties such that $C_N(\Omega)$ describes a generalized Chebyshev function:

- $x_n(\Omega_n) = \pm\infty$ where Ω_n is either a transmission zero or infinity.
- In-band (i.e., $-1 \leq \Omega \leq 1$), $1 \geq x_n(\Omega) \geq -1$ (x_n is bounded between ± 1).
- At $\Omega = \pm 1$, namely the passband edges, $x_n(\Omega) = \pm 1$.

By developing the three conditions above, the function is found to be

$$x_n(\Omega) = \frac{\Omega - \frac{1}{\Omega_n}}{1 - \frac{\Omega}{\Omega_n}} \tag{3.26}$$

and Fig. 3.2 shows an example of the function $x_n(\Omega)$ for a transmission zero at $\Omega = 1.4$. The vertical lines in the plot mark the edges of the passband.

[3]From this point onwards, the formulation is brought from the s-plane into the Ω-plane (i.e. setting $s = j\Omega$, where Ω is the real lowpass frequency variable) for simplicity. This lowpass frequency is referred as Ω not to mess with the bandpass angular frequency, commonly termed, ω.

[4]Note that the interval of $\operatorname{arccosh}(x)$ is $[1, \infty)$. Therefore for a correct analysis of $C_N(\Omega)$, one might make use of the identity $\cosh\theta = \cos j\theta$ [9] yielding the following expression for $\Omega \leq 1$

$$C_N(\Omega) = \cos\left[\sum_{n=1}^{N} \cos^{-1}(x_n(\Omega))\right] \tag{3.24}$$

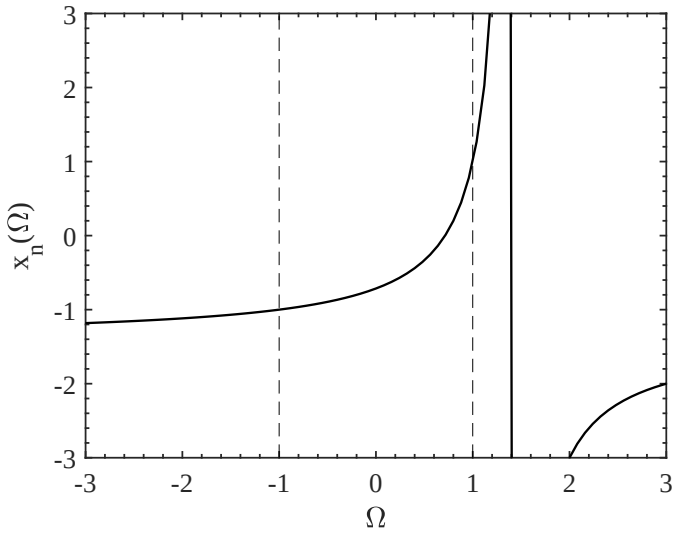

Figure 3.2: Function $x_n(\Omega)$ for $\Omega_n = 1.4$

Having presented the characteristic function to compute, the first step of the computation procedure is to define polynomial $P(\Omega)$ from the set of transmission zeros of the filter, that are prescribed as an input to the method, as

$$P(\Omega) = \prod_{n=1}^{N} (\Omega - \Omega_n) \tag{3.27}$$

yielding a monic polynomial.

Once $P(\Omega)$ is known, the method to find $F(\Omega)$ is a recursive computation of N steps developed in [121] and refined in the book by Cameron *et al.* in Section 6.3 [9]. Starting from (3.25), replacing the $\cosh(x)$ term by its logarithmic identity and after some simplification that is not replicated here, the expression can be broken down to a multiplication of sums and subtractions of two terms,

$$c_n = \left(\Omega - \frac{1}{\Omega_n}\right) \quad \text{and} \quad d_n = \Omega' \sqrt{1 - \frac{1}{\Omega_n^2}} \tag{3.28}$$

where $\Omega' = \sqrt{\Omega^2 - 1}$.

Additionally, the recursive technique defines two auxiliary polynomials $U(\Omega)$ and $V(\Omega)$, used along the N iterations: at each iteration, a new value of $U_i(\Omega)$ and $V_i(\Omega)$ is computed from $U_{i-1}(\Omega)$ and $V_{i-1}(\Omega)$, and the i-th root of $P(\Omega)$, namely Ω_i. If there are less than N transmission zeros, the $N - n_{\text{tz}}$ remaining iterations use input $\Omega_i = \infty$.

The first iteration, $i = 1$, starts as follows

$$U_1(\Omega) = c_1 \quad \text{and} \quad V_1(\Omega) = d_1 \tag{3.29}$$

and from $i = 2$ to $i = N$, the polynomials are computed as:

$$U_i(\Omega) = c_i U_{i-1} + d_i V_{i-1}(\Omega) \tag{3.30a}$$

$$V_i(\Omega) = c_i V_{i-1} + d_i U_{i-1}(\Omega) \tag{3.30b}$$

After N iterations, polynomial $U_N(\Omega)$ has the roots of the numerator of $C_N(\Omega)$, that is, the roots of $F(\Omega)$, and thus, monic polynomial $F(\Omega)$ can be directly built. All roots of $F(\Omega)$, as expected, lie on the real axis of Ω (i.e., on the imaginary axis of s).

Computation of ε and ε_r

At this point, monic polynomial $P(\Omega)$ has been defined from a set of input transmission zeros and $F(\Omega)$ has been computed such that function $C_N(\Omega)$ is a generalized Chebyshev function. With the objective to compute common denominator polynomial $E(\Omega)$ via (3.12), their normalization constants ε and ε_r need to be computed. As stated in (3.8), such normalization constants ensure $P(s)$ and $F(s)$ are monic and at the same time play a role in defining the return loss level of the function. In the case of Chebyshev functions, their value can be found by prescribing a desired return loss level at the edges of the passband (i.e., $s = \pm j$, equivalently $\Omega = \pm 1$) as

$$\varepsilon = \frac{1}{\sqrt{1 - 10^{-RL/10}}} \left| \frac{P(\Omega)}{E(\Omega)} \right|_{\Omega=\pm j}. \tag{3.31}$$

However, since $E(\Omega)$ is found through (3.12) and not known yet, a more useful expression can also be found by looking at the definition of the S-parameters:

$$\frac{\varepsilon}{\varepsilon_r} = \frac{1}{\sqrt{10^{-RL/10} - 1}} \left| \frac{P(\Omega)}{F(\Omega)} \right|_{\Omega=\pm 1} \tag{3.32}$$

Note that constant ε_r that can be assessed from parameter S_{11} and that for a network featuring transmission zeros at infinity (i.e., $N - n_{\text{tz}} > 0$), $S_{21}(\pm\infty) = 0$ and because of the conservation of energy condition (3.9) $S_{11}(\pm\infty) = 1$. Therefore, for those networks, it is clear that $\varepsilon_r = 1$. On the other hand, for fully canonical networks the evaluation of transmission at infinite frequency has a finite value and therefore, the conservation of energy at $\Omega = \pm\infty$ yields,

$$\varepsilon_r = \frac{\varepsilon}{\sqrt{\varepsilon^2 - 1}} \tag{3.33}$$

thus finding a set of equations to find both normalization constants once $P(\Omega)$ and $F(\Omega)$ are known.

Derivation of the common denominator polynomial

The only remaining unknown to complete the computation of the generalized Chebyshev function is common denominator polynomial $E(\Omega)$. Exploiting Feldtkeller's equation in (3.12) there exist two options to find it: either compute the double-degree polynomial $E(\Omega)E(\Omega)^*$ that has $2N$ roots and apply the Hurwitz condition to take only those roots on the upper half of the Ω-plane (equivalently,

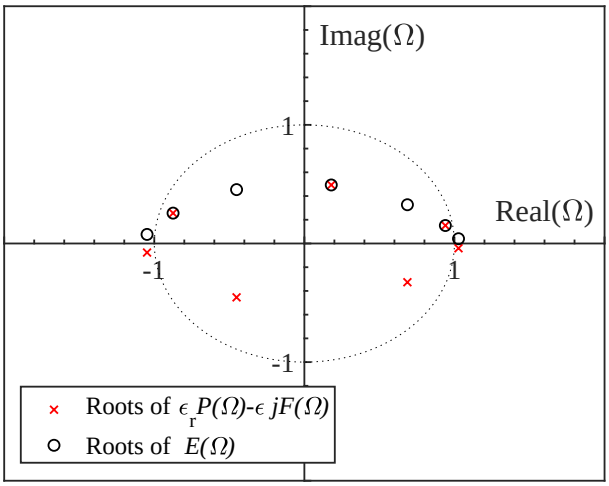

Figure 3.3: Comparison of the roots of $\varepsilon_r P(\Omega) + \varepsilon j F(\Omega)$ and $E(\Omega)$ on the Ω-plane.

the left hand side of the s-plane) or apply what is known as the alternating pole method, proposed in [123].

This interesting method arises from the expansion of (3.12), here in the s-domain for simplicity when considering paraconjugation operations, grouping the conjugated and the non-conjugated terms separately. For example, assuming a fully canonical network,

$$\varepsilon^2\varepsilon_r^2 E(s)E(s)^* = [\varepsilon_r jP(s) + \varepsilon F(s)]\,[\varepsilon_r jP(s)^* + \varepsilon F(s)^*] + j\varepsilon\varepsilon_r\,[F(s)P(s)^* - P(s)F(s)^*] \tag{3.34}$$

where the j term on $P(s)$ comes from fulfilling orthogonality because $N - n_{\text{tz}}$ is even. Notice that the rightmost term of (3.34), i.e., $F(s)P(s)^* - P(s)F(s)^*$, would be the orthogonality condition (3.11) only if $F(s) = F_{22}(s)$. Such equality only holds if all the roots of $F(s)$ lie on the imaginary axis of s (on the real axis of Ω) because the roots of $P(s)$ have already been constrained to lie on the imaginary axis or in complex conjugate pairs. For generalized Chebyshev functions, this is the case and thus, (3.34) simplifies to the product of two terms, one the conjugated of the other. With that, it is possible to recover $E(\Omega)$ by only rooting the expression $\varepsilon_r P(\Omega) + \varepsilon j F(\Omega)$, thus avoiding to compute the roots of a polynomial of degree $2N$, to obtain a set of roots like the one shown in Fig. 3.3 with red crosses. To finally achieve the roots of $E(\Omega)$ the Hurwitz criterion must be imposed by changing the sign of the imaginary part of all roots on the lower half of the Ω-plane. The depicted roots correspond to an example fully canonical function of 7-th order with RL = 18 dB and transmission zeros $\Omega_{tz} = [1.2, -2.5, 1.7, -1.6, 3.3, -2.1, 2.1]$ rad/s, whose polynomial response evaluation is shown in Fig. 3.4a along its characteristic function $C(\Omega)$ in Fig. 3.4b.

The alternating pole method is here highlighted since in the chapter of this thesis devoted to multiplexer synthesis, the fact that roots of polynomials become complex impedes the application of this concept and justifies a discussion on the numerical stability of the overall synthesis method.

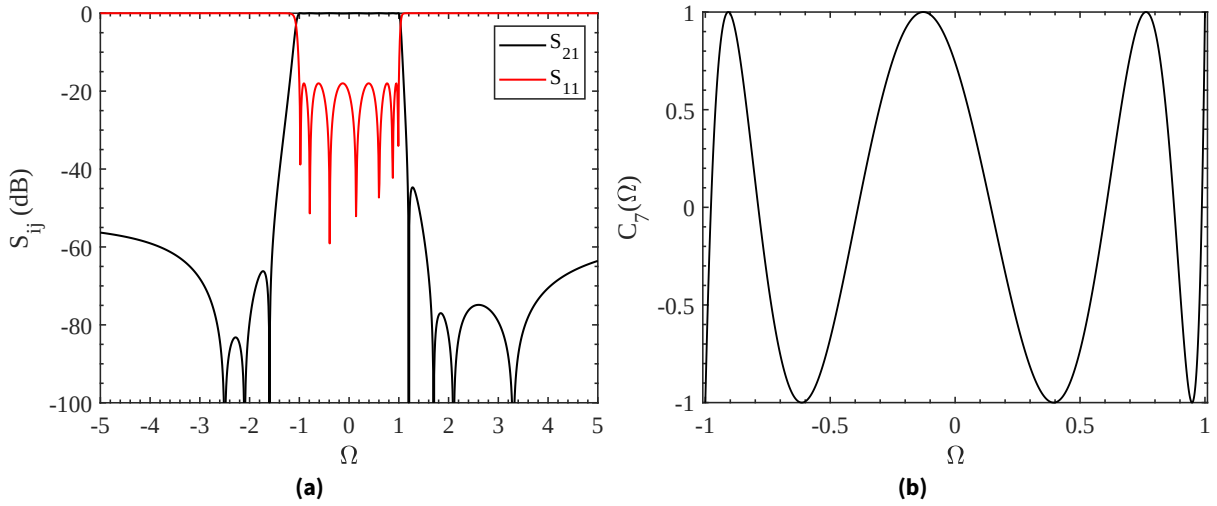

Figure 3.4: Example of a generalized Chebyshev fully canonical function of 7-th order, RL = 18 dB and Ω_{tz} = [1.2, -2.5, 1.7, -1.6, 3.3, -2.1, 2.1] rad/s. (a) Evaluated S-parameters. (b) Normalized characteristic function $C_7(\Omega) = F(\Omega)/P(\Omega)$.

3.3 Asymmetric Transfer Function Impact on Prototype Networks

Following the procedure described in the previous section, the set of characteristic polynomials composing an arbitrary generalized Chebyshev function can be computed. At this point, consider that from (3.2) it is simple to obtain a relation between the polynomials and the normalized input impedance of the filter function and thus the objective of the synthesis could be stated as finding the circuital elements that implement such input impedance. However, before diving into the synthesis methods that allow to do so, let us discuss some details regarding the mathematical domain in which synthesis takes place.

It has already been stated that filter synthesis is performed in a normalized frequency domain, also commonly called the lowpass domain, in which transfer functions are functions of the complex variable s, centered around the zero frequency and defining the passband to span the range $s = [-j, j]$ rad/s (that is, both negative and positive pulsation frequencies) and related to network parameters through a normalized reference impedance of 1 Ohm. As a result, working in such a normalized domain entails that circuits implementing the computed transfer functions of the variable s need be composed of normalized lumped reactive elements[5], i.e., capacitors and inductors, whose units are farads and henries, respectively. Moreover, considering that the impedances of the mentioned reactive elements are first-degree functions of s it is clear that the circuit implementing an arbitrary filter function of degree N is composed of N such reactive elements.

However, the objective of filter synthesis is to finally obtain the circuital components that im-

[5]For lossless passive networks. If lossy networks are considered, resistors other than the unitary terminating impedances should be considered.

plement a desired filter response in the bandpass domain (a response centered around f_0) and to connect both domains, a bilateral frequency transformation function is devised as follows,

$$\Omega = \frac{\omega_0}{\omega_2 - \omega_1}\left(\frac{\omega}{\omega_0} - \frac{\omega_0}{\omega}\right) \tag{3.35}$$

being ω the bandpass angular frequency variable, ω_1 and ω_2 the passband edge frequencies and ω_0 the center frequency of the passband that is computed as the geometric mean of the edges. Commonly, the term $\omega_0/(\omega_2 - \omega_1)$ is grouped under variable α, namely the inverse of the relative or fractional bandwidth.

Such a transformation between the two domains has very interesting consequences that need to be reviewed to completely describe the synthesis of acoustic wave filters in the normalized domain. At first, to illustrate the use of (3.35), let us observe the case of a lumped inductor of value L in the normalized domain whose impedance is $Z(\Omega) = j\Omega L$. By simply applying (3.35) to such impedance assuming an arbitrary bandwidth and central frequency, note that a simple lumped inductor in the normalized domain becomes a second degree function of frequency after transformation:

$$Z(\omega) = \frac{j\alpha\omega L}{\omega_0} + \frac{\alpha\omega_0 L}{j\omega} \tag{3.36}$$

By simple inspection, such an impedance is that of a series LC tank, whose resonance frequency ω_r is ω_0 and whose elements are

$$L_r = \frac{\alpha L}{\omega_0} \qquad \text{and} \qquad C_r = \frac{1}{\alpha\omega_0 L}. \tag{3.37}$$

On the other hand, by direct analysis, a lumped capacitor in the normalized domain becomes a parallel LC tank with $\omega_r = \omega_0$ after transformation.

Although the scope of this thesis is focused on bandpass filters, it is worth mentioning that if instead of a bilateral transformation as in (3.35), a simple scaling in terms of frequency is used, for example stating $\Omega = \omega/\omega_c$ where ω_c is the cutoff frequency, a lowpass filter can be obtained. Equivalently, the inverse of the mentioned scaling would lead to a highpass filter. Notice that such frequency scaling, that ultimately expands the transfer function in the normalized domain to have $\Omega = 1$ exactly at ω_c does not imply any change of function order and so, lowpass filters are composed of reactive elements and not resonators. Moreover, note also that (3.35) is a bilateral transformation and thus, it also translates the transfer function into the negative half of the spectrum. While such a negative part does not have a material meaning when using the expression to transform the synthesized lumped components to the bandpass domain, it has mathematical effects when facing the synthesis of filters directly in the bandpass domain. To completely represent the filter, a transfer function computed directly on variable ω must incorporate all roots corresponding to the filter response in the negative half of the spectrum, thus drastically increasing polynomial order and leading to numerical stability issues, as mentioned at the beginning of this chapter.

Back to the original discussion, an important conclusion from (3.35) is that lumped elements in the normalized domain translate into resonators whose resonance is at the central frequency of the filter, f_0. This, a fundamental aspect of the design of synchronous all-pole filters [9, 19, 20], entails also a very important limitation. Consider, for example, a synthesized prototype network that is composed only of N elements, capacitors and inductors. Irrespective of their disposition, a concept also known as the network topology, from the fact that only capacitors and inductors are present it is observable that such a network can only implement functions that are symmetric with respect to the zero frequency: either all-pole or having finite transmission zeros but in symmetric pairs. That is because given $Z_L = sL$ and $Z_C = 1/sC$, the resulting impedance function, can only have purely real coefficients in the variable s (purely complex in Ω) and thus only have roots distributed symmetrically along the imaginary axis.

However, it is known that asymmetric responses exist and, in this case, are the ones of interest for acoustic wave ladder filters. From a mathematical standpoint, introducing asymmetry in a transfer function, for example, to have independent control of the transmission zeros above and below the passband, entails that both polynomials $P(s)$ and $F(s)$ must have complex coefficients (alternating between real and imaginary if all roots lie on the imaginary axis). Assuming this fact, it is clear that a network implementing such an asymmetric response cannot be only composed of capacitors and inductors. To this end, Baum introduced a fictitious element, the frequency-invariant reactance (FIR) commonly noted jB as admittance or jX as impedance, as a mathematical tool [126] that due to its lack of frequency dependence does not increment total transfer function order but allows to set complex coefficients on the impedance due to its reactive nature. As an example of their use, let us think of the normalized domain prototype circuit of a parallel LC resonator whose resonance frequency is not located at f_0 but at an arbitrary in-band position. In the normalized domain, that would mean a circuit whose admittance is null at a frequency different than $s = 0$. Considering a simple shunt capacitor, resonance would take place exactly at ω_0 because the admittance of the capacitor is null at $s = 0$. However, by adding a FIR element in parallel to the capacitor, let it be jB, the resulting admittance would have the form $Y_c = sC + jB$, yielding a null admittance at $s = -jB$.

Whereas FIR elements enable the fundamental property of transfer function asymmetry, they entail an important limitation due to their lack of a circuital equivalent in the bandpass domain. While frequency-dependent reactive elements in the normalized domain become LC resonators in the bandpass domain through (3.35), there is no way to implement a reactance that is constant with respect to frequency, as stated by Foster's theorem [116]. As a consequence, in the bandpass domain, an FIR can at most be approximated by a reactive element, achieving exact reactance equality only at a single point in frequency (the frequency of transformation) and thus, with such an approximation being valid only in a narrow bandwidth around it. It is a commonly accepted within the microwave filter community that such an approximation is valid for filter fractional bandwidths up to 5%.

As a simple depiction of the narrowband approximation of FIRs in the bandpass domain, Fig.

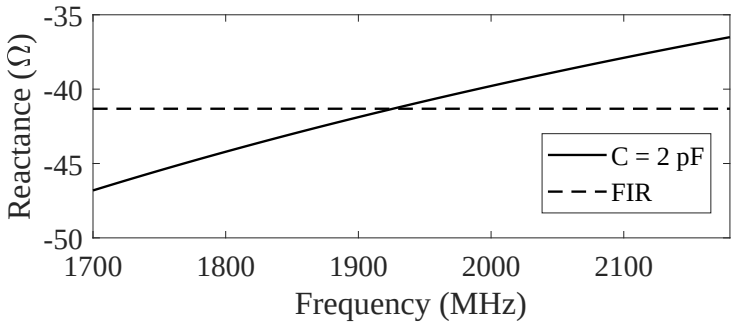

Figure 3.5: Reactance versus frequency of an ideal FIR $jX = -j41.3$ Ohm and a 2 pF capacitor that approximates the FIR at f = 1920 MHz.

3.5 shows the reactance of both a FIR and a 2 pF capacitor that approximates it at $f = 1920$ MHz. As expected, notice that the further from the frequency of reactance equivalence, the larger the deviation from the desired reactance to implement, a fact that ultimately defines the narrowband nature of the transformation in (3.35) when dealing with asymmetric responses. More importantly, the selection of the frequency of reactance equivalence between FIR and their reactive counterparts in the bandpass domain must also be carefully considered due to its impact on the final response obtained in the bandpass domain: the frequency to which FIR are transformed into reactive elements defines the point at which the normalized response is exactly replicated in the bandpass domain. Therefore, if FIRs are transformed at f_0, it is the in-band response (insertion and return loss equiripple) that suffers no deviation from the ideal transfer function, while the exact position of transmission zeros in the bandpass domain might differ slightly due to them being further away from f_0. In general terms, also in the context of this thesis, it is common to use the central frequency of the filter as the transformation frequency for FIRs, to maintain the in-band response of the filter unaltered.

3.4 Normalized Prototype Network of the Acoustic Wave Resonator

After discussing the effects of transfer function asymmetry and the mathematical foundation behind frequency-invariant reactance elements, it is necessary to present the normalized prototype that represents the Butterworth - Van Dyke model (the circuital representation of the electrical performance of an acoustic wave resonator) in the normalized domain so that fully canonical transfer functions can be synthesized in the form of acoustic wave ladder filters.

Let us recall that the BVD model features two resonances, series (f_s) and parallel (f_p), the first being directly related to the motional arm composed of a series LC tank with elements C_a and L_a. From this observation, and considering the frequency transformation in the previous section, it can be stated that the motional arm must be represented with a lumped inductor in the normalized domain. However, notice also that such a series resonance, defined by the thickness of the piezoelectric material for BAW resonators or by the pitch of the interdigital transducer for SAW resonators, is not

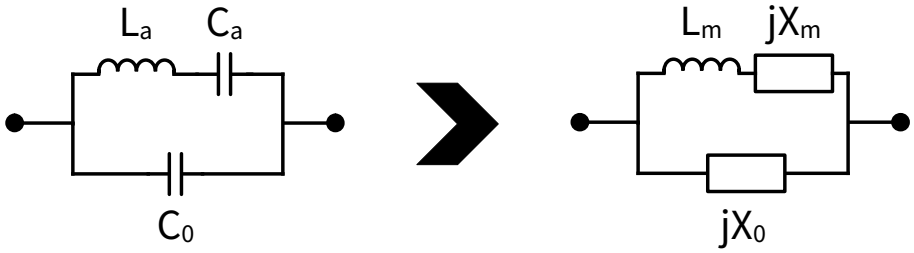

Figure 3.6: Butterworth - Van Dyke model of an acoustic wave resonator (left) and its normalized prototype network (right). FIR elements are circuitally represented as white rectangular boxes.

placed at the central frequency of the filter but at the position of transmission zeros below the passband (those placed by shunt AW resonators) or at different positions inside the passband (in the case of series AW resonators). Therefore, with the objective of representing resonators with different f_s values within a filter, an FIR element in series with the mentioned inductive element is required in the motional arm of the normalized prototype.

Regarding the static arm of the BVD, notice that it does not feature a resonance per se and therefore cannot be composed of a frequency-dependent element in the normalized domain. Consequently, the static capacitor C_0 is modeled as an FIR X_0 in the normalized domain, yielding the normalized prototype network shown in Fig. 3.6 whose normalized input impedance can be computed as follows:

$$Z_{\text{in}}(\Omega) = \frac{jX_0\,(\Omega L_m + X_m)}{\Omega L_m + X_m + X_0} \tag{3.38}$$

Observe the interesting fact that since the AW ladder filter is a fully canonical network of order N, the normalized prototype network of each AW resonator must implement a rational impedance function with numerator and denominator polynomials of at most first degree and thus, can only feature a frequency-dependent element, in this case inductor L_m.

At this point, to find the relation between the BVD and the normalized prototype elements, let us separately equate the impedance of each arm of each model at the central frequency of the filter, as discussed in the previous section. Starting with the static branch let us equate[6] both models introducing Z_0, the reference impedance, so as to denormalize the prototype from the assumed unitary loads:

$$\begin{aligned} Z_s(\Omega)Z_0 &= Z_s(\omega) \\ jX_0Z_0 &= \frac{1}{j\omega C_0}\Big|_{\omega=\omega_0} \end{aligned} \tag{3.39}$$

thus obtaining an expression for the static capacitance C_0,

$$C_0 = -\frac{1}{\omega_0 Z_0 X_0}. \tag{3.40}$$

[6]Stating Z_s from *static* to avoid confusion with reference impedance Z_0.

In terms of the motional arm, following the same equation procedure, two unknowns L_a and C_a are considered.

$$\begin{aligned} Z_m(\Omega)Z_0 &= Z_m(\omega) \\ j(X_m + \Omega L_m)Z_0 &= j\left(\omega L_a - \frac{1}{\omega C_a}\right) \\ \left[X_m + \alpha L_m\left(\frac{\omega}{\omega_0} - \frac{\omega_0}{\omega}\right)\right]Z_0 &= \left(\omega L_a - \frac{1}{\omega C_a}\right) \end{aligned} \tag{3.41}$$

A second equation can be obtained by differentiating (3.41) with respect to ω and then, one can isolate the two unknowns by evaluating $\omega = \omega_0$:

$$L_a = \frac{Z_0}{2}\left(\frac{2\alpha L_m + X_m}{\omega_0}\right) \tag{3.42}$$

$$C_a = \frac{2}{Z_0}\frac{1}{\omega_0(2\alpha L_m - X_m)} \tag{3.43}$$

With the above expressions, the normalized prototype of the AW resonator has been presented in its circuital form, that is, as a set of connected lumped elements. However, in order to facilitate the forthcoming description of the synthesis procedure, and to understand the different nature that series and shunt AW resonators have from a network synthesis perspective, it is interesting to revisit the normalized prototype circuit by introducing immitance inverters. In brief, in this case taking its admittance version for convenience, an admittance inverter of value J Siemens is a two-port network whose input admittance is $Y_{\text{in}} = J^2/Y_L$ when a load admittance Y_L is connected at its output [125].

To introduce admittance inverters into the equivalent circuit, let us connect one of the terminals of the presented normalized prototype to ground, as is the case of a shunt AW resonator. Note that the motional arm, composed of inductor L_m and FIR X_m can be also interpreted, in admittance terms, as a unit capacitor in parallel with an FIR of susceptance value b that is dangling from the static branch FIR of susceptance value B through an admittance inverter of value J_r. The equivalence between the BVD, its normalized prototype and this interpretation introducing admittance inverters is shown in Fig. 3.7. To describe the complete equivalence of both representations of the prototype, note the input admittance of the proposed circuit is

$$Y_{\text{in}}(s) = jB + \frac{J_r^2}{s + jb} \tag{3.44}$$

yielding the same behaviour of the normalized BVD model: at $s = -jb$ the admittance becomes infinite, placing a transmission zero at $\Omega = -b$, and similarly there is a position where the admittance is zero. The position of the TZ is only dependent on the value of FIR b, that can either be positive or negative. This structure, that is not only exploited for acoustic wave resonators but for other microwave structures, is commonly called an extracted pole section since the structure itself is responsible for placing a transmission zero. In this case, the choice of assuming a shunt AW resonator is not arbitrary but important since it allows to state that the motional arm of such resonator is responsible for a transmission zero below the passband, that is, at $\Omega < 0$, thus setting $b > 0$.

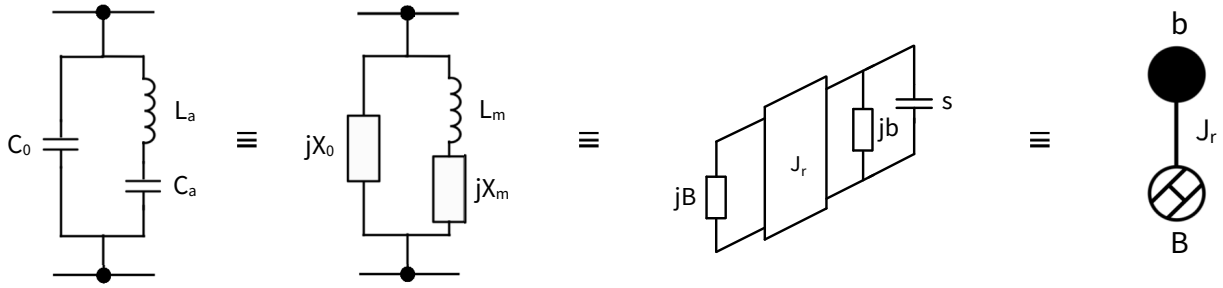

Figure 3.7: Nodal interpretation of the Butterworth - Van Dyke model in the normalized domain for the case of a shunt resonator.

With this, the relation between elements b, B and J_r and the normalized prototype of the BVD for a shunt resonator are, as developed by Giménez in [23, 124]:

$$X_{0-\mathrm{SH}} = -\frac{1}{B} \tag{3.45a}$$

$$L_{m-\mathrm{SH}} = \frac{1}{J_r^2} \tag{3.45b}$$

$$X_{m-\mathrm{SH}} = \frac{b}{J_r^2} \tag{3.45c}$$

Moreover, given the proposed interpretation of the normalized prototype of the BVD including an admittance inverter, the so-called nodal representation of the network can also be introduced as shown at the right end of Fig. 3.7 where white dashed circles are FIRs, black lines correspond to admittance inverters and black nodes are capacitors to ground that might have an FIR in parallel setting their frequency of null admittance at a frequency different than zero. Letter b above the black node states the value of such FIR and so, the frequency where the node imposes zero admittance.

While the circuital view of the prototype as in Fig. 3.6 is closely related to the final BVD model, from a network synthesis perspective it is interesting to introduce the concept of nodal representation since it has become a common method of network description in the microwave filter community due to its capability of easily representing the network in terms of resonators and couplings between them[7]. Although no electromagnetic couplings between resonances are involved in the construction of AW ladder filters, the presence of the introduced inverters is absorbed by circuital transformations but is very interesting to face the synthesis of acoustic wave filters with concepts originally developed for electromagnetic resonators.

At this point, note that the equivalence between the nodal interpretation of the normalized BVD

[7] As a brief justification, such a nodal view of the network stems, among many other factors, from the introduction of immitance inverters in the design of microwave filters to represent electromagnetic coupling between resonators, popularized by Cohn in [119] and later generalized by Levy in [127], and also from the proposal of the coupling matrix by Atia, Williams and Newcomb in [128, 129] to deal with the synthesis of multicoupled cavity filters.

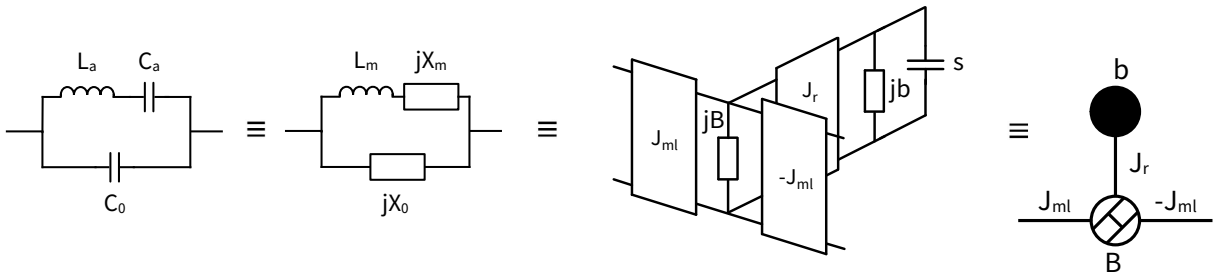

Figure 3.8: Nodal interpretation of the Butterworth - Van Dyke model in the normalized domain for the case of a series resonator. Underscript *ml* refers to the main line of the filter.

with a shunt resonator has been derived by considering that the motional arm is the one in charge of placing the transmission zero and thus, it can be directly related with the value b of the FIR in the dangling section. However, for a series AW resonator, that places a transmission zero above the passband with its f_p, such an equivalence requires an additional step, as shown in Fig. 3.8. Such step is related to the serialization of the extracted pole section since given the behavior of admittance inverters, it can be easily demonstrated that an arbitrary series impedance can be equivalently implemented as a shunt admittance placed between two admittance inverters of same value and opposite sign. While this structure is very similar to that of a shunt AW resonator except for the two extra admittance inverters, in this case the dangling section is not directly the motional arm of the normalized BVD since the transmission zero is placed by f_p of the resonator and so, $b < 0$.

Taking the above facts into the analysis, the equivalence between the nodal elements and the normalized BVD is defined as follows:

$$X_{0-\mathrm{SE}} = \frac{B}{J_{ml}^2} \tag{3.46a}$$

$$L_{m-\mathrm{SE}} = \frac{B^2}{J_r^2 J_{ml}^2} \tag{3.46b}$$

$$X_{m-\mathrm{SE}} = \frac{B}{J_{ml}^2}\left(b\frac{B}{J_r^2} - 1\right) \tag{3.46c}$$

Note that now the resonance frequency of the motional arm is not directly related to b but to a combination of B, Jr and b, as expected since the dangling section is now related to f_p instead of f_s. More importantly, considering the natural behavior of an AW resonator as stated by the BVD model, note that for X_0 to become a negative FIR and thus be approximated by a capacitor C_0, a given nature or sign of FIR element B is required, yielding $B < 0$ for shunt resonators and $B > 0$ for series. This fact, that has very important implications in the synthesis of AW filters, is discussed in detail in Ch. 4.

Once the nodal equivalents of both series and shunt resonators are known, the complete nor-

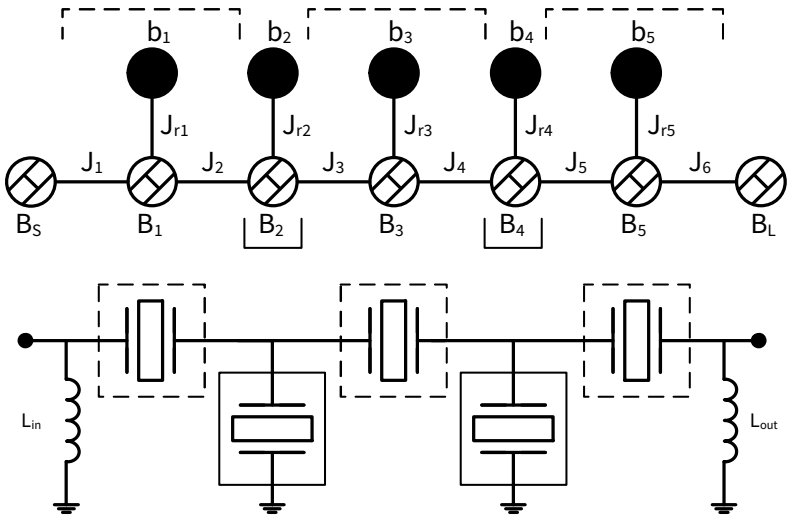

Figure 3.9: Equivalence between the nodal representation (top) and the final ladder topology (bottom) of an N=5 AW filter starting in series resonator. Solid underlined sections are shunt resonators and dashed overlined sections are series resonators. Input and output FIR elements B_S and B_L are input and output inductors L_{in} and L_{out}.

malized prototype of an AW ladder filter can also be represented in nodal terms as shown in Fig. 3.9 for a 5th order filter starting in series resonator, noting that series resonators can only be represented in this way if $J_1 = -J_2, J_3 = -J_4$ and $J_5 = -J_6$. This yields the nodal form of the complete filter that is exploited to perform the extraction of synthesized elements with the synthesis procedure presented in a forthcoming section of this chapter. Notice that the network features two FIR elements B_S and B_L at the source and load nodes, approximated as shunt input and output reactive elements after prototype de-normalization as either capacitors or inductors depending on the sign of $B_{S/L}$, that are inherent to networks placing transmission zeros through extracted pole sections.

3.4.1 The Role of Source and Load FIRs

In the previous equivalence between the AW ladder filter and its nodal form in the normalized domain, the presence of source and load FIR nodes B_S and B_L has been introduced. Although the need of such elements is a widely accepted fact in the microwave acoustics community [17, 130–133] that is commonly associated to impedance matching issues, their role is in fact an inherent aspect of an inline network that is composed of N extracted pole sections each independently responsible for a finite transmission zero. To justify this aspect it is important to carefully consider input reflection phase (i.e., phase of parameter $S_{11}(s)$ also noted as $\angle S_{11}(s)$), a sometimes forgotten feature of filter transfer functions.

Let us start the discussion directly from a nodal perspective, by taking the diagram of Fig. 3.9 as an example, and considering the elements that compose the first series resonator. That is, mainline inverters J_1 and J_2, FIR B_1 and the dangling section composed of J_{r1}, b_1 and a unit capacitor. If one

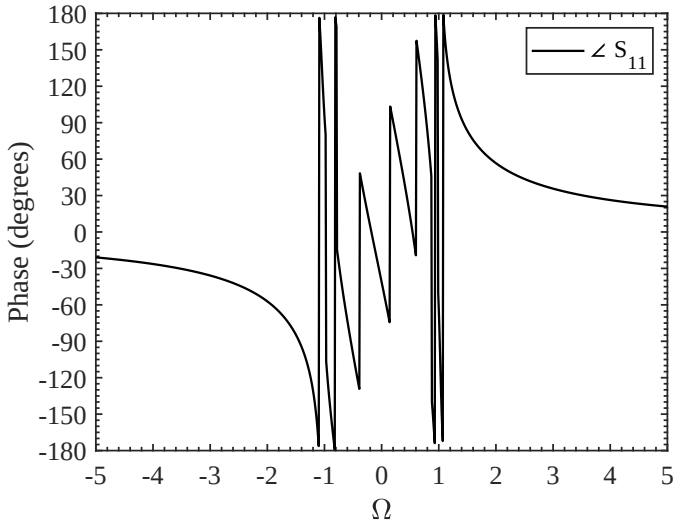

Figure 3.10: Intrinsic input reflection phase of the 7-th order generalized Chebyshev transfer function depicted in Fig. 3.4a.

inspects the input admittance of such structure (looking inwards from the left port of J_1, neglecting NRN B_S) exactly at the frequency $s = -jb_1$, in this case a positive frequency because $b_1 < 0$ since it corresponds to a series AW resonator, the result is $Y_{\text{in}} = 0$, an open circuit, and thus a reflection phase of zero degrees. This is, as expected, congruent with the fact that such transmission zero represents the anti-resonance frequency of a series AW resonator. However, let us also consider the intrinsic reflection phase of a generalized Chebyshev function, the one to implement with an AW ladder filter, as shown in Fig. 3.10 for the example function of 7th order computed in Fig. 3.4a. Notice that while there is a horizontal asymptote towards zero degrees as s tends to infinity, at frequencies outside the passband $s \in (-\infty, -j] \cup [j, \infty)$, $\angle S_{11}$ is different than zero. Therefore, if one assumes the network starts directly at the left port of J_1 and the first transmission zero is located at, for example, $s = j1.2$ rad/s, note that the reflection phase imposed by the transfer function and the reflection phase intrinsic to the first series AW resonator do not match.

Clearly, to fulfill such a transfer function reflection phase with the presented structure, an additional FIR element is required at the input port (also at the output regarding the last resonator of the filter if the filter is observed from the load node) such that it acts as a phase matching element and accommodates the remaining reflection phase of the generalized Chebyshev function at the position of the first transmission zero. Following this rationale, note that the role of mainline FIRs (e.g., B_1), although ultimately part of each AW resonator, is that of phase matching elements to their adjacent resonators.

However, let us review a very important mathematical property related to the phase of complex numbers. Recalling the definition of S_{11} in (3.19), note that by multiplying $S_{11}(s)$ by a complex number of unitary modulus and phase θ_{add}, the magnitude of $S_{11}(s)$ is maintained while its phase is

shifted, what allows to modify the reflection phase of the transfer function as follows,

$$S_{11}(s) = \frac{F(s)/\varepsilon_r}{E(s)} e^{j\theta_{\text{add}}} \tag{3.47}$$

where θ_{add} must be in radians. Such an additional phase term has very important implications in the synthesis and design of acoustic wave filters, as is discussed in detail in Ch. 4, but, as an introduction related to the role of source and load FIR elements, note that source element B_S is required as long as $\angle S_{11}(j\Omega_1) \neq 0°$ when starting in series resonator. However, notice that it is possible to find an additional phase term θ_{add} such that it ensures a reflection phase of zero degrees at the exact position $s = j\Omega_1$ and is computed as:

$$\theta_{\text{add}} = -\arg\left(\frac{F(s)/\varepsilon_r}{E(s)}\Big|_{s=j\Omega_1} \right). \tag{3.48}$$

Applying such a shift would yield a synthesized network implementing the same transfer function, in magnitude terms, as the originally computed through the method in Sec. 3.2, but without requiring source element B_S because of the imposed reflection phase.

To close this brief discussion, that is re-taken in detail in Ch. 4, it is interesting to mention that it is common practice to apply such phase shift term directly to polynomial $F(s)$, yielding $F'(s) = F(s)e^{j\theta_{\text{add}}}$, and that through the definition of scattering parameters from the characteristic polynomials in (3.19) and (3.17), reflection phase modification at the input port results in a modification of output reflection phase, i.e., $\angle S_{22}(s)$, in an antisymmetric manner. That is, $\theta_{\text{add}-11} = -\theta_{\text{add}-22}$.

3.5 Available Network Synthesis Techniques

After describing the procedure to compute a generalized Chebyshev transfer function and the normalized prototype of the acoustic wave ladder filter along some of its particularities, the only remaining point is to introduce the mathematical techniques that allow to transform the set of characteristic polynomials of the transfer function into the circuital elements that implement it. In general terms there are two main approaches to filter synthesis, each with its own features and specific applications, that are the coupling matrix and the extracted pole techniques. In both cases, the set of characteristic polynomials describing the transfer function is used to obtain an immitance function on which mathematical operations are performed to obtain the final circuital form of the network. In the case of the coupling matrix, such operations involve initially obtaining an initial topology called transversal network and then sequentially transform it until the desired topology is reached, while with the extracted pole technique, the procedure is based on sequentially extracting circuital elements from the overall impedance function, similar to the original approach by Darlington [117]. Although the one exploited in this thesis is the latter, both techniques deserve a description to understand their main advantages and applications.

The extracted pole technique was initially proposed by Rhodes and Cameron in [134] exploiting phase shifters to enable the realization of sections that were directly responsible of a transmission zero in the network. This technique was later extended with the introduction of non-resonant nodes (NRNs) [135], network nodes that are solely composed of an FIR as the case of element B shown in Fig. 3.7, and their application to the synthesis of inline filter including extracted pole sections in [136] without resorting to phase shifters[8]. This method, that initially could handle at most two transmission zeros was later extended by Amari and Macchiarella [137] to enable even inline fully canonical networks. This latter contribution is the basis on which the synthesis method for AW filters in [124] is built. The aforementioned contributions all extract network elements from an overall admittance function of s, in the form of an inline network, what ultimately limits the synthesis of networks that require couplings other than the main line. To this end, Tamiazzo and Macchiarella extended the method to include cross-couplings in [138] by using the ABCD or chain matrix as the vehicle for element extraction, as is described in the next section of this chapter.

On the other hand, the concept of coupling matrix was initially proposed by Atia, Williams and Newcomb in [128,129] as a method to represent and synthesize microwave filters composed of multicoupled resonators. Such a coupling matrix is interpreted from an admittance point of view and can be understood as the adjacency matrix of a graph since it includes all information related to how all nodes in the network are coupled to each other. As covered in detail in [9] (Ch.8 and 9), a fundamental reference regarding coupling matrix synthesis, this method starts by computing the so-called transversal topology, in which all nodes are in parallel to each other and only coupled to source and load, as the eigenvalue decomposition of the overall admittance of the filter function. Such a transversal topology, that already implements the desired response, can then be reconfigured into alternative topologies by applying similarity transformations in the form of rotations to the matrix since such transformations do not affect matrix eigenvalues and thus, neither the network response. This is a crucial implication of this approach since at any point through the process the response provided by the coupling matrix is the desired transfer function defined at the beginning. Thanks to this, it is possible to assess if a given transfer function can be accommodated by a desired topology and, if not, highlight the additional elements that need to be considered to implement it.

Interestingly, note the fact that considering an arbitrary fully canonical transfer function of order N, the initial transversal topology obtained through eigenvalue decomposition of such function features N resonant nodes. Thus, considering source and load nodes, yielding a coupling matrix of dimensions $N+2$ x $N+2$. However, for an inline topology made of extracted pole sections as the one shown in Fig. 3.9 implementing the same transfer function, note that the addition of NRNs gives rise to a network with $2N+2$ nodes, thus being described with a coupling matrix of dimensions $2N+2$ x $2N+2$. Even further, the N eigenvalues of both matrices are not equal what clearly indicates that

[8] From this point onwards, terms NRN and FIR might be used interchangeably as is commonly done in the literature. The term non-resonant node contrasts with resonant node (RN) a common term to refer to black nodes in nodal diagrams, those nodes that ultimately transform into LC resonators.

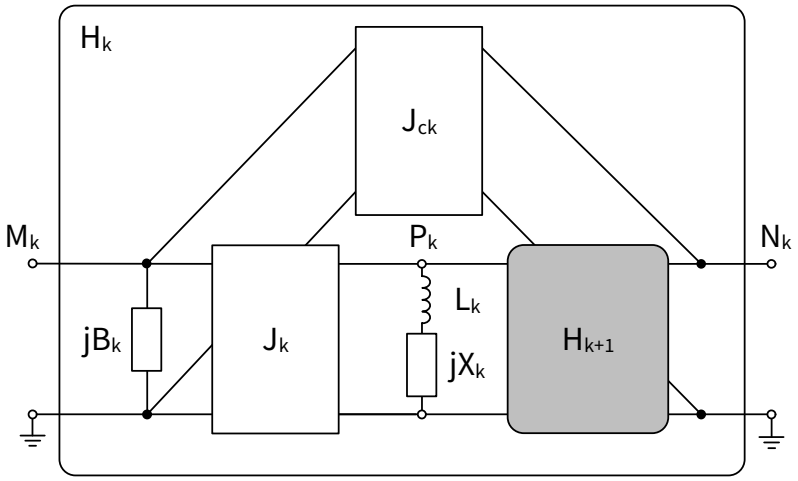

Figure 3.11: Subnetwork considered at the k-th step of the recursive synthesis procedure.

obtaining the inline extracted pole topology through coupling matrix rotations implies non-similar matrix transformations. Initially, this was the main reason that impeded the synthesis of AW ladder filters through the coupling matrix method and extracted pole techniques were fundamental. However, recent contributions by Caicedo Mejillones [139, 140] have broken the barrier between both methods and Acosta [141] has extended such concepts to synthesize AW ladder filters through coupling matrix rotations.

3.5.1 Extracted Pole Technique

The synthesis method implemented in the context of this thesis is the extracted pole technique based on ABCD matrix extractions as in the work by Tamiazzo and Macchirella [138], that allows to synthesize networks including resonant and non-resonant nodes not only as pure inline but also in the form of cross-coupled topologies. Although the cross-coupling synthesis feature is not exploited in this thesis, it has been already applied to AW filters to explore the effects of electromagnetic feedthrough through the package of a filter in [27, 28].

The proposed synthesis method is a recursive process of $N+1$ steps that move along the topology, extracting prototype elements at each step, and that can be applied from source to load, load to source or alternating source and load extractions following a set of indices M_k, N_k and P_k, as proposed by Tamiazzo, that can be exploited to face alternative topologies that include cross-couplings, such as, for example, the quadruplet. Such indices are depicted in Fig. 3.11, that represents the network situation that is faced at each step of the recursive extraction: H_k is the subnetwork considered at the k-th step, and H_{k+1} is the remaining network for step $k+1$. J_k is the main line admittance inverter, jB_k is the FIR element of the main line NRN (B_i in the nodal network in Fig. 3.9, J_{ck} is a cross-coupling embracing the main line of the network from node M_k to node N_k, and inductance L_k and FIR jX_k are the serialized equivalent of a dangling resonator branch shown in Figs. 3.8 and 3.7

originally composed of J_{rk}, b_k and a unit capacitor, through the simple equivalence:

$$L_k = \frac{1}{J_r^2} \qquad X_k = \frac{b}{J_r^2} \tag{3.49}$$

Note the equations are those presented in (3.45) for a shunt AW resonator but here let us highlight an important feature of the extraction procedure that is closely related to the role that main line FIRs have in terms of phase matching between extracted pole sections. Elements extracted at the k-th iteration, i.e., FIR jB_k and the dangling section L_k and jX_k do not belong to the same AW resonator but to different sections. For example, considering $k = 1$, the first extraction of the procedure, B_1 would be the input NRN B_S and L_1 and jX_1 would correspond to the first AW resonator because these are the remaining elements that can be extracted when evaluating the overall immitance function at the frequency where the extracted section places a transmission zero. Moreover, this clarification is important not to confuse numbering in Fig. 3.9 with the subindex k used to indicate the iteration of the process.

As already introduced, the mathematical form in which the computed transfer function is used for element extraction is the ABCD matrix, a common tool in network theory, that can be expressed in the following form,

$$[ABCD] = \frac{1}{jP(s)/\varepsilon}\begin{bmatrix} A(s) & B(s) \\ C(s) & D(s) \end{bmatrix} \tag{3.50}$$

where polynomials $A(s)$, $B(s)$, $C(s)$ and $D(s)$ are related to the polynomial coefficients of $F(s)/\varepsilon_r$ and $E(s)$, as described in appendix A.2.[9] Therefore, after computing the generalized Chebyshev transfer function, the ABCD polynomials can be computed and the extraction procedure can start.

Extraction of an Extracted Pole section

Since AW ladder filters implement fully canonical functions the following explanation focuses on the case of extracted pole sections that place transmission zeros at exactly the roots of $P(s)$ but, for completeness, it must be mentioned that this method allows to extract also either resonant nodes at infinity, extracted pole sections at arbitrary frequencies $j\Omega_k$ that are not roots of $P(s)$ using cross-couplings and even dual transmission zeros as proposed in [142]. Therefore, following the network perspective depicted in Fig. 3.11, the first thing to extract in any synthesis step is cross-coupling J_{ck}, a step that is included here for completeness. The value of such cross-coupling can be computed as

$$J_{ck} = -\frac{P_k(j\Omega_k)}{B_k(j\Omega_k)} \tag{3.51}$$

where $j\Omega_k$ is the transmission zero implemented by the set of elements to be extracted at the k-th iteration. Note that as long as TZ Ω_k is a root of $P(s)$, $J_{ck} = 0$. If such cross-coupling exists, the overall ABCD polynomials should be updated to reflect the fact that the coupling has been extracted,

[9] The usage of B_k as the nomenclature for the FIR element at the k-th iteration might lead to confusion with polynomial $B(s)$. Hence, frequency dependence on s is always depicted to avoid confusion.

following the expressions in [138], not noted here because $J_{ck} = 0$ for AW ladder filters. However, to maintain notation consistency, let us call the remaining chain matrix as $[ABCD]'_k$. At this point, the element to be extracted is FIR element B_k, in charge of ensuring the proper reflection phase for the forthcoming extracted pole section. Such an FIR element is computed as follows:

$$B_k = \frac{D'_k(j\Omega_k)}{B'_k(j\Omega_k)}. \tag{3.52}$$

After computing B_k, it must be extracted from the remaining network by updating the ABCD polynomials as

$$[ABCD]''_k = \frac{1}{jP''_k(s)}\begin{bmatrix} A''_k(s) & B''_k(s) \\ C''_k(s) & D''_k(s) \end{bmatrix} = \frac{1}{jP'_k(s)}\begin{bmatrix} A'_k(s) & B'_k(s) \\ C'_k(s) - B_k A'_k(s) & D'_k(s) - B_k B'_k(s) \end{bmatrix}. \tag{3.53}$$

At this point, the next element to extract is main line admittance inverter J_k between nodes M_k and P_k. For reasons that are discussed after this method, the value of such main line inverters is fixed to unity and alternates in sign between adjacent extracted pole sections. Therefore, imposing $J_k = 1$, the remaining ABCD polynomials need be updated to $[ABCD]'''_k$, as follows:

$$[ABCD]'''_k = \frac{1}{jP'''_k(s)}\begin{bmatrix} A'''_k(s) & B'''_k(s) \\ C'''_k(s) & D'''_k(s) \end{bmatrix} = \frac{1}{jP''_k(s)}\begin{bmatrix} -jC''_k(s) & -jD''_k(s) \\ -jA''_k(s) & -jB''_k(s) \end{bmatrix}. \tag{3.54}$$

Once at node P_k, elements L_k and jX_k remain as the last to be extracted at this k-th synthesis step. Considering the equivalence with the dangling section elements in (3.49) and knowing that the section being extracted places TZ $j\Omega_k$, it is already known that $b_k = -\Omega_k$. Moreover, let us inspect the input admittance as in (3.44), now from node P_k and evaluated at $j\Omega_k$,

$$Y_{in}(j\Omega_k) = \frac{D'''_k(j\Omega_k)}{B'''_k(j\Omega_k)} = \left.\frac{J^2_{rk}}{s - j\Omega_k}\right|_{s=j\Omega_k} \tag{3.55}$$

yielding the typical partial fraction expansion form of a residue divided by a pole. With this interpretation, applying the Heaviside cover-up method such residue, i.e., J_{rk}, can be computed as,

$$J^2_{rk} = \left.\frac{D'''_k(s)}{B'''_k(s)/(s - j\Omega_k)}\right|_{s=j\Omega_k} = \frac{D'''_k(j\Omega_k)}{\tilde{B}_k(j\Omega_k)} \tag{3.56}$$

where term $\tilde{B}_k$ is the result of dividing B'''_k over the root $j\Omega_k$.

After computing J_{rk} all elements of the dangling section are known because $b_k = -\Omega_k$ and the ABCD polynomials must be updated so to extract the computed dangling section, yielding the $[ABCD]$ matrix of the remaining subnetwork H_{k+1}:

$$[ABCD]_{k+1} = \frac{1}{j\tilde{P}_k(s)}\begin{bmatrix} \tilde{A}_k(s) & \tilde{B}_k(s) \\ \tilde{C}_k(s) & \tilde{D}_k(s) \end{bmatrix} = \frac{(s - j\Omega_k)}{jP'''_k(s)}\begin{bmatrix} \dfrac{A'''_k(s)}{(s - j\Omega_k)} & \dfrac{B'''_k(s)}{(s - j\Omega_k)} \\ \dfrac{C'''_k(s) - J^2_{rk}\tilde{A}_k(s)}{(s - j\Omega_k)} & \dfrac{D'''_k(s) - J^2_{rk}\tilde{B}_k(s)}{(s - j\Omega_k)} \end{bmatrix} \tag{3.57}$$

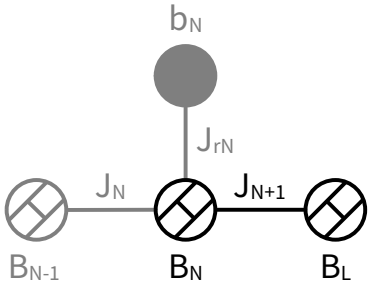

Figure 3.12: Nodal view of the elements faced at the last iteration of the synthesis. In grey are those elements that have already been extracted.

At this point, the degree of all ABCD polynomial has reduced by one and thus, an extracted pole section has been synthesized completing one step of the recursive synthesis procedure. For a network of order N composed of N extracted pole sections, this same procedure should be repeated N times. After that, step $k+1$ is reached and the focus directs to how to end the synthesis after all roots of $P(s)$ have been considered.

Final step

Once all extracted pole sections have been extracted, notice from Fig. 3.9 that the only remaining elements are a main line admittance inverter (J_{N+1}) placed between two NRNs B_N and B_L, the load node, as in Fig. 3.12.

Let us chain the ABCD matrix of each element, to observe the composition of the remaining ABCD matrix after the N-th step of the synthesis,

$$[ABCD]_{N+1} = \frac{1}{J_{N+1}} \begin{bmatrix} -B_N & j \\ j(J_{N+1}^2 + jB_nB_L) & -B_L \end{bmatrix} = \frac{1}{jP_{N+1}(s)} \begin{bmatrix} A_{N+1}(s) & B_{N+1}(s) \\ C_{N+1}(s) & D_{N+1}(s) \end{bmatrix} \tag{3.58}$$

noting that now $P_{N+1}(s)$ has no remaining roots and thus, is a constant. Therefore, since the N transmission zeros of the network have already been used, the evaluation of the three remaining elements is done at infinite frequency.

The first element to be extracted is main line admittance inverter J_{N+1}, that, due to the lack of a dangling section after it, must be computed as a cross-inverter, similar to (3.51) but as a limit to infinite frequency,

$$J_{N+1} = \lim_{s\to\infty} -\frac{P_{N+1}(s)}{B_{N+1}(s)} = -\frac{P_{N+1}}{B_{N+1}} \tag{3.59}$$

and such inverter must be extracted from the remaining ABCD matrix as follows:

$$\begin{aligned} [ABCD]'_{N+1} &= \frac{1}{jP'_{N+1}(s)} \begin{bmatrix} A'_{N+1}(s) & B'_{N+1}(s) \\ C'_{N+1}(s) & D'_{N+1}(s) \end{bmatrix} = \\ &= \frac{1}{j(P_{N+1}(s) + J_{N+1}B_{N+1}(s))} \begin{bmatrix} A_{N+1}(s) & B_{N+1}(s) \\ C_{N+1}(s) + 2J_{N+1}P_{N+1}(s) + J_{N+1}^2 B_{N+1}(s) & D_{N+1}(s) \end{bmatrix}. \end{aligned} \tag{3.60}$$

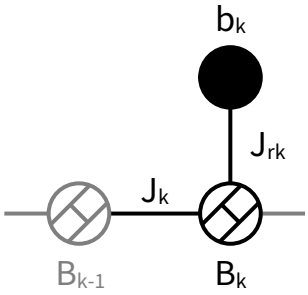

Figure 3.13: Nodal elements faced in the k-th iteration of the synthesis.

At this point, only two NRNs remain. At first, let us compute B_N, the FIR located at M_k, also evaluated at infinity[10].

$$B_N = \lim_{s\to\infty} \frac{D'_{N+1}(s)}{B'_{N+1}(s)} = \frac{D'_{N+1}}{B'_{N+1}} \tag{3.61}$$

As before, the ABCD matrix must be updated to extract B_N:

$$\begin{aligned}[ABCD]''_{N+1} &= \frac{1}{jP''_{N+1}(s)} \begin{bmatrix} A''_{N+1}(s) & B''_{N+1}(s) \\ C''_{N+1}(s) & D''_{N+1}(s) \end{bmatrix} = \\ &= \frac{1}{jP'_{N+1}(s)} \begin{bmatrix} A'_{N+1}(s) & B'_{N+1}(s) \\ C'_{N+1}(s) - B_N A'_{N+1}(s) & D'_{N+1}(s) - B_N B'_{N+1}(s) \end{bmatrix}.\end{aligned} \tag{3.62}$$

Finally, only the load FIR B_L remains. However, to face it, the network must be flipped. To achieve this turn of the network, [138] proposes exchanging polynomials $A(s)$ and $D(s)$ in the matrix. After exchanging these polynomials, the computation of B_L involves applying (3.61) and (3.62) once again. After updating this final extraction, the remaining ABCD matrix is empty and therefore the whole network is fully synthesized.

3.5.2 Unitary Main Line Admittance Inverters

During the description of the synthesis procedure, main line admittance inverters have been set as unitary and alternating in sign between adjacent extracted pole sections. To explain the origin of such imposition and the consequences it has, let us consider an extracted pole section extraction step, as the one shown in Fig. 3.13, assuming that FIR element B_{k-1} has already been extracted.

The input admittance of such section can be written as follows,

$$Y_{\text{in}}(s) = \frac{J_k^2}{jB_k + \dfrac{J_{rk}^2}{s + jb_k} + Y_{\text{rem}}(s)} \tag{3.63}$$

[10] In (3.61) B'_{N+1} is polynomial $B'_{N+1}(s)$ but as it is of zero degree, has no frequency dependence. Must not be confused with any FIR element.

with $Y_{\text{rem}}(s)$ being the admittance of the subsequent sections of the network. In fact, the expression can be reordered as,

$$\frac{J_k^2}{Y_{\text{in}}(s)} = jB_k + \frac{J_{rk}^2}{s + jb_k} + Y_{\text{rem}}(s) \tag{3.64}$$

what in turn can be expressed in a partial fraction expansion form, where the dangling section admittance inverter J_{rk} can be obtained as,

$$J_{rk}^2 = J_k^2 \,\text{residue}\left(\frac{1}{Y_{\text{in}}(s)}\right)\Big|_{s=j\Omega_k} \tag{3.65}$$

that is, the general form of (3.56) for an arbitrary value of mainline inverter J_k.

Clearly, the value of inverters J_k and J_{rk} cannot be separately computed, but only their ratio, what in fact allows a degree of freedom to set one with respect to the other. In the scope of AW ladder filters, Fig. 3.8 has already introduced that main line admittance inverters are used for the serialization of extracted pole sections placing TZs above the passband into series AW resonators, what is only attainable if both inverters are of same magnitude and opposite sign. Therefore, imposing $J_k^2 = 1$ simplifies the computation.

However, one important issue related to the final step of the synthesis procedure must be contemplated. As stated in (3.59), the last main line inverter cannot be assumed as unity and has to be extracted as a cross-coupling evaluating at infinite frequency. While this is a mandatory step for a proper conclusion of the synthesis, it imposes that this last admittance inverter J_{N+1} might not be unitary what in turn might impede the serialization of its adjacent extracted pole section into a series AW resonator.

To ensure the proper value of this last inverter, $J_{N+1}^2 = 1$, let us analyze the input admittance of the last step in Fig. 3.12,

$$Y_{\text{in}} = jB_N + \frac{J_{N+1}^2}{jB_L + G_L} \tag{3.66}$$

where G_L is the output port conductance that has been originally defined as $G_L = 1$. Having this expression and having finished the synthesis procedure (i.e., all elements are known), let us try to find a new set of elements B_N and B_L that hold the equation while imposing $J_{N+1} = 1$. At first, the expression can be separated in real and imaginary parts,

$$\text{Re}(Y_{\text{in}}) = \frac{G_L}{B_L^2 + G_L^2} \tag{3.67a}$$

$$\text{Im}(Y_{\text{in}}) = B_N - \frac{B_L}{B_L^2 + G_L^2} \tag{3.67b}$$

and the new values of FIRs B_N and B_L can be isolated as

$$B_L = \pm\sqrt{\frac{G_L - G_L^2\,\text{Re}(Y_{\text{in}})}{\text{Re}(Y_{\text{in}})}} \tag{3.68}$$

Table 3.1: BVD model elements of the n7 uplink filter without phase modification.

Resonator	1 (SE)	2 (SH)	3 (SE)	4 (SH)	5 (SE)	6 (SH)	7 (SE)	8 (SH)	9 (SE)
L_a (nH)	61.77	20.12	101.78	20.22	103.29	20.21	101.78	20.12	61.77
C_a (fF)	62.86	209.14	38.66	206.18	38.14	206.25	38.66	209.14	62.86
C_0 (pF)	1.08	3.59	0.66	3.54	0.65	3.54	0.66	3.59	1.08
k^2_{eff} (%)	6.7	6.7	6.7	6.7	6.7	6.7	6.7	6.7	6.7
L_{in} (nH)	4.58	L_{out} (nH)	4.58						

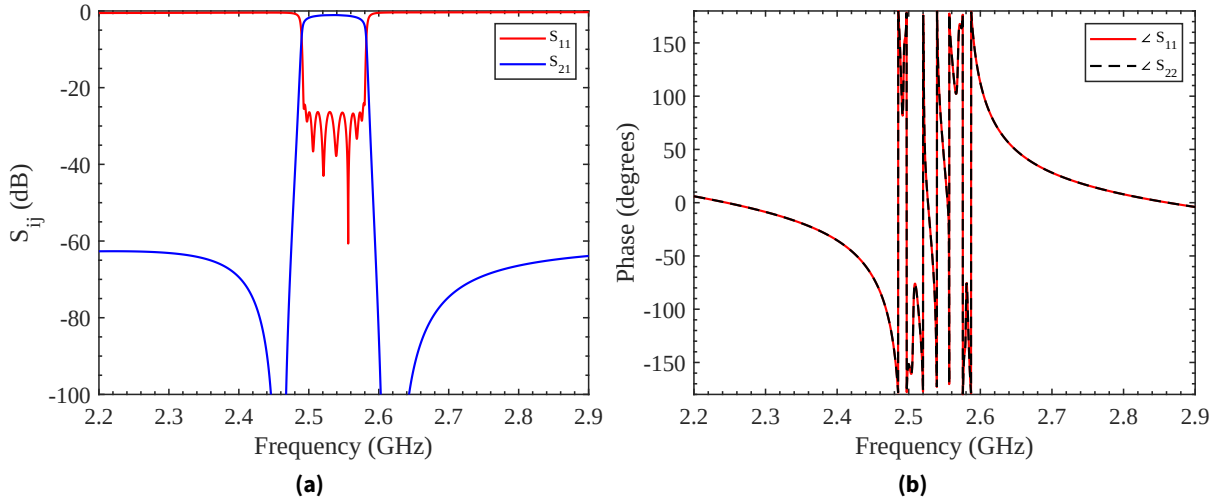

Figure 3.14: Simulated magnitude and phase response of the n7 uplink filter synthesized without any reflection phase modification.

and

$$B_N = \text{Im}(Y_{\text{in}}) + \frac{B_L}{B_L^2 + G_L^2}. \tag{3.69}$$

If a unitary load conductance is assumed to maintain the desired impedance match, note that it must hold that $\text{Re}(Y_{\text{in}}) < 1$. Otherwise, if $\text{Re}(Y_{\text{in}}) > 1$, B_L becomes purely imaginary what in turn, considering its reactive nature, translates into a purely resistive element. To avoid such situation, cases where equating $J_{N+1} = 1$ is not possible are addressed by mismatching the network at the output node by imposing $G_L = 1/\text{Re}(Y_{\text{in}})$ and leaving $B_L = 0$.

It must be mentioned that the equivalence in terms of admittance of the originally synthesized values and the new FIR elements found through setting $J_{N+1} = 1$ only holds in magnitude but not in terms of phase. While this does not impose any distortion of the filter response, output reflection phase is different than that fixed originally in the transfer function due to this admittance redistribution. Such an impact in phase, that has interesting implications in this thesis in Ch. 4, is studied in deep in [25].

3.6 Synthesized Filter Example

After presenting the complete procedure to synthesize an AW ladder filter implementing a generalized Chebyshev response, this section provides examples of synthesized filters and, throughout the discussion, introduces the importance of reflection phase as a design parameter. To lead the discussion, let us take the case of a 5G n7 uplink band, that spans from 2500 to 2570 MHz, as an example vehicle and let us assume that the AW technology to implement this example are aluminum nitride (AlN) BAW resonators. As introduced along the previous chapter, such AlN BAW resonators are capable of providing k^2_{eff} up to 6.7% and thus, let us take it as the electromechanical coupling coefficient that all the resonators in the example filter need to comply with. Note that this choice is made for this demonstrative example but the proposed synthesis methodology is equally applicable to any AW resonator technology and electromechanical coupling value. To complete the boundary conditions for this example section, the modified BVD model in [16] is used to include the finite quality factor of AW resonators in the simulation by assuming $Q_{\text{AW}} = 1500$ and a quality factor of $Q_{\text{L}} = 50$ is assumed for input and output inductors. In this context, the implemented loss model is a simplified version that considers a finite quality factor for both resonances in the form of a series resistance in the motional arm and an additional resistance in parallel to C_0, yielding very good results for demonstration purposes. Nevertheless, refined versions of the modified BVD that model loss dependencies with respect to resonator area, frequency and geometry also exist but are tightly related to resonator technology and commonly fall within the intellectual property of the main AW device manufacturers. Finally, in terms of topology, let us assume a 9th order filter starting in series resonator, that is, having 5 series and 4 shunt resonators.

As described throughout this chapter, the input parameters to the proposed synthesis methodology are a given ladder topology order, a set of N TZs, a return loss value and the passband edge frequencies. From them, the method provides the BVD models that implement the response defined by such parameters. Leveraging on this connection between the desired response and the resonators that implement it, the synthesis process of an AW ladder filter complying with a set of specifications and technological constraints (e.g., the fact that all resonators require $k^2_{\text{eff}} = 6.7\%$ so that they can be AlN BAW resonators), can be faced as a search among all possible filters of order N to select the one with highest compliance with specifications and constraints. As an example of this, let us search for an n7 uplink filter compliant with the conditions above, in this case, without altering the filter function reflection phase in any form. The input parameters of this example filter are $\Omega_{tz} = [2.1092, -1.9554, 1.6825, -1.6731, 1.6508, -1.6733, 1.6827, -1.9554, 2.1092]$ rad/s, RL = 25 dB and the aforementioned passband edges of the n7 uplink band, and yield the synthesized elements shown in Table 3.1, clearly showing how all resonators require the same k^2_{eff} and the presence of L_{in} and L_{out} as the implementation of source and load NRNs. Given the synthesized values and the mentioned Q values, the response of the synthesized filter can be simulated providing the response depicted in magnitude and reflection phase terms in Figs. 3.14a and 3.14b, respectively. Notice that since no phase shift has

Table 3.2: BVD model elements of the previous n7 uplink filter with $\theta_{\text{add}} = -68.7°$.

Resonator	1 (SE)	2 (SH)	3 (SE)	4 (SH)	5 (SE)	6 (SH)	7 (SE)	8 (SH)	9 (SE)
L_a (nH)	33.90	29.53	149.40	29.68	151.62	29.67	149.41	29.53	34.15
C_a (fF)	119.07	142.47	26.34	140.47	25.98	140.52	26.34	142.47	118.15
C_0 (pF)	1.17	2.45	0.45	2.41	0.44	2.41	0.45	2.45	1.16
k^2_{eff} (%)	11.1	6.7	6.7	6.7	6.7	6.7	6.7	6.7	11.1
L_{in} (nH)	-	L_{out} (nH)	-						

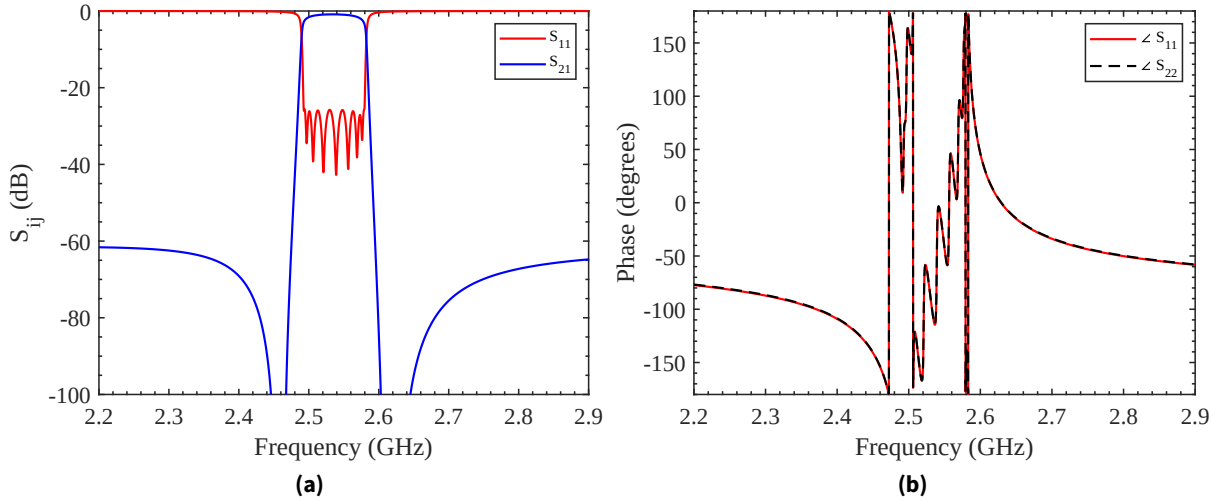

Figure 3.15: Simulated magnitude and phase response of the n7 uplink filter synthesized with same parameters as Fig. 3.14a but adding shift $\theta_{\text{add}} = -68.7°$ to $F(s)$ to avoid the presence of the input reactive element.

been added to $F(s)$, reflection phase depicts the same shape outlined in Fig. 3.10 but now, due to the narrowband approximation of FIRs after frequency transformation, without depicting a horizontal asymptote towards 0° but a clear phase slope for frequencies far from f_0. Additionally, notice that in this case, $\angle S_{11} = \angle S_{22}$ due to the network being physically symmetric with respect to the central resonator (resonator 5), a case that is known to yield $J_{N+1} = 1$ by nature thus not imposing any phase difference in output reflection with respect to the phase defined at the transfer function level.

Considering the previous synthesized result and observing the need to implement input and output shunt inductors, an undesired aspect due to the large size of inductors either on laminate or as lumped elements, let us recall the content of Sec. 3.4.1 regarding the use of reflection phase at the transfer function level through adding a shift θ_{add} to polynomial $F(s)$, to avoid the presence of source FIR following (3.48). To capture the impact of modifying the reflection phase of the filter, let us take the same n7 uplink example parameters just synthesized (i.e., same TZs and RL value) and let us compute the necessary phase shift through (3.48) yielding $\theta_{\text{add}} = -68.7°$. A negative shift since the first resonator is series, thus placing a TZ above the passband, and the intrinsic phase of

Table 3.3: BVD model elements of a new n7 uplink filter without input reactive element and all AlN resonators.

Resonator	1 (SE)	2 (SH)	3 (SE)	4 (SH)	5 (SE)	6 (SH)	7 (SE)	8 (SH)	9 (SE)
L_a (nH)	35.60	29.49	134.80	27.71	134.04	27.86	133.97	27.67	81.72
C_a (fF)	111.65	142.48	29.23	150.68	29.42	149.83	29.42	151.77	47.96
C_0 (pF)	1.92	2.45	0.50	2.59	0.50	2.57	0.50	2.60	0.83
k^2_{eff} (%)	6.7	6.7	6.7	6.7	6.7	6.7	6.7	6.7	6.7
L_{in} (nH)	-	L_{out} (nH)	10.9						

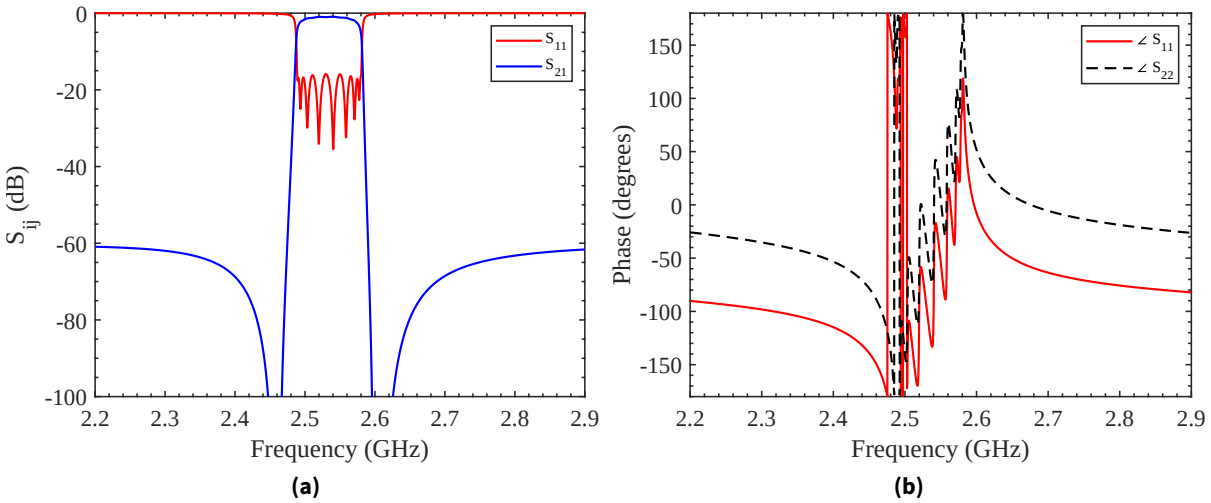

Figure 3.16: Simulated magnitude and phase response of the new n7 uplink filter synthesized to avoid the presence of the input reactive element while requiring k^2_{eff} = 6.7% for all resonators.

the generalized Chebyshev function is positive at that position. Taking this phase shift and adding it to polynomial $F(s)$, note that the obtained function is the same in terms of magnitude but the modification of the phase leads to the synthesis output depicted in Table 3.2 and the simulated response shown in Figs. 3.15a and 3.15b.

At first, in terms of response, notice that the magnitude response is that of Fig. 3.14a, with the only differences in RL shape being related to the circuital element differences and their impact in narrowband approximation effects, while the reflection phase response shows now a clear horizontal asymptote towards the applied phase shift. However, as the most interesting aspect of this example, notice the differences in synthesized elements with respect to those in Table 3.1. With the simple modification of reflection phase, note that the same magnitude response is implemented now with a set of resonators whose C_0 has changed, in this case being smaller than the previous example, what in turn results in less resonator area, and now with the first and last resonators requiring a larger electromechanical coupling. While this result might seem better than the previous one, avoiding input and output reactive elements and requiring less resonator area, note that it would not be feasi-

ble with AlN BAW technology due to the filter requiring more than one electromechanical coupling value (i.e., more than one piezoelectric material). However, such an example highlights the important role that reflection phase can play in the synthesis of AW ladder filters.

At this point, to demonstrate that such an n7 uplink filter can still comply with AlN BAW technology without implementing the input reactive element, let us search for a filter again but now also imposing the phase condition to avoid L_{in} from the very beginning. Imposing the same out-of-band rejection specs and having TZs and RL value as degrees of freedom, input parameters $\Omega_{tz} =$ [1.3464, -1.7826, 1.5974, -1.5962, 1.5738, -1.5916, 1.5959, -1.7696, 1.7509] rad/s, RL = 15.3 dB and $\theta_{\text{add}} = -86.6°$, yield the synthesized results in Table 3.3 and the simulated response in Figs. 3.16a and 3.16b, respectively. Note that now the response is slightly different in magnitude than before due to the fact that TZs and RL have changed to comply with all resonators having $k^2_{\text{eff}} = 6.7\%$ and that, due to the network being asymmetric in this case, now input and output reflection phases do not depict the same value due to the redistribution of J_{N+1}. From an implementation perspective, consider that now L_{out} is different than zero but has a very large value that at the n7 frequencies can be neglected with minor implications in output matching and that as observed before, the obtained resonators are smaller than those of the initial n7 example.

3.7 Chapter Summary

This chapter provides an introduction to the basics of the synthesis procedure for AW ladder filters, from the initial step of computing the transfer function to implement to the extraction of the elements implementing such response and their transformation in the form of BVD models. Stating the fundamental expressions to formulate the general form of Chebyshev filter functions and justifying the introduction of frequency invariant reactances as a necessary step to implement asymmetrical responses, the normalized equivalent of the BVD model is introduced both from a circuital and a nodal perspective allowing to interpret the AW ladder filter as an inline extracted pole network. From such an interpretation, the extracted pole technique is introduced as the method to compute the elements implementing a given admittance function.

Moreover, the extracted pole nature of the network is also fundamental to understand the role of input and output non-resonant nodes and their intrinsic relation to reflection phase. Exploiting the fact that a phase shift can be added to $F(s)$ without affecting the magnitude of the transfer function, the three n7 uplink example filters demonstrate that reflection phase becomes a key parameter for AW ladder filter design and justify the discussion to which the following chapter is devoted.

CHAPTER 4

Reflection Phase as a Key Design Parameter

The present chapter provides a detailed description of how the analytical control of the reflection phase of a filter function at the polynomial level is a key design parameter with important implications in the context of acoustic wave ladder filters. In Ch. 3 the application of network synthesis to AW filters is introduced highlighting transmission zeros and return loss as the main degrees of freedom in the definition of the filter function to synthesize, whereas the role of phase is briefly outlined through the inherent relation between the extracted pole nature of the AW ladder and the presence of input and output non-resonant nodes in the network. In that specific case, the addition of a phase shift term to polynomial $F(s)$ is proposed to avoid their presence. While simple, such an operation opens the path to include reflection phase as a degree of freedom to tailor the filter function and exploring its impact is the main driver of the findings described in this chapter.

Starting from extending the phase modification to avoid the input and output FIRs to enable the direct synthesis of duplexer-oriented filters (that is, filters that are ready to be connected in a duplexer configuration), this chapter then focuses in the specific considerations related to AW ladder filters starting in shunt resonator and their close relation with reflection phase. After that, the chapter revisits a phase modification definition that allows to independently control $\angle S_{11}$ and $\angle S_{22}$ and exploits it to describe an application of the synthesis method to compose dual-band devices through the parallel connection of two ladder filters. Finally, the chapter explores how to exploit phase reflection modification to break the alternation in sign of transmission zeros in AW ladder filters and presents a manufactured prototype filter using the LNOI platform presented in Ch. 2.

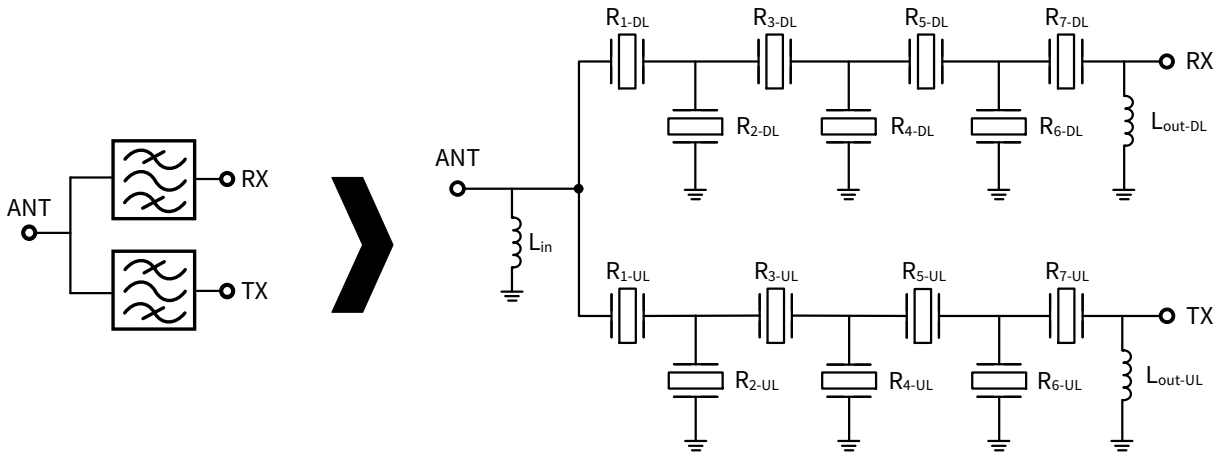

Figure 4.1: Basic schematic of a duplexer and its circuital form in the context of acoustic wave ladder filters.

4.1 Duplexer-oriented Filters

In the presentation of the synthesis procedure in the previous chapter, the filter is faced as a standalone two-port network connected between two reference impedance loads. While such an approach is already very useful, let us focus here in the specific case of duplexers, a commonly used configuration in RF-FEMs, and how the proposed network synthesis procedure is applicable to their design. In the context of wireless communications, duplexers are a widely used structure for frequency-division duplex (FDD) bands, those in which the transmit (TX) and receive (RX) channels are at different frequencies and used concurrently. Therefore, the objective of composing duplexer devices is being able to connect a pair of filters to a single antenna, as shown in the schematic in Fig. 4.1, while maintaining the performance of both filters.

While at first such structure might seem straightforward, the construction of a duplexer is not as simple as connecting two individually-designed filters to a common port. Since each filter is not only connected to the antenna impedance but also to the impedance that each filter imposes on the other, impedance loading is a fundamental aspect to address. Using a simple example, at a frequency $f_{0,RX}$, i.e., the central frequency of the RX band, if one observes into the antenna port of the duplexer, two paths exist: the RX and the TX. Although at that frequency the RX filter is matched to the antenna impedance and the TX filter is practically a perfect reflect condition, with magnitude approaching unity and an arbitrary phase term, the superposition of the signal directly flowing from the antenna into the RX and the signal reflecting off the TX interface can produce a destructive interference and thus lead to degradation of the RX filter response. Equivalently, this behavior is replicated when considering a signal coming from the TX port that must be radiated through the antenna, but then considering the reflect condition that the RX filter is imposing at the TX passband frequencies. Interestingly, note that the key to the mentioned interference is the arbitrary phase term of the practically

perfect reflection condition imposed by the rejecting filter and clearly, if two filters are not designed carefully to compose a duplexer, this interference is the cause of a dramatic distortion of the filter responses.

However, focusing on the reflection phase of each filter and considering that it can be tailored to impose a null phase at the position of the first transmission zero of a filter to avoid implementing the input reactive element (as covered in Ch. 3), notice that the same rationale can be applied to the synthesis of filters that are ready to perform in a duplexer configuration now by tailoring the phase such that each filter has a null reflection phase at the central frequency of their counterpart filter, namely f_{CB}, where CB stands for counter band. Note that such a null reflection phase is equivalent to stating that each filter behaves as an open-circuit at f_{CB}.

To this end, let us then revisit expression (3.48) from the previous chapter, but now at another evaluation point $s = j\Omega_{CB}$, namely the normalized counter band frequency, resulting in

$$\theta_{\mathrm{CB}} = -\arg\left(\frac{F(s)/\varepsilon_r}{E(s)}\bigg|_{s=j\Omega_{\mathrm{CB}}}\right) \tag{4.1}$$

where equivalently, $-\theta_{\mathrm{CB}}$ is the inherent phase of the generalized Chebyshev filter function at the center frequency of the counter band. To compute the frequency $j\Omega_{\mathrm{CB}}$, one can easily map a frequency f_{CB} to its respective position in the normalized domain through the well-known bilateral frequency transformation (3.35) considering that the passband edges of the filter being synthesized are at $\Omega = \pm 1$.

With this definition, polynomial $F(s)$ can then be shifted as

$$S_{11}(s) = \frac{F(s)/\varepsilon_r}{E(s)} e^{j\theta_{\mathrm{add}}} \tag{4.2}$$

for $\theta_{\mathrm{add}} = \theta_{CB}$ and the synthesis procedure can be applied seamlessly. It is important to state that through this phase modification, since null phase is imposed at a frequency that is different than $j\Omega_1$, the input reactive element cannot be avoided. However, a duplexer can then be implemented with a single reactive element at the common port, as shown in Fig. 4.1 without resorting to more complex phase shifting structures as in [143].

Let us finally highlight some aspects of this phase modification application by noticing that that applying a shift $\theta_{\mathrm{add}} = \Omega_{\mathrm{CB}}$ imposes a null phase only at a single frequency but cannot be imposed along the entire counter band passband. However, the deviation from a perfect null phase is slight (in the order of $\pm$ 20°) and thus the obtained duplexer response only suffers a very moderate deviation from the originally synthesized equiripple return loss obtained if the filter is evaluated as standalone. On top of this fact, consider also the narrowband nature of the frequency transformation due to the use of FIRs to represent the AW ladder filter. As already explained in the previous chapter, since the equivalence between FIRs and reactive elements is imposed at the filter central frequency f_0 to ensure the least deviation from the ideal function inside the passband, at frequencies far away from

Table 4.1: Butterworth - Van Dyke model elements of the n7 duplexer example.

n7 uplink - $\theta_{\text{add-UL}} = -39.83°$

Resonator	1 (SE)	2 (SH)	3 (SE)	4 (SH)	5 (SE)	6 (SH)	7 (SE)
L_a (nH)	69.46	28.98	132.26	29.20	132.26	28.98	69.46
C_a (fF)	56.56	144.94	29.79	142.97	29.79	144.93	56.56
C_0 (pF)	0.97	2.49	0.51	2.45	0.51	2.49	0.97
k^2_{eff} (%)	6.7	6.7	6.7	6.7	6.7	6.7	6.7
L_{in} (nH)	13.91	L_{out} (nH)	13.91				

n7 downlink - $\theta_{\text{add-DL}} = 38.67°$

Resonator	1 (SE)	2 (SH)	3 (SE)	4 (SH)	5 (SE)	6 (SH)	7 (SE)
L_a (nH)	79.27	13.55	88.85	13.66	88.85	13.55	79.27
C_a (fF)	44.50	282.27	40.44	278.60	40.44	282.27	44.50
C_0 (pF)	0.76	4.85	0.69	4.79	0.69	4.85	0.76
k^2_{eff} (%)	6.7	6.7	6.7	6.7	6.7	6.7	6.7
L_{in} (nH)	3.31	L_{out} (nH)	3.31				

it there is a considerable deviation specially in reflection phase terms. Therefore, one must consider the relative distance between the bands being duplexed to assess the application of this method. In any case, the proposed phase modification for duplexers is best suited for closely spaced bands, those that are actually harder to match.

Moreover, for completeness, notice that the duplexer shown in Fig. 4.1 features two filters that start in series resonator. While the fact that an open circuit loading condition is required to compose a duplexer independent of the resonator configuration each filter starts with, filters starting in shunt resonator need a specific handling of reflection phase as is covered in a forthcoming section.

4.1.1 Duplexer Example

To quickly demonstrate the usefulness of the proposed approach to duplexer-oriented synthesis, an n7 duplexer (uplink 2500 - 2570 MHz, downlink 2620 - 2690 MHz) is synthesized to be implemented with AlN BAW resonators (i.e., $k^2_{\text{eff}} = 6.7$ %) using the following as synthesis input parameters: for a 7th order n7 uplink filter, RL = 16 dB, Ω_{UL} = [1.6704, -1.7771, 1.5884, -1.5947, 1.5884, -1.7771, 1.6704] and phase shift $\theta_{\text{add-UL}} = -39.83°$ and for a 7th order n7 downlink filter, RL = 18.5 dB, Ω_{DL} = [2.4581, -1.9995, 1.8150, -1.8150, 1.8150, -1.9995, 2.4581] and phase shift $\theta_{\text{add-DL}} = 38.67°$.

After synthesis and transformation of each filter, the BVD model elements that compose both filters of the duplexer are summarized in Table 4.1. Notice that the input inductors of both filters are

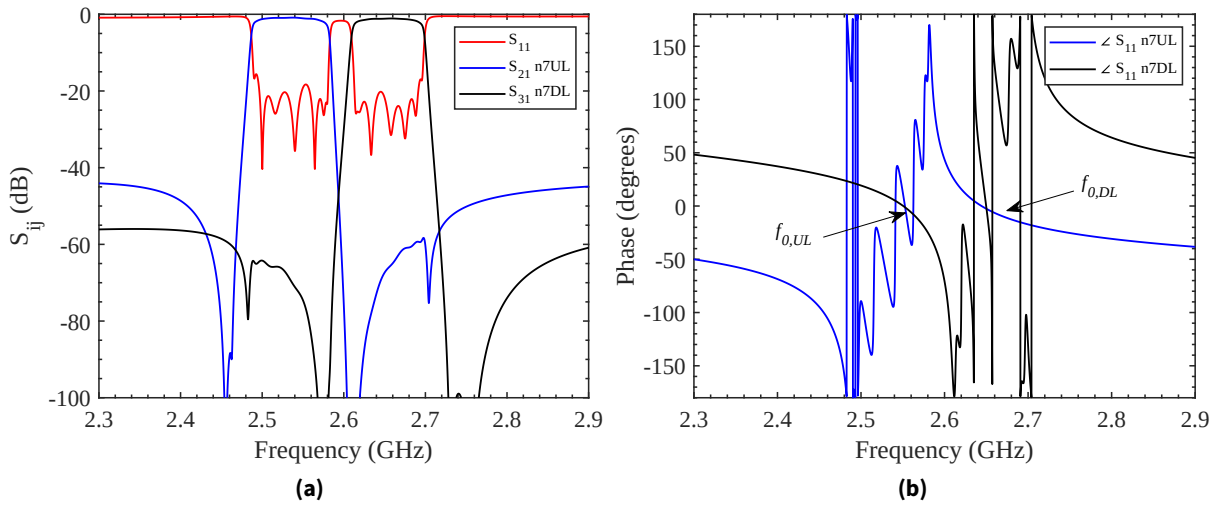

Figure 4.2: Simulated response of the n7 duplexer synthesized by modifying the reflection phase of each channel. (a) Magnitude response of the duplexer assuming $Q_{AW} = 1500$ and $Q_L = 50$. (b) Simulated reflection phase of each filter evaluated as a two-port network.

merged into a single inductor of value $L_{DPX} = 2.67$ nH and also that the shunt inductor at the output of the n7 uplink channel can be neglected due to its large value. With the computed elements, assuming a quality factor $Q_{AW} = 1500$ for acoustic resonators and $Q_L = 50$ for inductors, the response of the duplexer is simulated and depicted in Fig. 4.2a. The achieved value of reflection phase after synthesis is shown in Fig. 4.2b that depicts the reflection phase of both filters when evaluated as standalone devices.

4.2 Acoustic Wave Ladder Filters Starting with Shunt Resonator

Up to this section, all examples of AW ladder filters and even the equivalence between the normalized prototype network and the ladder filter have been presented through filters starting in series resonator. Although historically that is the traditional representation of the ladder [17, 144], ladder filters starting in shunt resonator are also of interest. For example, since each resonator in the ladder is directly responsible for a transmission zero of the filter and odd-order series-starting filters depict one more zero above than below the passband, shunt-starting filters are an interesting asset when aiming for higher rejection at the lower stopband of the filter. That might be the case of a downlink filter requiring high rejection to its adjacent uplink band.

Prior to diving into the details of this section and to justify the origin of this study, let us introduce an interesting observation derived from the revision of shunt-starting filter examples both from industry and academia: in many occasions, the implementation of shunt-starting AW ladder

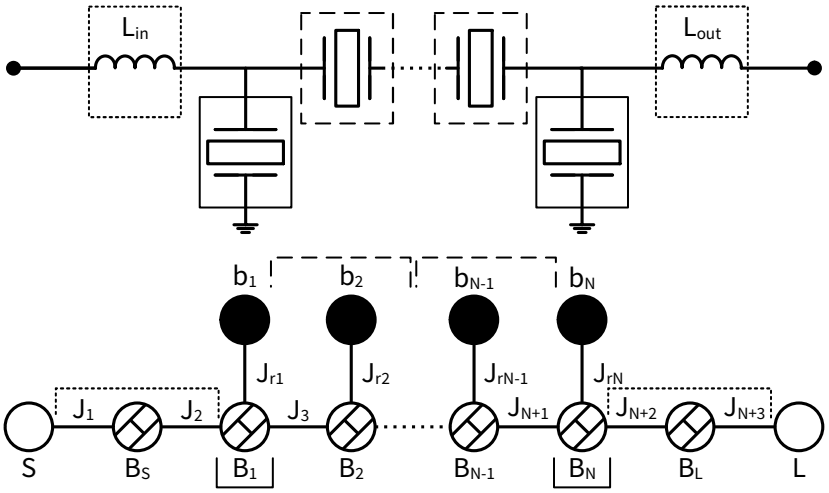

Figure 4.3: Equivalence between the ladder topology starting in shunt resonator (top) and its nodal representation (bottom). Solid underlined sections are shunt resonators, long-dashed overlined sections are series resonators and short-dashed overlined sections are the input and output series elements. Since B_S and B_L are shunt admittances, are serialized between two inverters J_i of opposite sign and equal magnitude.

filters requires two reactive elements at the input of the filter. A shunt element followed by a series element. One clear example is the Band 25 duplexer in [11] in which both filters start in shunt and feature two reactive elements at their input ports[1]. Interestingly, AW ladder filter cases that sometimes required more than a single input element were already mentioned in direct bandpass synthesis studies [120, 145], without diving in deep into the root cause.

To understand the reason behind the need of more than one reactive element at the input and the specific role of phase in it, let us initially revisit the nodal prototype of the network when considering a shunt resonator at the input. Going back to Fig. 3.9 from the previous chapter showing the equivalence between the normalized nodal representation and the ladder topology, notice that due to the first resonator being series, admittance inverters J_1 and J_6 are absorbed by their adjacent extracted pole sections for serialization purposes. Therefore, input and output NRNs, B_S and B_L become shunt reactive elements after frequency transformation. In the case of a filter starting in shunt resonator (equivalent situation to ending in shunt) note that the admittance inverter connecting B_S with B_1 (the first extracted pole section) is not absorbed when transforming the first resonator and so, after transformation, NRN B_S and an admittance inverter would remain to be implemented. Since the implementation of that remaining inverter, either in the form of a π or a T reactive network, is not acceptable due to size constraints, such an inverter must be absorbed in a circuital transformation.

[1]While the uplink filter clearly features two reactive elements at the input, the downlink filter appears to feature a single one but the authors comment that an input shunt capacitor has been merged into the the first resonator of the uplink filter.

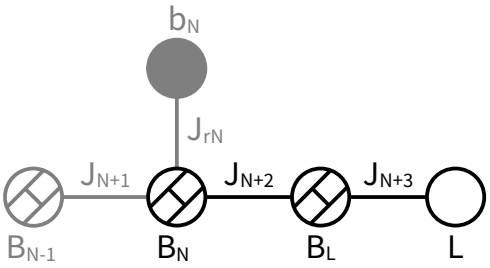

Figure 4.4: Nodal view of the elements faced at the last iteration of the synthesis when the filter ends in shunt resonator. In grey are those elements that have already been extracted.

4.2.1 Nodal Representation and Additional Extraction Steps

To attain such objective, the nodal equivalent of a ladder filter starting in shunt is shown in Fig. 4.3 depicting a general case of order N. Notice here that in order to achieve complete serialization of all elements and feature series input and output reactive elements, additional admittance inverters must be considered at the input and output ports. Therefore, source (S) and load (L) nodes are now unitary conductance ($G = 1$ S) nodes with no zero imaginary part and are connected to NRNs B_S and B_L, respectively, via two additional admittance inverters. Note that inverters J_1 and J_2 are absorbed in the serialization of NRN B_S and so, as already introduced in the previous chapter, must be of equal magnitude and opposite sign.

Considering this nodal equivalent, the synthesis procedure described in Ch. 3 requires a slight modification to account for the additional admittance inverters specifically at iterations $k = 1$ and $k = N + 1$. Regarding the first iteration, the only modification is to extract a unitary inverter J_1 with expression (4.3) (replicated here for clarity) prior to proceeding as in Ch. 3 with the only consideration that the sign of the inverter J_2 extracted after finding NRN B_S must have the opposite sign of J_1.

$$[ABCD]'_k = \frac{1}{jP_k(s)} \begin{bmatrix} -jC_k(s) & -jD_k(s) \\ -jA_k(s) & -jB_k(s) \end{bmatrix} \tag{4.3}$$

Regarding the last iteration, the required modification involves adding two steps and the remaining network to extract is depicted in Fig. 4.4. As already introduced in the previous chapter, in this last extraction step, all elements are extracted as an evaluation at infinity due to the remaining admittance having zero degree. While in the case of ending in series resonator, only elements B_N, B_L and the inverter connecting them remained, in this case an additional inverter connecting B_L and load node L needs to be considered. Note also that the last inverter should be evaluated as a cross-inverter at an infinite frequency to ensure the complete extraction of the network. However, note that in this case, if such cross-inverter is evaluated at the beginning of this last iteration, it would connect NRN B_N with output terminal L, imposing an actual cross-coupling bypassing NRN B_L. Therefore, to correctly extract the inverter between B_N and B_L, admittance inverter J_{N+3} must be extracted prior to any other element.

Table 4.2: Normalized prototype elements of the example N=7 shunt-starting network.

Section	1	2	3	4	5	6	7
B_k	-0.1261	-7.2909	1.4959	-14.1572	2.0471	-14.1179	-0.0685
b_k	1.7	-1.97	2.5	-3	3.3	-4	1.8
J_{rk}	0.8244	3.5159	1.9526	6.4863	2.6182	7.3840	0.4170
B_S	-1.4332		B_L	-0.5108		J_{10}	-0.6963

As already described and as proposed by Tamiazzo [138], a turn in the reference point of the network is equivalent to exchanging polynomials $A(s)$ and $D(s)$ and thus, when facing this last iteration, the first step is to turn the network, then extract a unitary J_{N+3} again with (4.3) taking its sign in consideration with respect to the sign imposed for J_{N+1} and then turn the network another time to go back to the position of B_N. At this point, J_{N+2} can be extracted as a cross-inverter at an infinite frequency following the same procedure outlined in the previous chapter for the final extraction step of the synthesis. With this, following the mentioned modifications, a shunt-starting AW ladder filter can be completely synthesized, in this case considering single input and output reactive elements.

4.2.2 Reflection Phase and Feasibility Regions

Having described the nodal representation of a filter starting in shunt resonator and the additional steps required to accurately synthesize it, it is possible to compute the elements of an example. Let us define a 7th order network with prescribed transmission zeros $\Omega_{TZ} = [-1.7,\ 1.97, -2.5,\ 3, -3.3,\ 4, -1.8]$ (note that the first and last TZs are negative, thus the filter starts and ends with a shunt AW resonator), return loss RL = 18 dB and leaving the intrinsic phase of the generalized Chebyshev function unaltered (i.e., $\theta_{\text{add}} = 0°$), to obtain the normalized elements summarized in Table 4.2 after synthesis.

Focusing on the synthesized elements notice the fact that the sign of NRNs B_1 and B_7, those that ultimately become the C_0 of the first and last resonators, have the opposite sign to that expected. Following the expressions relating B_k elements and their correspondence with the static branch of the BVD model (3.45) (3.46), note that C_0 is related to B_k as follows,

$$C_{0-SE} = -\frac{1}{\omega_0 B_k}\frac{1}{Z_0} \tag{4.4a}$$

$$C_{0-SH} = \frac{B_k}{\omega_0}\frac{1}{Z_0} \tag{4.4b}$$

stating that the sign of B_k elements is of paramount importance to allow the transformation of the synthesized model into BVD models: for series resonators, $B_k < 0$ and conversely, for shunt resonators $B_k > 0$. Therefore, in a ladder topology, the sign of B_k elements alternates. However, the synthesized elements of the example network depict an unexpected behaviour in the first and last positions and such B_k would transform into the following set of capacitors C_0 = [-0.218, 0.237, 2.584,

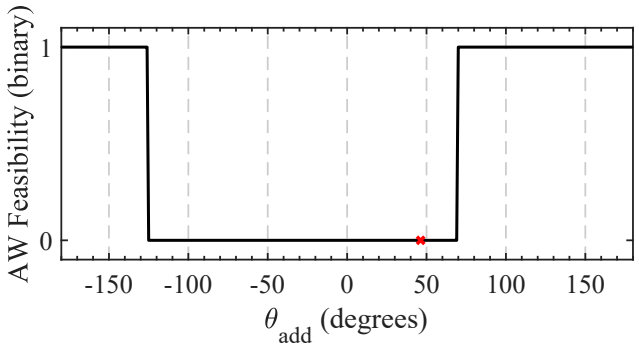

Figure 4.5: Feasibility map of the example 7th order filter starting in shunt. Binary (1) indicates all C_0 values are feasible in terms of AW technology. (0) means first and/or last resonator C_0 are negative. Red cross is placed at $\theta_{\text{add-CB}}$ for duplexer-oriented synthesis assuming counter band is n3 uplink.

0.122, 3.537, 0.122, -0.118] pF if using the central frequency of an n3 downlink band (1805 - 1880 MHz), for example. Notice that the static branch of the first and last resonators transforms into a negative capacitor, what can also be interpreted as a capacitor with positive reactance value or an *inductive* nature. Clearly, such behavior is not feasible in terms of AW resonators because it contradicts the capacitive nature of the piezoelectric transducer and thus cannot be represented with a BVD model.

It is interesting to highlight that the elements depicted in Table 4.2 correspond to the output of the synthesis before applying the last inverter redistribution explained in the previous chapter and thus, the value of such last inverter is stated in the table as J_{10}. Since the redistribution of the non-unitary inverter involves a new value for elements B_N and B_L and its equations, (3.68) (3.69), already assume the correct sign of element B_N to be feasible, the fact that both first and last resonators feature an inductive behavior could be masked. More importantly, note that such redistribution entails a modification of the output phase, as introduced in Ch. 3 and thus points at the relation between phase and the unexpected sign of the two NRNs.

As already outlined in the discussion of two synthesized filters with different reflection phase modifications in the previous chapter and as initially covered by Silveira in [26] (Ch. 3) for series starting filters, tailoring the reflection phase of a filter has an impact on all C_0 of the filter. Therefore, at this point let us bring reflection phase into play to inspect the filter example starting in shunt resonator for different values of the phase modification term θ_{add}. By synthesizing the network while sweeping for all possible values of reflection phase, i.e., $\theta_{\text{add}} \in [-180°, 180°]$, a feasibility binary map can be obtained as shown in Fig. 4.5, where 1 stands for all $C_0 > 0$ and 0 means that C_{01} and/or C_{07} are negative. Additionally, assuming once again an n3 downlink case, let us consider that the counter band (n3 uplink) is located at $\Omega_{CB} = -2.36$ rad/s and so, note the map features a red cross at the θ_{add} value that is required to impose $\angle S_{11} = 0°$ at the center of the counter band.

While it is already clear that for $\theta_{\text{add}} = 0°$ (i.e. leaving the intrinsic phase of the Chebyshev

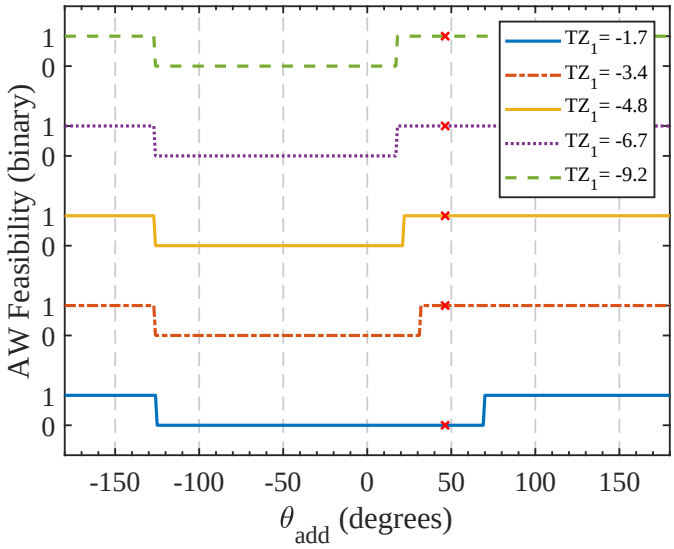

Figure 4.6: Feasibility map of the example 7th order filter starting in shunt sweeping the first TZ. Red cross is placed at $\theta_{\text{add-CB}}$ for duplexer-oriented synthesis assuming counter band is n3 uplink.

function) the network is not feasible, trying to synthesize such shunt-starting filter as a duplexer-oriented filter with the proposed set of TZs and RL leads to a non-feasible solution, as well. Clearly, there is a wide region of phases, centered around $\theta_{\text{add}} = 0°$, where the network is not feasible, but the filter becomes feasible for large values of θ_{add}.

To complete the observation, let us take the same analysis with respect to θ_{add} and repeat it for different positions of the first transmission zero departing further from the passband (i.e., more negative values of Ω_1) again considering the same network example than before and taking $\Omega_1 =$ [-1.7, -3.4, -4.8, -6.7, -9.2]. Note that the first transmission zero corresponds to the resonance frequency f_s of the first resonator of the filter. The result of this second experiment is depicted in the feasibility maps in Fig. 4.6 showing that the upper edge of the feasibility region (the phase addition at which the filter becomes feasible) is closely related to the position of the first TZ, coming closer to $\theta_{\text{add}} = 0°$ as the TZ moves further from the passband, at some point allowing feasibility of the duplexer-oriented filter, and thus narrowing the range of phases for which the filter is non-feasible. Interestingly, notice that the transition edge in the left half of the map (that for negative values of θ_{add}) is invariant, what highlights the relation of that edge with the last TZ of the network (again, the f_s of the last resonator) that is kept unaltered in this experiment.

Revisiting the orthogonality conditions derived in the previous chapter and inspecting the results, the edges of the feasibility regions can actually be computed in advance with (4.5), where $\theta_{\text{up-SH}}$ and $\theta_{\text{low-SH}}$ are, respectively, the positive and negative values of θ_{add} at the transition from feasible to non-feasible when starting in shunt resonator, and Ω_1 and Ω_N are the normalized position, in rad/s, of the first and last TZs. Interestingly, these values are the ones proposed by Giménez [124] to avoid the external reactive elements at input and output for filters starting in series resonator be-

cause by adding a shift of θ_{up} to $F(s)$, then $\angle S_{11}(j\Omega_1) = 0°$ and therefore no source element B_S is required. In the case of shunt-starting filters, these phase values represent the border from capacitive to inductive behaviour of the static branch of the first and last resonators.

$$\theta_{\text{up-SH}} = -\angle S_{11}(j\Omega_1) \qquad \theta_{\text{low-SH}} = \angle S_{22}(j\Omega_N) \tag{4.5}$$

Therefore, for a shunt-starting AW filter with arbitrary TZs and RL, the following condition on the θ_{add} value that yields feasible solutions can be derived:

$$\theta_{\text{add}} \in [-180°, \theta_{\text{low-SH}}] \cup [\theta_{\text{up-SH}}, 180°] \tag{4.6}$$

Additionally, revisiting now the intrinsic reflection phase of a generalized Chebyshev function (as depicted in Fig. 3.10) note that the closer a lower stopband TZ is to the passband, the more negative the phase at its position is. From (4.2) and (4.6) it is clear that a shunt-starting filter is feasible as long as $\angle S_{11}(j\Omega_1) \geq 0°$. Therefore, since to design a duplexer the condition $\angle S_{11}(j\Omega_{\text{CB}}) = 0°$ must be imposed, it is easily seen that only when the first TZ is placed below the center frequency of the counter band (for the case in which the counter band is below the passband), the filter starting in shunt resonator and featuring a single input element will be feasible, because the two restrictions above must hold.

This allows to define the condition in the normalized domain as

$$\Omega_1 \leq \Omega_{\text{CB}} \tag{4.7}$$

or more specifically in terms of the actual resonator frequencies, as

$$f_{s1} \leq f_{\text{CB}} \tag{4.8}$$

where f_{s1} is the series resonance of the first resonator and f_{CB} is the central frequency of the counter band.

Finally, let us highlight that the appearance of negative C_0 values is not only a phenomenon of filters starting in shunt and the same situation can be analyzed for filters starting with series resonator. For simplicity, let us take the same example network but now switching the sign of all TZs (i.e., Ω = [1.7, -1.97, 2.5, -3, 3.3, -4, 1.8] rad/s and RL = 18 dB) so that it starts in series resonator and let us repeat the same sweep computation, synthesizing for all θ_{add} and moving the first TZ away from the passband. In this case to larger values, or equivalently, moving the antiresonance frequency (f_p) of the first resonator up in frequency. For consistency, the counter band is assumed to be n3 uplink again. The results of this analysis are shown in Fig. 4.7 depicting that for $\theta_{\text{add}} = 0°$ the filter has all $C_0 > 0$ by nature and that the feasibility regions with respect to phase have an opposite behaviour to those of shunt-starting cases.

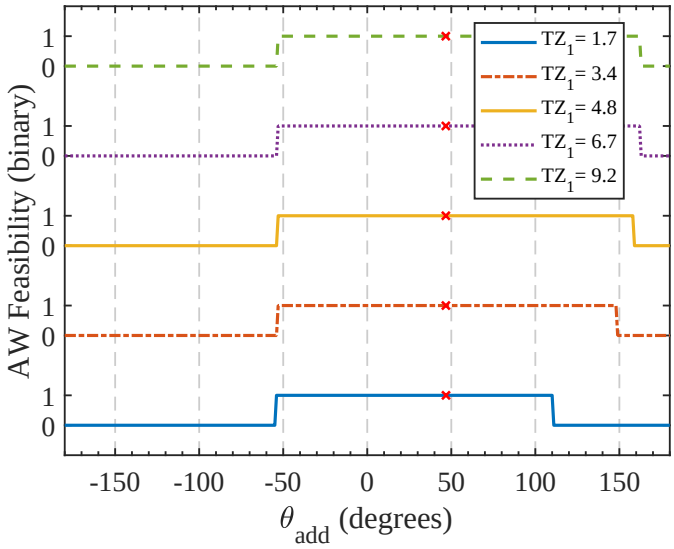

Figure 4.7: Feasibility map of the example 7th order filter starting in series sweeping the first TZ. Red cross is placed at $\theta_{\text{add-CB}}$ for duplexer-oriented synthesis assuming counter band is n3 uplink.

A series-starting filter is feasible without modifying the reflection phase and is naturally capable of accommodating the duplexer-oriented phase condition. Again, the edges, now $\theta_{\text{up-SE}}$ and $\theta_{\text{low-SE}}$, bounding the feasibility region of these filters can be computed as $\theta_{\text{up-SE}} = 180 - \angle S_{11}(j\Omega_1)$ and $\theta_{\text{low-SE}} = -180 + \angle S_{22}(j\Omega_N)$ yielding the interval of feasible phases for AW filters starting in series:

$$\theta_{add} \in [\theta_{low-SE}, \theta_{up-SE}]. \tag{4.9}$$

From this result, a curious but also interesting conclusion might be drawn. When designing a filter starting in series, feasible solutions arise intrinsically without any modification to the reflection phase of the filter function. Therefore, in an optimization-based design that does not take control of the phase, solutions will by nature be away from the cases where the first and last resonators require an inductive behavior.

Moreover, since for most duplexer band pairs the reflection phase required to reduce loading effects is closer to 0° than to 180°, filters starting in series are directly feasible without considering conditions on the position of TZs or the addition of extra input elements. Again, an optimization-based design will require less computational effort to find a duplexer filter solution with single reactive elements. This might partly be the reason why the initial AW ladder filter examples started in series resonator [17] and thus might have influenced the industrial trend since, as explained in [11], the design process is sometimes started with an optimization over an already marketed design.

In general, the point to highlight is that an AW ladder filter starting with series resonator featuring single input and output reactive elements is capable of implementing a generalized Chebyshev function by nature without the need of any reflection phase modification.

From the shunt-starting filters viewpoint, the key aspect is that an AW ladder starting in shunt

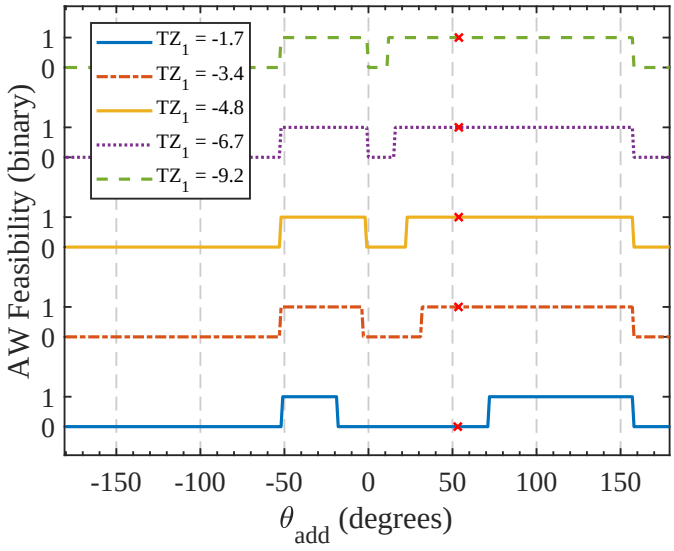

Figure 4.8: Feasibility map of the example 6th order filter starting in shunt sweeping the first TZ. Red cross is placed at the duplexer phase requirement.

cannot accommodate a generalized Chebyshev function unless its reflection phase is modified in accordance with the proposed feasible values, also affecting the design of duplexer-oriented filters.

It is important to highlight that the examples discussed in this section are all odd-order filters, that is, that start and end in the same resonator configuration. However, since even-order filters are also possible implementations, an equivalent evaluation of the feasibility of such filters is interesting. For a filter of even order, the first and last resonators are connected in opposite configuration, that is starting in shunt and ending in series, or vice versa. Hence, when analyzing the feasibility of the filter with respect to θ_{add} results depict a more complicated scenario, as shown in Fig. 4.8. The network for this experiment is a 6-th order filter with RL = 18 dB and TZs Ω = [-1.7, 1.97, -2.5, 3, -3.3, 4], again synthesized as an n3 downlink filter.

Notice that now the resulting feasibility regions are a superposition of two different behaviors. Around $\theta_{\text{add}} = 0°$ the network is not feasible because the shunt resonator at the beginning of the network requires an inductive static branch and, again, since the network starts in shunt, the conditions for duplexer feasibility apply. On the other hand, for $\theta_{\text{add}} = 180°$ the network is also not feasible because for such reflection phases, it is the final resonator (now in series) that requires an inductive static branch (as seen in Fig. 4.7). Therefore, for even order networks starting in shunt, selection of the reflection phase is more complicated than for those of odd order. The general description of the feasible values of θ_{add} is in this case also related to the rest of TZs and requires further research.

4.2.3 Double-element Solution for Shunt-starting Duplexers

The study in this section is driven by the fact that it is common to find shunt-starting filters featuring two input elements when part of a duplexer and the findings attained through a synthesis approach show that condition (4.8) must hold for a shunt-starting filter with a single input element to be feasible when imposing the phase required to avoid loading effects.

In terms of AW technology, fulfillment of such condition on f_{s1} (the resonance frequency of the first resonator) has important implications in material and resonator specifications. Placing f_{s1} below the central frequency of the counter band entails enlarging the effective electromechanical coupling coefficient (k^2_{eff}) to obtain a resonator whose f_s is below f_{CB} while its antiresonance f_p is in band. To exemplify this situation, consider AlN for BAW offering a $k^2_{\text{eff}} \approx 6.7\%$ [146], two situations arise: either the duplexer spacing is small enough to technologically fulfill (4.8) or the uplink (UL) and downlink (DL) are spaced apart and the required pole-zero distance exceeds resonator capabilities, as might be the case of an n66 pair (1710 - 1780 MHz UL, 2110 - 2200 MHz DL). As a solution for those cases where k^2_{eff} is not enough to place f_{s1} where required, it is possible to use an additional reactive element at the input port so that an arbitrary set of TZs is feasible to design a shunt-starting duplexer-oriented filter.

To provide the synthesis view of this element, start by considering the reflection phase shift implemented by a shunt FIR B_{S1} with (4.10). If this shunt admittance is placed at the source node S in Fig. 4.3, it can be used to implement a phase such that the remaining network after its extraction has the desired sign of NRNs B_k to yield all positive C_0. Element B_{S1} thus transforms into a shunt reactive element and its role is to ensure feasibility while B_{S2} (previously B_S in Fig. 4.3) transforms into the common series reactive element in shunt-starting filters, whose role is phase matching to the first AW resonator.

$$\theta_{S1} = \arctan\left(\frac{-2B_{S1}}{1 - B_{S1}^2}\right) \tag{4.10}$$

Solving (4.10) for a given value of θ_{S1} yields two solutions of different sign and hence, two elements of different nature after transformation. The positive sign transforms to a shunt capacitor and the negative to a shunt inductor. Therefore, the type of element can also be chosen to convenience. The procedure to synthesize this additional element is to compute its admittance value from the expression, giving a value to θ_{S1} and then extracting it from the overall ABCD matrix, as done with B_S, prior to the extraction of main-line inverter J_1.

4.2.4 Solution for Stand-alone Odd-order Shunt-starting Filters

In the case the filter to synthesize is not aimed to compose a duplexer, it must not implement an specific reflection phase and therefore the availability of solutions increases. Since the phase is now liberated, one interesting option for stand-alone filters is to avoid the input reactive element to reduce filter footprint and avoid the drawbacks of low Q inductors on laminate or as surface mount devices (SMD). To do so, the reflection phase can be tailored so that the value of element B_S is zero. In this case, inverters J_1 and J_2, that are of opposite sign, neutralize each other and the filter network starts directly at the first shunt resonator. To obtain $B_S = 0$ after the extraction of J_1, the phase addition to the filter function is the one that fixes that $\angle S_{11}(j\Omega_1) = \pm 180°$. Therefore,

$$\theta_{\text{add}} = -180° - \angle S_{11}(j\Omega_1) \tag{4.11}$$

and as already shown in (4.6), this phase shift value falls inside the feasible region of a shunt-starting filter.

On the other hand, the reflection phase can be brought as a free design parameter if the input/output reactive elements are allowed. Since the role of B_k elements is phase matching between extracted-pole sections, modifying the reflection phase has an effect in the values of all C_0 elements and can help find solutions with specific objectives such as minimum area. If it is not used as a design variable, selecting a phase of $\theta_{\text{add}} = 180°$ ensures feasibility, as a rule of thumb.

4.2.5 Examples and Experimental Validation

With the objective of validating the findings regarding shunt-starting AW ladder filters, this section provides two different examples. At first, the proposed phase rules are validated through a post-manufacturing analysis of a filter at 4.5 GHz and secondly, the synthesis procedure applied to shunt-starting filters is demonstrated with an n7 duplexer in which the downlink filter features two reactive elements at the input port.

Validation on a C-Band Filter

The synthesis analysis of an already manufactured filter is proposed as a validation vehicle of the phase conditions derived in the previous section. The filter is a third order C-Band device presented in [83, 147] as a novel demonstration of the potential of Lamb wave modes on thin film $LiNbO_3$ plates [81, 148] in the context of attaining high electromechanical coupling values. These resonator designs, in this case exploiting the first order asymmetric mode (A1), achieve k^2_{eff} in the order of 20%, fitting the requirements of new 5G bands with fractional bandwidths above 10%. The proposed filter starts in shunt resonator, is physically symmetric (first and last resonators are equal) and is originally designed through optimization, thus becoming a clear example to demonstrate the validity of the

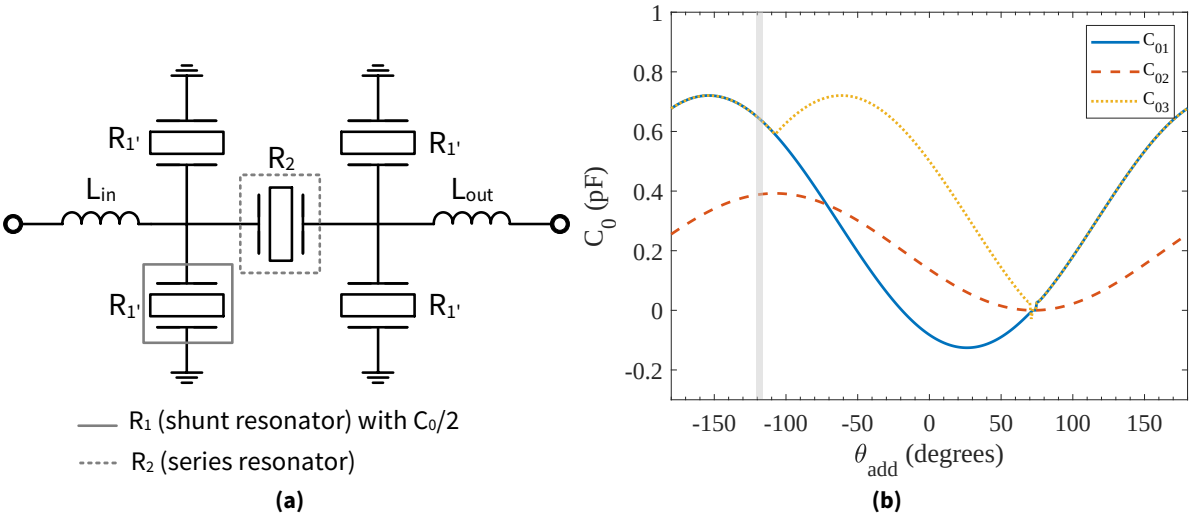

Figure 4.9: (a) Schematic of the 4.5 GHz third order filter fabricated in [83]. (b) C_0 with respect to θ_{add} for the synthesis model of the filter. The grey area marks the reflection phase modification required to obtain the values of the fabricated filter.

Table 4.3: Synthesized BVD model elements of the 4.5 GHz filter.

Resonator	L_a (nH)	C_a (fF)	C_0 (fF)	k^2_{eff} (%)
1 and 3	12.12	135.52	642.4	20.5
2	15.62	81.15	388.9	20.5
L_{in} (nH)	0.1865		L_{out} (nH)	0.1865

proposed conditions. The schematic of the filter is shown in Fig. 4.9a, highlighting that the shunt resonators, having a total $C_0 = 640$ fF have been implemented as two equal resonators in parallel (320 fF each) to ease manufacturing and to achieve a more compact filter layout. On the other hand, the series resonator has a capacitance $C_0 = 380$ fF.

As already discussed, a shunt-starting filter whose reflection phase is left unaltered, that is, showing a horizontal asymptote towards 0°, should depict negative-valued capacitances in the first and last resonators. Considering the values of the manufactured filter it is clear that its reflection phase must depict an asymptote towards a value within the feasible region in (4.6). Hence, the synthesis method can be exploited to explore which phase modification θ_{add} is required to obtain the values of the fabricated device. For fitting purposes, the passband of this filter is defined as having edges at $(4045 - 4640)$ MHz and center frequency $f_0 = 4332$ MHz, thus a FBW of 13.7 %. Through denormalization using the proposed passband specs, the input parameters that define the objective generalized Chebyshev function are RL = 15.1 dB and a TZs Ω = [-1.59, 2.18, -1.59].

At first, let us compute the synthesis without altering the reflection phase of the function ($\theta_{\text{add}} = 0°$), what yields, as expected, static capacitors $C_{01} = -82.6$ fF, $C_{02} = 137.7$ fF and $C_{03} = 500.7$ fF.

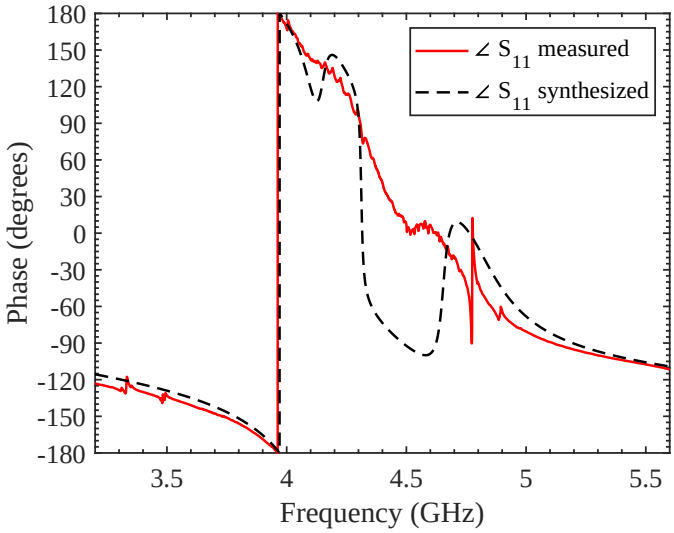

Figure 4.10: Reflection phase comparison between the fabricated filter in [148] and the synthesized filter.

The fact that the last resonator already yields a positive C_0 is due to the redistribution of the non-unitary inverter after the synthesis, that actually imposes the correct sign of NRN B_N through the redistribution equations (3.68)(3.69). To analyze which is the required phase addition let us compute a sweep along all possible values of θ_{add} for the static capacitance of each resonator, yielding the result shown in Fig. 4.9b.

Note that the larger variation of C_0 with respect to phase is observed for the first and last resonators, the first becoming negative around $\theta_{\text{add}} = 0°$ (i.e. no added phase). The phase shift value for which the values estimated by the original authors of the filter [83, 148] is highlighted in grey in Fig. 4.9b showing that they are only achieved for a phase addition of $\theta_{\text{add}} = -119°$ on S_{11}. With this information, the generalized Chebyshev function can be shifted in terms of refleciton phase and can be synthesized, obtaining the BVD model elements summarized in Table 4.3.

The synthesized response can be simulated using the BVD models and the measured Q factor of the resonators, that is estimated to be 200 on average [148]. With the simulated response, a direct comparison of the reflection phase of the measurement and the synthesized filter is depicted in Fig. 4.10 showing a good agreement. Clearly, the fabricated filter shows the mentioned asymptote at the phase of $-119°$ that is needed to obtain a feasible filter with the given C_0 and the same k^2_{eff} on all resonators.

The comparison in terms of magnitude is shown in Fig. 4.11a, showing the measurement, and Fig. 4.11b showing the simulated response using again the computed BVD reactance model of the synthesized filter with the mentioned Q factor. The measured and simulated magnitude responses agree in terms of the obtained out-of-band rejection levels and the shape of the passband but show considerable differences in the in-band region. To justify such disagreement it is important to con-

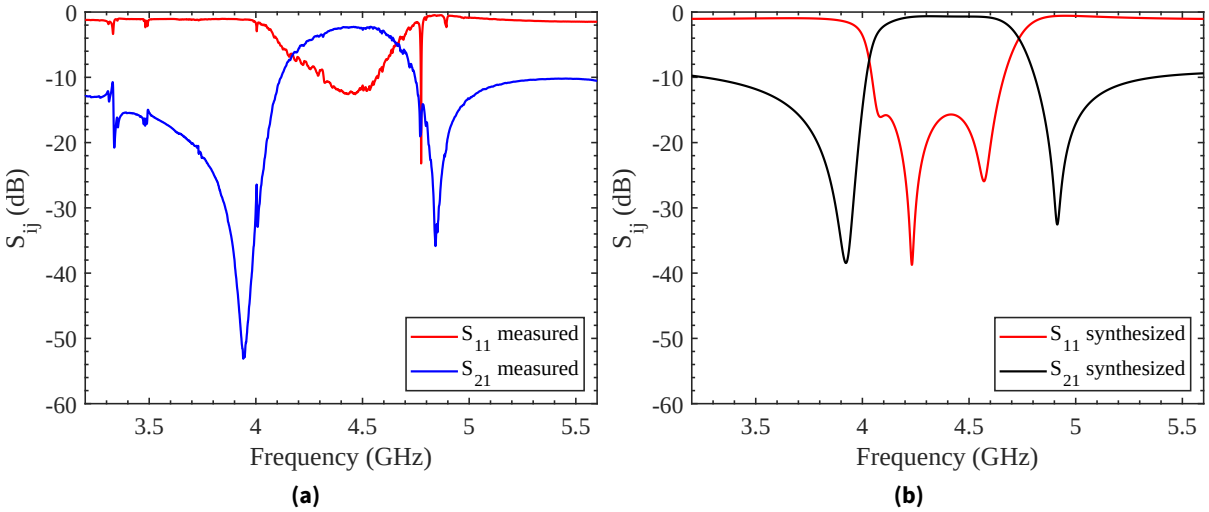

Figure 4.11: Magnitude response of the shunt-starting 4.5 GHz filter. (a) Measured magnitude response. (b) Simulated response of the synthesized BVD reactance model assuming $Q_{AW} = 200$.

sider that the filter is originally designed through optimization and not following the output of the synthesis and also that there are multiple effects regarding parasitics and layout that need to be considered for a correct assessment of the response. Among other, the authors consider that some distortions of the response in Fig. 4.11a are related to layout parasitics at 4.5 GHz adding inductance in series to shunt resonators (thus widening the obtained k^2_{eff}) and to the lithography accuracy in the definition of the resonator pitch, among others. For example, the absence of clear reflection zeros may be caused by deviations in the antiresonance frequency (f_p) of the series resonator. However, while the phase does not describe the in-band shape of a traditional equiripple response, preserves the horizontal asymptote that is the key factor of the proposed discusion, since the reflection phase at frequencies away from the passband is mainly defined by the static capacitance of resonators. Additionally, one must consider that the loss model used for simulation with the BVD models is rather simplified as an initial approximation and an advanced characterization of the technology could provide a more complex loss model along with spurious modes modeling to obtain a simulation result closer to the measured performance.

Synthesized n7 Duplexer

To demonstrate the synthesis of duplexer-oriented shunt-starting filters featuring two reactive elements at the input let us a consider an n7 duplexer example (uplink 2500-2570 MHz and downlink 2620-2690 MHz) with the objective of implementing the downlink filter starting in shunt resonator to attain large rejection towards the uplink filter. Even further, to highlight the versatility of duplexer-oriented synthesis, the uplink filter of this example is re-used from the duplexer presented in Section 4.1, whose synthesized values are shown in Fig. 4.1. For consistency, the downlink filter for this ex-

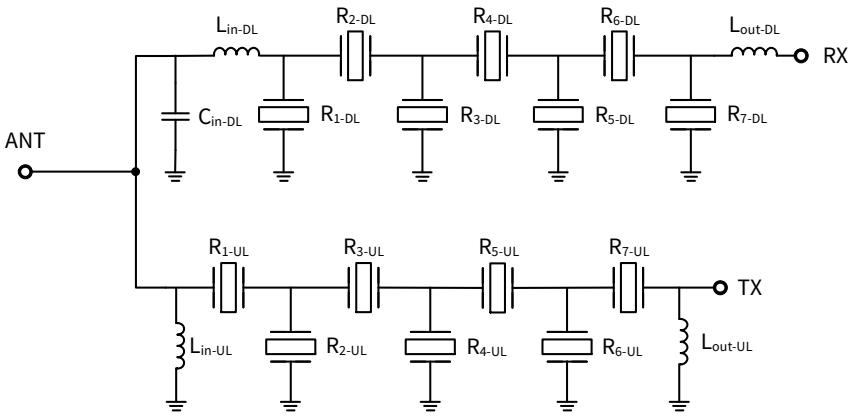

Figure 4.12: Schematic view of the n7 duplexer with n7 downlink filter starting in shunt and featuring two input reactive elements C_{in} and L_{in}.

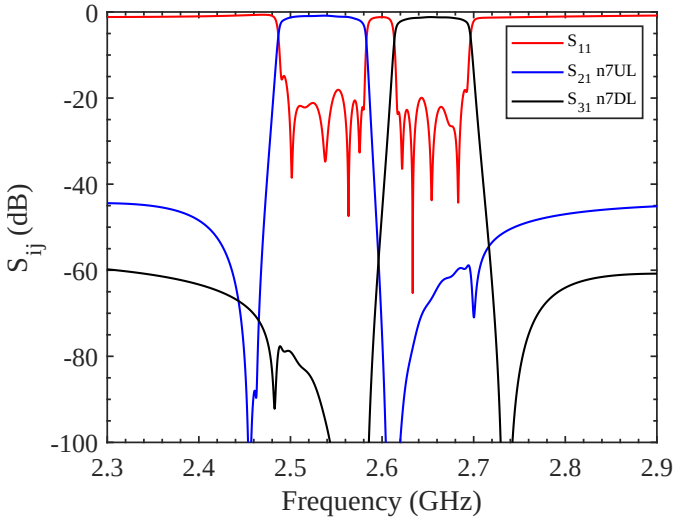

Figure 4.13: Simulated response of the synthesized n7 duplexer with n7 downlink filter starting in shunt and featuring two input reactive elements.

ample is synthesized to be implemented with AlN BAW resonators as well (i.e., $k^2_{\text{eff}} = 6.7\%$).

The input parameters for the synthesis method of the n7 downlink filter are $\Omega_{\text{n7-DL}} = [-2.75, 2.11, -1.94, 1.95, -1.94, 2.11, -2.24]$ and RL = 17.7 dB with a phase modification term $\theta_{\text{add}} = 34.5°$. The double element is extracted to implement a reflection phase of $\theta_{S1} = -86.7°$ using (4.10) selecting the positive solution as $B_{S1} = 0.9446$ to obtain an input shunt capacitor. Finally, the synthesized BVD model elements of the filter are shown in Table 4.4. Let us highlight that from the downlink perspective, in the normalized domain $\Omega_{\text{CB}} = -3.51$ rad/s and thus, the first TZ (-2.75 rad/s) does not fulfill (4.7) but thanks to the double element solution, the obtained filter is feasible. The schematic of the duplexer, showing the two input elements of the downlink branch and a single shunt inductor at the uplink branch, is shown in Fig. 4.12 and the simulated response of the duplexer, assuming $Q_{AW} = 1500$, $Q_L = 50$ and $Q_C = 100$, is shown in Fig. 4.13.

Table 4.4: Butterworth - Van Dyke model elements of the n7 downlink filter with two input elements.

n7 downlink - $\theta_{\text{add-DL}} = 34.5°$

Resonator	1 (SH)	2 (SE)	3 (SH)	4 (SE)	5 (SH)	6 (SE)	7 (SH)
L_a (nH)	20.34	160.89	20.19	162.04	20.20	157.71	30.79
C_a (fF)	191.03	22.23	188.41	22.17	188.31	22.68	124.55
C_0 (pF)	3.28	0.38	3.24	0.38	3.23	0.39	2.14
k^2_{eff} (%)	6.7	6.7	6.7	6.7	6.7	6.7	6.7
C_{in} (pF)	1.13		L_{in} (nH)	3.30		L_{out} (nH)	1.32

4.3 Dual Band Parallel-Connected AW Ladder Filters

The discussion on reflection phase control as an enabler of duplexer-oriented filters in this chapter is centered around the application of the duplexer phase condition at the input port of the two filters to be duplexed. While this is the most common situation and duplexers are an important filter implementation in the context of mobile communications, the possibility to also control reflection phase at the output port might be of interest as an approach to dual band applications. Although there are methods to synthesize and design filters implementing two (or more) passbands, specially in the context of waveguide and coaxial cavity filters, [9, 149–152] and also some synthesis methods have been proposed in the context of acoustic wave technologies [153, 154], a simple approach to compose a dual band device is the direct parallel connection of two AW ladder filters provided that both filters do not interfere each other in terms of reflection at neither of the ports, as observed in some commercial examples [155] and in the schematic in Fig. 4.14.

Clearly, composing the proposed parallel-connected structure while attaining the desired dual band performance has important implications in the reflection phase of both filters, as already discussed in this chapter, but not only at the input port but on both simultaneously. However, note that the discussion up to this point has exploited the modification of reflection phase by directly applying a shift to polynomial $F(s)$ (4.2) and, as also introduced in Ch. 3, considering the orthogonality condition of S-parameters and their definition in terms of characteristic polynomials (3.19), directly shifting the phase of polynomial $F(s)$ entails imposing a predefined phase both on input reflection phase ($\angle S_{11}$) and output reflection phase ($\angle S_{22}$) since $F_{22}(s)$ is directly the paraconjugate of $F(s)$.

Therefore, with the phase modification procedure in (4.2) there is no degree of freedom to control the output reflection phase and thus, an alternative method to tailor reflection phase of the transfer function while fulfilling the orthogonality of S-parameters is required. To this end let us exploit a specific definition of the phase initially proposed in [156] with the purpose of imposing extracted pole sections on a transversal coupling matrix, that was later exploited in [25, 157] to study the relations between reflection phase and the last non-unitary admittance inverter in inline fully canonical

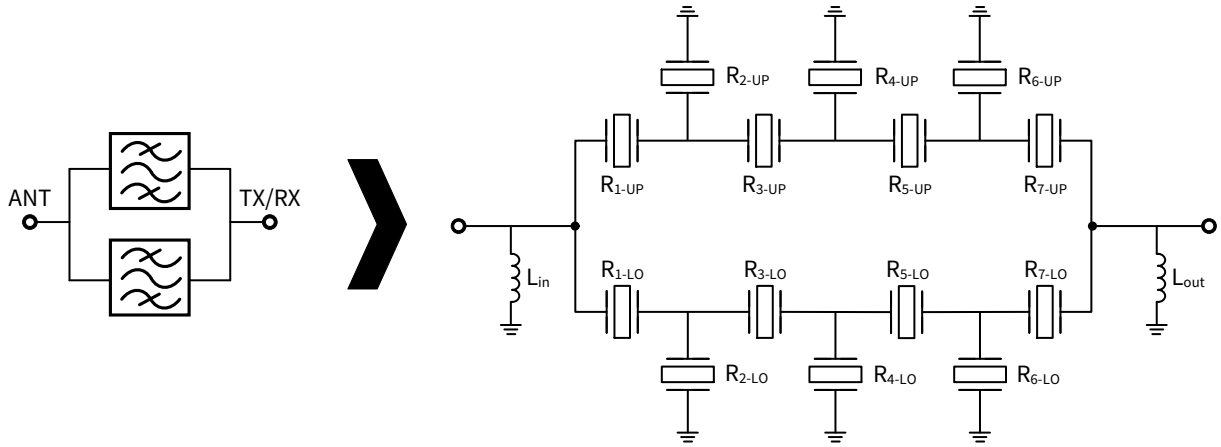

Figure 4.14: Schematic view of the proposed dual band device composed by two parallel-connected AW ladder filters where subscripts *LO* and *UP* refer to the lower and upper passbands of the final response.

networks.

Let us start by revisiting the definition of the transfer function S-parameters with respect to characteristic polynomials (3.8),

$$S_{11}(s) = \frac{F'_{11}(s)/\varepsilon_r}{E'(s)} \tag{4.12a}$$

$$S_{22}(s) = \frac{F'_{22}(s)/\varepsilon_r}{E'(s)} \tag{4.12b}$$

$$S_{21}(s) = S_{12}(s) = \frac{P(s)/\varepsilon}{E'(s)} \tag{4.12c}$$

where the dashed polynomials are modified versions of the original polynomials as,

$$F'_{11}(s) = F(s)\sqrt{a/b} \tag{4.13a}$$

$$F'_{22}(s) = (-1)^N F(s)^*\sqrt{b/a} \tag{4.13b}$$

$$E'(s) = \frac{E(s)}{\sqrt{ab}}. \tag{4.13c}$$

Terms a and b are complex numbers of unitary modulus that come defined, similar to (4.2), from the phase shifts ψ and ϕ to the input and output reflection phases, respectively, as:

$$a = e^{j\psi} \qquad b = e^{j\phi} \tag{4.14}$$

Note that this modification is able to control both input and output reflection phases by introducing a phase modification of polynomial $E(s)$ thus altering also, to comply with orthogonality, the transfer phase (i.e., $\angle S_{21}$).

Considering the proposed phase definition, as already developed for duplexers, if two filters need to be connected in parallel at both ports, the most important condition to fulfill is imposing that

Table 4.5: Butterworth - Van Dyke model elements of the n66-n25 dual band device example.

n66 uplink

Resonator	1/7 (SE)	2/6 (SH)	3/5 (SE)	4 (SH)
L_a (nH)	81.31	50.05	127.87	56.44
C_a (fF)	101.32	177.91	64.93	156.38
C_0 (pF)	1.74	3.06	1.11	2.68
k^2_{eff} (%)	6.7	6.7	6.7	6.7
$L_{\text{in/out}}$ (nH)	11.11			

n25 uplink

Resonator	1/7 (SE)	2/6 (SH)	3/5 (SE)	4 (SH)
L_a (nH)	122.56	27.02	139.99	27.99
C_a (fF)	57.38	281.43	50.99	270.10
C_0 (pF)	0.98	4.84	0.87	4.64
k^2_{eff} (%)	6.7	6.7	6.7	6.7
$L_{\text{in/out}}$ (nH)	6.16			

each of the filters depicts a reflection phase of 0° at the central frequency of its partner filter. That is, for the lower band (LO) filter with respect to the upper band (UP) filter, $S_{11-LO}(f_{0-UP}) = 0°$ and $S_{22-LO}(f_{0-UP}) = 0°$ and vice versa. By inspection, note that such condition at both ports implies that $\angle S_{11} = \angle S_{22}$.

At this point, note also an additional fact that has been outlined in previous sections. Since the presence of a non-unitary admittance inverter at the end of the network is avoided through an admittance redistribution and such operation has an effect on the output reflection phase, to maintain the phase imposed on S_{22} through (4.12c) at the transfer function level, an additional condition must be imposed on the parameters that define the network to synthesize. The work in [157] demonstrates that the only possibility to obtain all unitary mainline admittance inverters while imposing that $\angle S_{11} = \angle S_{22}$ implies that the network be physically symmetric. In terms of the AW ladder filter that entails resonators need be equal in pairs, [(1,N), (2,N-1), (3, N-2), ...] where N is the order of the filter and N is odd, with respect to the center resonator of the filter. Equivalently, the set of transmission zeros must be symmetric with respect to the central TZ.

To exemplify the proposed approach, let us present the example of an n66 uplink (1710 - 1780 MHz) and n25 uplink (1850 - 1915 MHz) dual band device composed of two filters, individually synthesized with their reflection phases tailored with (4.13c). This situation, a dual band device implementing two uplink passbands is of interest, for example, in the context base stations in which the two bands feed the same low noise amplifier path, as is the case of the n1 and n3 uplink dual

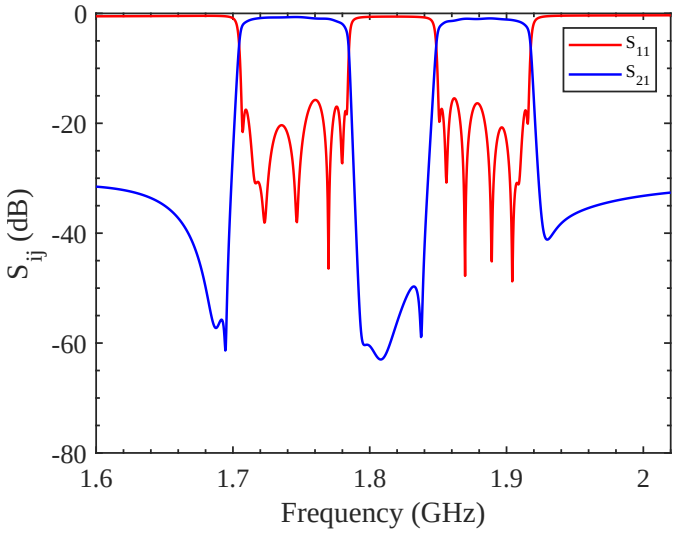

Figure 4.15: Simulated response of the n66n25 uplink dual band device.

band device by Qorvo [155]. For this example, the filters have been designed to implement AlN BAW resonators (i.e., $k^2_{\text{eff}} = 6.7\ \%$) and the synthesized BVD model elements are depicted in Table 4.5. The input parameters for the synthesis of each filter are $\Omega_{\text{n66-UL}} = [1.5244, -1.5363, 1.3344, -1.3240, 1.3344, -1.5363, 1.5244]$, RL = 15.8 dB and phase terms $\psi_{\text{n66-UL}} = \phi_{\text{n66-UL}} = -28.75°$, for the n66 uplink, and $\Omega_{\text{n25-UL}} = [2.1023, -1.8098, 1.6410, -1.6382, 1.6410, -1.8098, 2.1023]$, RL = 15.2 dB and phase terms $\psi_{\text{n25-UL}} = \phi_{\text{n25-UL}} = 21.74°$, for the n25 uplink. Note the symmetry of the transmission zero sets. The simulated response of the obtained dual band device after connecting both filters in parallel at input and output and merging port inductors into $L_{\text{in/out}} = 3.96$ nH, is shown in Fig. 4.15. This simulation assumes $Q_{AW} = 1500$ for AW resonators and $Q_L = 50$ for the input and output shunt inductors.

The obtained response requires a detailed description to introduce the main limitation of this approach to dual band responses. Clearly, both passbands are clearly constructed and well matched (within the passband, $S_{11} < -15dB$)). However, note the clear distortion of the response in the out-of-band region, both away from the passbands and between them, since the deep transmission zeros expected from each AW ladder filter are not present. The observed fading of TZs when the two filters are connected in parallel is related to the presence of a reactive cross-coupling between the filters as introduced in [27]. Considering the capacitive nature of the AW ladder in the OoB region, although reflection phase has been set to depict an open-circuit at the central frequency of the partner filter, each filter acts as a capacitive path to its partner given its finite OoB rejection level. While the presence of such reactive path could ideally be considered when synthesizing each filter [138] to obtain the desired response when both filters are connected in parallel, due to its strength it triggers the appearance of complex roots of the filter function (complex TZs), that cannot be implemented by extracted pole sections and thus, by AW resonators [27, 28, 136]. Similarly, note that the parallel-connected approaches in [150, 151] also describe such OoB distortion but, since they cover cases of filters placing TZs at infinite frequency, the strength of the undesired cross-coupling is minimal and

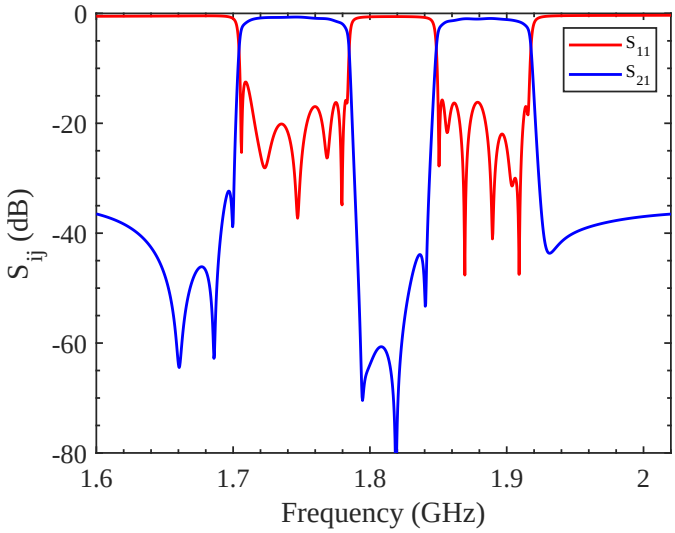

Figure 4.16: Simulated response of the n66n25 uplink dual band device when considering ground inductors joining shunt resonators 2 and 4.

distortion is highly reduced.

Notice, therefore, that in the case of AW ladder filters the observed OoB distortion when connecting the filters in parallel cannot be tackled through the synthesis and the obtained fly-back levels in the OoB region correspond to those of the least rejecting filter. This is an intrinsic limitation of this dual band approach. However, there is still the possibility of improving the final response by trying to reduce the strength of the mentioned reactive path in parallel. An interesting method to achieve that is to exploit the additional TZs provided by the coupling of two shunt resonators via a small inductor in their ground path as proposed in [158]. A very common practice in AW ladder filters. Given the many available combinations between the shunt resonators of both filters, let us propose an example in this case adding two small inductors of 0.2 nH connecting the second and fourth shunt resonators of each filter to ground (i.e., a 0.2 nH inductor joining the ground terminals of $R_{2\text{-LO}}$ with $R_{4\text{-LO}}$ and another 0.2 nH inductor joining $R_{2\text{-UP}}$ and $R_{4\text{-UP}}$ given the schematic in Fig. 4.14). The simulated response of the structure with the simple addition of these two inductors is shown in Fig. 4.16 for the same simulation conditions above. Notice the increase in OoB rejection (6 $\sim$ 8 dB) in both fly-back levels and note the appearance of additional transmission zeros both below the n66 band and between the passbands.

In general, the parallel-connected approach to dual-band AW filters is the most straightforward solution and offers some advantages: a simplified design process since it can be seen as the design of two independent ladder filters and the possibility to reuse already fabricated devices along with external matching elements to impose the described phase conditions that allow to connect both filters in parallel. However, the limitations of this approach need to be considered. First, this approach does not provide full control of the final response of the structure since it is composed of

two independent AW ladder filters. Although the final response is effectively dual-band, is not the implementation of a synthesized dual-band filter function rather than the best-effort combination of two individual filters.

Additionally, there is a limitation in terms of achievable rejection given the cross-coupling effect provided by the finite OoB rejection of the individual filters, as exposed above. In terms of device dimensions this approach directs to the least compact solution given the need to fabricate two separate ladder filters to be connected at the package level, what might yield increased packaging complexity as well. In general, this approach provides filter design simplicity in exchange of performance in terms of the achievable steepness and rejection using AW technology.

To close this brief discussion on dual band devices, the proposal in this thesis is framed within the discussion of applications of reflection phase control in AW filter synthesis. However, the topic of dual band devices composed of acoustic wave resonators is originally introduced in [159] by proposing the so-called double-ladder topology from a circuital perspective and is later reviewed to provide a synthesis method for it in [152], exploiting a nodal equivalent composed of double dangling resonator sections. Moreover, going beyond the synthesis solution to the double ladder topology, the recent contribution [154] by the group hosting this thesis closes the complete discussion on acoustic wave dual band filters by proposing the synthesis of a regular ladder topology implementing a dual band response and provides a comparison between the parallel-connected approach in this thesis, the double ladder and the regular ladder case.

4.4 Breaking the Ladder

The complete discussion in Sec. 4.2 is centered around the fact that if reflection phase is not properly considered and controlled, unfeasible filters might be obtained as the output of the synthesis procedure. As a summary, the findings demonstrate that filters showing negative values of C_0 (inductive behaviour of the static branch of the BVD) at the first and/or last resonators are obtained when series-starting filters depict reflection phases tending to $\pm$ 180° or when shunt-starting filters feature reflection phases towards 0°. The discussion has, therefore, focused on how to avoid such situations and has provided a set of rules on how to handle the synthesis of shunt-starting filters since, for them, the natural reflection phase of a Chebyshev function yields unfeasible results.

Moreover, note that such discussion is supported on considering a widely accepted fact that has already been introduced in Ch. 1 and 3. A series AW resonator in the ladder topology places a transmission zero above the passband with its f_p, keeping its f_s in-band, while a shunt resonator places a transmission zero below the passband with its f_s, while keeping its f_p inside it. This brief explanation is the fundamental paradigm of AW ladder filter design and is also the driving argument of some of the findings in this thesis. To mention some literature examples providing that fundamental view

of the ladder, consider [11, 17, 31, 160], among many others. At the same time, while the AW ladder topology is very useful since it directly ties resonator frequencies with transmission zeros of the response, it is also a rigid configuration in terms of achieving more advanced responses. For example, it entails a limitation in the number of TZs at each side of the passband for a given filter order due to the alternating disposition of resonators along the ladder, what ultimately limits the achievable skirt steepness of the filter.

If ones tries go beyond this framework, for example trying to impose that a series resonator of the filter actually places a transmission zero below the passband, maintaining the other resonance, f_s, inside the passband clearly results in a resonator for which $f_s > f_p$. As introduced in this chapter, such statement has an effect in terms of the BVD model, requiring an inductive static branch or, equivalently, a negative C_0, what has already been demonstrated from a synthesis perspective showing that extracted pole sections placing TZs at positive normalized frequencies are related to $B_k < 0$ and vice versa in (4.4).

Interestingly, diving into an exercise of logical double negation, let us observe that the undesired feature of reflection phase that leads to unfeasible filters and that is widely discussed in Sec. 4.2 to highlight phase regions where a change in the sign of C_0 appears, can actually be exploited here to counteract the fact that a series resonator placing a TZ below the passband should be unfeasible, and vice versa. In other words, one can exploit reflection phase control to violate the ladder rules twice and synthesize filters in which the first and/or the last resonators place transmission zeros in unexpected positions, hence allowing novel responses such as, for example, 7th order filters starting in series placing five zeros below the passband and two above. Nevertheless, note that at the expense of achieving advanced responses with a simple AW ladder topology one has to consider that since phase is used to ensure the proper sign of C_0, it cannot be exploited for the other purposes such as avoidance of the input reactive element or duplexer-oriented filters.

Since the particular relations between phase and feasibility have been discussed in detail in Sec. 4.2 in this chapter, let us introduce this interesting exploit of reflection phase through the direct discussion of examples, both in the case of series-starting and shunt-starting filters, each of them having its own particularities. To complete the discussion, a manufactured example is demonstrated on the LNOI platform presented in Ch. 2 implementing an N=3 filter starting in shunt with two transmission zeros above the passband and a single one below.

4.4.1 Series-starting Case

Considering a filter starting in series resonator, Fig. 4.7 shows that such a filter becomes unfeasible for reflection phases closer to ± 180°. With this fact in mind, let us take an N=7 filter example and consider the following set of transmission zeros Ω_{SE} = [-1.4035, -1.8887, 1.8771, -1.6688, 1.8771, -1.8887, -1.4035] rad/s and RL = 20 dB, noticing that the first and last TZs are negative (i.e., below

Table 4.6: Butterworth - Van Dyke model elements of the 3820 - 3980 MHz filter with 5 TZs below the passband.

3820 - 3980 MHz - $\theta_{\text{add}} = -139.8°$				
Resonator	1/7 (SE)	2/6 (SH)	3/5 (SE)	4 (SH)
L_a (nH)	4.32	3.66	19.69	3.67
C_a (fF)	440.05	492.26	83.87	486.59
C_0 (pF)	5.80	6.49	1.10	6.42
k^2_{eff} (%)	8.5	8.5	8.5	8.5
$L_{\text{in/out}}$ (nH)	1.18			

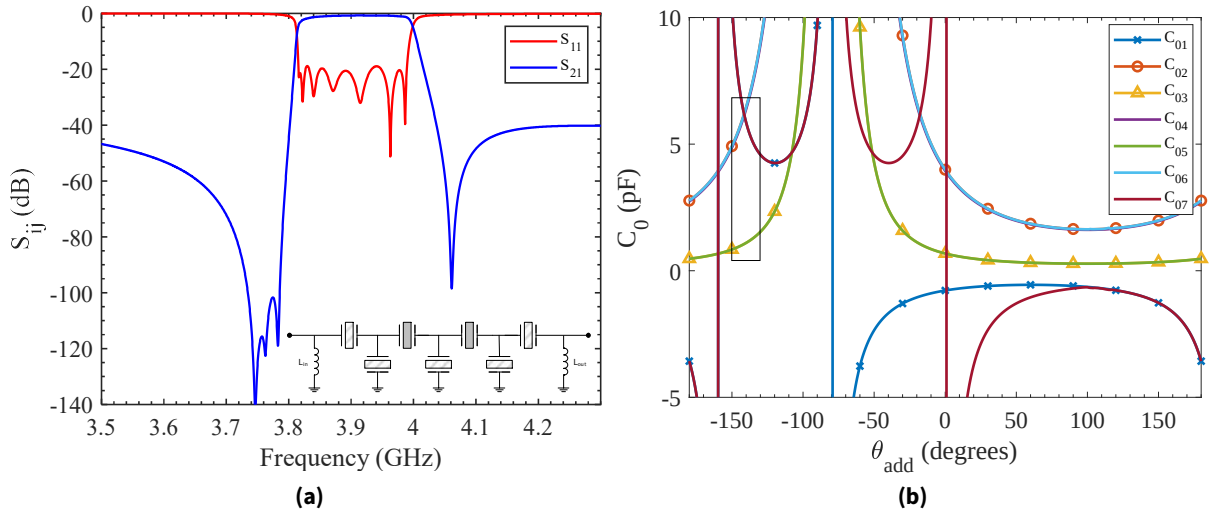

Figure 4.17: Example of series-starting filter featuring 5 TZs below the passband and 2 TZs above. (a) Simulated magnitude response of the filter. Dashed resonators in the schematic inset place TZs below the passband and solid resonators place them above. (b) Evolution of C_0 values with respect to θ_{add} for this example filter. The rectangle highlights the selected phase region where the filter is feasible.

the passband) while positive values for these TZs are expected for series-starting filters. Note also the symmetry of TZs with respect to the center of the array. In this case, this is a condition to impose if both the first and the last resonators are to implement a TZ in the opposite stopband since to attain the, now desired, change of sign in C_0 on both resonators, reflection phase must be controlled both at input and output. As discussed in the dual band device section, to control output reflection phase one must avoid redistribution of the last admittance inverter and therefore must consider physically symmetric networks such that the inverter has a unitary value by nature.

With the proposed set of TZs and RL, considering a phase modification of $\theta_{\text{add}} = -139.8°$ and an arbitrary passband defined between 3820 and 3980 MHz, the BVD model elements summarized in Table 4.6 compose the response shown in Fig. 4.17a assuming $Q_{AW} = 1500$ and $Q_L = 50$. In this occasion, the filter has been synthesized for a $k^2_{\text{eff}} = 8.5\%$ on all resonators, what can be the case

of BAW resonators made of ScAlN (Scandium Aluminum Nitride) [59, 146] or also of $LiTaO_3$ SAW resonators [50], for example. It is worth highlighting the skirt slope and the rejection attained at the lower stopband due to imposing the presence of 5 TZs. Note also, from the BVD elements in the table that resonators 1 and 7 have $f_p = 3783$ MHz (the actual transmission zero) while having $f_s = 3647$ MHz, far below the passband. Since the filter has been synthesized for this specific purpose, all resonators have the necessary impedance such that they compose the desired transfer function while depicting such an unexpected distribution of frequencies that contradicts the traditional paradigm of the AW ladder filter.

To demonstrate the impact of phase in the proposed example, the relation between reflection phase and C_0 is depicted in the plot in Fig. 4.17b showing the evolution of C_0 with respect the modification applied to reflection phase of the filter function of the example TZs and RL. The black box indicates the required phase modification to attain feasibility and same k^2_{eff} on all resonators. It is interesting to highlight that internal resonators (2 to 6) do not see a change in the reactive nature of their static branch along the entire range of phases, but their value is modified. Following the content derived in Sec. 4.2, one would expect a series-starting filter to be feasible for θ_{add} values close to 0° but, in this case, due to imposing that resonators 1 and 7 place TZs below the passband, the filter is not feasible at such phases (as expected) but shows a feasible phase region for negative θ_{add} values. Note that in a regular series-starting case, the now feasible phase region is the range of phases for which the filter becomes unfeasible in terms of AW technology. For completeness, notice also that values of C_{01} and C_{07} with respect to θ_{add} in Fig. 4.17b show a different behavior although they correspond to two resonators placing the same transmission zero. Although the network is physically symmetric and redistribution of the last admittance inverter is avoided, as stated by the orthogonality condition of S-parameters, a phase addition as in (4.2) affects input and output reflection in an asymmetric manner.

To conclude the discussion, the passband of the selected synthesized example, arbitrarily defined between 3820 and 3980 MHz, is chosen to demonstrate an interesting feature of this double violation of reflection phase rules, when applied to series-starting cases. Note that although the band is high in frequency the synthesized resonators require large values of C_0, something slightly contradictory if one considers that as frequency increases, capacitors must be smaller to match a reference 50 Ω load. Since higher values of C_0 can be obtained, the proposed effect of reflection phase modification appears as an interesting option for very high frequency filters (above 10 GHz) at which AW resonators might become prohibitively small. As a last remark, note that this approach can be applied not only to both the first and last resonators of the network, thus having to impose physical symmetry of the network, but also on only one of them, opening the possibility to have the first series resonator placing its TZ below the passband and the last resonator acting as an average series resonator, thus having freedom on the TZ it implements above the passband.

Table 4.7: Butterworth - Van Dyke model elements of the 1480 - 1550 MHz filter with 5 TZs above the passband.

1480 - 1550 MHz - $\theta_{\text{add}} = -36.4°$				
Resonator	1/7 (SH)	2/6 (SE)	3/5 (SH)	4 (SE)
L_a (nH)	525.16	720.51	138.98	655.84
C_a (fF)	19.67	15.15	85.96	16.82
C_0 (pF)	0.25	0.20	1.13	0.22
k^2_{eff} (%)	8.5	8.5	8.5	8.5
$L_{\text{in/out}}$ (nH)	10.53			

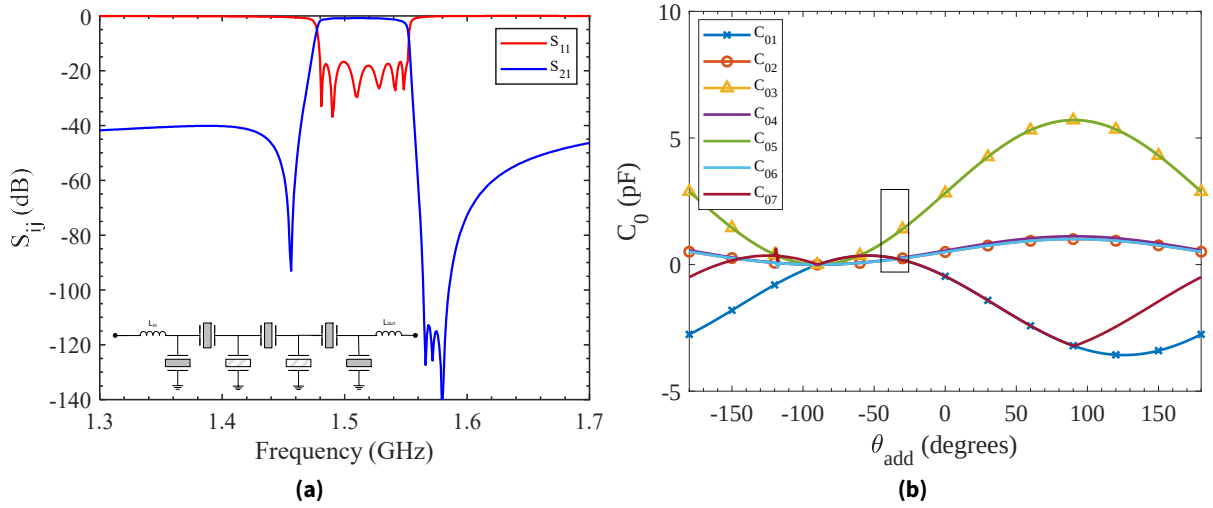

Figure 4.18: Example of series-starting filter featuring 5 TZs above the passband and 2 TZs below. (a) Simulated magnitude response of the filter. Dashed resonators in the schematic inset place TZs below the passband and solid resonators place them above. (b) Evolution of C_0 values with respect to θ_{add} for this example filter. The rectangle highlights the selected phase region where the filter is feasible.

4.4.2 Shunt-starting Case

In contrast to the example in the above paragraphs, let us consider a filter starting in shunt resonator but now imposing that the first and last resonators place their transmission zeros above the passband with their f_s. As already introduced, to accomplish this change in nature of both resonators, physical symmetry of the network must be imposed and thus, let us define the set of TZs as $\Omega_{\text{SH}} = [1.4118, 1.8353, -1.7630, 1.5869, -1.7630, 1.8353, 1.4118]$ rad/s with RL = 17.5 dB to obtain, considering a passband defined between 1480 and 1550 MHz and a phase shift addition $\theta_{\text{add}} = -36.4°$, the BVD model elements depicted in Table 4.7. Again, this shunt-starting example is synthesized to require $k^2_{\text{eff}} = 8.5\%$ on all resonators.

The simulated response of the synthesized filter considering the quality factors of the previous

example is shown on Fig. 4.18a, showing very high rejection and a steep skirt at the upper band-edge of the filter. To highlight the role of the first and last resonators, notice their f_s is at 1565 MHz, the position of the TZ that is closer to the upper band-edge, while their f_p lies at 1624 MHz, outside the passband, and consider the behavior of C_0 against the phase shift added depicted in Fig. 4.18b. Clearly, the evolution of all C_0 is opposite to that shown for series-starting filters, offering a feasible region for negative θ_{add} values close to 0° (thus closer to the intrinsic phase of a generalized Chebyshev function). Note that in this case, the obtained capacitance values are smaller than those expected for this frequency range offering the possibility to design low frequency filters that do not require very large resonator areas, an issue that is common for the bands that lie below 1 GHz.

Nevertheless, the presence of large input and output inductors, in this case in series configuration, must be commented as an intrinsic drawback of the method since they cannot be avoided because reflection phase is being exploited to attain feasibility of the first and last resonators. By nature, this approach to place TZs in unnatural positions is strongly related with reflection phase regions that trigger large values of NRNs B_S and B_L and results in an increased complexity to implement input and output inductors.

4.4.3 Demonstrative Example on LNOI

To demonstrate the actual implementation of the discussed synthesis approach to filters implementing responses originally not attainable with the AW ladder topology, this section presents a manufactured example of third order ladder filter starting in shunt resonator but featuring two transmission zeros above the passband and a single one below. The technology of implementation is the LNOI platform presented in Ch. 2 and thus considers an electromechanical coupling of approximately 17%. For this example, let us propose a set of transmission zeros $\Omega_{\text{LNOI}} = [1.5093, 2.9893, -4.4804]$ rad/s, therefore only imposing a change of nature on the first resonator, a return loss level of 20 dB and a required phase shift of $\theta_{\text{add}} = -32.69°$. Note the consistency of this phase value to the range highlighted in Fig. 4.18b. Regarding frequency transformation, considering the frequency range at which the proposed LNOI structure shows the highest performance let us define the passband between 1440 - 1530 MHz, hence a fractional bandwidth of 6.5%. With the proposed parameters, the application of the synthesis method yields the BVD model elements shown in Table 4.8.

From the synthesized parameters and considering a phase velocity of the SH_0 mode of 3975 m/s in the proposed LNOI platform with the characteristics discussed in Ch. 2, the transducer pitch ($\lambda/2$) of the resonators can be computed as shown in Table 4.8 along the number of fingers and IDT aperture of each resonator. The layout of the proposed filter is shown both in drawing and in an SEM image in Fig. 4.19a. The measurement of the filter is conducted with GSG probes and thus a coplanar probing structure is implemented around the filter. Additionally, note that due to resonator 3 requiring a larger C_0, its implementation is split into two resonators of half the capacitance to

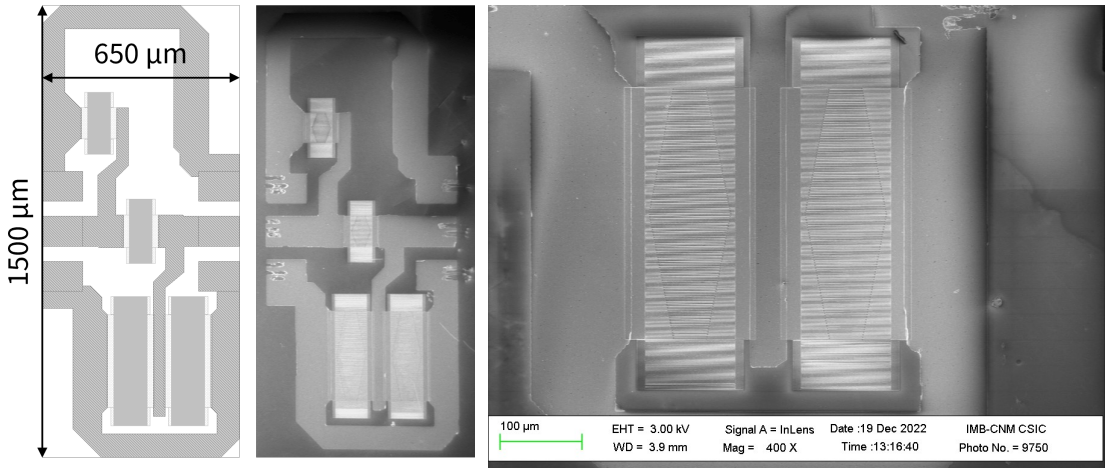

Figure 4.19: Images and schematic of the manufactured filter on LNOI. (a) Drawing and SEM image of the complete filter layout showing the co-planar probing pads, ground leads and resonators. Dimensions are highlighted in the layout drawing. (b) SEM image of the second shunt resonator, composed as the parallel connection of two equal resonators. The IDT apodization pattern is observable.

Table 4.8: Butterworth - Van Dyke model elements and physical resonator parameters of the 1440 - 1530 MHz LNOI filter. NF stands for number of fingers and Ap. stands for IDT aperture.

1440 - 1530 MHz - $\theta_{\text{add}} = -32.69°$

Resonator	L_a (nH)	C_a (fF)	C_0 (pF)	k^2_{eff} (%)	f_s	Pitch (μm)	NF / Ap. (μm)
1 (SH)	127.10	82.07	0.49	16.9	1558	1.27	81 / 65
2 (SE)	133.02	84.40	0.50	16.9	1502	1.32	81 / 65
3 (SH)	16.75	872.00	5.30	16.9	1316	1.51	2x (201 / 100)
L_{in} (nH)	3.68		L_{out} (nH)	3.61			

ease layout distribution as shown in Fig. 4.19b where the apodization of the IDT pattern is clearly observable. As discussed at the beginning of this thesis, an apodization ratio of 60% is selected.

After measuring the filter on a probe station, input and output inductors of 3.6 nH have been considered a posteriori through co-simulation with the S-parameter models of Murata's SMD RF inductors. Finally, the measured response of the proposed filter is shown in Fig. 4.20a superimposed with the simulated response using the synthesized BVD models. Additionally, the wideband measured response of the filter up to 6 GHz is shown in Fig. 4.20b and both the input and output reflection phases, both from measurement and simulation, are shown in Fig. 4.20c and 4.20d. Let us highlight the agreement between measurement and simulation, clearly depicting the required reflection phase to allow the first shunt resonator to place a TZ above the passband. Nevertheless, it is important to state that the difference in insertion loss between simulation and measurement is related to the high sheet resistance of both electrodes and leads, that is not accurately considered in

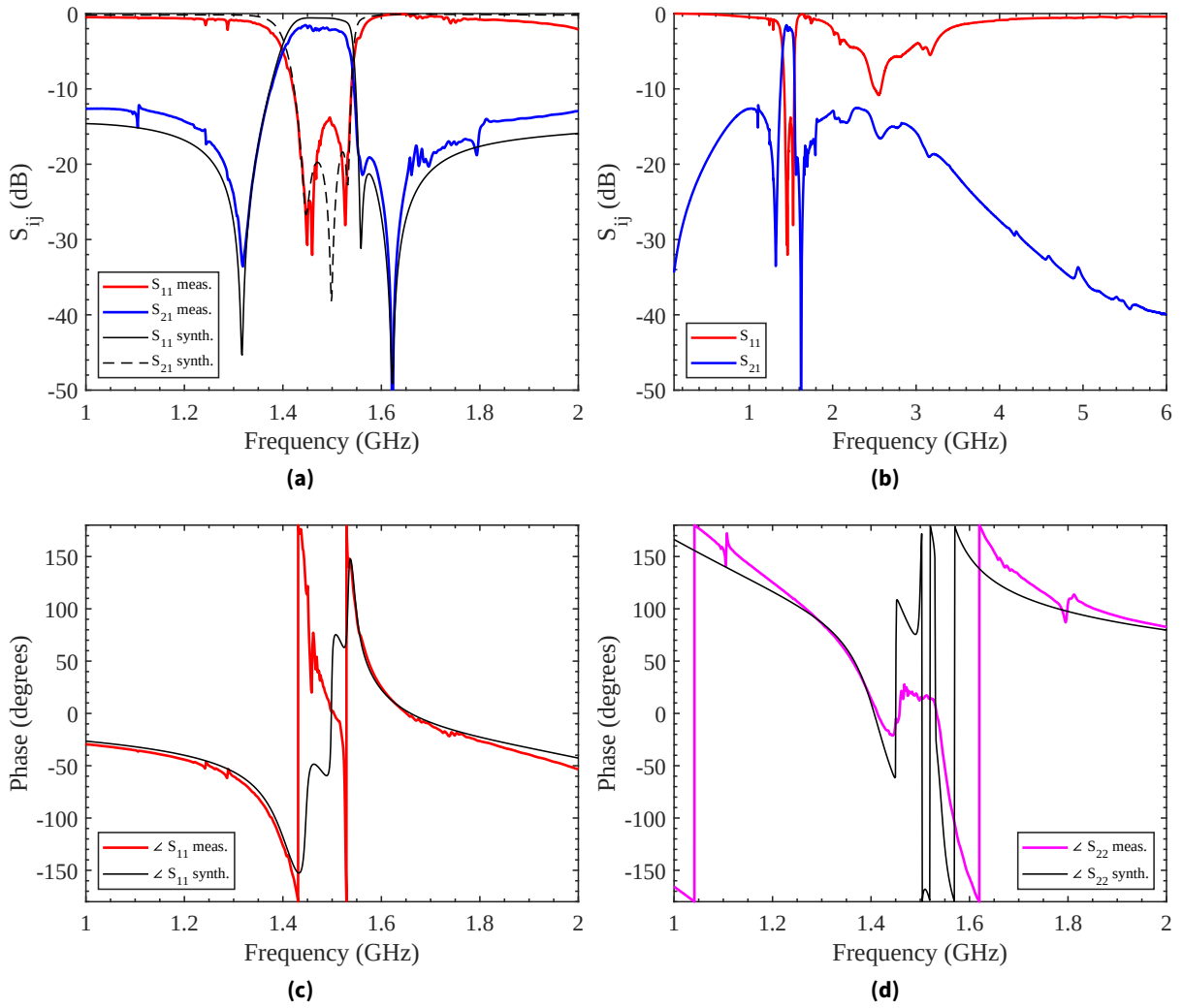

Figure 4.20: Measurement and synthesis simulation of the LNOI prototype. (a) Narrowband response measurement and synthesis simulation assuming Q_{AW} = 400. (b) Wideband measured response from 100 MHz to 6 GHz. (c) Input reflection phase measurement and synthesis. (d) Output reflection phase measurement and synthesis.

the simulation model.

Interestingly, the monotonically increasing rejection towards higher frequencies observed in Fig. 4.20b is related to the inherently lowpass behavior of the underlying structure of the filter. Considering the large inductors in series at the input of the filter with the shunt capacitance that each shunt resonator implements at frequencies far from resonance, a rudimentary lowpass filter structure (series inductance and shunt capacitance) is composed effectively enhancing rejection at higher frequencies.

4.5 Chapter Summary

This chapter provides an overview of the key role of reflection phase in the synthesis of acoustic wave ladder filters. Starting from its use as a degree of freedom to design duplexer-oriented filters, i.e., filters implementing an open circuit condition at the center of their partner filter in the duplexer, the phase is used as a discussion vehicle to explore the feasibility of shunt-starting filters and the intrinsic relation they have with reflection phase. Thanks to it, rules on how to handle shunt-starting filters when designing a duplexer and the necessary steps to synthesize a filter featuring two input elements are proposed along synthesized examples.

Building on the use of phase to design duplexers, the approach to achieve a dual band device by duplexing a pair of filters both at input and output is reviewed from a synthesis perspective, exploiting an additional method to modify both the input and output reflection phases of a filter function in an independent manner. Finally, a curious application of the relation between filter feasibility and reflection phase is exploited to attain filters where some resonators place transmission zeros at unnatural positions. Such an approach allows to compose responses with for example 5 zeros below the passband and 2 zeros above, using a 7th order ladder starting in series resonator. This approach is in the end demonstrated on a manufactured filter using the lithium niobate on insulator platform introduced at the beginning of this thesis.

CHAPTER 5

Analytical Synthesis of Star Junction Acoustic Wave Multiplexers

Extending from the content of previous chapters that have covered the synthesis of standalone filters, that is, two-port networks, this chapter is devoted to a network synthesis method for a fundamental type of devices in mobile communications: multiplexers (MUXs). As presented in Ch. 1, carrier aggregation schemes introduced in LTE represent a key technique to increase usable bandwidth and thus achieve higher channel capacity. These CA approaches, in which multiple bands are processed concurrently, rely on the possibility of having multiple filters, one per each of the bands being aggregated, connected to the same antenna node. Therefore, the challenge for AW technology is to provide multiplexer devices that implement multiple AW filters all sharing the same input port while maintaining the desired performance. The importance of multiplexer modules has been extensively described [11,13,70,161,162] and represents a true design challenge when considering not only size and performance specifications of each filter but also the added complexity of reactive loading between filters, now K for a K-channel multiplexer, as already presented for duplexer-oriented filters in Ch. 4.

Previous works have been devoted to techniques for AW multiplexer design such as the addition of extra reactive elements at the junction node as in [163], only applicable to sufficiently spaced bands and based on optimization, or the more recent work in [164] based on optimization and response fitting with arbitrary BVD circuital models. From a network synthesis perspective, the topic has also been faced in [26, 165] through the concept of minimum susceptance networks but individually considering the filter function of each channel and only evaluating the interaction between channels after their separate synthesis, thus not providing a complete analytical description of the multiplexer behaviour. This chapter, however, describes the methodology to face multiplexer synthesis using multiport filter functions that completely contain the loading effects of the multiplexer

already in the normalized domain. This proposed method builds on the fundamental contributions by Tammiazzo and Macchiarella in [166–169] originally developed for coaxial cavity duplexers and later extended to multiplexers, and extends them into fully canonical functions for acoustic wave technologies. Other interesting contributions to the field of multiplexer synthesis directed to waveguide and coaxial cavity technologies are [170–173], all with assumptions that hinder their application to microwave acoustic filters.

This chapter initially provides a brief discussion of the main multiplexer configurations used with AW devices and then presents the mathematical framework and rationale of the proposed method along with a brief discussion of previous synthesis approaches to multiplexers. After that, the chapter dives deep into the computation of fully canonical multiport functions to represent the AW multiplexer response with polynomials of the s variable and also describes foundations of *cepstral* analysis applied to the the computation of high order polynomials. This chapter is then completed with synthesized examples of multiplexers in AW technology, a discussion of the implications of prototype denormalization in the context of multiplexer devices and with remarks on the numerical stability of this method and proposals for its further extension.

5.1 Current AW Multiplexer Configurations

Many multiplexer configurations are available in the field of microwave filters, most of them specially developed for coaxial and waveguide cavity filters since the 1970s, and a detailed description of them is provided in [9] (Ch. 18). In general terms, multiplexer configurations can be divided among those using extra microwave devices such as hybrid couplers or circulators to minimize filter interaction, sometimes called directional configurations, and the so-called manifold multiplexers in which the device is only composed of channel filters and appropriate phase lengths among them and the common port.

From an AW technology perspective, however, given the achievable degree of miniaturization and the stringent requirements in terms of space, not all of them are applicable and the predominant configuration is the star junction, a sub-type of the manifold in which all channel ladder filters are connected directly to the common node without any additional phase length. A schematic representation of a star junction multiplexer is shown in Fig. 5.1a for a quadplexer configuration (four channels). Additionally, due to space reasons and to allow an optimal footprint of the multiplexer also the so-called herringbone configuration, another sub-type of the manifold, is employed although in a lesser extent than the star junction and is characterized by having the filters connected in pairs to a common node and then using appropriate phase lengths between each pair to distribute them along the manifold, as shown in Fig. 5.1b for the same quadplexer example. Examples by AW device manufacturers of these two configurations can be found, among others, in [174, 175] regarding the star junction and in [162, 176] as examples of the herringbone configuration. It must be noted that

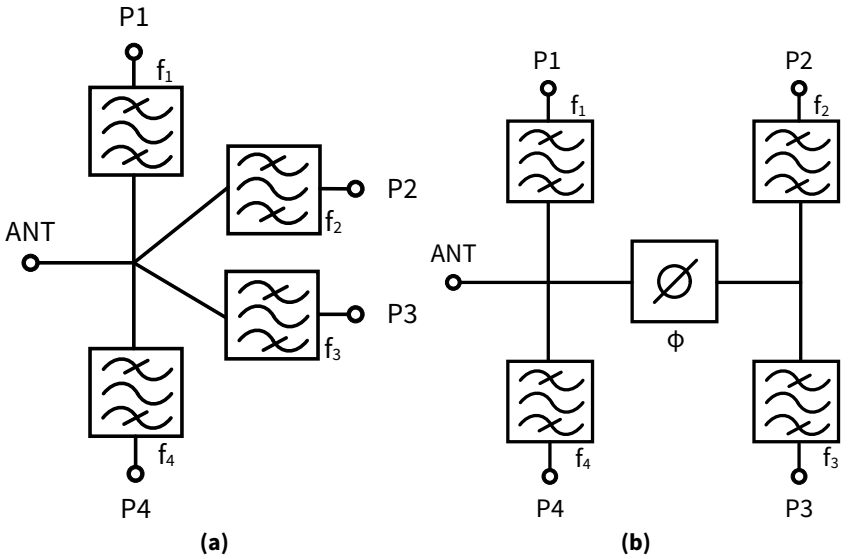

Figure 5.1: Schematic representations of the two most used configurations for AW multiplexers for an arbitrary quadplexer example. (a) Ideal star junction and (b) ideal herringbone configurations.

due to the reduced dimensions of AW filters with respect to electromagnetic wavelengths, the implementation of phase lengths in the form of transmission lines is not feasible due to space restrictions and phase shifters such as in Fig. 5.1b are implemented with lumped elements in the laminate, as depicted in [176].

For the purpose of this thesis, the proposed synthesis method is focused on the star junction multiplexer, the most common configuration, but the mathematical formulation developed and the computation of fully canonical multiport functions are applicable to the derivation of a method for the herringbone configuration. A topic that is left as a future line of research.

5.2 Comparison with Previous Methods

As introduced, and also as outlined all throughout this thesis, there is a clear interest for synthesis techniques that transform the early stages of AW filter design into an analytical process. Multiplexers, along with their core role inside mobile device RF modules, have now the entity of a complete device rather than the connection of individually designed filters and so, there is growing interest in developing their own synthesis and design techniques. To this end, the methodology proposed in this chapter is specifically developed to fill such gap.

Let us start by recalling the duplexer design procedure depicted in Ch. 4 with which a duplexer avoiding reactive loading between filters is obtained via the precise modification of the reflection phases (i.e., $\angle S_{11}$) of the two filters composing it. Notice that this procedure is based on adding an extra step, the modification of the phase, to the synthesis of two standalone filters, one for each

band, with each filter implementing a generalized Chebyshev function with the added feature that they are duplexer-oriented. That is, they depict a reflection phase of zero (an open circuit) at the center frequency of their counter-band and thus, minimize their reactive interaction. Although this approach is demonstrated and widely applied, notice that it is not a completely analytical solution of the duplexer *per se* but a loading mitigation approach exploiting the degree of freedom provided by reflection phase.

For MUXs, at a first glance one could think of a brute-force approach in which the K filters composing the multiplexer are synthesized independently to implement a Chebyshev function, each with a particular phase shift $\theta_{\text{add}-k}$ on polynomial $F(s)$, such that the loading between filters is the least possible. However, note that such method leads to an optimization loop in which each filter only has one extra degree of freedom (the added phase term) and that can only provide a best-effort solution. Moreover, take into account that a MUX covers multiple bands, thus encompassing a wide bandwidth, and consider that an exact value of reflection phase can only be fixed at a single frequency point given the horizontal asymptote behaviour of reflection phase in the OoB region of each filter. On top of that, considering the narrowband nature of the transformation from normalized to bandpass domain has a direct impact on the exactitude to which such phase value can be controlled, such a solution based on finding K suitable added phase values lends itself to a brute-force optimization approach after the independent synthesis of the K filters.

To improve the results of the latter approach, previous works on the application of filter synthesis to AW multiplexers by Silveira in [26] studied the use of minimum susceptance networks (as introduced in [177]), the ones providing the least reactive loading to adjacent channels, either in the form of singly terminated functions [165, 178] or as generalized Chebyshev functions whose reflection phase is not altered (i.e., $\theta_{\text{add}} = 0°$). However, notice that this approach, although more sophisticated than the initial brute-force scheme, is not an analytical method to synthesize the entire multiplexer and can be considered also as a loading mitigation method[1]. By considering the synthesis of each channel independently, the method does not provide any a priori information of the MUX response when channels are connected (e.g., cannot independently define the RL at the common port of each channel nor can predict the obtained OoB rejection level) and thus lacks a direct connection between the mathematical description of the multiplexer response to implement and its circuital implementation. It is based on the use of the functions that are known to provide the least loading to adjacent bands and in relying on a post optimization stage on the final MUX response that must try to obtain the better possible response from the one obtained after the synthesis of each filter.

[1]Whereas the first approach involves K phase terms, one per filter, such that at $f_{0,k}$, the central frequency of the k-th filter, the superposition of reflection phases of all other filters compose an open circuit condition, the minimum susceptance network approach directly exploits networks whose reflection phase is as close to zero as possible to naturally impose an open circuit condition. Both approaches are analytical when considering the independent synthesis of each channel but do not provide any analytical information of the entire multiplexer bandwidth.

To face AW multiplexer synthesis from a completely analytical point of view considering the entire multiplexer bandwidth, this thesis proposes a method capable of defining the entire multiplexer response, including loading effects and considering the channel frequency spacing, already at the normalized frequency domain. To this end, the proposed method is capable of computing the characteristic polynomials of the entire multiplexer through an iterative procedure in the form of a multiport function that implements an equiripple return loss response at the common port with all reflection zeros located on the imaginary axis. From it, the method derives a new set of polynomials for each of the channel filters comprising the multiplexer, that are distorted (compared to an equiripple Chebyshev function) when evaluated as a two-port function but in the exact way such that they implement an equiripple response when all the channels are connected together at the star junction. The fact that the channel filter functions need be distorted, for example showing complex-valued reflection zeros, to implement an equiripple return loss in the multiplexer, and that the distortion of a given channel is fixed by the rest of channels composing the multiplexer indicates that only modifying the reflection phase of a set of Chebyshev channels leaving all reflection zeros unaltered, yields a result far from optimal.

In the proposed method, from the distorted channel transfer functions, the synthesis of each ladder filter can be performed separately from the rest by exploiting the known techniques for AW ladder filters in [124, 141]. Such an analytical procedure allows to search among many multiplexer responses (all of them equiripple) for the desired function that accommodates both the technology and response requirements. It must be highlighted that, as opposed to previous works, the multiport function incorporates all the loading effects between channel filters (e.g., the increase in out-of-band rejection and the appearance of additional transmission zeros) what allows a complete evaluation of the multiplexer response at the polynomial level. This complete consideration yields better results than trying to minimize channel interaction by controlling the reflection phase of each channel filter. The proposed method acts as a key step in the design of AW multiplexers since it allows to decompose the multiplexer design challenge into the design of K channel filters that implement the distorted responses computed with the method.

5.3 Framework for Star Junction Multiplexer Synthesis

Before diving into the mathematical framework of the proposed method, it is important to briefly provide a clearer view to the star junction topology of AW multiplexers, to which the method is applied. Fig. 5.2 depicts an schematic view of such MUX configuration, in this case using the standard symbol of AW resonators, depicting a ladder topology in each of the channels. The fact that each channel filter starts in series resonator is not a random choice but an important condition to mention. As it has been extensively covered in Ch. 4, AW ladder filters starting in series or shunt resonator differ in the fact that their reflection phases have opposite behaviours. A series-starting

filter depicts a reflection phase assymptote towards 0° and a shunt-starting filter depicts it towards 180°. Therefore, it is to be expected that the most favorable channel filter topology when aiming to construct a MUX is that all channels start in series resonator such that their reflection phases are already close to behaving as open-circuits in the out-of-band region. This fact was already demonstrated by Silveira when proving that a Chebyshev function whose phase is unaltered (thus able to be implemented as a series-starting AW ladder filter) is a minimum susceptance network. For this reason, the method presented in this chapter is initially developed by assuming that all channels in the MUX are series-starting ladder filters. Nevertheless, this does not imply that no shunt-starting filters can be part of a MUX by using this method. Following the findings described in Ch. 4 for shunt-starting duplexer-oriented filters, having a shunt-starting AW filter whose reflection phase tends to 0° is possible if two reactive elements are used at the input of the filter.

Additionally, the star-junction schematic in Fig. 5.2 depicts the presence of a shunt inductor L_{in} at the common port of the multiplexer, also called the MUX inductor and already observed in many examples in the literature such as [163,176], among others, that in this method is the result of merging the input shunt inductor of each of the channel filters. Accordingly, each channel features its output reactive element required by nature in AW ladder filters[2]. For completeness, notice that this is the simplified reactive model from which the synthesis is derived but at subsequent stages of the multiplexer design where EM effects need to be considered, the star-junction features additional effects. For example, although the miniaturization provided by AW technology leads to very small electrical lengths of traces connecting the ladder filters to the common node, their EM effect should be considered in a complete full-wave simulation of the device.

Having presented the details of the MUX configuration, the first step of any synthesis method is modeling the transfer function to realize in terms of rational polynomial functions. To ease the comparison with the multiplexer formulation, let us recall that the response of an N-th order AW ladder filter (a two-port network) is modeled in the normalized frequency domain $s = \sigma + j\Omega$ with the characteristic polynomials $F(s)$, $P(s)$ and $E(s)$ that define the S-parameters as

$$S_{11}(s) = \frac{F(s)/\varepsilon_r}{E(s)} \qquad S_{21}(s) = \frac{P(s)/\varepsilon}{E(s)} \tag{5.1}$$

where ε and ε_r are normalization constants different than unity. The roots of $F(s)$ correspond to the reflection zeros, the roots of $P(s)$ are the transmission zeros and the roots of $E(s)$ are the poles. Thus, for a fully canonical function, $deg\,(F(s)) = deg\,(P(s)) = deg\,(E(s)) = N$. For a standalone filter, the passband is defined in the $s = [-j, j]$ interval and the polynomials, considering a fully canonical (FC) generalized Chebyshev filter function, are computed following the procedure in Ch. 3 to find $F(s)$ and the alternating pole method in [123] to determine $E(s)$. After synthesis, the s domain is transformed to the bandpass domain via the well-known bilateral transformation function in Ch. 3

[2]As already discussed in Ch. 3 the input and output reactive elements of each AW ladder filter have a fundamental phase role and are present in multiplexers since reflection phase cannot be freely exploited to avoid them.

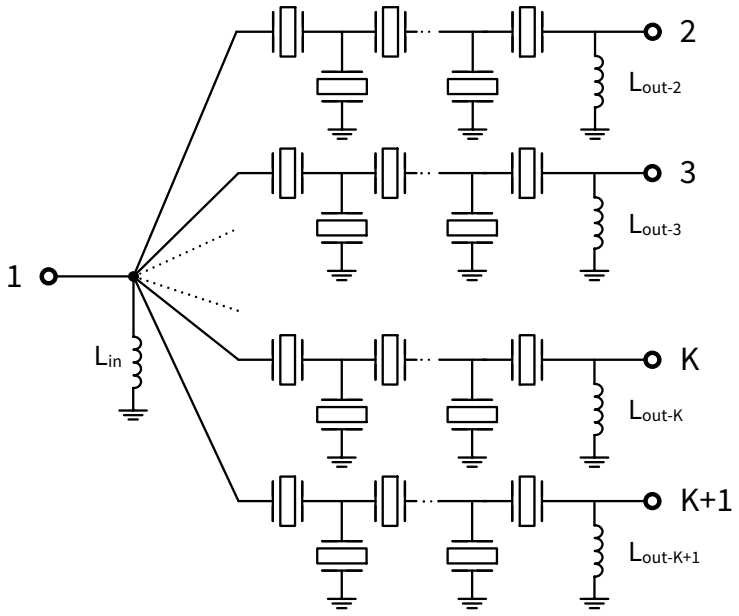

Figure 5.2: Schematic depiction of an AW star junction multiplexer: AW ladder filters connected to an ideal star junction with a multiplexer inductor L_{in}.

considering the filter fractional bandwidth (FBW) and central frequency (f_0) establishing $s = -j$ as the lower corner frequency ($f = f_1$) and $s = j$ as the upper corner ($f = f_2$).

However, the objective of this method is to analytically find the characteristic polynomials in s that define each channel filter such that when connected together they compose an equiripple return loss (RL) response. That is, channels that are defined to be equiripple when subject to the loading of their partner filters but that depict a clearly distorted response when observed as independent two-port functions. As introduced, to find these polynomials it is necessary to compute a polynomial representation of the entire multiplexer itself. That is, a set of characteristic polynomials that model a network of $K + 1$ ports in the s domain.

Let us then consider an ideal star junction, a set of K FC channels and let N_k be the order of the k-th channel[3]. Following the rationale of (5.1), it is clear that the numerator polynomial defining the reflection zeros at the input port of the network (the equivalent of $F(s)$) and the common denominator polynomial (the equivalent of $E(s)$) must be of order $M = \sum_{k=1}^{K} N_k$. Then, following the nomenclature introduced in [168], the S-parameters of a K-channel multiplexer can be defined as

$$S_{11}(s) = \frac{u_0 U(s)}{D(s)} \qquad S_{k1}(s) = \frac{t_k T_k(s)}{D(s)} \tag{5.2}$$

where u_0 is the normalization constant of monic polynomial $U(s)$ whose roots are the reflection zeros at the input port, $T_k(s)$ are the monic transmission polynomials whose roots are the transmission zeros (TZs) of each channel plus the additional TZs that appear due to the loading, t_k is the normal-

[3]As a convention, from this point onward, channels are assigned an index k with respect to their frequency position within the multiplexer in a low to high manner.

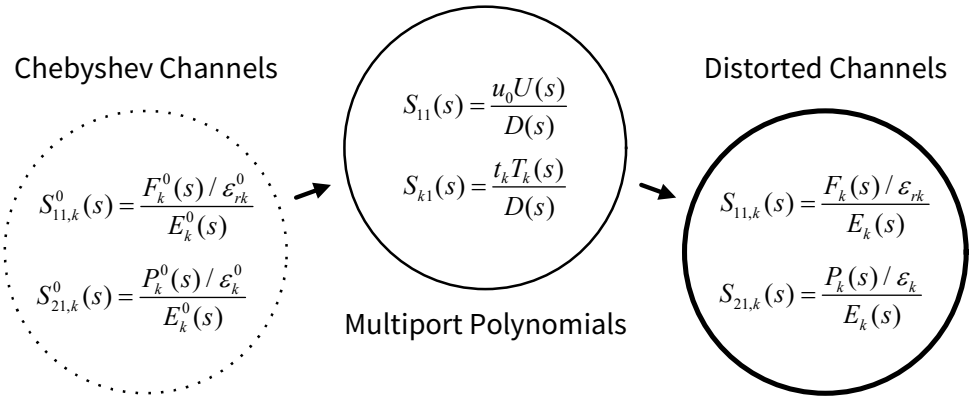

Figure 5.3: Conceptual map of the polynomial computation procedure within the multiplexer synthesis framework. Starting from an ideal Chebyshev seed per channel, a multiport function can be computed to describe an ideal multiplexer response. From the multiport function, a set of distorted channel polynomials can be derived and then synthesized independently. The synthesized channels compose the AW multiplexer response when connected to an ideal star junction.

ization constant of each $T_k(s)$ and $D(s)$ is the common denominator polynomial whose roots are the poles of the multiport network. For a multiplexer composed of fully canonical channels, thus implementing a fully canonical multiport function, $u_0 \neq 1$ and $t_k \neq 1$. Interestingly, although the k-th channel features N_k transmission zeros the order of each $T_k(s)$ polynomial is also M, as is justified in the following section, because it includes additional TZs that appear due to loading effects. It is important to state that the polynomial definition in (5.2) defines K passbands within the original $s = [-j, j]$ interval, each in its respective position such that their equivalence with the bandpass domain is $s = -j \rightarrow f = f_{1-LO}$, where f_{1-LO} is the lower corner frequency of the lowest frequency channel and $s = j \rightarrow f = f_{2-UP}$, where f_{2-UP} is the upper corner frequency of the highest frequency channel.

The key of the proposed method is that if the multiport function defined in (5.2) is known, a set of channel polynomials, following (5.1), can be derived. These new channel functions are the ones to be synthesized and that describe the response of each channel when evaluated as a two-port network. To describe the complete rationale of this chapter, Fig. 5.3 depicts a conceptual map with the complete procedure to compute the distorted channel polynomials. Starting by assuming an ideal fully canonical Chebyshev response at each channel (i.e. $F^0_k(s)$, $E^0_k(s)$, $P^0_k(s)$, ε^0_k, ε^0_{rk}, noted with an upperscript zero) the multiport function is computed through an iterative method. The initial channel polynomials of the k-th channel can be computed given the input parameters N_k, RL_k and Ω_{zk} (the k-th set of transmission zeros in the normalized frequency domain) following the procedure in Ch. 3 and the objective of the iterative method is to find the set of polynomials $D(s)$, $U(s)$ and $T_k(s)$ along with u_0 and t_k that describe an ideal multiport response whose common port RL is equiripple within each channel. From the computed multiport polynomials, a new set of channel polynomials and normalization constants ($F_k(s)$, $E_k(s)$, $P_k(s)$, ε_k and ε_{rk}, now noted without upperscript) can be

derived and independently synthesized.

5.4 Fully Canonical Multiport Polynomials

This section is devoted to the polynomial formulation of the multiport function, the iterative procedure to compute it and the mathematical steps to derive the distorted channel polynomials from it. The proposed formulation builds on the pioneering method in [168] following a similar nomenclature and revisits part of its content to provide a particular formulation for fully canonical channels.

At first, let us justify why the formulation in (5.2) and the proposed polynomial degrees are adequate for a multiport function. At this point, assume that $F_k(s)$, $E_k(s)$, $P_k(s)$, ε_k and ε_{rk}, the distorted channel polynomials of an arbitrary multiplexer with K channels and the related normalization constants are already known. Given the distorted channel functions and considering the star-junction topology in Fig. 5.1a, let us define the input admittance of the multiport network as

$$Y_{\text{in}}(s) = \sum_{k=1}^{K} Y_{\text{in},k}(s) = \sum_{k=1}^{K} \frac{1 - S_{11,k}(s)}{1 + S_{11,k}(s)} \tag{5.3}$$

where $Y_{\text{in},k}(s)$ and $S_{11,k}(s)$ are the input admittance and S_{11} parameter of the k-th channel, respectively.

Considering the relation between S-parameters and characteristic polynomials stated in (5.1), and defining term $f_k = 1/\varepsilon_{rk}$ as the normalization constant of $F_k(s)$ for simplicity [179], the input admittance of each channel can be expanded as

$$Y_{\text{in},k}(s) = \frac{1 - S_{11,k}(s)}{1 + S_{11,k}(s)} = \frac{E_k(s) - f_k F_k(s)}{E_k(s) + f_k F_k(s)} = \frac{1 - f_k}{1 + f_k} \frac{\dfrac{E_k(s) - f_k F_k(s)}{1 - f_k}}{\dfrac{E_k(s) + f_k F_k(s)}{1 + f_k}} = g_k \frac{D_k(s)}{S_k(s)}. \tag{5.4}$$

Where, dropping the s dependence henceforth for simplicity and reserving upper case letters for polynomials and lower case letters for constants, polynomials D_k and S_k along new normalization constant g_k are defined as follows:

$$D_k = \frac{E_k - f_k F_k}{1 - f_k} \tag{5.5}$$

$$S_k = \frac{E_k + f_k F_k}{1 + f_k} \tag{5.6}$$

$$g_k = \frac{1 - f_k}{1 + f_k} \tag{5.7}$$

Notice that due to the fully canonical nature of each channel, all $f_k \neq 1$ and that polynomials D_k and S_k are both monic and of degree N_k since E_k and F_k are both monic and of degree N_k.

By bringing (5.5), (5.6) and (5.7) into (5.3) and expanding the sum to find a common denominator, the overall input admittance of the multiplexer, Y_{in}, is

$$Y_{\text{in}} = \sum_{k=1}^{K} Y_{\text{in},k} = \sum_{k=1}^{K} g_k \frac{D_k}{S_k} = \frac{\sum_{k=1}^{K} g_k D_k \prod_{i=1,i\neq k}^{K} S_i}{\prod_{k=1}^{K} S_k} \tag{5.8}$$

providing an expression linking a network of K ports with the characteristic polyomials of each channel filter composing it. Notice the fact the numerator term is the sum of K terms, one per filter, each of which results from the multiplication of polynomial D_k and polynomials S_i, indicating how this formulation incorporates information of how one channel is affected by the rest of channel filters.

Joining (5.8) with the definition of S_{11} from Y_{in}, the channel polynomials are then related to the multiport polynomials defining the common port S_{11} in (5.2):

$$S_{11} = \frac{1 - Y_{\text{in}}}{1 + Y_{\text{in}}} = \frac{1 - \sum_{k=1}^{K} g_k \frac{D_k}{S_k}}{1 + \sum_{k=1}^{K} g_k \frac{D_k}{S_k}} = \frac{\prod_{k=1}^{K} S_k - \sum_{k=1}^{K} g_k D_k \prod_{i=1,i\neq k}^{K} S_i}{\prod_{k=1}^{K} S_k + \sum_{k=1}^{K} g_k D_k \prod_{i=1,i\neq k}^{K} S_i} = \frac{u_0 U(s)}{D(s)} \tag{5.9}$$

The normalization constant u_0 of the common port S_{11} is related to all terms in (5.9) since D_k and S_k are both of the same degree and is defined as follows:

$$u_0 = \frac{1 - \sum_{k=1}^{K} g_k}{1 + \sum_{k=1}^{K} g_k} \tag{5.10}$$

Up to this point, evaluating the star-junction configuration assuming that the distorted channels are known has provided two expressions that can be directly related to polynomials $U(s)$ and $D(s)$ (the numerator and denominator of (5.9)) and so, the common port return loss is obtained as a relation between all F_k and E_k polynomials in the multiplexer. Going back to (5.2), applying the same reasoning but now on the transmission term, i.e., S_{k1}, yields

$$S_{k1} = \frac{t_k T_k(s)}{D(s)} = \frac{S_{21,k}(1 + Y_{\text{in},k})}{1 + Y_{\text{in}}} = \frac{\frac{p_k P_k}{E_k}(1 + Y_{\text{in},k})}{1 + Y_{\text{in}}} \tag{5.11}$$

where term p_k is the normalization constant of $P_k(s)$ defined as $p_k = 1/\varepsilon_k$.

Substituting (5.8), (5.4) and (5.9) into (5.11):

$$\begin{aligned} S_{k1} &= \frac{\frac{p_k P_k}{E_k}\left(1 + g_k \frac{D_k}{S_k}\right)\prod_{k=1}^{K} S_k}{\prod_{k=1}^{K} S_k + \sum_{k=1}^{K} g_k D_k \prod_{i=1,i\neq k}^{K} S_i} = \frac{p_k P_k \left(\frac{S_k + g_k D_k}{E_k S_k}\right)\prod_{k=1}^{K} S_k}{D(s)} \\ &= \frac{p_k P_k \left(\frac{S_k + g_k D_k}{E_k}\right)\prod_{i=1,i\neq k}^{K} S_i}{D(s)} \end{aligned} \tag{5.12}$$

Therefore, transmission polynomials $T_k(s)$ and their respective normalization constants t_k can be related to the distorted channel polynomials as follows:

$$T_k = P_k \prod_{i=1, i\neq k}^{K} S_i \tag{5.13}$$

$$t_k = p_k \frac{1+g_k}{1+\sum_{k=1}^{K} g_k} \tag{5.14}$$

The expressions above are a very interesting result that confirms that transmission polynomial $T_k(s)$ is also of order M and depicts N_k zeros that come from the original transmission zeros of $P_k(s)$ and additional $M - N_k$ zeros that are due to the reactive loading between the filters of the multiplexer. Therefore, notice that a multiport function contains, already in the normalized frequency domain, the complete representation of the multiplexer. To exemplify the appearance of these extra TZs, observe that the response of the duplexer presented in [180] or in the example in Ch. 4 in this thesis depicts extra zeros when the two filters are connected at the common port.

Observation of the obtained expressions allows to highlight an interesting characteristic of the distorted polynomials. Since the objective is to compute a multiport function whose common port return loss is equiripple and similar to a generalized Chebyshev response, all reflection zeros of the multiplexer common port (i.e., the roots of $U(s)$) must lie on the imaginary axis of s, what implies that all coefficients of $U(s)$ must be real. From such observation and inspecting the denominator of (5.9) it can be inferred that the coefficients of polynomials F_k composing the equiripple multiplexer will be complex and thus their roots will be on the complex plane. Thus, implementing a distorted response when evaluated as a two-port network.

5.4.1 Iterative Procedure

The formulation presented in the prior paragraphs demonstrates the soundness of defining a multiport response using (5.2) by assuming the distorted channel polynomials $f_k F_k(s)$, $E_k(s)$, $p_k P_k(s)$ are known. However, as outlined in the diagram in Fig. 5.3, the objective it to derive the channel polynomials from a known multiport function. Thus, the objective now is computing the multiport polynomials $D(s)$, $U(s)$ and $T_k(s)$ that implement our desired multiplexer response: as introduced above, a common port return loss that is as equiripple as possible within the passband of each channel to obtain the highest OoB rejection and best passband ripple. In contrast with two-port generalized Chebyshev functions for which there is a closed solution for a given set of TZs and return loss [9,121] as has been discussed in Ch. 3, there is no exact solution (as noted in [179]) to find the roots of $U(s)$ for a set of multiplexer TZs such that the response is perfectly equiripple. To overcome this, an iterative method is proposed starting by computing a set of ideal generalized Chebyshev polynomials for each channel. As demonstrated in this work, the result is very close to being perfectly equiripple.

Let us consider K independent channel polynomials that are ideal fully canonical Chebyshev functions, namely $f_k^0 F_k^0(s), E_k^0(s), p_k^0 P_k^0(s)$, for the k-th channel. By computing these initial ideal functions, the set of transmission zeros and the desired return loss of each of the channels, have already been set. However, since the multiport polynomials define K passbands within the $s = [-j, j]$ range, the starting channel polynomials need to be linearly mapped to their respective position within that frequency range considering each channel fractional bandwidth and central frequency, $f_{0,k}$. Since K functions must be placed inside a general $s = [-j, j]$ range, each function must be compressed and displaced. This can be easily achieved by solving an equation (5.15) relating s, the normalized frequency variable of the multiplexer, and s', the normalized frequency variable of each ideal channel function, by using the relative position of each channel within the $s = [-j, j]$ range. Knowing the compression and displacement factors a and b, the roots of polynomials F_k^0, E_k^0 and P_k^0 can be mapped.

$$s = as' - b \tag{5.15}$$

Having the starting polynomials, the solution to achieve a practically equiripple result is assuming that the M roots of $U(s)$ are the roots of all $F_k^0(s)$ polynomials, namely $\{zF_k^0\}$ [168]. With this decision, $U(s)$ can be uniquely defined and the iterative method can start.

$$U(s) = \prod_{k=1}^{K} \left(\prod_{i=1}^{N_k} (s - zF_{k,i}^0) \right) \tag{5.16}$$

Knowing $U(s)$ and having $f_k^0 F_k^0(s)$, $E_k^0(s)$ and $p_k^0 P_k^0(s)$, let us compute a first estimate of monic polynomial $S^0(s)$, the product of all $S_k^0(s)$ polynomials, as:

$$S^0(s) = \prod_{k=1}^{K} S_k^0 = \prod_{k=1}^{K} \frac{E_k^0(s) + f_k^0 F_k^0(s)}{1 + f_k^0} \tag{5.17}$$

Sub-polynomials $S_k^0(s)$ can be obtained by computing the roots of $S^0(s)$ and sorting the roots in ascending imaginary part (i.e., in ascending normalized frequency): the first N_1 roots build $S_1^0(s)$, the following N_2 roots correspond to $S_2^0(s)$ and so on. Having all $S_k(s)$, the first iteration of monic polynomial $T_k^0(s)$ can be computed with (5.13) since the roots of $P_k(s)$ are the same of $P_k^0(s)$. This latter assumption is clear since reactive loading between channels in a multiplexer does not alter the position of the intrinsic TZs of each channel filter.

At this point, constants u_0^0 and t_k^0 and common denominator polynomial $D^0(s)$ remain unknown in this first iteration. Notice that u_0^0 and t_k^0 are responsible for setting the desired return loss value at the passband edges of each filter (let them be Ω_{ck}) and therefore, an equation regarding the modulus of $S_{11}(s)$ at the band edges can be obtained by imposing the desired RL.

$$|S_{11}(j\Omega_{ck})|^2 = \frac{(u_0^0)^2 \, |U(j\Omega_{ck})|^2}{|D^0(j\Omega_{ck})|^2} = 10^{\frac{-RL_k}{10}} \tag{5.18}$$

However, since $D^0(s)$ is not known yet, one can resort to Feldtkeller's equation regarding unitarity of S-parameters (avoiding the 0-th superscripts for formulation simplification):

$$D(s)^2 = u_0^2 U(s)U^*(-s) + \sum_{k=1}^{K} t_k^2 T_k(s)T_k^*(-s) \tag{5.19}$$

Substituting (5.19) into (5.18), after setting ratios $r_k^0 = t_k^0/u_0^0$ as the unknowns and applying some manipulation, the following equation can be derived.

$$\sum_{k=1}^{K} \left(r_k^0\right)^2 \left|T_k^0(j\Omega_{ck})\right|^2 = \left(10^{\frac{RL_k}{10}} - 1\right) \left|U(j\Omega_{ck})\right|^2 \tag{5.20}$$

Since K ratios are unknown, only K edge frequencies are required to evaluate (5.20). As recommended in [168], Ω_{ck} is selected as the lower edge frequency for the first $\lceil K/2 \rceil$ channels and the upper edge frequency is selected for the remaining channels.

From (5.20), a linear system of equations can be constructed as

$$\mathbf{r} = \mathbf{A}^{-1} \cdot \mathbf{b} \tag{5.21}$$

where $\mathbf{r}$ is a k x 1 array, $\mathbf{A}$ is a k x q matrix and $\mathbf{b}$ is a q x 1 array whose elements are

$$r_k = \left(\frac{t_k^0}{u_0^0}\right)^2 \tag{5.22}$$

$$A_{kq} = \left|T_q^0(j\Omega_{ck})\right|^2 \tag{5.23}$$

$$b_q = \left(10^{\frac{RL_q}{10}} - 1\right) \left|U(j\Omega_{cq})\right|^2 \tag{5.24}$$

being $k, q = 1, ..., K$.

Having ratios $(r_k^0)^2$, notice that (5.19) can be revisited, yielding

$$\left(\frac{D(s)}{u_0^0}\right)^2 = U(s)U^*(-s) + \sum_{k=1}^{K} \left(r_k^0\right)^2 T_k(s)T_k^*(-s) \tag{5.25}$$

what in turn allows to obtain $D(s)$. Notice that the roots of $D(s)^2$ and $D(s)^2/u_0^2$ are the same and thus, to find $D^0(s)$ one can compute the right hand side of (5.25), find its roots ($2M$ roots since it is a polynomial of double degree) and then reconstruct $D^0(s)$ by taking only those roots whose real part lies in the left-half plane of s (Hurwitz stability criterion).

Root factorization of polynomial $D(s)^2$ can directly be obtained by using general methods such as the *roots* command in Matlab that computes the eigenvalues of the Frobenius companion matrix of the polynomial. However, such approach is known to be ill-conditioned and therefore suffers of numerical instabilities for high order polynomials due to the finite numerical accuracy of double

precision arithmetics. In this thesis, the recommendation is to use *cepstral* analysis tools to compute $D(s)$ and extend the numerical stability of the method by avoiding the factorization of $2M$-degree polynomials for multiplexers of total order M. Since a complete section of this chapter (namely Sec. 5.5) is devoted to the use of the *cepstrum* method as applied to Feldtkeller's equation as proposed in [181, 182], a deeper discussion of the detailed *cepstrum* method is not provided here and it is assumed that $D(s)$ has been accurately computed via (5.25).

Knowing monic polynomial $D(s)$, the only remaining step is to split ratios $(r_k^0)^2$ into u_0^0 and t_k^0 separately. To do so, a linear system of equations can be found by imposing unitarity of S-parameters,

$$\left|S_{11}^0(s)\right|^2 + \sum_{k=1}^{K} \left|S_{k1}^0(s)\right|^2 = 1 \tag{5.26}$$

noticing that by solving the system in (5.23) and (5.24), a desired return loss value has been imposed at a set of corner frequencies Ω_{ck}. Thus,

$$\left|S_{11}^0(j\Omega_{ck})\right|^2 = 10^{\frac{-RL_k}{10}} \tag{5.27}$$

what combined with (5.26) and the definition of S_{k1} in (5.11), yields

$$\sum_{k=1}^{K} \left|S_{k1}^0(s)\right|^2 = \sum_{k=1}^{K} \left|\frac{t_k^0 T_k^0(s)}{D^0(s)}\right|^2 = 1 - 10^{\frac{-RL_k}{10}} \tag{5.28}$$

what allows to find constants t_k^0.

The system of equations is defined as

$$\mathbf{t} = \mathbf{J}^{-1} \cdot \mathbf{w} \tag{5.29}$$

where $\mathbf{t}$ is a k x 1 array, $\mathbf{J}$ is a k x q matrix and $\mathbf{w}$ is a q x 1 array whose elements are

$$t_k = \left(t_k^0\right)^2 \tag{5.30}$$

$$J_{kq} = \left|\frac{T_q(j\Omega_{ck})}{D(j\Omega_{ck})}\right|^2 \tag{5.31}$$

$$w_q = \left(1 - 10^{\frac{-RL_q}{10}}\right) \tag{5.32}$$

being $k, q = 1, ..., K$.

Clearly, coefficient u_0^0 can now be obtained from any combination of t_k^0 and its related ratio r_k^0 isolating u_0^0 from (5.22).

Following all the previous steps, up to this point the procedure has found the 0-th iteration of the multiport polynomials and their related normalization constants. Then, notice again an interesting relation in (5.9): the numerator and the denominator of the expression directly relate to $U(s)$ and

$D(s)$, respectively. Since the 0-th iteration of these two polynomials is known, notice that by summing numerator and denominator of (5.9) and considering the leading coefficient u_0 in (5.10), the following expression is obtained:

$$D(s) + u_0 U(s) = 2S(s) \tag{5.33}$$

What leads to the computation of a new version of polynomial $S(s)$. Notice that since the multiport polynomials at their 0-th iteration have been obtained by assuming an initial $S^0(s)$ polynomial using a set of ideal Chebyshev channel functions and then multiple conditions have been imposed to derive the rest, the $S(s)$ polynomial obtained via (5.33) differs from the initial guess $S^0(s)$. Therefore, let it be $S^m(s)$ and so, let us derive again a new set of sub-polynomials $S_k(s)$, under superscript m, by sorting the roots of $S^m(s)$ in ascending order and applying the same procedure presented to compute a new iteration of the multiport polynomials, i.e. u_0^m, t_k^m, $T_k^m(s)$ and $D^m(s)$. Notice that numerator polynomial $U(s)$ is not altered throughout the procedure as has been uniquely defined in (5.16). Based on such assumption, a refined version of the multiport polynomials that implement an equiripple return loss with reflection zeros at the position of the zeros introduced in $U(s)$ is obtained at each iteration of the presented procedure. At the end, the proposed iterative procedure is halted by comparing the evolution of the roots of $S^m(s)$ with respect to $S^{m-1}(s)$ once they reach a predefined degree of convergence. For the purpose of this thesis, let such convergence be 10^{-3}. As a summary of the entire iterative process to compute the multiport function, Fig. 5.4 depicts the flowchart of the procedure.

5.4.2 Derivation of the Distorted Channel Polynomials

Referring back to the conceptual map in Fig. 5.3, the transition between the first and second parts of this multiplexer synthesis method has been described in detail in section 5.4.1. Starting from an ideal Chebyshev function for each channel, a complete multiport function of the multiplexer has been computed and is now in its polynomial form. As described at the beginning of this chapter, the rationale behind computing the multiport function is being able to derive a new set of channel polynomials that already incorporate the inter-channel loading information (i.e., a deliberate distortion) so that each channel filter can be independently synthesized with the network synthesis techniques already presented in this thesis. Therefore, at this point, given the computed u_0, $U(s)$, t_k, $T_k(s)$ and $D(s)$, the objective is to separate the multiport response into the distorted channel polynomials that compose it.

Let us trace back to expression (5.4) that relates the k-th distorted channel polynomials $E_k(s)$ and $F_k(s)$ with sub-polynomials $D_k(s)$ and $S_k(s)$. Notice that $S(s)$ is known as an output of the iterative procedure to find the multiport function and thus can be split into the $S_k(s)$ sub-polynomials by sorting its roots in ascending imaginary part as done throughout all iterations. Therefore, the two unknowns to find a relation between the distorted channel polynomials are constants g_k (related to

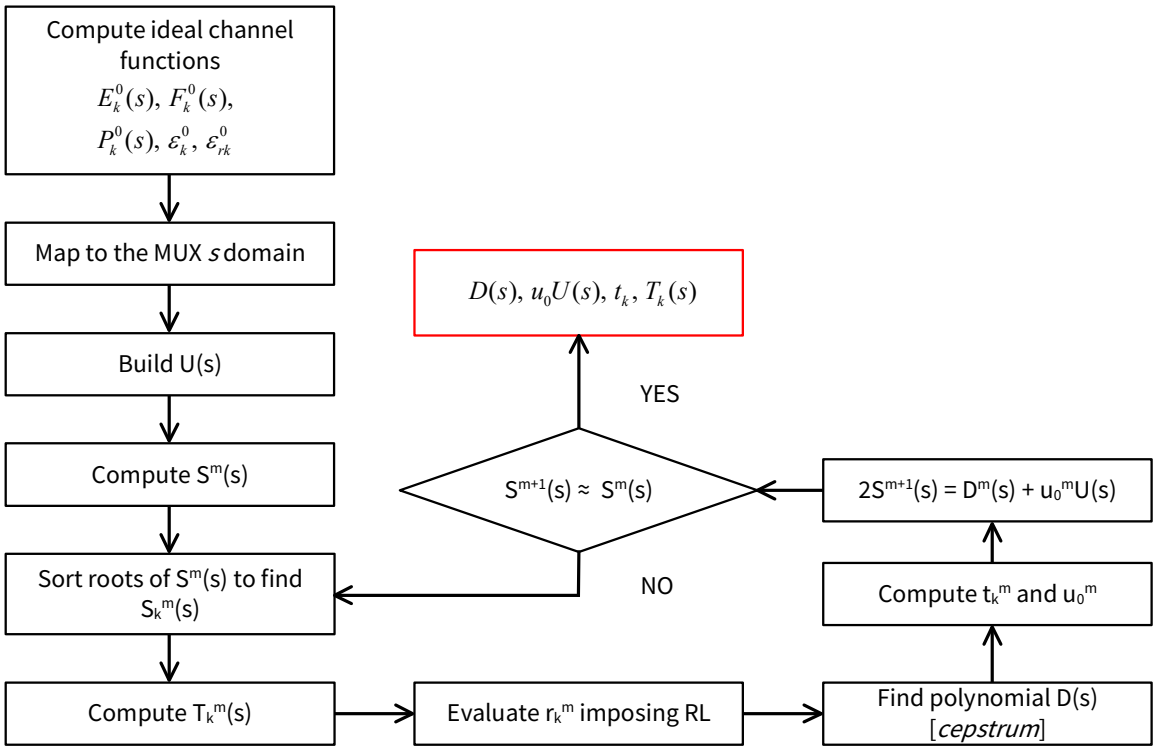

Figure 5.4: Flowchart of the iterative procedure to compute the fully canonical multiport function starting from ideal Chebyshev functions per channel.

the normalization constant f_k in (5.7)) and sub-polynomials $D_k(s)$.

At first, let us focus on the derivation of constants f_k. At this point, constant u_0 is known and is ultimately composed by all g_k terms in (5.10). At the same time, notice that constant t_k is also related both to the g_k terms and to the unknown normalization constants p_k of polynomials $P_k(s)$ in (5.14). To find the unknowns it is useful to consider that the distorted channel polynomials describe a two-port network and so, conditions regarding the unitarity of S-parameters for lossless two-port networks can be used. Resorting to an expression already presented in Ch. 3, the normalization constants of $P_k(s)$ and $F_k(s)$ can be related as:

$$\varepsilon_{rk} = \frac{\varepsilon_k}{\sqrt{\varepsilon_k^2 - 1}} \tag{5.34}$$

resorting to $f_k = 1/\varepsilon_{rk}$ to ease formulation, one can easily derive the following expression:

$$p_k = \sqrt{-f_k^2 + 1} \tag{5.35}$$

Substituting (5.35) into (5.14), the following expression is obtained:

$$t_k = \sqrt{-f_k^2 + 1}\frac{1 + g_k}{1 + \sum_{k=1}^{K} g_k} \tag{5.36}$$

Taking into account that g_k is related to f_k in (5.7) and that the summation term can be related to u_0 from (5.10) as

$$\sum_{k=1}^{K} g_k = \frac{1-u_0}{1+u_0} \tag{5.37}$$

expression (5.36) has f_k as its single unknown and has the following solution:

$$f_k = \frac{\left(t_k\left(1+\sum_{k=1}^{K} g_k\right)\right)^2 - 4}{-\left(t_k\left(1+\sum_{k=1}^{K} g_k\right)\right)^2 - 4} \tag{5.38}$$

Once all f_k are known, all p_k terms can be obtained by simply applying the relation in (5.35).

At this point, notice that all g_k terms are already known (from f_k and (5.7)) along all $S_k(s)$ sub-polynomials. Therefore, the objective is finding sub-polynomials $D_k(s)$ to retrieve the channel polynomials from (5.4). From its definition in (5.5), $D_k(s)$ is a monic polynomial of degree N_k and thus, from its N_k+1 coefficients, only N_k are unknown. To find them, one can resort to finding N_k points at which the value of $D_k(s)$ is known to enable polynomial interpolation.

To this end, let us take the monic polynomial $D_k(s)$ and define, for the k-th channel,

$$D'_k(s) = D_k(s) - s^{N_k}. \tag{5.39}$$

In order to find N_k points in which to evaluate $D'_k(s)$ consider that (5.9) defines $D(s)$ as follows:

$$D(s) = \prod_{k=1}^{K} S_k(s) + \sum_{k=1}^{K} g_k D_k(s) \prod_{i=1, i\neq k}^{K} S_i(s) \tag{5.40}$$

Notice that knowing $S_k(s)$, the N_k roots of $S_k(s)$ (let them be called zS_k) are known and that evaluating (5.40) at zS_k would yield

$$D(zS_k) = \frac{g_k}{1+\sum_{k=1}^{K} g_k}\left(\left(D'_k(zS_k) + zS_k^{N_k}\right)\prod_{i=1, i\neq k}^{K} S_i(zS_k)\right) \tag{5.41}$$

where the denominator of the leading normalization term is the denominator of u_0 in (5.10), needed here since $D(s)$ has been defined monic and u_0 contains both the numerator and denominator leading coefficients.

From (5.41), notice that the value of $D'_k(s)$ at zS_k can be formulated as

$$D'_k(zS_k) = \frac{D(zS_k)}{\frac{g_k}{1+\sum_{k=1}^{K} g_k}\prod_{i=1, i\neq k}^{K} S_i(zS_k)} - zS_k^{N_k} \tag{5.42}$$

therefore, allowing to construct a linear system of N_k equations with the matrix form

$$\mathbf{d'_k} = \mathbf{V_k^{-1}} \cdot \mathbf{h_k} \tag{5.43}$$

where $\mathbf{d'_k}$ is an N_k x 1 array containing the N_k unknown coefficients of $D'_k(s)$, namely

$$d'_l = d_{N_k - l} \tag{5.44}$$

and $\mathbf{h_k}$ is an N_k x 1 array whose elements are the evaluation of $D'_k(s)$ at the l-th root of the set zS_k using (5.42)

$$h_l = D'_k(zS_{k,l}) \tag{5.45}$$

for $l = 1, ..., N_k$.

Interestingly, the N_k x N_k $\mathbf{V_k}$ matrix is a Vandermonde matrix, a well-known matrix used in polynomial interpolation [183], defined as

$$V_{lm} = \left(zS_{k,l}\right)^{N_k - m} \tag{5.46}$$

for $m, l = 1, ..., N_k$.

At this point, solving the proposed system of equations for $\mathbf{d'_k}$ and appending to it a unitary leading coefficient uniquely defines the monic polynomial $D_k(s)$. Then, considering (5.5) and (5.6), the expression of polynomials $E_k(s)$ and $F_k(s)$ is obtained by summing and subtracting $S_k(s)$ and $D_k(s)$ from each other as

$$\begin{aligned} E_k(s) &= \frac{(1 + f_k)\, S_k(s) + (1 - f_k)\, D_k(s)}{2} \\ F_k(s) &= \frac{(1 + f_k)\, S_k(s) - (1 - f_k)\, D_k(s)}{2 f_k} \end{aligned} \tag{5.47}$$

what allows to compute the distorted polynomials of channel k. As stated at the beginning of this section, polynomial $P_k(s)$ is already known to implement the same roots as $P_k^0(s)$ and its normalization constant p_k has already been found through (5.35).

As indicated by the subscript k along subsection 5.4.2, this procedure must be computed for each of the channels in the multiplexer. Once the polynomials of each channel are computed, the synthesis of each prototype filter is performed separately, either through the well-known method in [124] based on element extraction from the input admittance, the ABCD matrix method presented in Ch. 3 or through the method based on coupling matrix rotations in [139,141]. After obtaining the lowpass prototype of each channel filter the synthesized elements must be de-normalized in terms of impedance and frequency to obtain the circuital parameters of each filter in terms of BVD models.

As is covered in the synthesis examples in this chapter, it is worth mentioning that the obtained channel polynomials define a two-port filter function in which the roots of polynomial $F_k(s)$ are not purely imaginary anymore, as happens for an equiripple Chebyshev function, but lie on the complex

plane. This displacement of $F_k(s)$ roots into the complex plane is the manifestation of the loading between channels of the multiplexer. Additionally, it must be noted that an acoustic wave ladder filter can perfectly implement a transfer function with complex roots of $F_k(s)$.

5.5 Cepstral Analysis of Feldtkeller's Equation

A key step in the iterative procedure presented in Section 5.4 is the computation of polynomial $D(s)$ from the already known polynomials $T_k(s)$ and ratios $r_k = t_k/u_0$. As stated through (5.19), such computation is possible by applying Feldtkeller's equation, a consequence of applying the unitarity of S-parameters to the characteristic polynomials of a lossless transfer function, and computing $D^2(s)$, a polynomial of double-degree. Such a polynomial can be factorized into its roots and by applying the Hurwitz stability criterion, that is, taking the roots on the left-hand side of the complex plane, stable polynomial $D(s)$ is uniquely defined. However, this procedure entails limitations related to the fact that the method deals with multiplexers. As stated at the beginning of the formulation, multiport functions entail dealing with polynomials of degree M, the sum of the order of each channel filter composing the MUX. Therefore, computing the roots of a polynomial of degree $2M$ becomes a challenge by itself.

It has already been briefly introduced that the most common way to compute the roots of a polynomial is computing the eigenvalues of a matrix whose characteristic polynomial is the monic polynomial to factor. A straightforward way to find a matrix with a desired characteristic polynomial is the so-called Frobenius companion matrix and the most common method to find its eigenvalues is the computing its Cholesky decomposition. However, since the companion matrix is a sparse matrix by nature, its decomposition is an ill-conditioned problem. Moreover, consider that the multiport function problem imposes that all roots of $D(s)$ are within the unit circle of the s-plane and diposed close to the $j\omega$ axis. Thus, as the order of the multiplexer increases, roots cluster even further and the more clustered roots are, the more significant digits are required to factor the roots of $D(s)$ appropriately.

The exposed facts lead to the presented multiport synthesis method only being numerically stable up to a total multiplexer order of $M = 18$ if resorting to the computation of the roots of $D^2(s)$. This maximum degree is even lower than that demonstrated by Macchiarella and Tammiazzo in [168] due to the channels being fully canonical, what adds a degree of asymmetry with respect to the center of the band into the reflection roots of each channel filter (as compared with the all-pole functions used in most cases in the cited reference) what in turn leads to more digits being necessary to correctly compute all roots of $D(s)$.

However, an acoustic wave multiplexer is commonly composed of high-order filters (7-th or higher) to achieve high rejection levels and thus, it is necessary to find a way to extend the numerical

stability of the proposed method. To do so, this section covers the application of *cepstral* analysis, a mathematical tool commonly applied in digital signal processing of echoes in voice processing and radar [184–186], to the use of Feldtkeller's equation as was proposed in [181,182]. This method, also called the *cepstrum* method is discussed in detail here since some steps are missing in the original contributions by Oldoni and Macchiarella and require a careful derivation.

To justify the application of *cepstral* analysis to the computation of multiport functions consider (5.25) and notice that after finding ratios r_k one could compute the module or magnitude of polynomial $D(s)$ over u_0 (i.e., $|D(s)/u_0|$). At the same time, since $D(s)$ is the common denominator polynomial of the multiport function, it is already known that it is a stable polynomial. Therefore, it is only the imaginary part of $D(s)$ that is actually unknown.

Let us introduce the complex cepstrum $\tilde{\mathbf{h}}$ of a sequence $\mathbf{x}$ as the inverse Fourier transform (IFT) of the natural logarithm of the spectrum of the sequence or, equivalently if the sequence is stable and causal (that is, has all its singularities within the unit circle of z), the inverse Z-transform of the logarithm of the Z-transform of the sequence.

$$\tilde{h}[n] = \mathcal{F}^{-1}\left\{\ln\left(\mathcal{F}\left\{x[n]\right\}\right)\right\} \tag{5.48}$$

The equivalence of this expression with its Z-transform version can be demonstrated by analyzing the aspect of $H(z)$, the Z-transform of a sequence, as having a numerator composed of a product of terms (zeros) in the form $(1-q_m z^{-1})$ and a denominator composed of a product of poles in the form $(1-p_n z^{-1})$. By taking the logarithm of such division the expression turns into the subtraction of two summations of terms of the form $\ln(1/(1-q_m z^{-1}))$. By considering the McLaurin expasion of each of these terms and considering all poles and roots lie inside the unit circle (because the sequence is stable and causal) the resulting expression is the definition of the inverse Z-transform what in turn is equivalent to the inverse Fourier transform since the region of convergence of the sequence includes the unit circle. From this, it can also be concluded that the complex cepstrum is purely stable if the sequence is stable, causal and finite.

Now, consider the case of taking the logarithm of the magnitude of the spectrum, what in fact is equivalent to taking only the real part of the complex logarithm. This is the definition of the real cepstrum

$$\tilde{h}_r[n] = \mathcal{F}^{-1}\left\{\ln\left(\left|\mathcal{F}\left\{x[n]\right\}\right|\right)\right\} \tag{5.49}$$

and, as demonstrated by Oppenheim and Schafer [184], is anticausal by nature and is the even part of the complex cepstrum.

$$\tilde{h}_r[n] = \frac{\tilde{h}[n] + \tilde{h}[-n]}{2} \tag{5.50}$$

Therefore, if one computes the real cepstrum of a stable sequence and removes its anticausal part, that is, padding with zeros the second half of the computed cepstrum (i.e., what would correspond to the negative frequencies of a Fourier transform), the complex cepstrum of the stable part of the

sequence is obtained. Notice here that the complex cepstrum $\tilde{h}$ includes both the magnitude and the phase information of the sequence and thus, it becomes a method to retrieve the phase information of a sequence when only its magnitude part is known.

Having the complex cepstrum, it is simple to direct back to the spectrum $X[n]$ of the original sequence by simply computing

$$X[n] = e^{\mathcal{F}(\tilde{h}[n])} \tag{5.51}$$

where e is used because the complex cepstrum has been defined through the natural logarithm (5.48).

Note that at this point $X[n]$ is the spectrum (including phase information) of a sequence from which the phase information was originally unknown. The objective then is to recover the coefficients of a polynomial, let us call it $D(z)$ for convenience, whose spectrum is $X[n]$ when it is evaluated along the unit circle of z (i.e., $z = e^{j\Omega}$).

Here, it is important to recall the definition of a root of unity as any number z for which $z^n = 1$ holds. When on the z domain, notice that evaluating a polynomial on variable z along the roots of unity is equivalent to computing its Fourier transform, or, in terms of a sequence, its Discrete Fourier Transform (DFT). Then, if one has the DFT of a sequence and the objective is to compute the polynomial that originated such DFT, the properties of the roots of unity allow to compute it in an efficient way and allow to demonstrate that by computing the DFT of the spectrum, since such spectrum is an evaluation of a polynomial along the roots of unity, the coefficients of the original polynomial are recovered.

After the brief mathematical justification of why *cepstral* analysis can be exploited to completely recover a polynomial from which the magnitude is known, let us present the *cepstrum* application to Feldtkeller's equation, as summarized in the flowchart in Fig. 5.5.

Starting from (5.25) the first step is to map polynomials $U(s)$ and $T_k(s)$ into the z-domain using the bilinear transform:

$$z = \frac{1+s}{1-s} \tag{5.52}$$

To keep polynomial $U(s)$ monic along the computation, ratio r_k is directly merged under constant tz_k in the z-domain.

Once polynomials $U(z)$ and $tz_k T_k(z)$ are known, the z-domain version of (5.25) can be evaluated along K points (take a power of 2 for maximum efficiency of the FFT algorithm, e.g., 2^{15}) $z = e^{j2\pi k/K}$ to obtain a sequence $\mathbf{y}$ of K samples corresponding to the DFT of $|D(z)/u_0|$. Then, compute the real cepstrum $\mathbf{h_r}$ by taking the inverse Fourier transform of the logarithm of $\mathbf{y}$ and impose causality to obtain the complex cepstrum $\mathbf{h}$ by setting the second half of the K samples of $\mathbf{h_r}$ to zero and multiplying the remaining samples by 2 to conserve the total energy of the sequence. Having the causal complex spectrum, return to the spectrum (now of $D(z)/u_0$) by applying (5.51).

From the computed spectrum, the coefficients of polynomial $D(z)/u_0$ can be recovered by com-

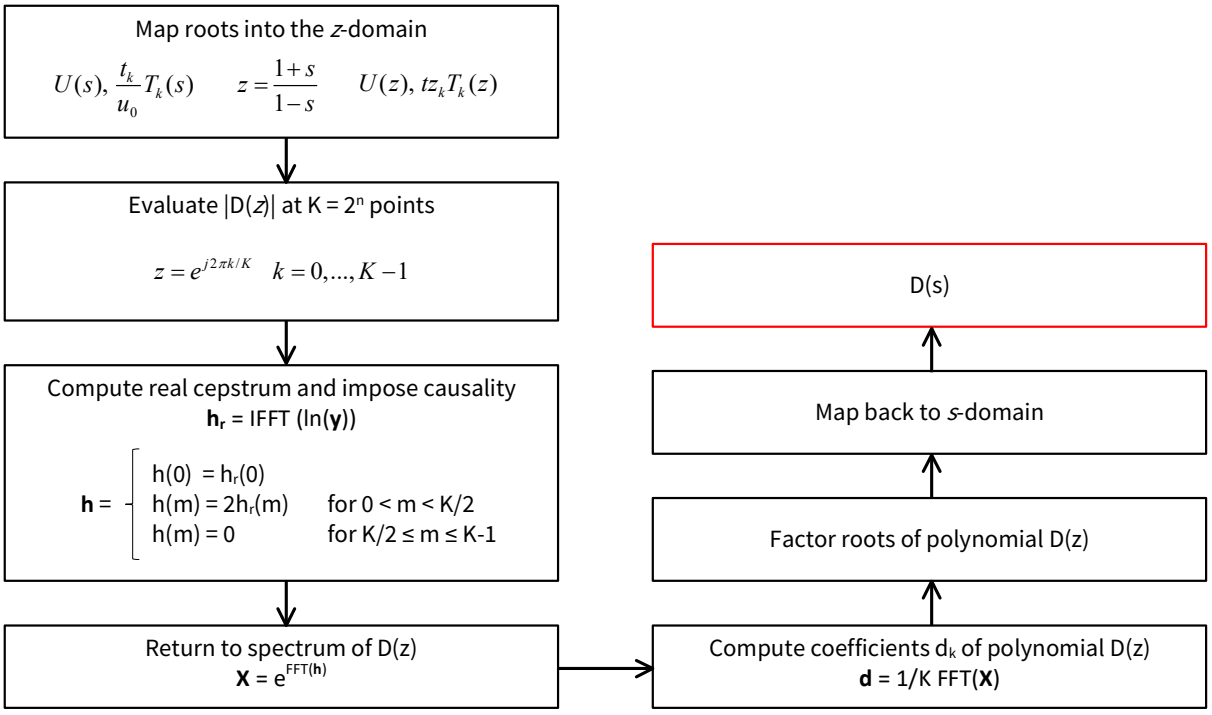

Figure 5.5: Flowchart of the *cepstrum* procedure to compute polynomial $D(s)$ without resorting to factorization of a double-degree polynomial.

puting the DFT of that spectrum and dividing by the amount of samples K of the sequence. The result of such operation is a K-sample sequence where all positions except the last and the $N-1$ first samples are zero. From the non-zero samples, the last corresponds to the leading coefficient of $D(z)/u_0$ and the remaining $N-1$ are the rest of coefficients in descending order. Having these coefficients the only remaining step is computing the M roots of polynomial $D(z)/u_0$ and map them back to the s-domain through the bilinear transformation in (5.52). At this point, monic polynomial $D(s)$ can be obtained from its set of roots.

This application of cepstrum analysis to the specific case of Feldtkeller's equation effectively allows to compute the roots M of polynomial $D(s)$ without having to compute $2M$ roots of a double-degree polynomial and thus extends the numerical stability of the multiplexer synthesis proposed in this thesis to a total order of $M = 35$.

5.6 Synthesis Examples

After presenting the mathematical formulation of the proposed multiplexer synthesis method, this section provides synthesized examples as a demonstration and as a vehicle to highlight interesting aspects of the attained solutions. At first, a synthesized quadplexer (i.e., four channels) is presented providing a detailed description of each of the steps to clarify computation and ease the reproduction

of this method. After the quadplexer example, this section discusses the comparison of a duplexer when synthesized with the proposed multiport method with respect to synthesizing it as two independent filters with controlled reflection phase (as proposed in Ch. 4). As a brief closing example, the multiport filter function of a pentaplexer composed of 7-th order channels is depicted as a demonstration of the current capabilities of the proposed method.

5.6.1 Band 3 - Band 1 LTE Quadplexer

A common carrier aggregation set is the combination of FDD LTE bands 3 and 1 (n3 and n1 in 5G nomenclature) and thus a quadplexer ($K = 4$) example in these bands is an interesting demonstration vehicle for the proposed synthesis method. The corner frequencies of the channels in this quadplexer are 1710 - 1785 MHz B3 uplink (UL), 1805 - 1880 MHz B3 downlink (DL), 1920 - 1980 MHz B1 uplink and 2110 - 2170 MHz B1 downlink and, for the sake of simplicity, 7-th order channels ($N_k = 7$ for all k, thus $M = 28$) are assumed. Moreover, the objective is to attain a minimum common port return loss (CPRL) of 10 dB. Without loss of generality, this example has been searched aiming to be implemented using standard aluminum nitride BAW resonators (i.e., $k_t^2 = 6.7\%$), but as already introduced, synthesis methodologies for AW technology are completely applicable to either type of resonator and electromechanical coupling value. As already stated at the beginning of this chapter, let us assume all channels start in series resonator.

Table 5.1: Synthesis input parameters of the Band 3 - Band 1 quadplexer.

k	1 (B3 UL)	2 (B3 DL)	3 (B1 UL)	4 (B1 DL)
N_k	7	7	7	7
RL_k	14.65	14.76	13.77	16
	$-0.5677j$	$-0.1609j$	$0.3295j$	$1.1626j$
	$-1.0862j$	$-0.6540j$	$-0.1982j$	$0.5514j$
	$-0.5692j$	$-0.0947j$	$0.2712j$	$1.0595j$
$j\Omega_k$	$-1.0514j$	$-0.6334j$	$-0.1849j$	$0.5484j$
	$-0.5701j$	$-0.1034j$	$0.2717j$	$1.0605j$
	$-1.0906j$	$-0.6706j$	$-0.2039j$	$0.5863j$
	$-0.5711j$	$-0.1644j$	$0.3307j$	$1.1636j$

Given the corner frequencies of each channel, the central frequency of the quadplexer is $f_{0-MPX} = \sqrt{2170 \cdot 1710} = 1926.3$ MHz and the overall fractional bandwidth of the quadplexer is $\mathrm{FBW}_{MPX} = (2170-1710)/f_{0-MPX} = 0.2388$. Hence, the respective positions of each channel within the normalized frequency domain are Band 3 UL $[-j, -0.6387j]$, Band 3 DL $[-0.5452j, -0.2039j]$, Band 1 UL $[-0.0275j, 0.2302j]$ and Band 1 DL $[0.7639j, j]$ as computed with (5.15). The input parameters required to start the multiport function synthesis procedure are the transmission zeros and

return loss value of each channel and are summarized in Table 5.1. Notice the method allows to set the RL level of each channel independently, what is an important asset to exploit to search for filters that comply with a given type of acoustic wave resonator technology. Array $j\Omega_k$ contains the transmission zeros of each channel, already mapped to the overall $[-j, j]$ range of s that contains the multiport function. These input parameters allow to compute the initial Chebyshev functions for each of the channel filters to start the iterative procedure described in subsection 5.4.1. By following the proposed method, after 4 iterations a convergence of 10^{-3} is achieved on $S(s)$ and the multiport function is completely computed obtaining $M = 28$ polynomials $u_0U(s)$, $D(s)$ and $t_kT_k(s)$. For reproducibility purposes and to discuss the nature of the roots of transmission polynomials, coefficients of polynomials $T_1(s)$, $U(s)$ and $D(s)$ are depicted in Table 5.2, in descending powers of s. From the computed polynomials, the multiport transfer function in the normalized domain can be evaluated using (5.2) to obtain the response depicted in Fig. 5.6.

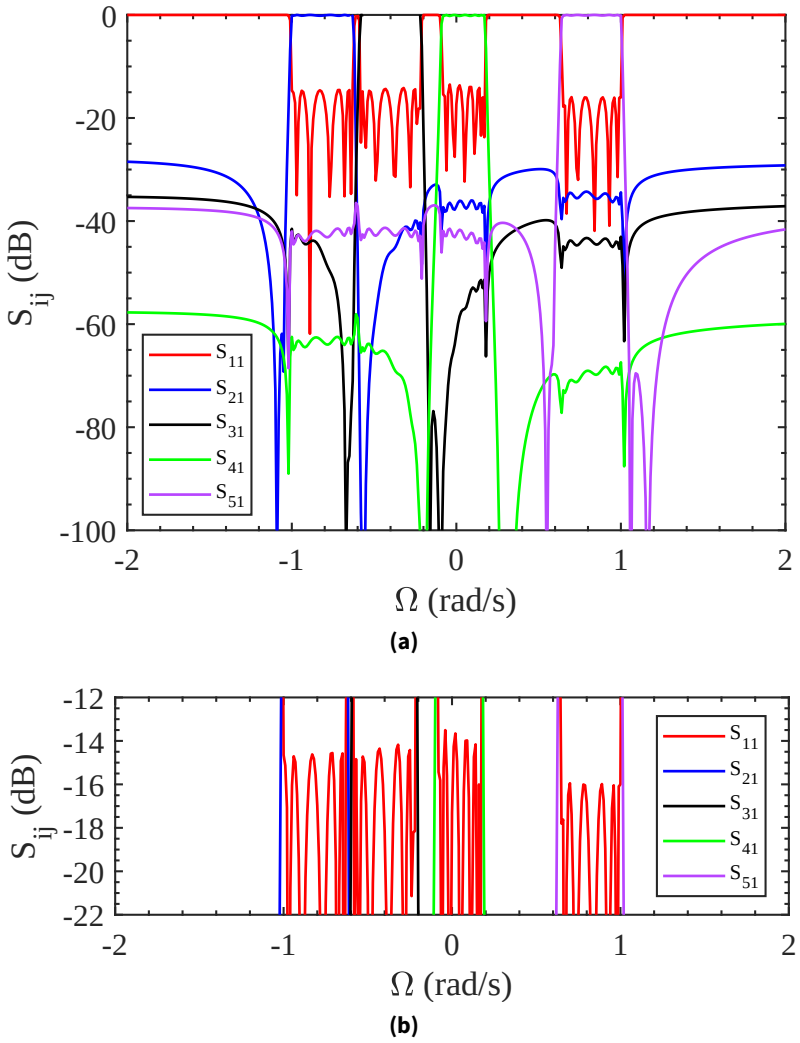

Figure 5.6: Multiport transfer function response of the B3/B1 quadplexer using the computed multiport polynomials $D(s)$, $u_0U(s)$ and $t_kT_k(s)$. (a) Overall response and (b) return loss close up to highlight the *quasi* equiripple response.

As expected, the multiport transfer function describes a *quasi* equiripple return loss within each of the passbands, whose level can be independently prescribed. The term *quasi* equirriple is used since, as already introduced, there is no closed solution to find the roots of $U(s)$ for a perfectly equiripple response and such roots are a-priori defined in the first step of the procedure. The result is the slight deviation that can be observed within each passband in Fig. 5.6b. Notice that the deviation is always slight (well below, 0.5 dB from $f_{1,k}$ to $f_{2,k}$) because the roots of $U(s)$ are directly the set of roots of the initial Chebyshev polynomials assumed per each channel (i.e., all $F_k^0(s)$) and at each iteration, the desired value of RL is fixed at one of the filter corner frequencies. This fact also states that the roots of $U(s)$ are thus purely imaginary, as depicted in Fig. 5.7a and so, the common port return loss describes deep and clear reflection zeros.

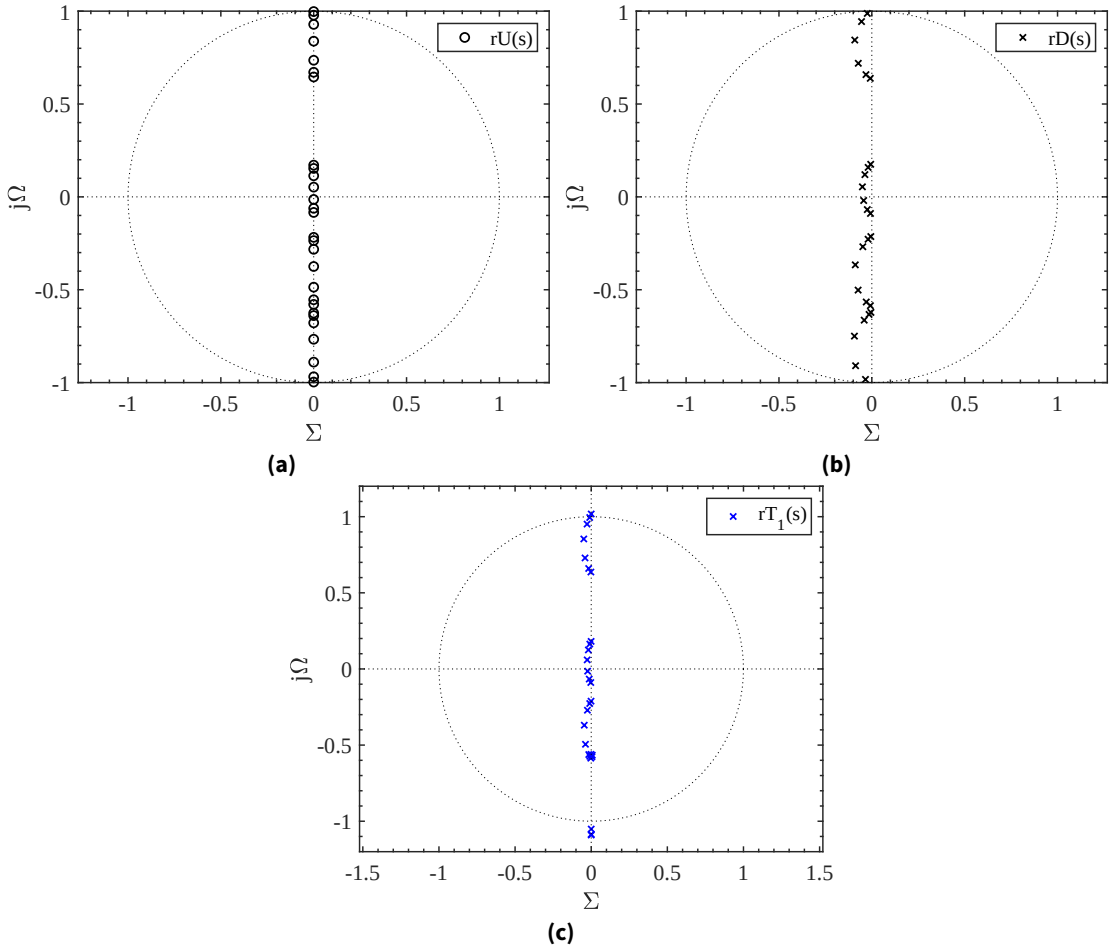

Figure 5.7: Distribution of roots on the s-plane of (a) polynomial $U(s)$, (b) polynomial $D(s)$ and (c) polynomial $T_1(s)$. Axes on the latter plot are extended since transmission zeros can be placed outside the unit circle of s.

From the point of view of transmission polynomials, notice that the multiport response not only depicts the set of transmission zeros defined as an input to the synthesis (those TZs related to the resonance frequencies of AW resonators) but also each channel incorporates $M - N_k$ additional

Table 5.2: Coefficients of the B3/B1 quadplexer common denominator $D(s)$, numerator polynomial $U(s)$ and transmission polynomial $T_1(s)$.

$D(s)$	$U(s)$	$T_1(s)$
1	1	1
$1.03936005 + 2.16834946j$	$2.16867590j$	$0.37766634 + 2.02523447j$
$3.57906717 + 2.15959595j$	3.03789843	$3.56697575 + 0.83347212j$
$3.10977772 + 11.01032612j$	$9.93752675j$	$1.06609130 + 9.81462929j$
$2.45491245 + 9.45692322j$	1.01016367	$3.07711405 + 3.57989699j$
$1.36359836 + 22.67889836j$	$18.46517927j$	$0.24985128 + 19.45370981j$
$-6.78230298 + 16.65528499j$	-7.29215084	$-4.11058274 + 6.14304776j$
$-5.61623489 + 23.89254436j$	$17.31406210j$	$-2.39218025 + 19.92100136j$
$-15.404946369 + 14.74625216j$	-13.22383613	$-10.87521232 + 5.23064705j$
$-9.90553667 + 12.83966355j$	$7.74675580j$	$-3.80176950 + 10.60153787j$
$-13.75828905 + 6.36865908j$	-10.47137938	$-9.78054204 + 2.0901762j$
$-7.25562645 + 2.28380927j$	$0.39599697j$	$-2.6309333 + 2.0728039j$
$-6.36652942 + 0.63524989j$	-4.3062260	$-4.4436214 + 0.1049349j$
$-2.72480074 - 0.98676254j$	$-1.13501733j$	$-0.9286489 - 0.5921175j$
$-1.48243147 - 0.52897135j$	-0.82669184	$-0.9936167 - 0.2168253j$
$-0.49200956 - 0.58561019j$	$-0.46629618j$	$-0.1514563 - 0.3822849j$
$-0.119596649 - 0.21041228j$	-0.02017704	$-0.0693474 - 0.0740161j$
$-0.02378223 - 0.10502164j$	$-0.06619433j$	$-0.0044099 - 0.0651516j$
$0.00902995 - 0.02760414j$	0.01308077	$0.0074511 - 0.0086907j$
$0.00319191 - 0.00605052j$	$-0.00186662j$	$0.00126489 - 0.00298265j$
$0.00129138 - 0.00103949j$	0.00085407	$0.0007656 - 0.0002817j$
$0.00024907 - 0.00009393j$	$0.00002844j$	$0.0000844 - 0.0000227j$
$(4.4799 - 5.9879j) \cdot 10^{-5}$	$1.8142 \cdot 10^{-5}$	$(2.1946 + 0.0271j) \cdot 10^{-5}$
$(5.4715 + 1.3025j) \cdot 10^{-6}$	$1.5969 \cdot 10^{-6}j$	$(1.6955 + 1.1070j) \cdot 10^{-6}$
$(5.3805 + 2.5349j) \cdot 10^{-7}$	$1.3044 \cdot 10^{-7}$	$(2.1938 + 1.1273j) \cdot 10^{-7}$
$(3.6332 + 3.6572j) \cdot 10^{-8}$	$1.5877 \cdot 10^{-8}j$	$(0.9603 + 1.9003j) \cdot 10^{-8}$
$(1.4330 + 2.8007j) \cdot 10^{-9}$	$7.3707 \cdot 10^{-11}$	$(0.3780 + 1.0061j) \cdot 10^{-9}$
$(0.1004 + 1.4008j) \cdot 10^{-10}$	$3.3199 \cdot 10^{-11}j$	$(-0.6170 + 5.8127j) \cdot 10^{-11}$
$(1.361 + 2.663) \cdot 10^{-12}$	$4.08 \cdot 10^{-13}$	$(-7.41 + 7.73j) \cdot 10^{-13}$
	u_0	t_1
	0.99903503	0.03866209

TZs, mainly complex, that are completely related to the reactive loading between channels as stated in (5.13). This is clearly observable in Table 5.2 since the coefficients of $T_1(s)$ are complex. The root distribution of this transmission polynomial is shown in Fig. 5.7c depicting $N_k = 7$ purely imaginary

Table 5.3: Coefficients of the B3 uplink channel polynomials of the B3/B1 quadplexer.

$E_1(s)$	$F_1(s)$	$P_1(s)$
1	1	1
$0.30472075 + 5.64914609\,j$	$-0.02008927 + 5.64539232\,j$	$5.50626669\,j$
$-13.5590953 + 1.46263724\,j$	$-13.59767161 - 0.08617433\,j$	-12.77345718
$-2.90251358 - 17.92379421\,j$	$0.15052164 - 18.09857803\,j$	$-16.179211645\,j$
$14.09328138 - 3.04795799\,j$	$14.37543392 + 0.13645387\,j$	12.08723276
$1.78641632 + 6.59191494\,j$	$-0.06728439 + 6.81347661\,j$	$5.32989100\,j$
$-1.69849049 + 0.55414454\,j$	$-1.78423244 - 0.01693619\,j$	-1.28569662
$-0.07108855 - 0.18601199\,j$	$0.00166910 - 0.19914300\,j$	$-0.13103100\,j$
	ε_{r1}	ε_1
	1.00074838	25.86232102

roots (the prescribed TZs), located at the bottom region of the plot since $k = 1$ is the B3 uplink filter, and 21 extra complex roots that are closely related to the reflection zeros of all other filters in the multiplexer. At frequencies far away from a given filter of the multiplexer, let it be $k = 1$ in this case, once the response has reached the finite OoB rejection level intrinsic to fully canonical functions, all other reflection zeros at the common port of the multiplexer result in all available energy at the junction flowing through the filter implementing each reflection zero (perfect match) and thus, all other filters experience an increase in their rejection at those exact frequencies. Through the proposed methodology, the mathematical description of the function already takes into account all these points by adding complex-valued transmission zeros to each transmission polynomial $T_k(s)$ and thus allows a perfect estimation of the attainable rejection level directly at the polynomial level. To complete the description of the polynomials composing the multiport function, notice that $D(s)$ is a complex-valued polynomial and thus all of its roots are located on the complex plane, as depicted in Fig. 5.7b. As expected, all roots lie on the left-half plane since stability has been imposed.

Once the multiport function is computed, the distorted channel polynomials $E_k(s)$, $P_k(s)$ and $F_k(s)$ along with normalization constants ε_k and ε_{rk} can be derived following the steps described in Sec. 5.4.2. For this quadplexer example, as a tool to allow evaluation of the method, the coefficients of the distorted polyomials of the $k = 1$ channel are depicted in Table 5.3, again in columns for descending powers of s. Additionally, Fig. 5.8 shows the polynomial response of the four recovered channels evaluated separately as two-port networks directly through (5.1).

It is interesting to highlight the fact that while polynomial $P_1(s)$ retains its originally prescribed purely imaginary transmission zeros, polynomial $F_1(s)$ now implements complex roots, as can be observed from its complex-valued coefficients, and, due to $F_1(s)$ being a numerator polynomial, can lie on both sides of the s-plane. Notice in Fig. 5.8, that the response obtained when evaluating the channel polynomials as two-port networks, is clearly distorted if compared to an equiripple Chebyshev

function. Such distortion, the one required by each channel to implement an equiripple response when connected to the junction is directly related to the compensation of loading between channels and materializes in the roots of polynomial $F_k(s)$ moving into the complex plane and the roots of $E_k(s)$ departing from their classical semi-elliptical disposition with respect to the $j\omega$ axis if the roots of $F_k(s)$ had been purely imaginary. This is observable in the root pattern in Fig. 5.8e that shows the roots of both $F_k(s)$ and $E_k(s)$ of the example quadplexer. Note that thanks to the proposed synthesis method, such a disposition of roots for each of the channels is obtained analytically and not resorting to brute-force optimization.

Once the distorted channel polynomials are derived, the lowpass prototype of each channel filter can be synthesized as a two-port network using one of the synthesis methods mentioned along this thesis, either the extracted pole technique or coupling matrix rotations, along with the lowpass prototype equivalent of the BVD model presented in [124] and in Ch. 3. Once the synthesis is complete, the normalized prototype elements need to be transformed in frequency and scaled in terms of impedance to obtain the BVD models of the resonators that compose each filter. Since a specific discussion is devoted to frequency denormalization for multiplexers in the next section, let us briefly state that each channel is denormalized to its own central frequency and fractional bandwidth and switch directly to the obtained elements that are summarized in Table 5.4. As stated at the beginning of the chapter, all ladder filters start in series resonator and therefore each filter features a shunt inductor at the input and output ports. From the four shunt inductors, one at the input of each filter, the MUX inductor at the junction in Fig. 5.2 is obtained as a merger of all of them in this case obtaining $L_{\mathrm{MUX}} = 1.82$ nH.

As stated, this quadplexer example is synthesized to be feasible using standard aluminum nitride (AlN) BAW resonator technology ($k^2_{\mathrm{eff}} = 6.7\%$). Having the BVD elements of the entire multiplexer, assuming an AW quality factor $Q_{\mathrm{AW}} = 1500$, modeled as in [16], and $Q_{\mathrm{L}} = 50$ for the input and output inductors, the simulated bandpass response of the entire multiplexer after transformation is shown in Fig. 5.9a depicting a CPRL better than 10 dB for antenna and output port impedances of 50 Ω. For completeness, and to provide a precise representation of how the channels are ready to be matched with each other at the common port, Fig. 5.10a depicts the S_{11} of each channel filter when seen as a two-port network and Fig. 5.10b shows the S_{11} of the quadplexer, both on Smith charts and plotting only for the in-band frequencies (i.e., from 1710 MHz to 2170 MHz).

To complete the presentation of this example, it is important to highlight the differences in terms of S_{11} observable between the original response of the multiport function in the normalized domain in Fig. 5.6b and the common port return loss simulated in the bandpass domain in Fig. 5.9a. Although the obtained CPRL complies with the expected 10 dB value, it is distorted with respect to the ideal equiripple return loss depicted by the multiport function. As is covered in a forthcoming section, these differences are strictly related to the inherent narrowband nature of the frequency transformation required to compute the resonator circuital elements from their normalized proto-

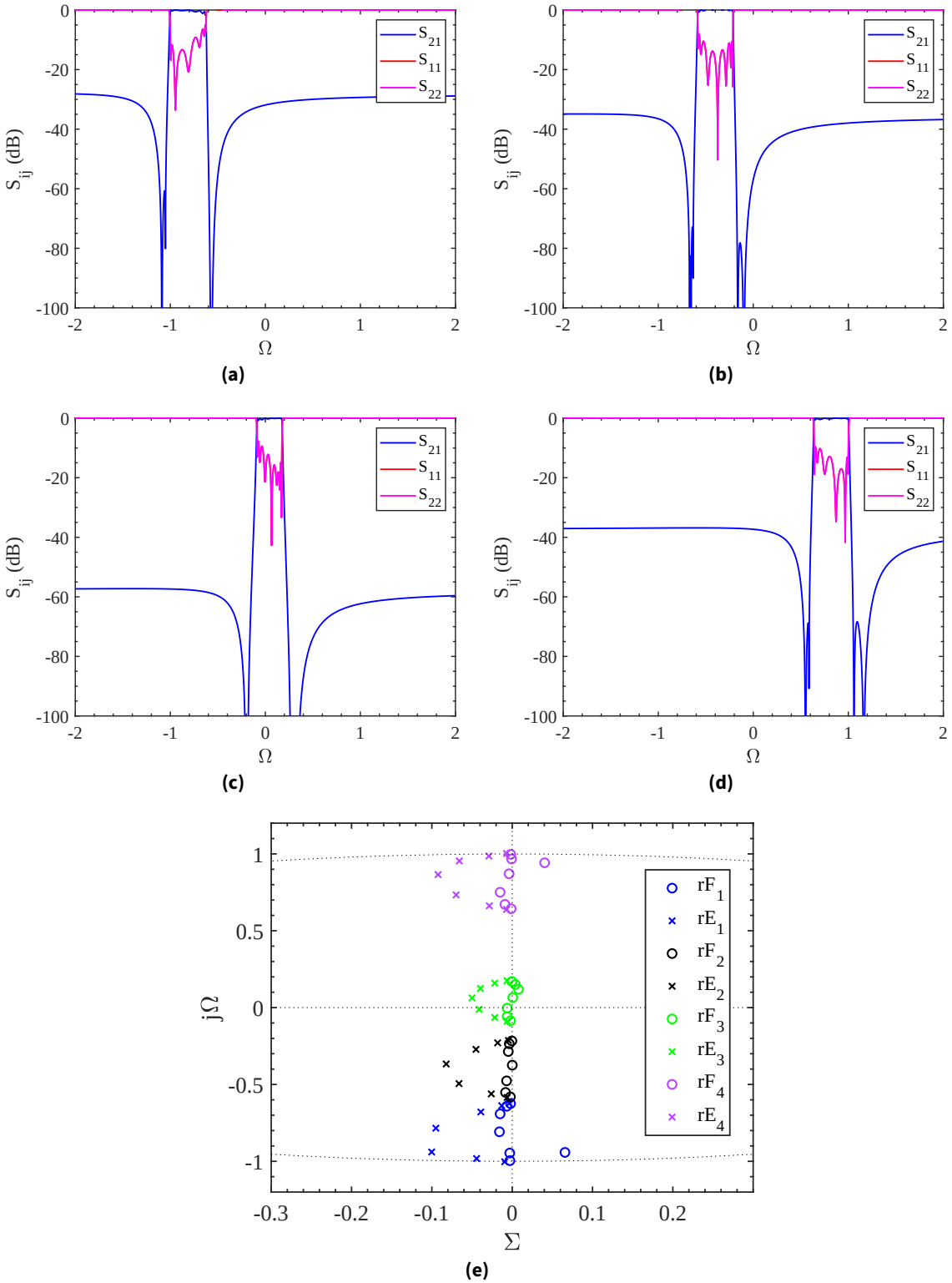

Figure 5.8: Channel polynomials response of the B3/B1 quadplexer example when each channel is evaluated as an individual two-port network. (a) $k = 1$ (B3 UL), (b) $k = 2$ (B3 DL), (c) $k = 3$ (B1 UL), (d) $k = 4$ (B1 DL) and (e) Root pattern of the distorted channel polynomials of the B3/B1 quadplexer. The dashed black lines are the axes and the contour of the unit circle on the $s = \Sigma + j\Omega$ plane.

Table 5.4: Butterworth - Van Dyke model elements of the B3/B1 quadplexer.

Band 3 uplink

Resonator	1 (SE)	2 (SH)	3 (SE)	4 (SH)	5 (SE)	6 (SH)	7 (SE)
L_a (nH)	66.04	59.44	128.94	64.66	126.31	58.76	54.43
C_a (fF)	125.20	149.21	64.11	136.09	65.43	151.11	151.73
C_0 (pF)	2.14	2.56	1.10	2.34	1.12	2.59	2.61
k^2_{eff} (%)	6.7	6.7	6.7	6.7	6.7	6.7	6.7
L_{in} (nH)	6.19	L_{out} (nH)	18.57				

Band 3 downlink

Resonator	1 (SE)	2 (SH)	3 (SE)	4 (SH)	5 (SE)	6 (SH)	7 (SE)
L_a (nH)	115.23	45.27	97.04	50.72	101.59	42.31	93.79
C_a (fF)	63.74	175.56	76.75	155.92	73.25	188.53	78.17
C_0 (pF)	1.09	3.01	1.31	2.67	1.25	3.23	1.33
k^2_{eff} (%)	6.7	6.7	6.7	6.7	6.7	6.7	6.7
L_{in} (nH)	8.72	L_{out} (nH)	7.02				

Band 1 uplink

Resonator	1 (SE)	2 (SH)	3 (SE)	4 (SH)	5 (SE)	6 (SH)	7 (SE)
L_a (nH)	152.64	24.88	157.24	24.88	157.95	24.56	139.89
C_a (fF)	43.04	284.27	42.35	283.39	42.15	288.34	46.95
C_0 (pF)	0.73	4.87	0.72	4.86	0.72	4.94	0.80
k^2_{eff} (%)	6.7	6.7	6.7	6.7	6.7	6.7	6.7
L_{in} (nH)	10.28	L_{out} (nH)	6.18				

Band 1 downlink

Resonator	1 (SE)	2 (SH)	3 (SE)	4 (SH)	5 (SE)	6 (SH)	7 (SE)
L_a (nH)	76.93	24.69	64.37	29.18	64.85	24.44	74.43
C_a (fF)	69.15	236.15	84.57	198.18	83.93	238.75	71.46
C_0 (pF)	1.18	4.05	1.45	3.40	1.43	4.10	1.22
k^2_{eff} (%)	6.7	6.7	6.7	6.7	6.7	6.7	6.7
L_{in} (nH)	5.71	L_{out} (nH)	3.81				

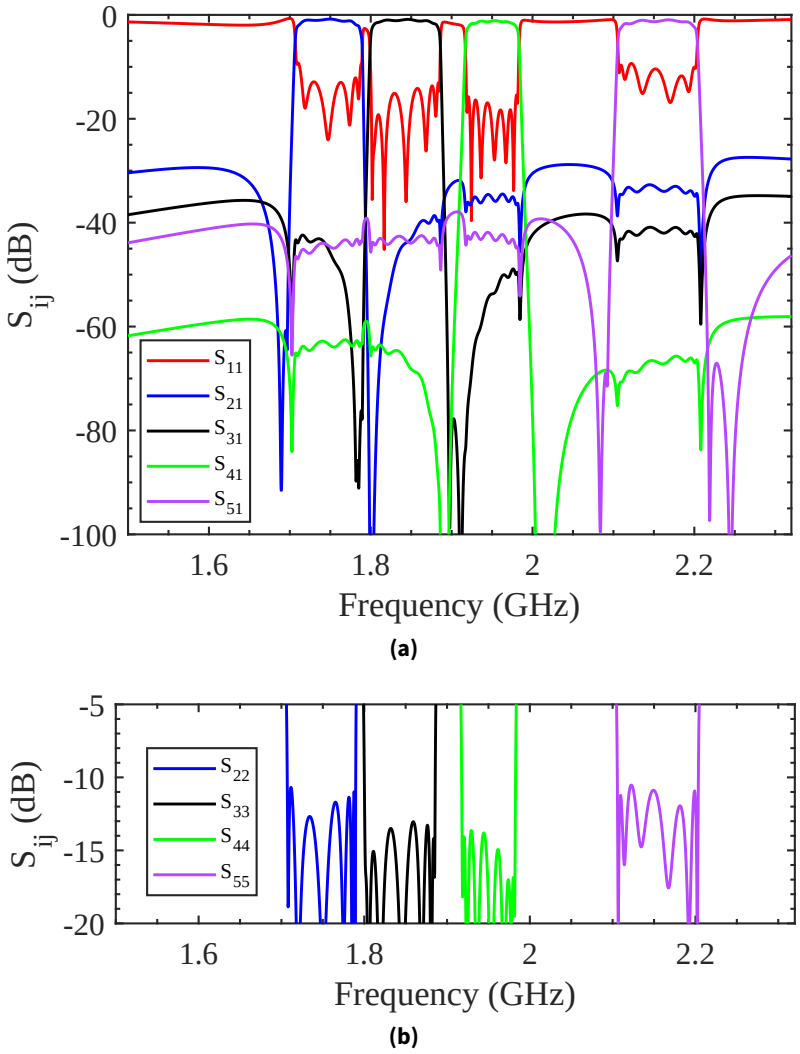

Figure 5.9: Simulated response of the synthesized B3/B1 quadplexer using the BVD model of each resonator and assuming $Q_{\text{AW}} = 1500$ and $Q_L = 50$. (a) Common port return loss and channel through response and (b) output return loss.

type equivalents. While this narrowband nature has already been discussed in this thesis in the scope of single filters, given the intrinsic wideband nature of multiplexers, its effect is more pronounced. Notice, for example, that the channel with the most return loss distortion is Band 1 downlink, the furthest one in terms of frequency. However, such deviation from the ideal return loss does not prevent the method from providing a useful solution.

In general terms, the obtained result directly after synthesis is the starting point from which a multiplexer design can be scaled into more complex circuital models such as BVD models including resonator area dependencies or featuring extra motional branches to model spurious modes or the addition of EM effects from layout, among others. Such higher-order effects impose changes to the response obtained from the synthesis and surely imply design optimization stages to consider all of

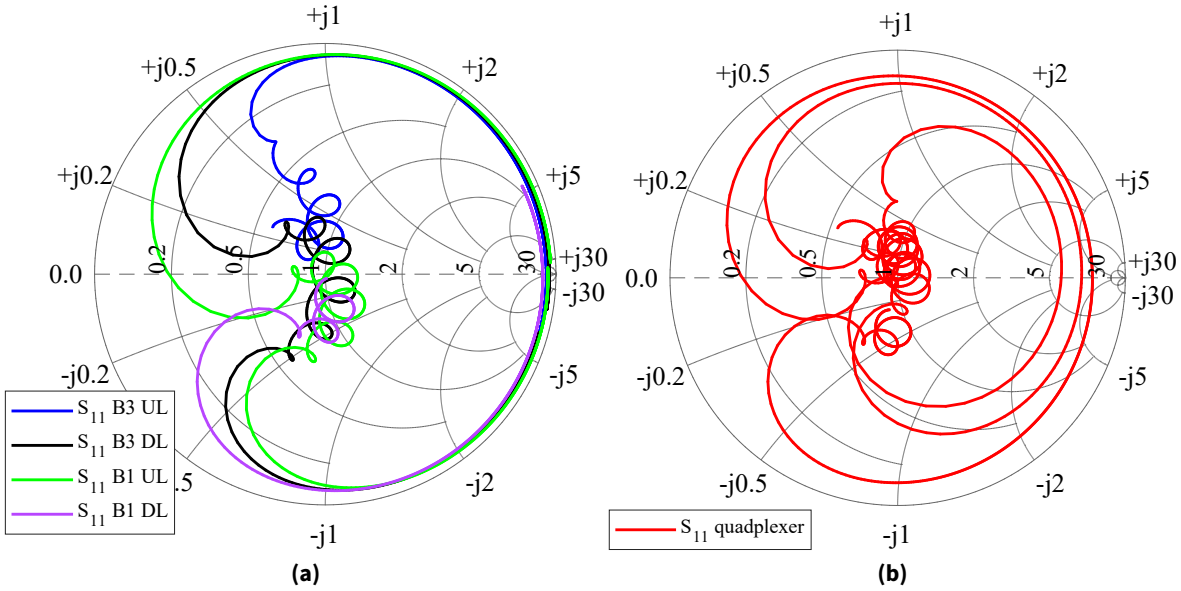

Figure 5.10: Smith chart plot of (a) the reflection coefficient of each channel filter when evaluated as an individual two-port network between and (b) the input reflection coefficient of the entire quadplexer at the antenna port, in both cases for frequencies from 1710 MHz to 2170 MHz and for 50 Ω loads.

them. However, the presented synthesis method provides the seed from which subsequent design stages can start and allows to quickly and analytically find a new seed design with another set of input constraints if needed.

5.6.2 Application to Duplexer Synthesis

To complement the description of a multiport function approach to synthesis, it is interesting to revisit the case of duplexers. A specific case that now can be faced using two different synthesis approaches: either through the correct modification of the reflection phase ($\angle S_{11}$) of each filter as described in Ch. 4 or analytically as a three-port function with the method presented in this chapter.

Let us take the Band 3 pair of bands and synthesize one filter per band using the *traditional* phase modification approach, that is, independent synthesis of each filter using a Generalized Chebyshev function with a phase shift added to polynomial $F(s)$, with the objective of using $k^2_{\text{eff}} = 6.7\%$ resonators and imposing a counter band rejection of at least 45 dB and 15 dB return loss. With these requirements, a solution is found using, RL = 15.22 dB, Ω_{UL} = [1.5183, -1.5922, 1.3975, -1.4006, 1.4046, -1.6129, 1.2746] and phase shift $\theta_{\text{add-UL}} = -38.79°$ for Band 3 uplink and RL = 15 dB, Ω_{DL} = [2.0348, -1.6415, 1.4647, -1.4519, 1.4647, -1.6415, 2.0348] and phase shift $\theta_{\text{add-DL}} = 36.33°$. The synthesized BVD models from such parameters are summarized in Table 5.5 and the inductors at the input of each filter can be merged into a duplexer inductor $L_{\text{DPX}} = 3.62$ nH. Having obtained this

Table 5.5: Butterworth - Van Dyke model elements of the B3 duplexer using reflection phase modification.

Band 3 uplink - $\theta_{add-UL} = -38.79°$

Resonator	1 (SE)	2 (SH)	3 (SE)	4 (SH)	5 (SE)	6 (SH)	7 (SE)
L_a (nH)	84.98	49.30	150.48	52.39	152.39	51.66	43.88
C_a (fF)	97.02	179.74	55.05	167.89	54.34	171.66	189.69
C_0 (pF)	1.66	3.09	0.94	2.88	0.93	2.95	3.26
k^2_{eff} (%)	6.7	6.7	6.7	6.7	6.7	6.7	6.7
L_{in} (nH)	15.48	L_{out} (nH)	-				

Band 3 downlink - $\theta_{add-DL} = 36.33°$

Resonator	1 (SE)	2 (SH)	3 (SE)	4 (SH)	5 (SE)	6 (SH)	7 (SE)
L_a (nH)	103.74	26.25	96.98	29.07	96.98	26.25	103.74
C_a (fF)	70.39	303.20	76.86	271.92	76.86	303.20	70.39
C_0 (pF)	1.21	5.21	1.32	4.67	1.32	5.21	1.21
k^2_{eff} (%)	6.7	6.7	6.7	6.7	6.7	6.7	6.7
L_{in} (nH)	4.74	L_{out} (nH)	4.74				

solution for the duplexer, notice that using the same set of TZs and RL on the multiport function method would lead to an output result not complying with all resonators having the same k^2_{eff}. Since the channel functions derived from the multiport function are distorted, the circuital elements implementing them must differ from those obtained from the synthesis of a generalized Chebyshev response. In general the impact is mostly noticed in the first, second and last resonators.

Therefore, to synthesize the duplexer through the multiport function approach and to allow a fair comparison, let the RL of each channel be maintained (i.e., $\text{RL}_{UL} = 15.22$ dB and $\text{RL}_{UL} = 15$ dB) and let us modify the TZs slightly so to achieve same k^2_t on all resonators. Such slight tweak yields (listing them renormalized to the two-port function s-domain, for comparison purposes) $\Omega_{UL} =$ [1.5099, -1.5698, 1.3923, -1.3983, 1.4039, -1.6121, 1.2817] and $\Omega_{DL} =$ [2.0010, -1.5892, 1.4570, -1.4493, 1.4640, -1.6407, 2.0070]. Notice the great similarity of this set of TZs with respect to the set used for the independent synthesis of each filter, with the larger differences observable in TZs 1, 2 and 7. In other words, resonators 1, 2 and 7 of each filter being the ones whose resonance frequency is different when comparing both solutions. Circuital elements in Table 5.6 correspond to the two channel filters of the Band 3 duplexer obtained through the analytical method in this chapter, in this case merging both input inductors into $L_{DPX} = 4.00$ nH.

To complement the comparison, Fig. 5.11 depicts the response comparison of each channel of the two synthesized duplexers (Figs. 5.11a and 5.11b for B3 uplink and B3 downlink, respectively)

Table 5.6: Butterworth - Van Dyke model elements of the B3 duplexer using the multiport function approach.

Band 3 uplink

Resonator	1 (SE)	2 (SH)	3 (SE)	4 (SH)	5 (SE)	6 (SH)	7 (SE)
L_a (nH)	99.22	50.65	149.34	52.58	152.19	51.63	44.89
C_a (fF)	83.12	174.81	55.48	167.26	54.42	171.77	185.37
C_0 (pF)	1.43	3.00	0.95	2.87	0.93	2.95	3.19
k^2_{eff} (%)	6.7	6.7	6.7	6.7	6.7	6.7	6.7
L_{in} (nH)	7.92	L_{out} (nH)	-				

Band 3 downlink

Resonator	1 (SE)	2 (SH)	3 (SE)	4 (SH)	5 (SE)	6 (SH)	7 (SE)
L_a (nH)	114.44	27.99	100.03	30.43	101.28	27.50	105.11
C_a (fF)	63.88	283.81	74.53	259.72	73.59	289.46	69.53
C_0 (pF)	1.09	4.88	1.28	4.46	1.26	4.98	1.19
k^2_{eff} (%)	6.7	6.7	6.7	6.7	6.7	6.7	6.7
L_{in} (nH)	8.13	L_{out} (nH)	5				

along with the common port return loss in 5.11c, where dashed lines correspond to the phase modification approach and solid lines correspond to the multiport synthesis approach. In both cases, the synthesized BVD models have been simulated assuming $Q_{\text{AW}} = 1500$ and $Q_L = 50$ for the inductors.

From a performance perspective, notice that both solutions implement almost exact responses both complying with 15 dB return loss with the small detail that the Band 3 uplink filter synthesized through the multiport function method depicts 1.2 dB better OoB rejection towards the Band 3 downlink filter. However, notice from the comparison in Tables 5.5 and 5.6 that the two filters synthesized through the multiport function method require smaller C_0 what ultimately is related to smaller resonator areas. Although it is a small difference (total capacitance with respect to the phase modification solution is 3% and 6.5% smaller for the uplink and downlink filters, respectively) it is worth a mention because the solution obtained through the multiport function method is not attainable with the phase modification approach: notice the latter always imposes a Chebyshev function to each filter while the first directs to distorted filters that perform as desired only when connected together. Nevertheless it must also be mentioned that the required common port inductor for the multiport function solution is slightly larger than the one required by the phase-modified duplexer.

In general terms, the comparison between the two approaches is not meant to conclude that one outperforms the other when applied to duplexer synthesis but is interesting to point out that two different solutions can be attained, effectively providing additional cases to consider. While on the one

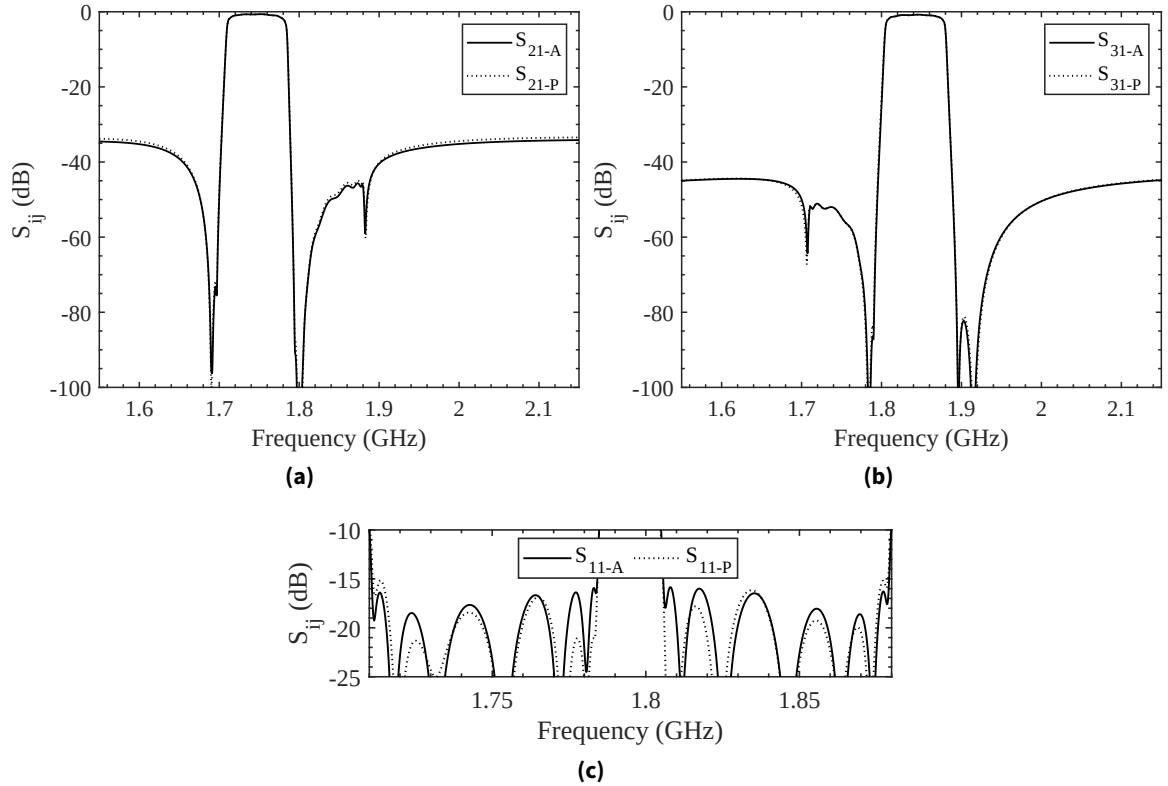

Figure 5.11: Simulated response comparison of the Band 3 duplexer synthesized with both approaches: solid is multiport approach (A stands for analytical) and dotted is reflection phase modification (P stands for phase) using $Q_{\text{AW}} = 1500$ and $Q_L = 50$. (a) Band 3 uplink response, (b) Band 3 downlink response and (c) common port return loss.

hand the multiport solution directs to slightly smaller capacitance values, the phase modification approach offers an added degree of filter reusability since the filter already implements an equiripple return loss response without being connected to its partner filter in the duplexer and could be used as a standalone filter, while channel filters obtained through the multiport synthesis method implement distorted responses when evaluated as individual two-port networks.

5.6.3 M = 35 Pentaplexer Example

As a final example, to illustrate the capabilities of the proposed synthesis method to scale in total multiplexer order, let us briefly present the multiport function of an example pentaplexer composed of 7-th order channels to compose an $M = 35$ multiport function. In this case, an arbitrary band between Band 1 uplink and downlink channels has been added.

Such multiport polynomials can be decomposed into distorted channel functions and then be synthesized as presented. It is interesting to highlight that the small deviation from equirripple return loss is in this case slightly more noticeable due to $M = 35$ being right at the limit of numerical

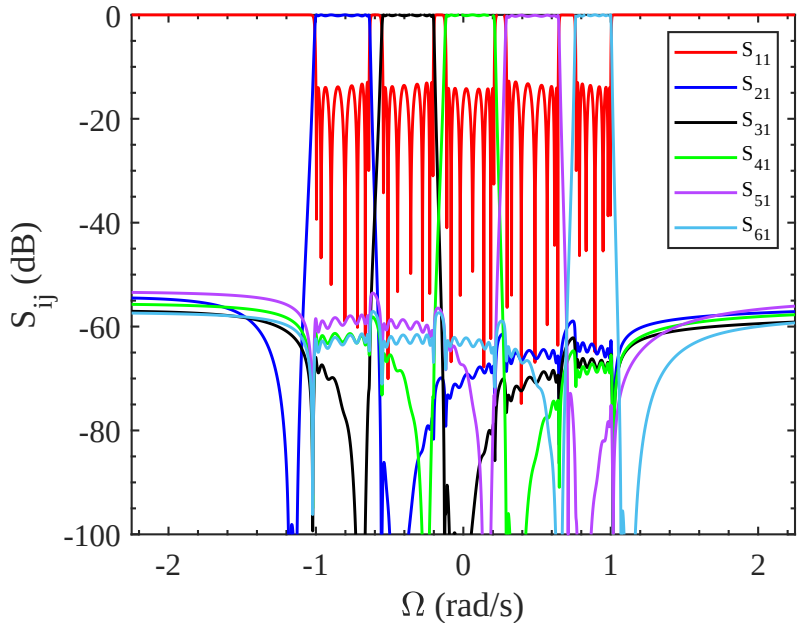

Figure 5.12: Multiport transfer function response of an example pentaplexer composed of 7-th order channels (i.e., $M = 35$) from the computed multiport polynomials $D(s)$, $u_0 U(s)$ and $t_k T_k(s)$.

stability when computing the roots of $D(s)$ what results in more difficulty for the iterative procedure to find convergence into the multiport function. In this case, computing the pentaplexer function requires 45 iterations to achieve the same degree of convergence on $S(s)$. A large contrast with respect to the 4 iterations required to converge into the quadplexer function in the example above.

5.7 Discussion of the Method

After presenting both the mathematical foundations of the method and a synthesized example of a quadplexer, this section is devoted to the discussion of details that play a fundamental role in the described procedure.

5.7.1 Implications of Frequency Transformation

As introduced in Ch. 3, the synthesis of circuital elements implementing a given transfer function of variable s takes place in the normalized frequency domain. In the case of two-port functions, the passband is defined inside the $s = [-j, j]$ rad/s interval and the transformation of elements from the normalized frequency domain to the actual bandpass domain is computed with the well-known bilateral transformation (5.53) already introduced:

$$\Omega = \frac{\omega_0}{FBW}\left(\frac{\omega}{\omega_0} - \frac{\omega_0}{\omega}\right) \tag{5.53}$$

Clearly, the above expression establishes a relation between $s = [-j, j]$ rad/s and $f = [f_1, f_2]$ Hz (the filter corner frequencies). However, from a multiplexer point of view, recall that a multiport filter function describes K passbands within the $s = [-j, j]$ interval and so, the distorted channel polynomials that are derived, each describe a passband in its own sub-interval within $s = [-j, j]$, as required by each channel's own fractional bandwidth within the entire multiplexer bandwidth, as is shown in the example polynomials in Fig. 5.8.

Let us briefly recall, as discussed in Ch. 3, that the lowpass prototype of an AW resonator due to its intrinsic equivalence with an extacted pole section is based on the use of frequency invariant reactance (FIR) elements. As already stated, FIRs are only a mathematical artifact needed in the normalized domain to represent non-resonant nodes [137,138] and due to the impossibility to physically implement FIRs in a real circuit [116], can only be approximated using reactances that only implement the desired value at a single point in frequency. This traditional assumption in the field of synthesis leads to a slight distortion of the response after it is transformed to the real frequency domain, but is considered valid for narrow bandwidths (i.e., FBW$<$ 5%).

Clearly, this assumption becomes a point to discuss when considering multiplexer synthesis. When facing the de-normalizaton of an entire multiplexer, two options can be considered: either transform the entire multiplexer as a block, let us take the previous quadplexer example and so $f_0 = 1926.3$ MHz and FBW$=$ 23.88% or transform each channel to its respective central frequency $f_{0,k}$ and FBW$_k$. To implement the first, channels must be synthesized directly in the form they are derived from the multiport function (i.e., as in Fig. 5.8) and for the second, channel polynomials must be re-normalized so that each channel passband is defined within $s = [-j, j]$ with (5.15) and then synthesized as common two-port functions.

To better illustrate the effects of both options, let us take an arbitrary triplexer composed of Band 3 uplink, Band 3 downlink and Band 1 uplink and let us synthesize and transform it following both alternatives. Fig. 5.13a depicts the triplexer multiport function in the normalized domain and Figs. 5.13b and 5.13c show the simulated response (using lossless BVD models) transforming the prototypes to the full multiplexer FBW and central frequency and to $f_{0,k}$ and FBW$_k$ respectively.

It is clearly observable in Fig. 5.13b how the result of transforming all channels to the entire FBW and the central frequency of the multiplexer does not yield an acceptable result because the two extreme channels are completely distorted. However, the central channel shows an almost perfectly equiripple return loss. That is because in this case the reactances that approximate the FIR elements of all filters are perfectly implementing the desired value of reactance exactly at the central frequency of the central filter (i.e., the central frequency of the multiplexer). Therefore, the further away from such central frequency, the higher the distortion suffered by the filters due to transformation. On the other hand, notice in Fig. 5.13c that through the second approach to frequency transformation all channels suffer the least distortion. That is because with this choice, each channel is transformed to

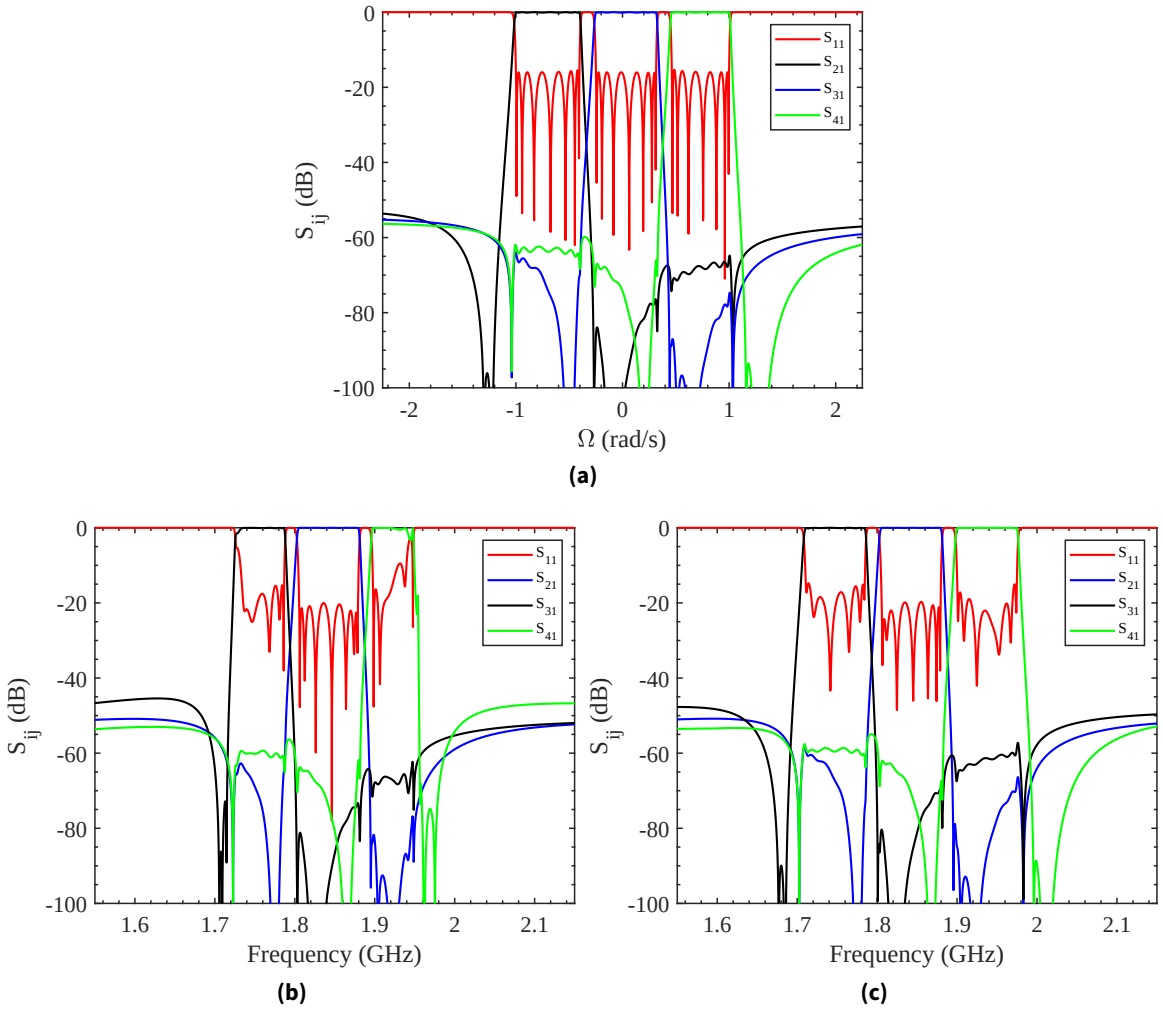

Figure 5.13: Response comparison of an arbitrary Band 3 uplink, Band 3 downlink and Band 1 uplink triplexer. (a) Triplexer multiport function response, (b) simulated triplexer response assuming lossless BVD models and transforming prototypes to the the multiplexer FBW and f_0 and (c) simulated triplexer response assuming lossless BVD models transforming each channel prototype to its own FBW and f_{0k}.

its own FBW (commonly, $\text{FBW}_k < 5\%$) and the best in-band performance is maintained. Therefore, that is proposed approach to follow for the presented method.

Finally, notice that the fact that FIR elements are approximated at each filter central frequency, is imposing the return loss degradation with respect to the multiport function response that is commented at the end of the quadplexer example discussion. The key of the proposed method is that the filters require the loading by their partner filters in the MUX to implement the desired equiripple response. However, due to such approximation of FIRs, the out-of-band reactive loading imposed by each of the filters slightly deviates from the originally prescribed loading in the normalized domain. This deviation results in the outermost channels of the MUX suffering the higher distortion. This is clearly observable in the Band 1 downlink filter of the presented quadplexer example. Given its displaced position with respect to the other three filters, it is subject to the deviations in terms of OoB

loading of the three other filters and thus depicts the most distorted return loss. In general terms, the closer the channels, the least the effects of frequency transformation are.

To close the discussion, consider that although frequency transformation imposes some degradation in the obtained multiplexer response, the originally prescribed return loss level values can be easily recovered, if desired, via a slight tuning of the first and second resonator C_0 of each channel filter to compensate for the deviated OoB loading.

5.7.2 Channels Starting in Shunt Resonator

The quadplexer example presented in this chapter, and also the discussed duplexer case, have complied with a condition stated at the very beginning of the chapter: all channels of the multiplexer are series-starting AW ladder filters. This condition, although also justified from many literature cases and from the concept of minimum susceptance networks, has been imposed at the moment of deriving the channel polynomials using (5.4) when normalization constant f_k has been defined as a real positive number and the expression has been fixed such that sub-polynomial $D_k(s)$ is monic.

Such an assumption is required since once the multiport function is known and channels are derived, decomposition of polynomial $D(s)$ to find its $D_k(s)$ sub-polynomials is only solvable if $D_k(s)$ is known to be monic and thus, its highest degree coefficient is not an unknown. The impact of this fact is channel polynomial $F_k(s)$ computed through (5.47) has a real and positive leading coefficient and therefore, as already discussed in detail in Ch. 4, imposes a reflection phase whose horizontal asymptote is located at 0°. As an example, Fig. 5.14 depicts the reflection phase of the Band 1 uplink channel polynomials from the quadplexer example showing the distinctive horizontal asymptote towards a null phase. As already discussed, such a reflection phase is inherently related to feasible filters starting in series resonator while a horizontal asymptote towards ±180° would be required to obtain a feasible shunt-starting filter.

Therefore, in the case a shunt-starting filter is required in the multiplexer module (for example, to achieve a higher rejection on the lower stopband of a given channel), directly trying to synthesize a shunt-starting filter with the obtained function would lead to the first and last resonators of the filter to be unfeasible. Since the distorted channel polynomials incorporate the necessary distortion to perfectly accommodate the reactive loading between channels, their reflection phase cannot be freely modified *a posteriori* by adding a phase shift to polynomial $F_k(s)$, if the joint multiport response is to be conserved. However, following the content derived in Ch. 4 some specific considerations can be applied: for cases where a shunt-starting filter must implement a function whose reflection phase has a horizontal asymptote towards 0°, more than a single reactive element at the input port are required.

Thus, the only possible option to implement a shunt-starting AW filter having a reflection phase

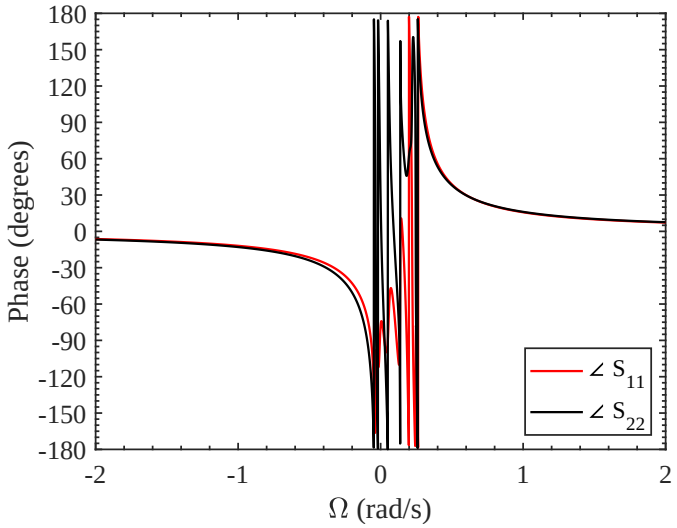

Figure 5.14: Reflection phase ($\angle S_{11}$ and $\angle S_{22}$) of the Band 1 uplink channel distorted polynomials.

asymptote at 0° is to proceed with the synthesis of two input reactive elements (one shunt and one series) as already demonstrated in this thesis. Not to increase component count at the common port, the shunt reactive element at the input of the channel must be fixed to be inductive while the series element can be chosen to be capacitive or inductive. Thus, the shunt inductor of the shunt-starting channel can be included in the MUX inductor.

While this rationale holds true for the presented formulation, the possibility to reformulate the initial polynomial definition to allow f_k to be complex and thus define channel polynomials whose reflection phase is a free parameter is left as an open topic for further research aiming for the possible implementation of multiplexers with shunt-starting channels without the need of two input reactive elements.

5.7.3 Maximum Multiplexer Order and Numerical Stability

Section 5.5 has outlined the use of cepstral analysis in the context of Feldtkeller's equation to overcome the numerical limitations inherent to polynomial root finding. As described throughout this chapter, the multiport synthesis method strongly relies in operations with the roots of polynomials of high degree to compute the multiport function and such operations are the ultimate factor limiting the maximum multiplexer order M that can be synthesized with this method. Thanks to the cepstrum, by avoiding the rooting of a double-degree polynomial, the proposed methodology is stable up to a maximum order of $M = 35$.

The main limiting factor that leads to numerical instabilities is the clustering of roots as the multiplexer order grows. This fact adds to fully canonical functions required for AW ladder filters adding an additional degree of asymmetry in the roots of $E(s)$ and $F(s)$ of each channel if compared to all-

pole channels [168] and increases the complexity of the problem. With the objective of extending the stability of this method beyond the current degree allowed by cepstral analysis, extended precision arithmetics approaches have been tested through the symbolic arithmetic engine in Matlab that allows to set an arbitrary number of significant digits. The main drawbacks of this approach are a noticeable increase in computation time (estimated to be 10 times slower) and the fact that the FFT algorithm is not yet available for extended precision, what entails computing the roots of polynomial $D^2(s)$.

For the purpose of this thesis, since such details are more related to the actual numerical implementation of this synthesis method inside a tool and concern trade-offs between computation time and maximum multiplexer order, extending the numerical stability of the proposed synthesis method is left as a future research topic, highlighting the promising option of using specific numerical toolboxes that allow extended precision FFT computation to exploit the cepstrum method along with symbolic operations.

5.7.4 Applications and Open Topics

Providing a general perspective of the proposed synthesis method, since it provides an analytical connection between a desired multiplexer response and its circuital implementation, let us highlight its capacity to provide seed designs at the circuital level that can be further expanded by including more complex features such as EM effects from layout or AW resonator models that include physical dependencies such as area or resonator geometry. A synthesized design, that implements a desired response defined at the mathematical level and fulfills technological constraints in terms of electromechanical coupling and area, among others, is the baseline from which further design decisions can be assessed. Additionally, such decisions can be rapidly re-evaluated and a new seed design can be obtained if any of the input requirements is modified.

In this sense, this method not only can be exploited as a way to obtain seed designs but also as an analysis tool to estimate the required technological parameters and filter characteristics to fulfill a given set of specifications. Thanks to being able to include all the interaction and loading between filters already at the normalized frequency domain by means of a multiport function, attainable rejections can be directly assessed and estimated having return loss level and channels transmission zeros as knobs.

Considering the content derived in this chapter, it is interesting to point out that the formulation of the multiport function serves as an starting vehicle to extend research in the direction of the analytical synthesis of the herringbone topology presented at the beginning of this chapter. Starting from the multiport function to implement the challenge lies in developing a novel formulation to derive the channel polynomials such that they are placed after suitable phase lengths. This approach, that is left as an open topic for further research, is of interest in the context of acoustic wave mul-

tiplexers to enable solutions in which laminate elements implement the required phase shift stages between portions of the multiplexer, in lumped form as in [176], yielding more favorable solutions from a technology point of view such as smaller areas of first and last resonators and more suitable values of electromechanical coupling.

Moreover, an interesting topic for further research in this method is the consideration of extended numerical precision techniques to extend the maximum multiport order that can be computed following the cepstrum approach.

5.8 Chapter Summary

In brief, this chapter provides an analytical methodology to synthesize a complete multiplexer composed of acoustic wave ladder filters connecting a multiport function definition in the normalized frequency domain with a set of distorted channel polynomials that are prepared to implement the desired multiplexer response only when they are connected with the partner filters of the synthesized multiplexer.

In parallel to the formulation of the method and the concepts that allow to describe a multiport network, due to the increased complexity of the proposed methodology that involves handling high order polynomials representing the entire multiplexer function, specific methods to avoid numerical issues when computing the roots, such as the cepstrum method, are presented in this chapter in the context of Feldtkeller's equation. Moreover, thanks to a division approach in which the functions to synthesize are distorted two-port networks, the synthesis methods known for standalone filters can be seamlessly applied without the need for multiport circuital extraction techniques.

The proposed methodology is thoroughly discussed, highlighting its main limitations in terms of maximum numerical order and frequency transformation, and examples are provided to demonstrate its application in the context of a set of carrier-aggregated LTE bands.

CHAPTER 6

Conclusions and Future Work

As discussed in the very initial chapters of this thesis, microwave acoustic resonators are the core technology for filtering devices in modern mobile communications RF-FEMs and, in the author's opinion, a bright future for them is expected as 5G is under deployment and 6G is already being developed. The ever-increasing number of filters per mobile device with the increasingly stringent size and performance requirements call for many years of competition between the already mature SAW and BAW technologies and promise an increasing number of challenges to solve. From a resonator performance standpoint some might be the already mentioned need of higher electromechanical coupling values to fulfill the larger bandwidths of new bands, fulfilling more stringent power handling requirements as new power classes are enabled or scaling up in frequency into the microwave region. In parallel, considering the system perspective, technical challenges are expected with the introduction of more complex multiplexing structures or even novel front-end architectures and the introduction of more carrier aggregation combinations, among others. It is in this context, to address current and future challenges that the connection between the fields of network synthesis and microwave acoustics provided in this thesis proves very useful both for industry and academia. As an example, the analytical techniques to synthesize microwave acoustic filters and multiplexers developed in this thesis cannot only be exploited directly as design tools to face current designs in an industrial environment but can also be used in the exploration and feasibility analysis of more complex solutions.

In general terms, the core of the discussion in this work is located in the application of network synthesis techniques to microwave acoustic technology filters and multiplexers, thus building the discussion both from the two-port and the multiport network perspective, but also considers the physical side of microwave acoustics by briefly presenting the main features of each resonator technology and discussing the performance of fabricated devices on a thin-film lithium niobate platform.

At the intersection of both the synthesis and physical sides of this thesis, a demonstrative filter exploiting a novel synthesis concept is presented and discussed as a demonstration of the impact of synthesis techniques in the complete design cycle from resonator design and mathematical computation of the transfer function to implement, to the fabrication of the filter prototype. Furthermore, it is important to state that the theoretical contributions to the synthesis of microwave acoustic filters and multiplexers have materialized in different software tools used for filter and multiplexer design and analysis.

As a first step, Ch. 2 is devoted to the technology side of this thesis and provides a description and discussion of the main types of microwave acoustic resonators. Starting from describing the two technologies that currently populate mobile devices RF-FEMs, BAW and SAW, to the more recent plate wave resonators exploiting Lamb and shear horizontal waves, the description presents the main advantages and disadvantages of each resonator type along their main frequency ranges of application. In line with the mentioned open challenges in microwave acoustics, the consideration of plate wave resonators is mainly driven by the possibility to attain higher electromechanical coupling values than those obtained with regular AlN BAW or $LiTaO_3$ SAW. In this context, with the double objective of diving into the physical considerations of acoustic resonator design and to characterize a platform to demonstrate the synthesis techniques proposed in this thesis, this chapter also presents fabricated examples of lithium niobate on insulator resonators exploiting the zeroth order shear horizontal mode at 1.5 GHz and discusses the design process from selecting the crystalline cut to the impact of both electrode thickness and IDT apodization on spurious mode excitation. The main outcomes of this discussion are that electrode thickness is a key factor to attain resonators without spurious modes above f_p, thanks to a reduction in phase velocity of the SH_0 mode for thicker electrodes hence leading unwanted modes into the stopband of the gratings, and that IDT apodization at a ratio of 60% is an optimum choice to suppress spurious transverse modes within the IDT without affecting the achievable electromechanical coupling. The overall performance figures of the proposed L-band resonators are $k^2_{\text{eff}} = 17\%$ and $Q_{\text{max}} \sim 750$, very promising results for further development of the resonator platform.

After the discussion of the physical side of this thesis, Ch. 3 provides the conceptual introduction to network synthesis techniques applied to acoustic wave filters presenting the circuital extraction technique that is exploited along the subsequent chapters of the work. At first, the chapter provides a brief historical introduction to network synthesis to accurately situate the development of the field and then presents the mathematical foundations that allow to extract the BVD model elements of all resonators that compose a filter implementing a given transfer function defined at the polynomial level. Besides the circuital extraction technique based on ABCD matrices the chapter also focuses on the generalized Chebyshev function as the filter function to be implemented and the method to compute it. Therefore, the chapter provides the connection between microwave networks and the mathematical representation of their responses. After presenting these concepts, examples of

acoustic wave ladder filters are provided to demonstrate that the key input variables to obtain a synthesized filter in which all resonators require the same k^2_{eff} value are not only transmission zeros and return loss value but also reflection phase.

Having briefly introduced the fact that controlling reflection phase has an impact on the outcome of the synthesis procedure, thus enabling to obtain two exact filter responses in terms of magnitude with different BVD elements, as demonstrated, Ch. 4 dives deep into the many impacts reflection phase has on AW filter synthesis and proposes methods in which they can be exploited. At first, the traditional case of duplexer-oriented design by controlling the input reflection phase of the two transfer functions to be duplexed is discussed but only for filters starting in series. The most common case. However, the chapter then discusses the synthesis of filters starting in shunt resonator and demonstrates that for them to be feasible in terms of microwave acoustic technology, that is, requiring all resonators to have a capacitive static arm, the intrinsic phase of a generalized Chebyshev function requires a modification. Through the discussion of the so-called feasibility plots, this work demonstrates that shunt-starting ladder filters require reflection phases towards 180° and then proposes rules to design shunt-starting duplexer-oriented filters. In line with many examples in the literature that show shunt-starting ladder filters featuring two reactive elements at the input port, the discussion demonstrates that such a double-element approach is necessary when facing a duplexer design with a shunt starting filter and proposes the method to synthesize it.

Building on the concepts extracted from the previous discussion, the chapter then proposes an alternative use of reflection phase that allows to compose dual band devices. In this case, by carefully considering the input and output reflection phases of two ladder filters, each implementing a given passband, through an specific formulation that allows to modify the phase term of S_{11} and S_{22}, independently, the duplexer-oriented phase condition introduced at the beginning of the chapter is exploited to duplex both at input and output and thus effectively achieve a device with two passbands. The main drawback to this approach is the fact that the out-of-band rejection of the final dual band response is not controlled from a synthesis perspective and is dominated by the least rejecting filter of the two ladders being connected. As a closing remark on this topic, the chapter also references a contribution by the group hosting this thesis that extends this view to dual band devices by proposing a complete synthesis of a dual band response with a simple ladder topology of acoustic resonators.

The final part of Ch. 4 is devoted to an interesting exploit of reflection phase that originates in the feasibility considerations derived for shunt-starting ladder filters. As demonstrated in the initial discussion, if the reflection phase of the generalized Chebyshev function is not properly considered, unfeasible BVD elements are obtained for the first and/or last resonators of the filter. Similarly, unfeasible BVD elements are also obtained if one tries to impose that a series resonator, for example, places a transmission zero below the passband while keeping its resonance frequency inside it. Considering the two facts, the discussion demonstrates how both reasons for resonator unfeasibility can

counter each other, in an exercise of double negation, to achieve ladder filters showing transmission zeros at uncommon positions. This interesting behaviour, that also shows promising features in terms of the achieved impedance values for resonators, is demonstrated with examples and with a manufactured filter using the lithium niobate on insulator platform discussed in Ch. 2. The filter is a third order device starting in shunt resonator that features two transmission zeros above the passband and a single one below.

Finally, Ch. 5 is devoted to a multiport network view of synthesis to propose a multiplexer synthesis methodology extending the current synthesis techniques that focus on two-port networks. The proposed technique is based on the computation of the complete multiplexer response in the normalized domain instead of a single passband response such that from the normalized multiport network a set of distorted channel functions can be derived. The distorted response is the one that each channel connected in the multiplexer must have such that when all channels are connected together, the desired multiplexer response is achieved. To this end, the formulation in this chapter is derived assuming a star junction topology, the most common topology in AW multiplexers, and an iterative method to compute the desired multiplexer response in the normalized domain is provided. From the multiport function, the method to derive the channel polynomials is provided and demonstrated with a Band 3 and Band 1 quadplexer example. In parallel to the method, the chapter also discusses the application of cepstral analysis to the computation of Feldtkeller's equation in order to achieve a maximum stable order of 35, allowing to synthesize pentaplexers with seventh order channels. The results obtained with the multiplexer synthesis method are very promising and open a long list of open topics for further research.

6.1 Future Work

In contrast to more traditional approaches to filter design based on brute-force optimization, synthesis techniques have demonstrated very powerful capabilities and are currently in use by some industrial players in the RF-FEM market. Backed by such interest, this thesis demonstrates advances in acoustic filter synthesis techniques and further extends them to consider even more complex networks with multiple ports. Whereas a closed theoretical description of the proposed techniques is provided in this thesis, multiple paths for further research need to be considered and are listed below as topics for further work.

Starting from a synthesis perspective, note that the process begins by the computation of the transfer function to implement. Because the generalized Chebyshev function is the optimum function in terms of flexibility in transmission zero definition and achievable out-of-band rejection it has traditionally been the function to exploit in any synthesis method for acoustic wave filters. However, note also that the proposed multiplexer synthesis method entails departing from perfectly equiripple filters and implementing clearly distorted responses. In the case of multiplexers, such distortion is

mandated by the loading of other filters at the common port. However, considering the particularities of microwave acoustic technology (consider homogeneous k^2_{eff} within the filter or size reduction, to name a few) departing from the generalized Chebyshev function is a path to explore with the aim of attaining responses that might be more attractive and, to this end, approaches such as the Remez algorithm have gained attention in recent times within microwave filter community.

Regarding the proposed multiplexer synthesis method, many open topics can be considered for further development. While some of them are already mentioned throughout Ch. 5, let us highlight the most important two. As discussed in the chapter, the proposed multiport synthesis technique derives the computation to obtain the distorted channel polynomials from the multiport function by assuming that the multiplexer topology to implement is a star junction. Such an assumption is the most common multiplexer configuration in the context of acoustic wave devices but the so-called herringbone topology, in which some channels are placed after suitable phase shifting sections, is also very interesting. In this scope, generalizing the method to allow the derivation of channels to be connected in a herringbone configuration with phase shift section of predefined value, is a very important topic to be addressed.

In parallel to multiplexer configuration, the other important topic to address is the numerical stability of the method and the maximum function order it can handle. Thanks to the cepstrum technique, numerical accuracy problems with root computation can be avoided up to order 35 but extending such maximum order is important to allow the consideration of higher order channels in the already considered quadplexer structures and to extend the number of bands considered in the multiport function. Extended numerical precision techniques are interesting for this objective but need careful consideration due to the use of FFT for the cepstrum method. Therefore, a careful mathematical consideration of the optimal method to compute the roots of the multiport function is a very interesting topic to consider.

Considering the manufactured devices presented in this thesis, the possibilities to improve resonator performance are multiple. At first, improving electrode conductivity and film quality is fundamental to improve resonator Q specially at the resonance frequency. Moreover, for a more complete depiction of the possibilities of the proposed platform, more complex responses with higher order can be addressed.

From a resonator structure perspective, to depart from the solidly-mounted structure already considered, further work is required to attain released membrane SH_0 resonators by etching through lithium niobate to etch the silicon underneath the resonator. In this case, the electrode thickness and IDT apodization conclusions provided in this thesis apply and improved k^2_{eff} and Q values are expected due to a better confinement of the wave. As a closing point, having explored the platform at the L band to avoid additional manufacturing complexities, scaling the SH_0 resonators up into the 7 to 10 GHz range is a topic of interest.

APPENDIX A

A.1 Polynomial Para-conjugation

Consider an N-th degree polynomial $Q(s)$ on $s = \Sigma + j\Omega$ and complex coefficients q_i for $i = 0,\ 1,\ 2, ...,\ N$. Then, operation $Q(s)^*$ is equivalent to $Q^*(-s)$. That is conjugating coefficients and changing sign on variable s. For example,

$$\begin{aligned} Q(s)^* = Q^*(-s) &= q_0^* - q_1^* s + q_2^* s^2 + ... + q_N^* s^N \text{for } N \text{ even} \\ Q(s)^* = Q^*(-s) &= q_0^* - q_1^* s + q_2^* s^2 + ... - q_N^* s^N \text{for } N \text{ odd} \end{aligned} \tag{A.1}$$

As the conjugation operation, noted $Q^*(s)$ reflects the roots of $Q(s)$ about the real axis, the para-conjugation operation, namely $Q(s)^*$ reflects the roots of $Q(s)$ about the imaginary axis. If the N complex-plane roots of $Q(s)$ are r_k, for $k = 0,\ 1,\ 2, ...,\ N$, then the para-conjugated roots will be $-r_k^*$. Then, during the construction of $Q(s)^*$ from the para-conjugated roots, term $(-1)^N$ must multiply the resulting polynomial to ensure the correct sign of the leading coefficient.

$$Q(s)^* = Q^*(-s) = (-1)^N \prod_{k=1}^{N} (s + r_k^*)$$

A.2 ABCD Polynomials

The transfer function of a two-port network connected between unitary terminations can be expressed in terms of an [ABCD] matrix as

$$[ABCD] = \frac{1}{jP(s)/\varepsilon} \begin{bmatrix} A(s) & B(s) \\ C(s) & D(s) \end{bmatrix}$$

where polynomials $A(s)$, $B(s)$, $C(s)$ and $D(s)$ are closely related to the coefficients of characteristic polynomials $E(s)$ and $F(s)/\varepsilon_r$.

In [9] (Ch.7), the following expressions are outlined to construct the [ABCD] polynomials for networks that might include FIRs.

$$A(s) = j\mathrm{Im}(e_0 + f_0) + \mathrm{Re}(e_1 + f_1)s + j\mathrm{Im}(e_2 + f_2)s^2 + \cdots + j\mathrm{Im}(e_N + f_N)s^N \tag{A.2a}$$
$$B(s) = \mathrm{Re}(e_0 + f_0) + j\mathrm{Im}(e_1 + f_1)s + \mathrm{Re}(e_2 + f_2)s^2 + \cdots + \mathrm{Re}(e_N + f_N)s^N \tag{A.2b}$$
$$C(s) = \mathrm{Re}(e_0 - f_0) + j\mathrm{Im}(e_1 - f_1)s + \mathrm{Re}(e_2 - f_2)s^2 + \cdots + \mathrm{Re}(e_N - f_N)s^N \tag{A.2c}$$
$$D(s) = j\mathrm{Im}(e_0 - f_0) + \mathrm{Re}(e_1 - f_1)s + j\mathrm{Im}(e_2 - f_2)s^2 + \cdots + j\mathrm{Im}(e_N - f_N)s^N \tag{A.2d}$$

for N even, and

$$A(s) = \mathrm{Re}(e_0 + f_0) + j\mathrm{Im}(e_1 + f_1)s + \mathrm{Re}(e_2 + f_2)s^2 + \cdots + \mathrm{Re}(e_N + f_N)s^N \tag{A.3a}$$
$$B(s) = j\mathrm{Im}(e_0 + f_0) + \mathrm{Re}(e_1 + f_1)s + j\mathrm{Im}(e_2 + f_2)s^2 + \cdots + j\mathrm{Im}(e_N + f_N)s^N \tag{A.3b}$$
$$C(s) = j\mathrm{Im}(e_0 - f_0) + \mathrm{Re}(e_1 - f_1)s + j\mathrm{Im}(e_2 - f_2)s^2 + \cdots + j\mathrm{Im}(e_N - f_N)s^N \tag{A.3c}$$
$$D(s) = \mathrm{Re}(e_0 - f_0) + j\mathrm{Im}(e_1 - f_1)s + \mathrm{Re}(e_2 - f_2)s^2 + \cdots + \mathrm{Re}(e_N - f_N)s^N \tag{A.3d}$$

for N odd.

On the other hand, if the characteristic polynomials are defined using the asymmetric definition of the phase exploited in Ch. 4, the computation of the [ABCD] polynomials is redefined as follows [25]:

$$A(s) = \frac{(E'(s) + F'_{11}(s))\,(E'(s) - F'_{22}(s)) + P^2(s)}{2E'(s)} \tag{A.4a}$$
$$B(s) = \frac{(E'(s) + F'_{11}(s))\,(E'(s) + F'_{22}(s)) - P^2(s)}{2E'(s)} \tag{A.4b}$$
$$C(s) = \frac{(E'(s) - F'_{11}(s))\,(E'(s) - F'_{22}(s)) - P^2(s)}{2E'(s)} \tag{A.4c}$$
$$D(s) = \frac{(E'(s) - F'_{11}(s))\,(E'(s) + F'_{22}(s)) + P^2(s)}{2E'(s)} \tag{A.4d}$$

Bibliography

[1] Ericsson, "Ericsson Mobility Report," Ericsson, Tech. Rep., Nov. 2022. [Online]. Available: https://www.ericsson.com/en/reports-and-papers/mobility-report/reports/november-2022

[2] C. Shannon, "Communication in the presence of noise," *Proc. IRE*, vol. 37, no. 1, pp. 10–21, Jan. 1949.

[3] S. Haykin and M. Moher, *Communication Systems*. Wiley, 2009.

[4] *User Equipment UE radio transmission and reception - Part 1: Range 1 Standalone (3GPP TS 38.101-1 version 17.7.0 Release 17) [Retrieved 01/01/2023]*, 3GPP Std. [Online]. Available: https://www.etsi.org/deliver/etsi_ts/138100_138199/13810101/17.07.00_60/ts_13810101v170700p.pdf

[5] *User Equipment UE radio transmission and reception - Part 2: Range 2 Standalone (3GPP TS 38.101-2 version 17.7.0 Release 17) [Retrieved 01/01/2023]*, 3GPP Std. [Online]. Available: https://www.etsi.org/deliver/etsi_ts/138100_138199/13810102/17.07.00_60/ts_13810102v170700p.pdf

[6] E. Dahlman, S. Parkvall, and J. Skold, *5G NR: The Next Generation Wireless Access Technology*. Academic Press, 2021.

[7] FCC. (2022) Table of Radio Spectrum Allocations. Federal Communications Commission. [Online]. Available: https://www.fcc.gov/file/21474/download

[8] Qorvo Inc. (2017) Qorvo 2017 Investor Day Presentation. Online. [Online]. Available: https://ir.qorvo.com/static-files/a3197955-4218-4e14-875f-5a52ad999408

[9] R. J. Cameron, C. M. Kudsia, and R. R. Mansour, *Microwave Filters for Communication Systems*. Wiley, 2018.

[10] R. Ruby, "A snapshot in time: The future in filters for cell phones," *IEEE Microw. Mag.*, vol. 16, no. 7, pp. 46–59, Aug. 2015.

[11] P. Warder and A. Link, "Golden age for filter design: Innovative and proven approaches for acoustic filter, duplexer, and multiplexer design," *IEEE Microw. Mag.*, vol. 16, no. 7, pp. 60–72, Aug. 2015.

[12] T. Bauer, C. Eggs, K. Wagner, and P. Hagn, "A bright outlook for acoustic filtering: A new generation of very low-profile SAW, TC SAW, and BAW devices for module integration," *IEEE Microw. Mag.*, vol. 16, no. 7, pp. 73–81, Aug. 2015.

[13] G. G. Fattinger, A. Volatier, M. Al-Joumayly, Y. Yusuf, R. Aigner, N. Khlat, and M. Granger-Jones, "Carrier aggregation and its challenges - or: The golden age for acoustic filters," in *IEEE MTT-S Int. Microw. Symp. Dig.*, 2016.

[14] S. Butterworth, "On electrically-maintained vibrations," *Proc. Phys. Soc. London*, no. 27, p. 410, 1914.

[15] K. S. van Dyke, "The piezo-electric resonator and its equivalent network," *Proc. IRE*, vol. 16, no. 6, pp. 742–764, Jun. 1928.

[16] J. Larson, P. Bradley, S. Wartenberg, and R. Ruby, "Modified Butterworth-Van Dyke circuit for FBAR resonators and automated measurement system," in *Proc. IEEE Int. Ultrason. Symp.*, 2000, pp. 863 – 868.

[17] K. Hashimoto, *RF Bulk Acoustic Wave Filters for Communications*. Artech House Books, 2009.

[18] R. Lu, M.-H. Li, Y. Yang, T. Manzaneque, and S. Gong, "Accurate extraction of large electromechanical coupling in piezoelectric MEMS resonators," *J. Microelectromech. Syst.*, vol. 28, no. 2, pp. 209–218, Apr. 2019.

[19] G. Matthaei, L. Young, and E. Jones, *Microwave Filters, Impedance-matching Networks, and Coupling Structures*, ser. Artech House Microwave Library. Artech House Books, 1980.

[20] I. Hunter, *Theory and Design of Microwave Filters*. Institution of Engineering and Technology, 2001.

[21] E. Corrales López, "Analysis and design of bulk acoustic wave filters based on acoustically coupled resonators," Ph.D. dissertation, Universitat Autònoma de Barcelona, 2011.

[22] M. Jimenez Blasco, "A coupling matrix vision for mobile filtering devices with micro-acoustic wave technologies. a systematic approach," Ph.D. dissertation, Universitat Autònoma de Barcelona, 2015.

[23] A. R. Giménez Bonastre, "RF filters and multiplexers based on acoustic wave technologies with ladder-type and cross-coupled topologies. Designing under a systematic strategy," Ph.D. dissertation, Universitat Autònoma de Barcelona, 2016.

[24] I. Evdokimova, "Direct bandpass methodology for synthesis and design of stand-alone filters and duplexers based on acoustic wave technologies," Ph.D. dissertation, Universitat Autònoma de Barcelona, 2018.

[25] A. Triano Notario, "Advanced synthesis techniques for parallel-connected and cross-coupled filters based on acoustic wave technologies," Ph.D. dissertation, Universitat Autònoma de Barcelona, 2020.

[26] P. Silveira Taboadela, "Systematic design methodology for acoustic wave filters integrated in multiplexers and codesigned modules," Ph.D. dissertation, Universitat Autònoma de Barcelona, 2021.

[27] A. Giménez and P. de Paco, "Involving source-load leakage effects to improve isolation in ladder acoustic wave filters," in *IEEE MTT-S Int. Microw. Symp. Dig.*, 2016.

[28] A. Triano, J. Verdu, P. de Paco, T. Bauer, and K. Wagner, "Relation between electromagnetic coupling effects and network synthesis for AW ladder type filters," in *Proc. IEEE Int. Ultrason. Symp.*, 2017.

[29] V. M. Ristic, *Principles of Acoustic Devices*. Wiley, 1983.

[30] W. Cady, "The piezo-electric resonator," *Proceedings of the IRE*, vol. 10, no. 2, pp. 83–114, 1922.

[31] W. P. Mason, "Electrical wave filters employing quartz crystals as elements," *Bell System Technical Journal*, vol. 13, no. 3, pp. 405–452, 1934.

[32] L. Espenschied, "Electrical wave filter," U.S. US Patent US1 795 204A, 1931.

[33] W. Mason, *Electromechanical Transducers and Wave Filters*, ser. Bell Telephone Laboratories series. D. Van Nostrand Company, 1948.

[34] D. Morgan, *Surface Acoustic Wave Filters*. Academic Press, 2007.

[35] R. M. White and F. W. Voltmer, "Direct piezoelectric coupling to surface elastic waves," *Appl. Phys. Lett.*, vol. 7, no. 12, pp. 314–316, Dec. 1965.

[36] C. C. W. Ruppel, "Acoustic wave filter technology–a review," *IEEE Trans. Ultrason., Ferroelectr., Freq. Control*, vol. 64, no. 9, pp. 1390–1400, Sep. 2017.

[37] E. Ash, "Surface wave grating reflectors and resonators," in *IEEE MTT-S Int. Microw. Symp. Dig.*, 1970.

[38] M. Berté, "Acoustic bulk wave resonators and filters operating in the fundamental mode at frequencies greater than 100 MHz," in *Proc. IEEE Intl. Freq. Control Symp.*, 1977.

[39] K. Lakin and J. Wang, "UHF composite bulk wave resonators," in *Proc. IEEE Int. Ultrason. Symp.*, 1980.

[40] R. Ruby and P. Merchant, "Micromachined thin film bulk acoustic resonators," in *Proc. IEEE Intl. Freq. Control Symp.*, 1994.

[41] W. Newell, "Tuned integrated circuits—a state-of-the-art survey," *Proceedings of the IEEE*, vol. 52, no. 12, pp. 1603–1608, 1964.

[42] K. Lakin, K. McCarron, and R. Rose, "Solidly mounted resonators and filters," in *Proc. IEEE Int. Ultrason. Symp.*, vol. 2, 1995, pp. 905–908.

[43] R. Thurston, "Historical note: Warren P. Mason (1900-1986) physicist, engineer, inventor, author, teacher," *IEEE Trans. Ultrason., Ferroelectr., Freq. Control*, vol. 41, no. 4, pp. 425–434, Jul. 1994.

[44] D. Morgan, "History of SAW devices," in *Proc. IEEE Intl. Freq. Control Symp.*, 1998.

[45] R. Weigel, D. Morgan, J. Owens, A. Ballato, K. Lakin, K. Hashimoto, and C. Ruppel, "Microwave acoustic materials, devices and applications," *IEEE Trans. Microw. Theory Techn.*, vol. 50, no. 3, pp. 738–749, Mar. 2002.

[46] C. S. McGahey, "Harnessing nature's timekeeper: a history of the piezoelectric quartz crystal technological community (1880-1959)," Ph.D. dissertation, Georgia Institute of Technology, 2009.

[47] J. F. Rosenbaum, *Bulk Acoustic Wave Theory and Devices*. Artech House, 1988.

[48] J. Verdú Tirado, "Bulk acoustic wave resonators and their application to microwave devices," Ph.D. dissertation, Universitat Autònoma de Barcelona, 2010.

[49] W. Smith, H. Gerard, J. Collins, T. Reeder, and H. Shaw, "Analysis of interdigital surface wave transducers by use of an equivalent circuit model," *IEEE Trans. Microw. Theory Techn.*, vol. 17, no. 11, pp. 856–864, Nov. 1969.

[50] K. Hashimoto, *Surface Acoustic Wave Devices in Telecommunications*. Springer Berlin Heidelberg, 2000.

[51] H. Bhugra and G. Piazza, Eds., *Piezoelectric MEMS Resonators*. Springer International Publishing, 2017.

[52] D. A. Feld, R. Parker, R. Ruby, P. Bradley, and S. Dong, "After 60 years: A new formula for computing quality factor is warranted," in *Proc. IEEE Int. Ultrason. Symp.*, 2008.

[53] R. Ruby, R. Parker, and D. Feld, "Method of extracting unloaded Q applied across different resonator technologies," in *Proc. IEEE Int. Ultrason. Symp.*, 2008.

[54] R. Jin, Z. Cao, M. Patel, B. Abbott, D. Molinero, and D. Feld, "An improved formula for estimating stored energy in a BAW resonator by its measured S11 parameters," in *Proc. IEEE Int. Ultrason. Symp.*, 2021.

[55] T. Pensala, "Thin film bulk acoustic wave devices. performance optimization and modeling," Ph.D. dissertation, Aalto University, Finland, 2011.

[56] K. Hashimoto, H. Asano, K. Matsuda, N. Yokoyama, T. Omori, and M. Yamaguchi, "Wideband love wave filters operating in GHz range on Cu-grating/rotated-YX-$LiNbO_3$-substrate structure," in *Proc. IEEE Int. Ultrason. Symp.*, 2004.

[57] R. Aigner, G. Fattinger, M. Schaefer, K. Karnati, R. Rothemund, and F. Dumont, "BAW filters for 5G bands," in *Int. Electron Devices Meet.*, 2018.

[58] A. Tag, M. Schaefer, J. Sadhu, A. Tajic, P. Stokes, M. Koohi, W. Yusuf, W. Heeren, H. Fatemi, F. Celii, J. Trujillo, C. Chanseob, Y. He, E. Silbar, E. Fuentes, T. Berer, M. AlJoumayly, and R. Rothemund, "Next generation of BAW: The new benchmark for RF acoustic technologies," in *Proc. IEEE Int. Ultrason. Symp.*, 2022.

[59] M. Akiyama, T. Kamohara, K. Kano, A. Teshigahara, Y. Takeuchi, and N. Kawahara, "Enhancement of piezoelectric response in scandium aluminum nitride alloy thin films prepared by dual reactive cosputtering," *Adv. Mater.*, vol. 21, no. 5, pp. 593–596, Dec. 2008.

[60] G. Fattinger, S. Marksteiner, J. Kaitila, and R. Aigner, "Optimization of acoustic dispersion for high performance thin film BAW resonators," in *Proc. IEEE Int. Ultrason. Symp.*, 2005.

[61] G. G. Fattinger, "BAW resonator design considerations - an overview," in *Proc. IEEE Intl. Freq. Control Symp.*, 2008.

[62] S. Marksteiner, J. Kaitila, G. Fattinger, and R. Aigner, "Optimization of acoustic mirrors for solidly mounted BAW resonators," in *Proc. IEEE Int. Ultrason. Symp.*, vol. 1, 2005, pp. 329–332.

[63] R. Aigner, "SAW and BAW technologies for RF filter applications: A review of the relative strengths and weaknesses," in *Proc. IEEE Int. Ultrason. Symp.*, 2008, pp. 582 – 589.

[64] F. Bi and B. Barber, "Bulk acoustic wave RF technology," *IEEE Microw. Mag.*, vol. 9, no. 5, pp. 65–80, Oct. 2008.

[65] R. Ruby, P. Bradley, Y. Oshmyansky, A. Chien, and J. Larson, "Thin film bulk wave acoustic resonators (FBAR) for wireless applications," in *Proc. IEEE Int. Ultrason. Symp.*, 2001.

[66] R. Ruby, M. Small, F. Bi, D. Lee, L. Callaghan, R. Parker, and S. Ortiz, "Positioning FBAR technology in the frequency and timing domain," *IEEE Trans. Ultrason., Ferroelectr., Freq. Control*, vol. 59, no. 3, pp. 334–345, Mar. 2012.

[67] G. Kovacs, M. Anhorn, H. Engan, G. Visintini, and C. Ruppel, "Improved material constants for $LiNbO_3$ and $LiTaO_3$," in *Proc. IEEE Int. Ultrason. Symp.*, 1990.

[68] K. Hashimoto, M. Kadota, T. Nakao, M. Ueda, M. Miura, H. Nakamura, H. Nakanishi, and K. Suzuki, "Recent development of temperature compensated SAW devices," in *Proc. IEEE Int. Ultrason. Symp.*, 2011.

[69] T. Takai, H. Iwamoto, Y. Takamine, H. Yamazaki, T. Fuyutsume, H. Kyoya, T. Nakao, H. Kando, M. Hiramoto, T. Toi, M. Koshino, and N. Nakajima, "Incredible high performance SAW resonator on novel multi-layerd substrate," in *Proc. IEEE Int. Ultrason. Symp.*, 2016.

[70] T. Takai, H. Iwamoto, Y. Takamine, T. Wada, M. Hiramoto, M. Koshino, and N. Nakajima, "Investigations on design technologies for SAW quadplexer with narrow duplex gap," in *IEEE MTT-S Int. Microw. Symp. Dig.*, 2016.

[71] E. Butaud, S. Ballandras, M. Bousquet, A. Drouin, B. Tavel, I. Huyet, A. Clairet, I. Bertrand, A. Ghorbel, and A. Reinhardt, "Innovative Smart Cut™ piezo on insulator (POI) substrates for 5G acoustic filters," in *Int. Electron Devices Meet.*, 2020, pp. 34.6.1–34.6.4.

[72] A. A. Nassar, "Excitation of surface waves with piezoeletric layers," Ph.D. dissertation, McGill University, 1983.

[73] E. Adler, "Electromechanical coupling to lamb and shear-horizontal modes in piezoelectric plates," *IEEE Trans. Ultrason., Ferroelectr., Freq. Control*, vol. 36, no. 2, pp. 223–230, Mar. 1989.

[74] Y. Jin and S. Joshi, "Propagation of a quasi-shear horizontal acoustic wave in Z-X lithium niobate plates [and conductivity sensor application]," *IEEE Trans. Ultrason., Ferroelectr., Freq. Control*, vol. 43, no. 3, pp. 491–494, May. 1996.

[75] I. Kuznetsova, B. Zaitsev, S. Joshi, and I. Borodina, "Investigation of acoustic waves in thin plates of lithium niobate and lithium tantalate," *IEEE Trans. Ultrason., Ferroelectr., Freq. Control*, vol. 48, no. 1, pp. 322–328, Jan. 2001.

[76] V. Yantchev and I. Katardjiev, "Design and fabrication of thin film lamb wave resonators utilizing longitudinal wave and interdigital transducers," in *Proc. IEEE Int. Ultrason. Symp.*, 2005.

[77] V. Yantchev and I. Katardjiev, "Micromachined thin film plate acoustic resonators utilizing the lowest order symmetric lamb wave mode," *IEEE Trans. Ultrason., Ferroelectr., Freq. Control*, vol. 54, no. 1, pp. 87–95, Jan. 2007.

[78] M. Kadota, T. Ogami, and T. Kimura, "Ultra wide band elastic resonators and their application: SH_0 mode plate wave resonators with ultra wide bandwidth of 29%," in *Proc. ISAF-ECAPD-PFM*, 2012.

[79] M. Kadota, T. Ogami, T. Kimura, and K. Daimon, "Tunable filters using wideband elastic resonators," *IEEE Trans. Ultrason., Ferroelectr., Freq. Control*, vol. 60, no. 10, pp. 2129–2136, Oct. 2013.

[80] M. Kadota and S. Tanaka, "Ultra-wideband ladder filter using SH_0 plate wave in thin $LiNbO_3$ plate and its application to tunable filter," *IEEE Trans. Ultrason., Ferroelectr., Freq. Control*, vol. 62, no. 5, pp. 939–946, May. 2015.

[81] S. Gong and G. Piazza, "Design and analysis of lithium–niobate-based high electromechanical coupling RF-MEMS resonators for wideband filtering," *IEEE Trans. Microw. Theory Techn.*, vol. 61, no. 1, pp. 403–414, Jan. 2013.

[82] S. Gong and G. Piazza, "Figure-of-merit enhancement for laterally vibrating lithium niobate MEMS resonators," *IEEE Trans. Electron Devices*, vol. 60, no. 11, pp. 3888–3894, Nov. 2013.

[83] Y. Yang, R. Lu, L. Gao, and S. Gong, "4.5 GHz lithium niobate MEMS filters with 10% fractional bandwidth for 5G front-ends," *J. Microelectromech. Syst.*, vol. 28, no. 4, pp. 575–577, Aug. 2019.

[84] R. Lu and S. Gong, "A 15.8 GHz A6 mode resonator with Q of 720 in complementarily oriented piezoelectric lithium niobate thin films," in *Proc. IEEE Intl. Freq. Control Symp.*, 2021.

[85] V. Plessky, S. Yandrapalli, P. Turner, L. Villanueva, J. Koskela, and R. Hammond, "5 GHz laterally-excited bulk-wave resonators (XBARs) based on thin platelets of lithium niobate," *Electron. Lett.*, vol. 55, no. 2, pp. 98–100, Jan. 2019.

[86] A. Kochhar, A. Mahmoud, Y. Shen, N. Turumella, and G. Piazza, "X-cut lithium niobate-based shear horizontal resonators for radio frequency applications," *J. Microelectromech. Syst.*, vol. 29, no. 6, pp. 1464–1472, Dec. 2020.

[87] T.-H. Hsu, K.-J. Tseng, and M.-H. Li, "Large coupling acoustic wave resonators based on $LiNbO_3/SiO_2/Si$ functional substrate," *IEEE Electron Device Lett.*, vol. 41, no. 12, pp. 1825–1828, Dec. 2020.

[88] S. Zhang, R. Lu, H. Zhou, S. Link, Y. Yang, Z. Li, K. Huang, X. Ou, and S. Gong, "Surface acoustic wave devices using lithium niobate on silicon carbide," *IEEE Trans. Microw. Theory Techn.*, vol. 68, no. 9, pp. 3653–3666, Sep. 2020.

[89] R. Su, J. Shen, Z. Lu, H. Xu, Q. Niu, Z. Xu, F. Zeng, C. Song, W. Wang, S. Fu, and F. Pan, "Wideband and low-loss surface acoustic wave filter based on 15^o YX-$LiNbO_3/SiO_2/Si$ structure," *IEEE Electron Device Lett.*, vol. 42, no. 3, pp. 438–441, Mar. 2021.

[90] J. Zou, V. Yantchev, F. Iliev, V. Plessky, S. Samadian, R. B. Hammond, and P. J. Turner, "Ultra-large-coupling and spurious-free SH_0 plate acoustic wave resonators based on thin $LiNbO_3$," *IEEE Trans. Ultrason., Ferroelectr., Freq. Control*, vol. 67, no. 2, pp. 374–386, Feb. 2020.

[91] J. Zou, "High-performance aluminum nitride lamb wave resonators for rf front-end technology," Ph.D. dissertation, UC Berkeley, 2015.

[92] R. Lu, Y. Yang, M.-H. Li, M. Breen, and S. Gong, "5-GHz antisymmetric mode acoustic delay lines in lithium niobate thin film," *IEEE Trans. Microw. Theory Techn.*, vol. 68, no. 2, pp. 573–589, Feb. 2020.

[93] H. J. McSkimin, "Measurement of elastic constants at low temperatures by means of ultrasonic waves–data for silicon and germanium single crystals, and for fused silica," *J. Appl. Phys.*, vol. 24, no. 8, pp. 988–997, Aug. 1953.

[94] M. Kadota, M. Esashi, S. Tanaka, Y. Kuratani, and T. Kimura, "High frequency resonators with wide bandwidth using SH_0 mode plate wave in thin $LiNbO_3$," in *Proc. IEEE Int. Ultrason. Symp.*, 2013.

[95] T. Omori, K. Matsuda, N. Yokoyama, K. ya Hashimoto, and M. Yamaguchi, "Suppression of transverse mode responses in ultra-wideband SAW resonators fabricated on a Cu-grating/15ºYX-$LiNbO_3$ structure," *IEEE Trans. Ultrason., Ferroelectr., Freq. Control*, vol. 54, no. 10, pp. 1943–1948, Oct. 2007.

[96] M. Solal, J. Gratier, R. Aigner, K. Gamble, B. Abbott, T. Kook, A. Chen, and K. Steiner, "Transverse modes suppression and loss reduction for buried electrodes SAW devices," in *Proc. IEEE Int. Ultrason. Symp.* IEEE, 2010.

[97] M. Solal, L. Chen, and J. Gratier, "Measurement and FEM/BEM simulation of transverse effects in SAW resonators on lithium tantalate," *IEEE Trans. Ultrason., Ferroelectr., Freq. Control*, vol. 60, no. 11, pp. 2404–2413, Nov. 2013.

[98] S. Stettler and L. G. Villanueva, "Transversal spurious mode suppression in ultra-large-coupling SH_0 acoustic resonators on YX36º-cut lithium niobate," *J. Microelectromech. Syst.*, pp. 1–11, 2023.

[99] M. Kadota, Y. Kuratani, T. Kimura, M. Esashi, and S. Tanaka, "Ultra-wideband and high frequency resonators using shear horizontal type plate wave in $LiNbO_3$ thin plate," *Jpn. J. Appl. Phys.*, vol. 53, no. 7, Jun. 2014.

[100] T.-H. Hsu, K.-J. Tseng, and M.-H. Li, "Wideband and high quality factor shear horizontal SAW resonators with improved temperature stability in LNOI platform," in *Proc. IEEE Intl. Freq. Control Symp.*, 2021.

[101] S. Wu, H. Qian, Z. Wu, F. Bao, G. Tang, F. Xu, and J. Zou, "Spurious-free shear-horizontal SAW resonators using $LiTaO_3/SiO_2$/Si substrate," in *Proc. IEEE Int. Ultrason. Symp.*, 2022.

[102] S. Wu, Z. Wu, H. Qian, F. Bao, G. Tang, F. Xu, and J. Zou, "High-performance SH-SAW resonator using optimized 30° YX-$LiNbO_3$/SiO_2/Si," *Appl. Phys. Lett.*, vol. 120, no. 24, Jun. 2022.

[103] R. Su, S. Fu, Z. Lu, J. Shen, H. Xu, H. Mao, Z. Xu, C. Song, F. Zeng, W. Wang, and F. Pan, "Near 30% fractional bandwidth surface acoustic wave filters with novel electrode configuration," *Progress in Natural Science: Materials International*, vol. 31, no. 6, pp. 852–857, Dec. 2021.

[104] R. H. Olsson, K. Hattar, S. J. Homeijer, M. Wiwi, M. Eichenfield, D. W. Branch, M. S. Baker, J. Nguyen, B. Clark, T. Bauer, and T. A. Friedmann, "A high electromechanical coupling coefficient SH_0 Lamb wave lithium niobate micromechanical resonator and a method for fabrication," *Sensors and Actuators A: Physical*, vol. 209, pp. 183–190, Mar. 2014.

[105] Y. Song and S. Gong, "Spurious mode suppression in SH_0 lithium niobate laterally vibrating MEMS resonators," in *Int. Electron Devices Meet.*, 2015.

[106] M. Faizan and L. G. Villanueva, "Optimization of inactive regions of lithium niobate shear mode resonator for quality factor enhancement," *J. Microelectromech. Syst.*, vol. 30, no. 3, pp. 369–374, Jun. 2021.

[107] S. Stettler and L. G. Villanueva, "Optimization of edge profile for improved anti-resonance quality factor in lithium niobate SH_0 resonators," in *Proc. IEEE Int. Ultrason. Symp.* IEEE, 2022.

[108] J. Shen, S. Fu, R. Su, H. Xu, Z. Lu, Z. Xu, J. Luo, F. Zeng, C. Song, W. Wang, and F. Pan, "High-performance surface acoustic wave devices using $LiNbO_3$/SiO_2/SiC multilayered substrates," *IEEE Trans. Microw. Theory Techn.*, vol. 69, no. 8, pp. 3693–3705, Aug. 2021.

[109] R. Su, S. Fu, Z. Lu, J. Shen, H. Xu, Z. Xu, R. Wang, C. Song, F. Zeng, W. Wang, and F. Pan, "Over GHz bandwidth SAW filter based on 32°Y-X LN/SiO_2/poly-Si/Si heterostructure with multilayer electrode modulation," *Appl. Phys. Lett.*, vol. 120, no. 25, Jun. 2022.

[110] M. E. van Valkenburg, *Introduction to Modern Network Synthesis*. Wiley, 1965.

[111] N. Balabanian, *Network Synthesis*, ser. Electrical Engineering series. Prentice-Hall, 1958.

[112] S. Cogollos Borrás, *Fundamentos de Teoría de Filtros*. Universitat Politècnica de València, 2017.

[113] S. Darlington, "A history of network synthesis and filter theory for circuits composed of resistors, inductors, and capacitors," *IEEE Trans. Circuits. Syst.*, vol. 46, no. 1, pp. 4–13, 1999.

[114] V. Belevitch, "Summary of the history of circuit theory," *Proceedings of the IRE*, vol. 50, no. 5, pp. 848–855, 1962.

[115] W. Cauer, "Die verwirklichung von wechselstromwiderständen vorgeschriebener frequenzabhängigkeit," *Archiv für Elektrotechnik*, vol. 17, pp. 355–388, 1926.

[116] R. M. Foster, "A reactance theorem," *Bell System Technical Journal*, vol. 3, no. 2, pp. 259–267, 1924.

[117] S. Darlington, "Synthesis of reactance 4-poles which produce prescribed insertion loss characteristics: Including special applications to filter design," *Journal of Mathematics and Physics*, vol. 18, pp. 257–353, 1939.

[118] R. Levy and S. Cohn, "A history of microwave filter research, design, and development," *IEEE Trans. Microw. Theory Techn.*, vol. 32, no. 9, pp. 1055–1067, Sep. 1984.

[119] S. B. Cohn, "Direct-coupled-resonator filters," *Proceedings of the IRE*, vol. 45, no. 2, pp. 187–196, 1957.

[120] I. Evdokimova, A. Giménez, J. Verdú, and P. de Paco, "Synthesis of ladder-type acoustic filters in the band-pass domain," in *Proc. 47th Eur. Microw. Conf.*, 2017, pp. 640 – 643.

[121] R. J. Cameron, "Fast generation of chebyshev filter prototypes with asymmetrically-prescribed transmission zeros," *ESA J.*, vol. 6, p. 83–95, 1982.

[122] H. Orchard and G. Temes, "Filter design using transformed variables," *IEEE Transactions on Circuit Theory*, vol. 15, no. 4, pp. 385–408, Apr. 1968.

[123] J. D. Rhodes and S. A. Alseyab, "The generalized chebyshev low-pass prototype filter," *International Journal of Circuit Theory and Applications*, vol. 8, no. 2, pp. 113–125, 1980.

[124] A. Giménez, J. Verdú, and P. de Paco, "General synthesis methodology for the design of acoustic wave ladder filters and duplexers," *IEEE Access*, vol. 6, pp. 47 969–47 979, 2018.

[125] D. M. Pozar, *Microwave Engineering*. Wiley, 2011.

[126] R. Baum, "Design of unsymmetrical band-pass filters," *IRE Transactions on Circuit Theory*, vol. 4, no. 2, pp. 33–40, 1957.

[127] R. Levy, "A generalized design technique for practical distributed reciprocal ladder networks," *IEEE Trans. Microw. Theory Techn.*, vol. 21, no. 8, pp. 519–526, Aug. 1973.

[128] A. Atia and A. Williams, "Narrow-bandpass waveguide filters," *IEEE Trans. Microw. Theory Techn.*, vol. 20, no. 4, pp. 258–265, Apr. 1972.

[129] A. Atia, A. Williams, and R. Newcomb, "Narrow-band multiple-coupled cavity synthesis," *IEEE Trans. Circuits. Syst.*, vol. 21, no. 5, pp. 649–655, 1974.

[130] R. Lanz and P. Muralt, "Bandpass filters for 8 GHz using solidly mounted bulk acoustic wave resonators," *IEEE Trans. Ultrason., Ferroelectr., Freq. Control*, vol. 52, pp. 938–948, Jun. 2005.

[131] S. Inoue, M. Iwaki, J. Tsutsumi, H. Nakamura, M. Ueda, Y. Satoh, and S. Mitobe, "A triple-beat-free PCS SAW duplexer," in *Proc. IEEE Int. Ultrason. Symp.*, 2012.

[132] S. Kreuzer, A. Volatier, G. Fattinger, and F. Dumont, "Full band 41 filter with high Wi-Fi rejection - design and manufacturing challenges," in *Proc. IEEE Int. Ultrason. Symp.*, 2015.

[133] M. Iwaki, T. Tanaka, M. Ueda, and Y. Satoh, "Design consideration on converged Rx SAW duplexer module for multiband RF front end," *IEEE Trans. Microw. Theory Techn.*, vol. 65, no. 11, pp. 4629–4635, Nov. 2017.

[134] J. Rhodes and R. Cameron, "General extracted pole synthesis technique with applications to low-loss TE011 mode filters," *IEEE Trans. Microw. Theory Techn.*, vol. 28, no. 9, pp. 1018–1028, Sep. 1980.

[135] S. Amari, U. Rosenberg, and J. Bornemann, "Singlets, cascaded singlets, and the nonresonating node model for advanced modular design of elliptic filters," *IEEE Microw. Wirel. Compon. Lett.*, vol. 14, no. 5, pp. 237–239, May. 2004.

[136] S. Amari and U. Rosenberg, "Synthesis and design of novel in-line filters with one or two real transmission zeros," *IEEE Trans. Microw. Theory Techn.*, vol. 52, no. 5, pp. 1464–1478, May. 2004.

[137] S. Amari and G. Macchiarella, "Synthesis of inline filters with arbitrarily placed attenuation poles by using nonresonating nodes," *IEEE Trans. Microw. Theory Techn.*, vol. 53, no. 10, pp. 3075–3081, Oct. 2005.

[138] S. Tamiazzo and G. Macchiarella, "Synthesis of cross-coupled prototype filters including resonant and non-resonant nodes," *IEEE Trans. Microw. Theory Techn.*, vol. 63, no. 10, pp. 3408–3415, Oct. 2015.

[139] S. C. Mejillones, M. Oldoni, S. Moscato, G. Macchiarella, M. D'Amico, and G. G. Gentili, "Accurate synthesis of extracted-pole filters by topology transformations," *IEEE Microw. Wirel. Compon. Lett.*, vol. 31, no. 1, pp. 13–16, Jan. 2021.

[140] S. Caicedo Mejillones, M. Oldoni, S. Moscato, G. Macchiarella, M. D'Amico, G. G. Gentili, and G. Biscevic, "Unified analytical synthesis of cascaded n-tuplets filters including nonresonant nodes," *IEEE Trans. Microw. Theory Techn.*, vol. 69, no. 7, pp. 3275–3286, Jul. 2021.

[141] L. Acosta, E. Guerrero, P. Silveira, J. Verdú, and P. De Paco, "Synthesis methodology of AW filters for RF applications based on matrix rotations to overcome round-off errors," in *Proc. IEEE Int. Ultrason. Symp.*, 2021.

[142] A. Gimenez and P. de Paco, "A dual-TZ extraction technique for the synthesis of cross-coupled prototype filters," *IEEE Microw. Wirel. Compon. Lett.*, vol. 26, no. 10, pp. 777–779, Oct. 2016.

[143] P. Bradley, R. Ruby, J. Larson, Y. Oshmyansky, and D. Figueredo, "A film bulk acoustic resonator (FBAR) duplexer for USPCS handset applications," in *IEEE MTT-S Int. Microw. Symp. Dig.*, 2001.

[144] K. Lakin, "Thin film resonators and filters," in *Proc. IEEE Int. Ultrason. Symp.*, 1999.

[145] I. Evdokimova, J. Verdú, and P. de Paco, "Bandpass phase correction methodology for ladder-type acoustic filters," in *Proc. 48th Eur. Microw. Conf.*, 2018, pp. 683 – 686.

[146] A. Hagelauer, G. Fattinger, C. C. W. Ruppel, M. Ueda, K. Hashimoto, and A. Tag, "Microwave acoustic wave devices: Recent advances on architectures, modeling, materials, and packaging," *IEEE Trans. Microw. Theory Techn.*, vol. 66, no. 10, pp. 4548–4562, Oct. 2018.

[147] Y. Yang, R. Lu, L. Gao, and S. Gong, "A C-band lithium niobate MEMS filter with 10% fractional bandwidth for 5G front-ends," in *Proc. IEEE Int. Ultrason. Symp.*, 2019, pp. 849 – 852.

[148] Y. Yang, R. Lu, A. Kourani, and S. Gong, "Advancing lithium niobate based thin film devices for 5G front-ends," in *IEEE MTT-S Int. Microw. Symp. Dig.*, 2019.

[149] G. Macchiarella and S. Tamiazzo, "Design techniques for dual-passband filters," *IEEE Trans. Microw. Theory Techn.*, vol. 53, no. 11, pp. 3265–3271, Nov. 2005.

[150] G. Macchiarella and S. Tamiazzo, "Synthesis of dual-band filters with parallel-connected networks," in *Proc. 44th Eur. Microw. Conf.*, 2014.

[151] H. Meng, P. Zhao, K.-L. Wu, and G. Macchiarella, "Direct synthesis of complex loaded chebyshev filters in a complex filtering network," *IEEE Trans. Microw. Theory Techn.*, vol. 64, no. 12, pp. 4455–4462, Dec. 2016.

[152] J. Verdu, E. Guerrero, L. Acosta, and P. de Paco, "Exact synthesis of inline fully canonical dual-band filters using dual extracted-pole sections," *IEEE Microw. Wirel. Compon. Lett.*, vol. 31, no. 12, pp. 1255–1258, Dec. 2021.

[153] L. Acosta, E. Guerrero, C. Caballero, J. Verdu, and P. de Paco, "Dual-band acoustic wave filter synthesis based on the conventional standalone ladder topology," in *Proc. IEEE Int. Ultrason. Symp.*, 2022.

[154] L. Acosta, E. Guerrero, J. Verdú, and P. de Paco, "Topology assessment for dual-band filters based on acoustic wave resonators," *IEEE Trans. Microw. Theory Techn.*, vol. 71, no. 4, pp. 1402–1411, Apr. 2023.

[155] (2020) Band 1 / band 3 dual BAW filter (QPQ1029). Qorvo, Inc. [Online]. Available: https://www.qorvo.com/products/p/QPQ1029

[156] Y. He, G. Wang, and L. Sun, "Direct matrix synthesis approach for narrowband mixed topology filters," *IEEE Microw. Wirel. Compon. Lett.*, vol. 26, no. 5, pp. 301–303, May. 2016.

[157] A. Triano, P. Silveira, J. Verdú, and P. de Paco, "Phase correction of asymmetrical chebyshev polynomials for extracted-pole fully canonical filters," in *IEEE MTT-S Int. Microw. Symp. Dig.*, 2019.

[158] P. Bradley and S. Ye, "Resonator filter with multiple cross-couplings," U.S. US Patent US8 902 020B2, 2014.

[159] J. Verdu, P. de Paco, and Ó. Menendez, "Double-ladder filter topology for a dual-band transmission response based on bulk acoustic wave resonators," *IEEE Microw. Wirel. Compon. Lett.*, vol. 20, no. 3, pp. 151–153, Mar. 2010.

[160] K. Lakin, "A review of thin-film resonator technology," *IEEE Microw. Mag.*, vol. 4, no. 4, pp. 61–67, Dec. 2003.

[161] P. Bradley, J. Kim, S. Ye, B. Yu, K. Grannen, D. Lee, D. Hula, and W. K. Kim, "4d-1 A 6-port film bulk acoustic resonator (FBAR) multiplexer for U.S. CDMA handsets permitting use of PCS, cellband, and GPS with a single antenna," in *Proc. IEEE Int. Ultrason. Symp.*, 2006, pp. 325–328.

[162] P. Bradley, J. Kim, S. Ye, P. Nikkel, S. Bader, and C. Feng, "12e-0 2x size and cost reduction of film bulk acoustic resonator (FBAR) chips with tungsten electrodes for PCS/GPS/800 MHz multiplexers," in *Proc. IEEE Int. Ultrason. Symp.*, 2007, pp. 1144–1147.

[163] T. Jamneala, P. Bradley, D. A. Feld, D. Clark, and A. Chien, "A generic passive matching network for multiplexers," *IEEE Trans. Ultrason., Ferroelectr., Freq. Control*, vol. 54, no. 6, pp. 1272–1275, Jun. 2007.

[164] S.-Y. Tseng, M.-Y. Yang, C.-C. Hsiao, Y.-Y. Chen, and R.-B. Wu, "Design for acoustic wave multiplexers with single inductor matching network using frequency response fitting method," *IEEE Open J. of Ultrason., Ferroelectr., Freq. Control*, vol. 2, pp. 140–151, 2022.

[165] P. Silveira, J. Verdú, and P. de Paco, "Star-junction multiplexer design under minimum susceptance networks approach," in *IEEE MTT-S Int. Microw. Symp. Dig.*, 2019.

[166] G. Macchiarella and S. Tamiazzo, "Synthesis of diplexers based on the evaluation of suitable characteristic polynomials," in *IEEE MTT-S Int. Microw. Symp. Dig.*, 2006.

[167] G. Macchiarella and S. Tamiazzo, "Novel approach to the synthesis of microwave diplexers," *IEEE Trans. Microw. Theory Techn.*, vol. 54, no. 12, pp. 4281–4290, Dec. 2006.

[168] G. Macchiarella and S. Tamiazzo, "Synthesis of star-junction multiplexers," *IEEE Trans. Microw. Theory Techn.*, Dec. 2010.

[169] G. Macchiarella, "Synthesis of star-junction multiplexers," *IEEE Microw. Mag.*, vol. 12, no. 6, pp. 101–109, Oct. 2011.

[170] A. Garcia-Lamperez, M. Salazar-Palma, and T. Sarkar, "Analytical synthesis of microwave multiport networks," in *IEEE MTT-S Int. Microw. Symp. Dig.*, 2004.

[171] P. Zhao and K.-L. Wu, "An iterative and analytical approach to optimal synthesis of a multiplexer with a star-junction," *IEEE Trans. Microw. Theory Techn.*, vol. 62, no. 12, pp. 3362–3369, Dec. 2014.

[172] D. Martinez Martinez, "Méthodologies et outils de synthèse pour des fonctions de filtrage chargées par des impédances complexes," Ph.D. dissertation, Universtié de Limoges, 2019.

[173] D. M. Martinez, S. Bila, F. Seyfert, M. Olivi, O. Tantot, and L. Carpentier, "Synthesis method for manifold-coupled multiplexers," in *Proc. 49th Eur. Microw. Conf.*, 2019.

[174] M. Li, C. Bildl, B. Schleicher, T. Purtova, S. Weigand, and A. Link, "A co-designed Band 1-Band 3 carrier aggregation power amplifier quadplexer in GaAs-HBT and BAW technologies," in *IEEE MTT-S Int. Microw. Symp. Dig.*, 2016.

[175] A. Contreras-Lizárraga, W. Ouyang, W. Zhang, J. McGann, F. Matsukura, T. Tanaka, M. Li, J. Tsutsumi, and A. Canabal, "A high-performance antenna-plexer for mobile devices," in *Proc. IEEE Int. Ultrason. Symp.*, 2020.

[176] M. Li, M. El-Hakiki, D. Kalim, T. young Kim, A. Link, B. Schumann, and R. Aigner, "A fully matched LTE-a carrier aggregation quadplexer based on BAW and SAW technologies," in *Proc. IEEE Int. Ultrason. Symp.*, 2014, pp. 77 – 80.

[177] G. Matthaei and E. Cristal, *Theory and Design of Diplexers and Multiplexers*. Academic Press, 1967, pp. 237–324.

[178] Y. Yang, M. Yu, X. Yin, and Q. Wu, "On the singly terminated and complementary networks," *IEEE Trans. Microw. Theory Techn.*, vol. 67, no. 3, pp. 988–996, Mar. 2019.

[179] G. Macchiarella and S. Tamiazzo, "Synthesis of microwave duplexers using fully canonical microstrip filters," in *IEEE MTT-S Int. Microw. Symp. Dig.*, 2009.

[180] K. Wang, D. Clark, L. H. Camnitz, and P. Bradley, "A UMTS-900 duplexer," in *Proc. IEEE Int. Ultrason. Symp.*, 2008, pp. 899–902.

[181] M. Oldoni, G. Macchiarella, and S. Bellini, "Accurate computation of poles of a lossless multiport network via cepstrum analysis," *IEEE Microw. Wirel. Compon. Lett.*, vol. 23, no. 2, pp. 57–59, Feb. 2013.

[182] M. Oldoni, "Synthesis and modelling techniques for microwave filters and multiplexers," Ph.D. dissertation, Politecnico di Milano, 2013.

[183] W. H. Press, S. A. Teukolsky, W. T. Vetterling, and B. P. Flannery, *Numerical Recipes 3rd Edition: The Art of Scientific Computing*, 3rd ed. USA: Cambridge University Press, 2007.

[184] A. Oppenheim and R. Schafer, "DSP history - from frequency to quefrency: a history of the cepstrum," *IEEE Signal Processing Magazine*, vol. 21, no. 5, pp. 95–106, Sep. 2004.

[185] J. Smith, *Introduction to Digital Filters: With Audio Applications*, ser. Music signal processing series. W3K, 2007.

[186] D. Childers, D. Skinner, and R. Kemerait, "The cepstrum: A guide to processing," *Proceedings of the IEEE*, vol. 65, no. 10, pp. 1428–1443, 1977.